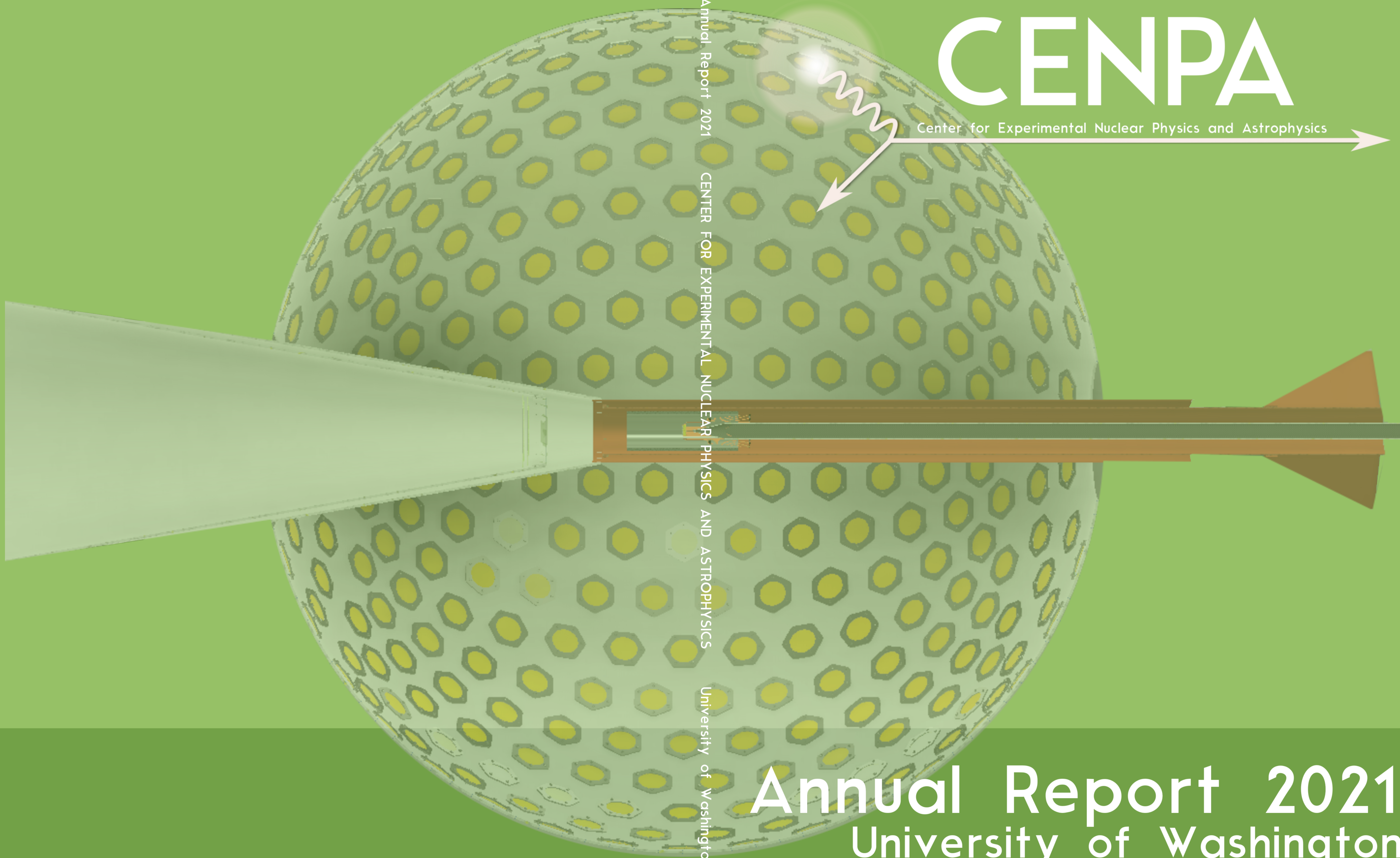

CENPA

Center for Experimental Nuclear Physics and Astrophysics

Annual Report 2021

University of Washington

Annual Report 2021 CENTER FOR EXPERIMENTAL NUCLEAR PHYSICS AND ASTROPHYSICS University of Washington

CENPA ANNUAL REPORT 2021

Center for Experimental Nuclear Physics and Astrophysics
University of Washington
March 1, 2022

Sponsored in part by the United States Department of Energy
under Grant #DE-FG02-97ER41020.

Cover: Second conceptual UW engineering design of the PIONEER liquid xenon calorimeter and pion stopping region (Sec. 4.11).

FOREWORD

We paused the production of our usual Spring Annual Report for two reasons. First, we wanted to better match the submission of our next 3-year funding proposal to DOE-NP, which is the largest grant at CENPA. That proposal was submitted in early November followng a comprehensive internal review or our science programs and progress. The second reason we delayed the Annual Report is based on the recovery pace from the COVID-19 shutdown. With improving conditions and vaccine mandates, the University of Washington transitioned in September, 2021 to full-time, normal operations and in-person classes. At CENPA, we thought it was time for another outdoor photo, complete with appropriate social distancing. While our normal Monday Meetings and Seminars remain mostly remote, CENPA labs have been buzzing, and slowly more remote work is transitioning back to campus. We are cautiously optimistic going forward, but ever mindful to keep health and safety as our top priorities. As the reader will find, there is much to share in this report. Please enjoy.

– David Hertzog –

Many members of CENPA were able to join for the return to our annual group outdoor photo in October 2021.

Back row: Grace Song, Winston DeGraw, Ryan Roehnelt, Ethan Muldoon, Clint Wiseman, Jason Detwiler, Drew Byron, Grant Leum, Nick Ruof, Sam Borden, Madison Durand, Brent Graner, Alejandro Garcia, Tim Van Wechel, Erik Shaw, David Peterson, James Sinnis

Third row: Brynn MacCoy, Alvaro Chavarria, Peter Kammel, Joshua LaBounty, Heather Harrington, Michaela Guzzetti, Conner Gettings, Matthew Kallander, Gray Rybka, Christian Nave, Charles Hanretty, Alexandru Hostiuc

Second row chairs: Eric Smith, Ida Boeckstiegel, Elise Novitski, Derek Storm, Hannah Binney, Michael Ross, Jens Gundlach, Duncan Prindle, Tatsumi Nitta

Front row chairs: Tom Burritt, Chelsea Bartram, David Hertzog, Hamish Robertson, Brittney Dodson, Eric Swanson

INTRODUCTION

The Center for Experimental Nuclear Physics and Astrophysics, CENPA, was established in 1998 at the University of Washington as the institutional home for a broad program of research in nuclear physics and related fields. Research activities — with an emphasis on fundamental symmetries and neutrinos — are conducted locally and at remote sites. In neutrino physics, three experiments are related to measuring its mass. CENPA is the lead US institution in the KATRIN tritium beta decay experiment, the supportive local tritium decay experiment TRIMS, and the site for experimental work on Project 8. We also study neutrinoless double beta decay as a collaborating institution in the MAJORANA ^{76}Ge, LEGEND-200, LEGEND (ton scale), and in a next-generation R&D effort with the SELENA experiment. Finally, our neutrino group is involved in the COHERENT neutrino-nucleus scattering experiment. The Muon Physics group developed and completed the MuSun experiment to measure muon capture in deuterium at the Paul Scherrer Institute in Switzerland. The main effort of the group at present is the high-precision measurement of the muon's anomalous magnetic moment at Fermilab, the first results of which were reported in April 2021. We have begun to develop a followup experiment to study rare pion decays, motivated by the $g-2$ findings. Our local fundamental symmetries program also includes an experiment using the local Tandem Van de Graaff accelerator to measure the Fierz interference in ^{6}He decay, using the CRES technique that was developed by Project 8.

In addition to the research directly supported by DOE's Office of Nuclear Physics through the CENPA core grant, other important programs are located at CENPA, forming a broader intellectual center with valuable synergies. The "Gravity" group carries out, with both DOE and NSF support, studies of the weak and strong Equivalence Principles, fundamental precepts of General Relativity, as well as searches for non-Newtonian forces such as those predicted by theories with extra dimensions. In addition, they participate in LIGO with unique instrumentation that aids the functioning and stabilization of the interferometers. The DOE Office of High Energy Physics supports the unique ADMX axion search experiment. The NSF supports the DAMIC experiment that looks for light dark matter.

CENPA is home to a large number of faculty, research faculty, postdoctoral scholars, graduate, and undergraduate students. The core professional engineering and technical staff provide diverse capabilities and skills such as state-of-the-art detector development, fabrication of custom electronics, large-scale computing, and design engineering. New advancements, capabilities, and ideas are regularly shared at seminars by CENPA members and visitors alike.

0.1 Personnel updates

David Hertzog is the recipient of the 2022 APS Tom W. Bonner Prize in Nuclear Physics for his work in precision muon physics. He has also been named the Arthur B. McDonald Distinguished Professor of Physics.

Hamish Robertson was awarded the 2021 APS DNP Mentoring award for his outstanding track record of training young (and not so young) scientists.

CENPA laboratory physicists Eric Adelberger, Jens Gundlach, and Blayne Heckel were awarded the 2021 Breakthrough Prize for their work on tabletop gravity where they have used a series of extraordinary torsion balances to probe physics beyond the Standard Model.

Brent VanDevender (PNNL), Project 8 physicist and Project Manager, was named an Affiliate Associate Professor at UW.

Research Assistant Professor Jarek Kaspar transitioned to a CENPA Research Scientist in 2020, and in 2021 was recruited to be a Scientist at Siemens Medical Systems.

Postdoctoral scholar Dan Salvat accepted a position as a Research Scientist at Indiana University.

ADMX postdoc Nicole Crisosto took a quantum computing industry position and Jihee Yang now has a staff position at PNNL. Tatsumi Nitta has joined the group as a postdoc. He has also been running the weekly CENPA Monday Meeting and Seminar series.

David Sweigart is leaving CENPA after a year in which he carried out outstanding work for LEGEND. We are beginning a search for his replacement. Marsteller and Schwendimann have both accepted offers and begin their postdoctoral positions in Spring 2022. Marsteller replaces Menglei Sun who played a key role in the analysis of the first KATRIN results. Schwendimann fills an open position in the muon group.

Our Michael Ross and Conner Gettings from Birmingham University have both begun postdoctoral scholar positions in the Gravity group. Christine Claessens from the University of Mainz has joined Project 8, and Alexander Marsteller from the Karlsruhe Institute of Technology will join Project 8 and KATRIN in the spring of 2022.

Machinist Jim Elms retired in October, 2021. Office Administrator Ida Boeckstiegel resigned from CENPA in November, 2021 to take on a new challenge at another UW unit. We are presently seeking replacements for Jim and Ida and wish them well.

Ryan Roehnelt joined the CENPA staff in August 2020. Ryan is a professional mechanical engineer with over 16 years of experience working in small startups, a DOE National Laboratory, and defense and space industry. In just over a year at CENPA, Ryan has made enormous contributions across the board to all projects as will be evident in the individual reports.

Since the last Annual Report, these CENPA graduate students completed their Ph.D. degrees: Raphael Cervantes (ADMX group), Nick Du (ADMX group), Jason Hempstead (Muon group), and Michael Ross (Gravity).

0.2 Recent Accomplishments

- The KATRIN experiment was fully commissioned and began data taking with tritium in 2018. With data from the first month-long neutrino mass run, a new limit of 1.1 eV was set, a factor of 2 below the previous world limit set 20 years before. Data about to be published further limits the mass to 0.8 eV, the first sub-eV limit.

- The TRIMS apparatus at CENPA concluded a one-year data-taking campaign with molecular tritium. Detailed ionic final-state branching-ratio results were published that precisely confirmed the theoretical predictions while strongly contradicting previous experimental results. TRIMS has successfully completed its running, and a quantitative explanation for the failure of the experiments of the 1950s has now been found and will be published.

- The first tritium spectrum with the new CRES (Cyclotron Radiation Emission Spectroscopy) technique has been obtained in Project 8. The small-scale "Phase-II" prototype at UW showed clearly the promise of this approach. Particularly important is confirmation that extremely low backgrounds are possible, with no events being detected above the endpoint in 82 days.
- MAJORANA DEMONSTRATOR data taking with enriched HPGe crystals is complete and numerous publications have been published in the past grant period or are currently in preparation. The enriched crystals were removed and are en route to LNGS in Italy to be combined with those from GERDA plus new crystals from both the US and Europe in the LEGEND-200 experiment.
- The next-generation LEGEND search for neutrinoless double beta decay has passed several important milestones this year. Construction of the LEGEND-200 apparatus is currently underway and data taking is expected to commence prior to the start of the coming grant period. The full-scale LEGEND-1000 project was reviewed favorably in the DOE "Portfolio Review" of neutrinoless double beta decay efforts in the US, and is preparing for a CD1 review in the coming year.
- The Selena program became established at CENPA achieving two R&D milestones: i) the most detailed measurement of the ionization response of amorphous selenium (aSe), and ii) the first demonstration of single-particle detection in a hybrid aSe/CMOS active pixel sensor.
- The anomalous magnetic moment of the muon – $(g-2)/2$ – may be signaling the presence of non-Standard Model contributions. We have completed four data-taking campaigns, fully analyzed and published Run-1, and have made improvements in many areas of the experiment. The Run-1 results confirm the previous measurements from the Brookhaven E821 experiment and, when averaged, increase the tension with respect to the Standard Model to 4.2 standard deviations.
- The analysis of the UW-led MuSun experiment has reached an advanced state, with several challenging systematic effects brought under control. A first physics publication is expected during the present grant cycle.
- The He6-CRES experiment is assembled and the apparatus observed CRES events from ^{83m}Kr using a broad bandwidth as is needed for beta decay data. We have demonstrated that the production of the needed activity of ^{6}He and ^{19}Ne is sufficient and we are now moving toward applying the CRES technique to measure spectra from these nuclei.
- CENPA also hosts a long-standing program in "tabletop gravity" using extraordinarily sensitive torsion balance pendulums to search for non Standard Model physics. These searches are continuing, along with innovative hardware contributions to Advanced LIGO.

- The ADMX (axion dark matter experiment (DOE, Gen-2 Dark Matter) is located at CENPA. ADMX is the only experiment sensitive to the plausible DFSZ axion coupling model and has recently doubled the mass range it explores.
- Chavarria leads the construction of DAMIC-M (NSF supported), a highly sensitive experiment to look for low-mass WIMPs and hidden-sector dark matter.

As always, we encourage outside applications for the use of our facilities. As a convenient reference for potential users, the table on the following page lists the capabilities of our accelerators. For further information, please contact Gary Holman, Associate Director (holman@uw.edu) or Eric Smith, Research Engineer (esmith66@u.washington.edu) CENPA, Box 354290, University of Washington, Seattle, WA 98195; (206) 543 4080. Further information is also available on our web page: `http://www.npl.washington.edu`.

We close this introduction with a reminder that the articles in this report describe work in progress and are not to be regarded as publications nor to be quoted without permission of the authors. In each article the names of the investigators are listed alphabetically, with the primary author underlined in the case of multiple authors, to whom inquiries should be addressed.

David Hertzog, Director — Gary Holman, Associate Director and Editor

TANDEM VAN DE GRAAFF ACCELERATOR

Our tandem accelerator facility is centered around a High Voltage Engineering Corporation Model FN purchased in 1966 with NSF funds, with operation funded primarily by the U.S. Department of Energy. See W. G. Weitkamp and F. H. Schmidt, "The University of Washington Three Stage Van de Graaff Accelerator," *Nucl. Instrum. Methods* **122**, 65 (1974). The tandem was adapted in 1996 to an (optional) terminal ion source and a non-inclined tube #3, which enables the accelerator to produce high intensity beams of hydrogen and helium isotopes at energies from 100 keV to 7.5 MeV.

Some Available Energy Analyzed Beams

Ion	Max. Current (particle μA)	Max. Energy (MeV)	Ion Source
^{1}H or ^{2}H	50	18	DEIS or 860
^{3}He or ^{4}He	2	27	Double Charge-Exchange Source
^{3}He or ^{4}He	30	7.5	Tandem Terminal Source
^{6}Li or ^{7}Li	1	36	860
^{11}B	5	54	860
^{12}C or ^{13}C	10	63	860
*^{14}N	1	63	DEIS or 860
^{16}O or ^{18}O	10	72	DEIS or 860
F	10	72	DEIS or 860
* Ca	0.5	99	860
Ni	0.2	99	860
I	0.001	108	860

*Negative ion is the hydride, dihydride, or trihydride.

Several additional ion species are available including the following: Mg, Al, Si, P, S, Cl, Fe, Cu, Ge, Se, Br and Ag. Less common isotopes are generated from enriched material. We recently have been producing the positive ion beams of the noble gases He, Ne, Ar, and Kr at ion source energies from 10 keV to 100 keV for implantation, in particular the rare isotopes ^{21}Ne and ^{36}Ar. We have also produced a separated beam of 15-MeV ^{8}B at 6 particles/second.

Contents

1 Neutrino Research

Overview of neutrino mass

In 1934 Fermi formulated his theory of beta decay, incorporating Pauli's postulated particle, the neutrino. The paper was rejected by the journal Nature as being "too remote from physical reality to be of interest to readers". Almost 90 years later the neutrino remains one of the most interesting particles in physics and cosmology.

We now know that the neutrino comes in three "flavors" electron, muon, and tauon, associated with the charged leptons. Super-Kamiokande and the Sudbury Neutrino Observatory showed that these flavors mix, explaining the anomalies in the atmospheric and solar neutrino fluxes. This oscillation between the neutrino flavors can be explained only if the neutrino has mass, in contradiction with the standard model of particle physics which assumed the neutrino to be massless. Oscillation experiments can determine only the differences of the squares of the masses, not the mass scale. The neutrino constitutes the first and, so far, the only dark matter observed in the cosmos. Observation of the cosmic microwave background and large-scale cosmic structures limit the sum of the three neutrino masses to be < 0.12 eV, but such limits are model dependent.

Direct measurement of the absolute neutrino mass scale is among the top priorities of modern nuclear physics. The most sensitive technique for a direct and model-independent mass determination is the tritium endpoint method[1]. The signal for neutrino mass emerges as a phase-space modification of the spectral shape at the beta endpoint, and is independent of whether neutrinos are Majorana or Dirac particles.

For 20 years, neutrino mass has been constrained by prior experimental work on tritium beta decay to be less than 2 eV, while at the lower end neutrino oscillations constrain the average mass of the 3 eigenstates to be at least 0.02 eV. The KATRIN experiment is an international tritium project in which the US has supplied the focal plane detector, its data-acquisition software, calibration systems for both ends of the KATRIN apparatus, and near-line analysis software. CENPA is the lead US institution. KATRIN's design goal is a 0.2-eV mass sensitivity limit, if the mass is not larger. KATRIN is now in operation, and will exhaust the quasidegenerate range of neutrino masses that are large compared to either of the mass differences measured in oscillation experiments, or measure the neutrino mass if it lies in that range.

Experiments like KATRIN that make use of molecular tritium rely on the theoretical prediction of the spectrum of excited states produced in the beta decay, because it is equivalent to a broadening of the spectral response. The neutrino mass effect is spread over a range of slightly differing endpoints for the excitations. A direct measurement of this spectrum is not possible, but experimental tests were made in the 1950s to determine if the branching ratios to various ionic final states (e.g. THe^+, T + He^+, etc.) were correctly predicted by the theory. Strong disagreement was found, and we report on our resolution of this issue in

[1] J. A. Formaggio, A. L. C. de Gouvêa, and R. G. H. Robertson, Phys. Reports, **914**, 1 (2021).

the ‘TRIMS’ experiment.

It is possible that the neutrino mass may turn out to be smaller than KATRIN can discover, 0.35 eV. While there may be ways to extend the reach of KATRIN somewhat, KATRIN approaches a fundamental limit for this type of experiment as a result of its sheer size and its use of molecular T_2. To advance significantly beyond requires a different approach. The goal of the next-generation tritium endpoint experiment is to reach the full range of neutrino masses allowed under the assumption of an inverted hierarchical ordering of neutrino mass eigenvalues. If a signal is seen, the effective mass is determined; otherwise the hierarchy is normal and the effective mass is less than 50 meV. In a new approach, called Project 8, cyclotron radiation emission spectroscopy (CRES) is being explored as a potential way to reach this threshold. Successful precision measurement of the energies of single electrons from ^{83m}Kr decay was achieved at CENPA in 2015, and in the past year the first small-scale tritium experiment in a waveguide cell was performed. With the completion of Phase II, the phased R&D program turns now to scaling up the apparatus size and to exploration of an atomic source for a future atomic tritium experiment.

KATRIN

1.1 KATRIN Overview

G. Bayarbaatar, A. Beglarian†, T. H. Burritt, P. J. Doe, S. Enomoto, J. A. Formaggio*, F. M. Fränkle†, A. Kopmann†, E. L. Martin§, D. S. Parno¶, D. A. Peterson, A. W. P. Poon‡, R. G. H. Robertson, M. Sun, T. D. Van Wechel, A. P. Vizcaya Hernández¶, J. F. Wilkerson§, and S. Wüstling†

Conceived in 2001, KATRIN is currently the most advanced experiment directly probing the mass of the neutrino and draws heavily on the experiences of the four preceding experiments (at Los Alamos, Livermore, Troitsk, and Mainz) that made use of molecular T_2 as a source. The Mainz and Troitsk experiments established the neutrino mass limit of 2 eV. By improving both statistics and systematics by approximately four orders of magnitude, KATRIN will achieve an order of magnitude improvement in the mass limit, reaching a sensitivity of 0.2 eV. The KATRIN apparatus is now fully commissioned at the Tritium Laboratory (TLK) of the Karlsruhe Institute of Technology (KIT) in Germany and has embarked on a 5-year program to directly probe the neutrino mass and search for other neutrino physics. The KATRIN apparatus is shown in Fig. 1.1-1.

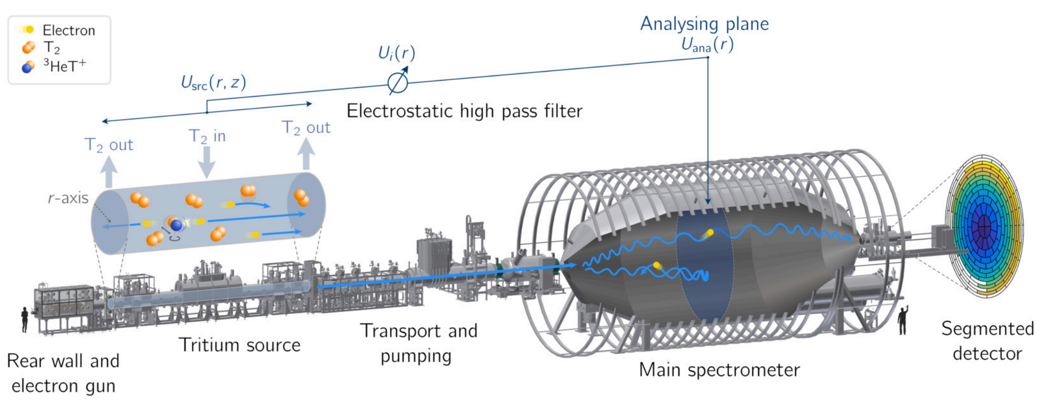

Figure 1.1-1. Principle of the KATRIN experiment. Gaseous molecular tritium circulates continuously through the source tube. Electrons from beta decay are magnetically guided towards the main spectrometer while tritium is pumped away. The main spectrometer floats at a negative, adjustable potential around 18 kV. Electrons with sufficient energy to surmount this barrier are detected in a 148-pixel silicon detector (in expanded view at right).

The TLK has the necessary license and expertise to handle and reprocess the 4 g of tritium

†Karlsruhe Institute of Technology, Karlsruhe, Germany.
*Massachusetts Institute of Technology, Cambridge, MA.
§University of North Carolina, Chapel Hill, NC.
¶Carnegie Mellon University, Chapel Pittsburgh, PA.
‡Lawrence Berkeley National Laboratory, Berkeley, CA.

used by KATRIN. Molecular tritium with an activity of $\sim 10^{11}$ Bq is contained in the source tube. A train of superconducting magnets guides the decay electrons adiabatically to the spectrometers. Differential and cryogenic pumping systems reduce the tritium entering the spectrometer by a factor of 10^{14}, an acceptable background level. The spectrometer shell and an internal wire electrode structure establish the retarding potential of the "analyzing plane" (in fact a surface of complicated shape). Electrons with sufficient energy to overcome this retarding potential pass to the focal plane detector (FPD). The UW led the design, commissioning, and installation of the FPD, which became the workhorse for commissioning KATRIN.

The integral beta spectrum is obtained by adjusting the retarding potential in steps around the endpoint energy of 18574 eV. The time spent at each step is chosen to optimize the sensitivity to neutrino mass, as seen in Fig. 1-2. The 1000-day period required to meet the sensitivity goal of 0.2 eV is divided into 60- to 90-day "campaigns" separated by maintenance periods.

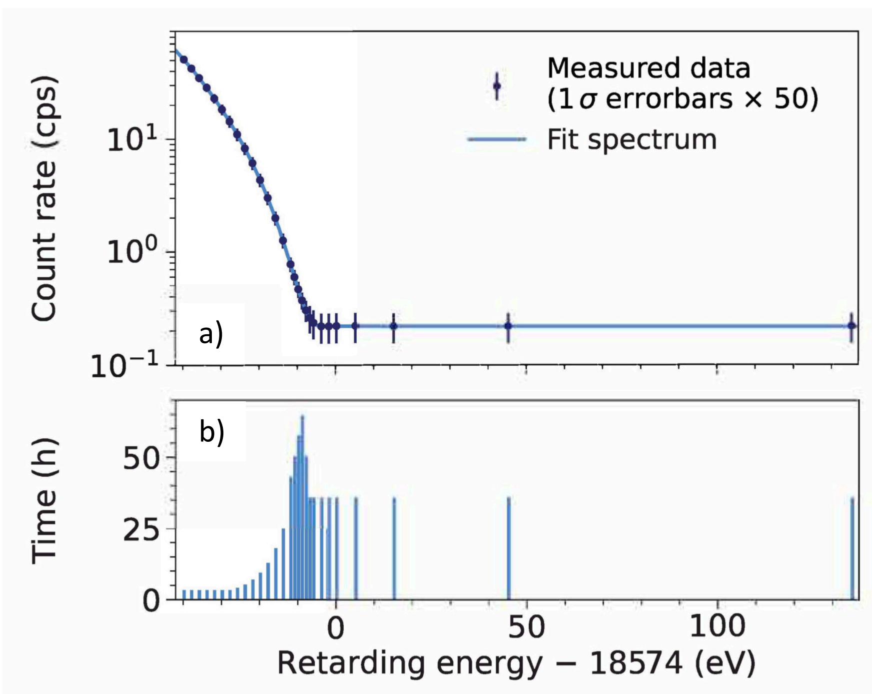

Figure 1.1-2. (top) Fit to the data around the endpoint of the tritium beta spectrum with 50X enlarged error bars. (bottom) Measurement time distribution at each retarding potential for KNM2.

Background sources such as cosmic rays, natural radioactivity, and intrinsic Penning traps negatively impact the KATRIN neutrino mass sensitivity. Additional background sources were subsequently discovered associated with radon emanating from the getter pumps and Rydberg atoms produced throughout the volume of the main spectrometer. The radon was reduced by LN_2 cooled baffles and the Rydberg atoms by moving the analyzing plane downstream in the spectrometer, at some loss of energy resolution.

Unexpected sources of systematic error were discovered associated with the Penning backgrounds and variations in the plasma potential of the source. These have been extensively studied and accounted for.

Tritium operations began in mid-2018 with a trial source activity of 5×10^8 Bq[1]. The first mass measurement campaign KNM1 followed mid-2019 with a source activity of 2.5×10^{10} Bq.[2] The source now operates at its design intensity of 9.5×10^{10} Bq. A new limit from KNM2 has just been accepted for publication in Nature Physics,[3] and KNM3 to KNM5 are in analysis. Much of KNM3 was spent studying sources of systematic error such as variations in the source potential. We are currently in the midst of KNM6, which will continue through 2021. The apparatus has had an uptime of approximately 90%; most downtime is attributed to problems with utilities such as HVAC, cryogenic supplies, and similar hardware.

Additional scientific achievements are limits on eV sterile neutrinos[4] and on relic neutrinos (in draft). A paper[5] describing the entire KATRIN apparatus including the FPD provides the technical reference for all subsequent science papers.

Data taking is divided into Katrin Neutrino Mass campaigns, KNM1, KNM2… etc., each of 60 days duration, interspersed with maintenance periods. An estimated 1000 days of tritium data will be required to meet the goal of 0.2 eV sensitivity to the neutrino mass.

UW is responsible for processing all run data from these campaigns. This includes data cleaning, quality monitoring and event-level analysis, producing processed-spectrum files for use by the collaboration. The initial campaigns, KNM1 and KNM2 combined provided data establishing the first sub-eV limit on the neutrino mass. They also identified challenging problems regarding backgrounds associated with radon from getter pumps and Rydberg atoms resulting from natural radioactivity, along with instrumental instabilities associated with the plasma potential of the tritium source and the retarding potential of the spectrometer.

To study these effects KNM3 emphasized systematic studies including operation in a new mode with a combined Kr + T_2 source to study plasma potentials and scattering in the source. The effects of varying biases on the rear wall, operation at a higher temperature as needed for Kr, and optimization of the column density were studied. The main background, Rydberg atoms, resulting from the decay of ^{210}Pb on the walls of the spectrometer and distributed uniformly throughout the volume of the spectrometer vessel, can be ionized by thermal radiation. Ionization electrons produced in the volume downstream of the analyzing plane are accelerated towards the detector and constitute a background. This downstream volume, and thus the Rydberg background, was reduced by moving the analyzing plane further downstream, albeit at the cost of reduced energy resolution. The analyzing plane evolves to a complex shape, and the detector pixels have characteristic resolution contributions. Extensive calibrations with the egun and Kr source were performed.

---

[1] M. Aker *et al.*, Eur. Phys. J. C **80**, 264 (2020).
[2] M. Aker *et al.*, Phys. Rev. Lett. **123**, 221802 (2019).
[3] M. Aker *et al.*, 2105.08533 (2021).
[4] M. Aker *et al.*, Phys. Rev. Lett. **126**, 091803 (2021).
[5] M. Aker *et al.*, 2103.04755 (2021).

Backgrounds associated with Rn from the NEG pumps were reduced to acceptable levels by operating the LN2 cooled baffles at a further reduced temperature. The shifted analysis plane also greatly reduced this background, which is now at 136 mcps, compared to 550 mcps at the time of commissioning of KATRIN. Notwithstanding the great progress in identifying and reducing sources of background, further reduction towards the 10 mcps level is necessary. The dominant background remains the Rydberg atoms. A novel approach to reducing this background, proposed by Hamish Robertson, takes advantage of the differing cyclotron radius of the signal and background electrons in the magnetic field. A carefully configured "obstacle course" will preferentially allow signal electrons to pass while blocking the background electrons. This is referred to as the Transverse Energy Filter (TEF). Colleagues at the University of Münster and Karlsruhe Institute of Technology have taken up the idea and are developing active (aTEF) and passive (pTEF) versions of the filter.

One particularly insidious systematic was discovered at UW by Sanshiro Enomoto, and it arises from the intrinsic Penning trap located between the pre-spectrometer and the main spectrometer. A description of this effect and its resolution is given in a following section.

The potential of the source is a critical parameter that was intended to be maintained by a gold-plated rear wall held at a fixed potential. It was discovered that the potential of the gold surface is a function of its radiochemical history. In addition, the non-uniform work function of the walls also influences the source potential. These effects were studied using a new, high-intensity Kr source. A technique has been developed using ozone to periodically clean the surface of the rear wall during the maintenance periods.

Other important systematic parameters to monitor are the source column density and the spectrometer retarding potential. The column density determines not only the event rate but also the electron energy loss mechanisms. The original plan to use spectrum deconvolution was difficult to accomplish. Time of flight from an electron gun looked promising but pileup in the detector would have resulted in a total of 1 year spent on this essential calibration. A new digital trapezoidal filter developed at UW allows the calibration to be accomplished in hours. The stability of the spectrometer retarding potential directly influences the spectrometer energy resolution. New techniques developed at UW now enable ripple as small as 10 mV to be detected on the 18 kV retarding potential. A minor but unexpected drift in the spectrometer retarding potential was also discovered by UW during the analysis of KNM1 and has now been corrected in the new Advanced Post Regulation system.

As a result of the past year's studies, a new set of operating parameters has been established that will be used for future data taking campaigns. Currently KNM6 is underway, and it is anticipated that by the end of 2021 we will have accrued 33% of the tritium data that was planned to reach the 0.2 eV goal.

KATRIN in its initial operation has generated notable publications, including a sub-eV limit on the neutrino mass (Nature Phys.), limits on eV sterile neutrinos (Phys. Rev. Lett.), new limits on relic neutrinos (in draft), and a technical magnum opus describing the entire KATRIN apparatus, including the US supplied detector system (J. Instr.).

The past year has seen significant changes in the KATRIN group at UW. Menglei Sun and Gwen Bayarbaatar, key participants in the data cleaning, quality monitoring, event-level analysis, and detector systematics studies have accepted positions in the local software industry. We are pleased to report that Alexander Marsteller from KIT has accepted our offer of a postdoctoral fellowship.

1.2 FPD Drift Analysis and Models

G. Bayarbaatar and S. Enomoto

In 2020, we noticed a jump in FPD gains of ∼400 eV that corresponds to a 0.06% jump in detection efficiency, which is not negligible. This gain jump is hypothesized to be resulting from fluctuations in the environmental parameters surrounding the experiment setup, including the temperature of the PIN diode wafer, temperature of the preamps, and temperatures of the ambient air electronics. We created a gain drift model to explain this jump - temperature sensor readouts of the detector mounting plate (“Carousel temperature”) and of the detector platform (“Detector platform temperature”) are taken as the independent variables and FPD gain (ADC or energy output per incident charge deposit) as the dependent variable.

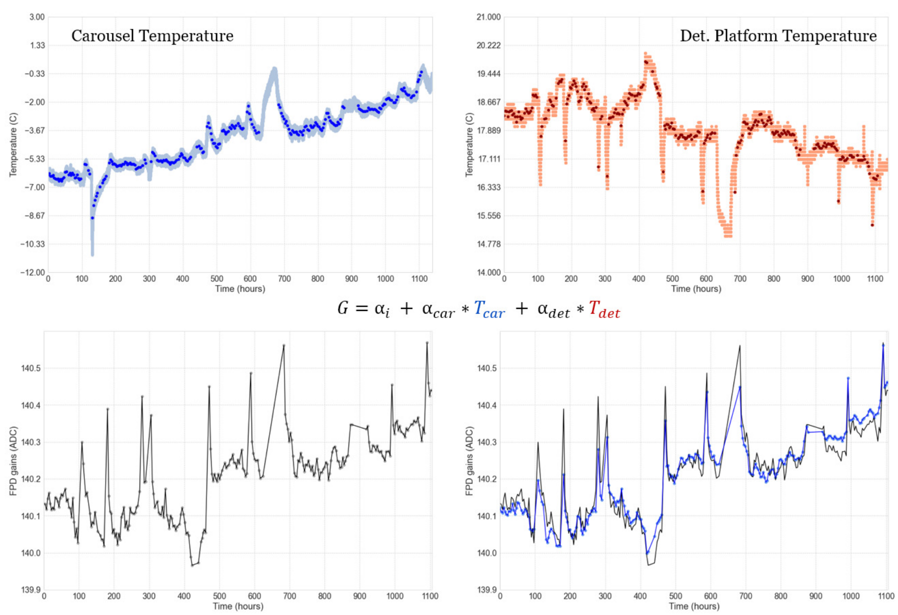

Figure 1.2-1. The raw carousel temperature is displayed on the top left, while the raw detector platform temperature is on the top right graph, both measured in Celsius. The scatter plots in both graphs are the run-averaged values of each temperature. The bottom left graph is the dependent variable, raw FPD gains (ADC values for 28.3 keV electrons), while in the bottom right graph, the model fit results are graphed in blue line plot over the raw FPD gain data. The gain drift model equation is written in the middle of the figure.

The gain drift model is represented by the equation in Fig. 1.2-1. The variable T_c stands for the carousel temperature data, the variable T_d stands for detector platform temperature, and the α_{car} and α_{det} variables are their respective dependence variables.

We performed a Least-Squares Minimization model with the Nelder-Mead (Downhill simplex) method to fit the FPD gains using the two temperature measurements. The α_{car} parameter was calculated to be 0.028 ± 0.0004 ADC/K or 0.0056 keV/K (electron at 28.3 keV), which makes carousel temperature directly correlated with the FPD gains. The α_{det} parameter was calculated to be -0.102 ± 0.0032 ADC/K or -0.026 keV/K (electron at 28.3 keV), which indicates detector platform temperature is inversely correlated with the FPD gains as suspected.

As pictured in the bottom right graph of Fig. 1.2-1, the model fit results agree with the raw FPD gains well except for the extreme values or peaks of the raw data. Possible explanations for the peak inaccuracy are variations in FPD pixels or time lag between detector platform temperature and the peak position measurements.

Fig. 1.2-2 shows gain drifts for each pixel during KNM4. In the distribution of pixel gains, a structure of quadrants exists, which corresponds to the four electronics modules ("Optical Sender Board", OSB). The OSB boards in ambient air convert the electrical signals from the preamps to optical and send out the signal through electrical isolation of the high voltage cage. According to the datasheet of the optical transmitter, Broadcom HFBR-1527, a temperature dependence of ~0.02 dB/K is expected.

The color map in Fig. 1.2-2 shows the gain drift for each pixel from the beginning of KNM4 to a run in the middle of KNM4. The top and bottom quadrants have relatively higher drifts compared to the left and bottom quadrants. The right quadrant has notably the lowest drifts, while conversely the top quadrant has the highest.

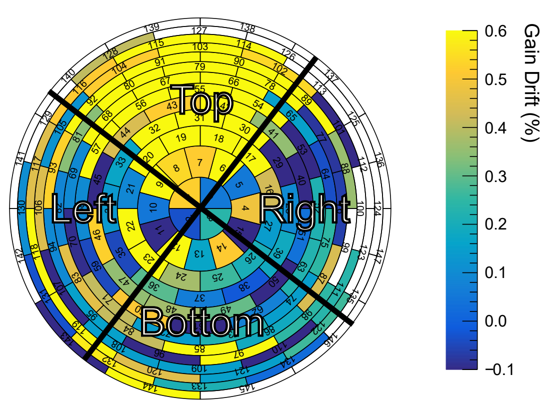

Figure 1.2-2. The four OSB boards correspond to the four quadrants on the FPD - top, right, bottom, and left. The color bar on the right represents the gain drift of each pixel during KNM4. Yellow representing highest drift and deep blue being lowest, there is a recognizable quadrant structure to this color map.

Given the observed quadrant structure, we performed the Nelder Mead model on data from each quadrant separately. The results shown in Fig. 1.2-3 indicate that using the higher drift quadrants - top and bottom - does give us better fit on the extreme values, while modeling the lower drift quadrants - left and right - results in poorer fit.

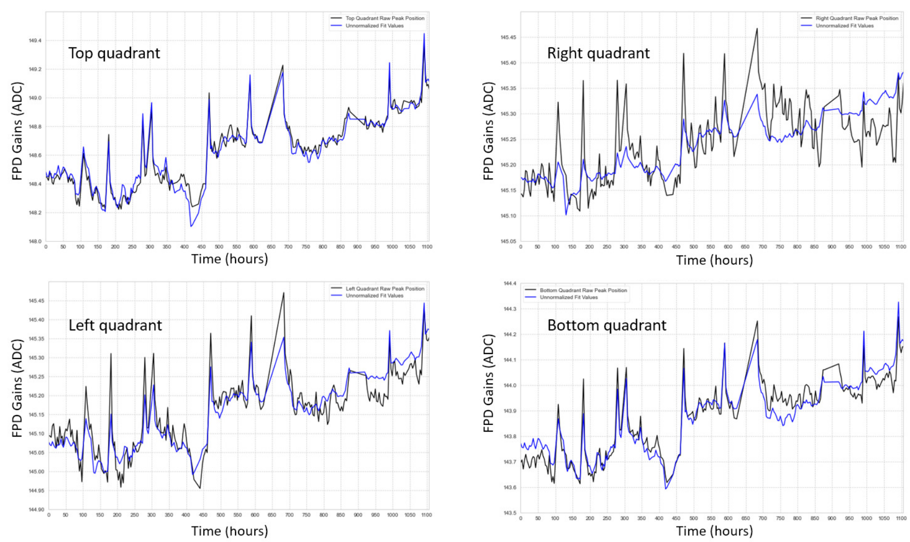

Figure 1.2-3. Results of the Nelder Mead model fit on the four FPD quadrants individually. The top left graph shows the top or the highest-drift quadrant, and the top right shows the right or lowest-drift quadrant. The bottom left shows the left quadrant, and the bottom right shows the bottom quadrant. In each graph, the model fit results are graphed in blue line plot over the black raw FPD gains data.

The detector platform temperature is not a direct measurement of the OSB temperatures. After noticing the problem, a new temperature sensor was installed on the OSB crate, but the accuracy is not as good as the platform temperature measurement, and also the data is not available for the past KATRIN measurements. Instead of directly using the OSB temperature measurement, we characterized the time lag between these two temperature measurements.

With parameterizing the lag, a χ^2 was constructed which compares the time-variation structures of the two temperature measurements. We found that our χ^2 minimization method produced better accuracy compared to the cross correlation method. Error estimation is straightforward in this way.

As shown in Fig. 1.2-4, the OSB and detector platform temperature data acquired during the KNM4 period are sectioned off into twelve time segments. The temperature data was normalized and offset was subtracted before χ^2 minimization.

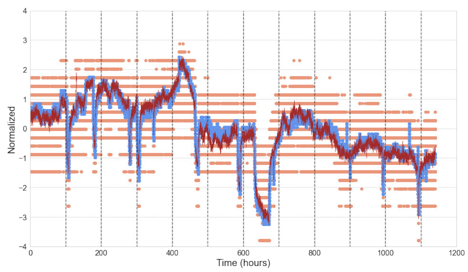

Figure 1.2-4. The left graph shows the normalized OSB and detector platform temperatures in red and blue scatter plots respectively. For a better presentation, the OSB temperature is averaged over 10 minutes and shown in a deep red line plot. The vertical black dashed lines in both graphs divide the entire data set into 12 time segments. For each time segment, the right graph shows the time lag at the minimum calculated χ^2. The minimization was successful on most segments, except for three.

χ^2 minimization is performed separately on each segment, where the time lag is scanned every 2 minute step and χ^2 is calculated for each step. The standard error or sigma in the χ^2 formula is calculated from the RMS of a relatively stable region in the OSB temperature data. In Fig. 1.2-5, the calculated χ^2 values are shown in a red scatter plot and the local minimum is represented by the vertical red dashed line. As χ^2 scatter plot carries fluctuations with it, we fit a parabolic curve (shown by the blue curve) to the scatter plot to get a more accurate minimum value, which is displayed by the vertical blue dashed line.

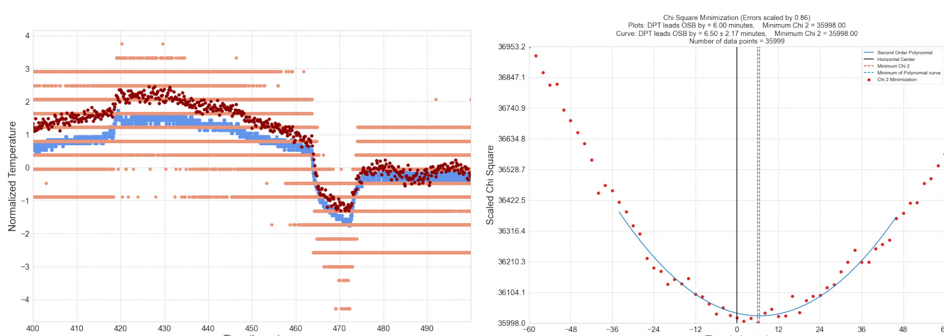

Figure 1.2-5. χ^2 minimization on a single time segment. Top: temperature data for this one segment, the same notation as Fig. 1.2-4. Bottom: the horizontal axis shows the time lag with which the χ^2 was calculated, and the vertical axis represents the calculated χ^2. The red scatter plots show the calculated χ^2, while the blue line is the parabolic curve, both plotted along with their minimum χ^2 values, each represented by a vertical dashed line in its respective color.

The calculated χ^2 minima ($\sim$42000) were significantly larger than the number of the degrees of freedom ($\sim$36000). This indicates inaccuracy of the model and/or underestimation of data errors; therefore, we scaled the raw χ^2 by their ratio, which is equivalent to inflating the data errors until data becomes consistent with the model, as a remedy for unaccounted systematics. The calculated time lags for the twelve sections are shown in the lower graph in Fig. 1.2-4. In three of the twelve sections, the minimum χ^2 value could not be determined, thus their time lags appear blank. The remaining time lags seem to be uniformly distributed, and all the estimated lags are within the 0 to 10 minute range. Given the small lag, we conclude that using the detector platform temperature for the OSB temperature is valid, though the variations among the OSB cards need to be considered.

1.3 Penning-Trap Background

S. Enomoto

In every experiment there exist fears for overlooked systematics and/or backgrounds. The worst case scenario for those is that the overlooked systematics / backgrounds have the same structure as the signal signature, in which case the indication could become visible only when the experiment reaches the final sensitivity, if ever noticed. On the other hand, we often think that existence of such systematics / backgrounds would be unlikely, because the way the experimental apparatus works (e.g., gaseous tritium & MAC-E filter & silicon detector) is quite different from the target physics process (e.g., neutrino mass modifying the beta spectrum shape).

We found that KATRIN actually had one such background that mimics the signature of the negative neutrino mass-squared almost perfectly. The source of the background was a Penning trap between the main spectrometer and pre-spectrometer (Fig. 1.1-1). It had been long known that the potential minimum between the spectrometers traps and accumulates electrons, which, in turn, generate background electrons that reach the detector through a somewhat complicated process: trapped electrons ionize residual gas and create positive ions, which are not blocked by the retarding potential and enter the main spectrometer. The positive ions create electrons by ionization of the residual gas or by impacting the vessel wall, where the impact can release excited hydrogen atoms which de-excite in the spectrometer volume, releasing an electron. In order to prevent trapped electrons from accumulating, a wiper was installed between the two spectrometers. During scans of the beta spectrum, where the retarding potential is changed step-wise per pre-defined schedule, the wiper is operated on every change of the retarding potential setting.

This Penning-trap background had been characterized extensively. The background rate strongly depends on the pre-spectrometer potential setting as it defines the depth of the trap, as well as the vacuum pressure of the spectrometers. With the nominal pre-spectrometer potential setting at -10 kV, the Penning trap background makes a negligible contribution to the total background rate, if the wiper is operated with intervals no longer than 500 s (Fig. 1.3-1-left).

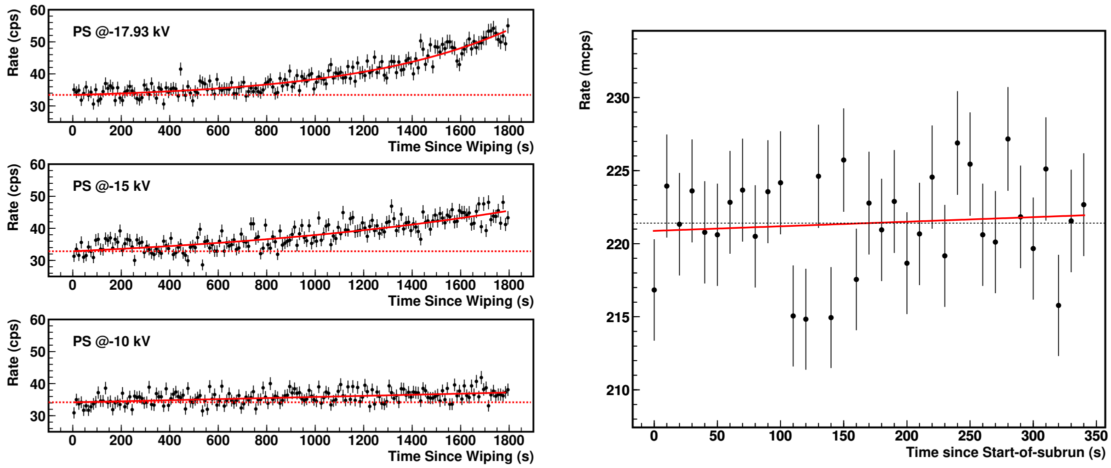

Figure 1.3-1. Background rates after wiping. Left: no tritium gas was injected, and the spectrometer magnetic field was configured to enhance detection of ion-induced backgrounds as well as other backgrounds. The plots show that the penning-trap background is largely reduced by a lower potential setting of the pre-spectrometer (PS). Right: all KNM2 *background* sub-runs (i.e., sub-runs with retarding potential above the tritium end-point) are accumulated. The best-fit slope is slightly positive but not significant ($< 0.2\sigma$).

Considering the longest allowed interval of the wiper operations, which defines the maximum length of measurement at one retarding potential setting ("sub-run") in each scan ("run"), the schedule of a scan (Measurement Time Distribution, MTD) was designed to maximize the sensitivity to neutrino mass, for the given KATRIN energy resolution and the total background rates (Fig. 1.1-2b). The optimization is based on the counting rates for various retarding potential settings, influence of the backgrounds and energy-loss systematics, and the signature of the signal (neutrino mass-squared); basically, long measurement time is allocated where the signal signature is large, balanced with equalization of the statistical errors.

What was overlooked here is the invisible time structure of the Penning-trap background. Although the rate itself is tiny and negligible compared to the total backgrounds, electrons are still accumulated in the trap and therefore the background rate increases over time. The longer a sub-run (= wiper operation interval) is, the higher the average background rate is in the sub-run. This makes the background spectrum shape the same as the MTD shape, which mirrors the signature of the neutrino mass signal. In the end, the background spectrum of the electrons generated in the apparatus has the same structure as the neutrino mass signal.

For the KNM2 measurement campaign, the increase is estimated to be 3 ± 3 μcps/s; for a 500 s long sub-run, this corresponds to only 0.4 electrons contributing to the increase on top of $\sim$ 150 other background electrons, which is basically invisible (Fig. 1.3-1-right). However, the similarity of the spectrum shape to the neutrino mass signature influences the estimation of the neutrino mass, and this 3 μcps/s slope translates to a neutrino mass-squared of -0.15 eV^2. If this slope were not noticed, it would have been a huge bias towards negative neutrino mass-squared, and now included in the model, the uncertainty of the slope is one of the largest systematics.

This MTD-dependent background can be easily eliminated by operating the wiper at a constant interval. Once this systematic was noticed during KNM 4 in late 2020, sub-runs were then divided into a equal-length blocks in order that all the sub-runs have the same average background rate. At the beginning of KNM5 in 2021, the pre-spectrometer potential was reduced to -100 V and wiper operation during a run has been withdrawn since then.

1.4 Detector upgrades

P. J. Doe, M. Kallander, and R. G. H. Robertson.

A number of detector upgrades are planned that aim to reduce the unexpected background associated with the production of Rydberg atoms within the main spectrometer and to obtain a better understanding of physical processes that influence the stability of the gaseous source.

- Detector wafer development: Background rejection can be enhanced by improving the energy resolution of the FPD wafer. Doe has engaged the Detector Laboratory at LBNL, which has developed a PIN architecture optimized for low-energy electron detection that is currently being evaluated at UW. Two wafers are currently under test using the apparatus shown in Fig. 1.4-1 . The wafer is mounted on a printed circuit board which is attached to a cryogenic tank containing a choice of refrigerants. A ^{241}Am source positioned beneath the wafer enables the energy resolution to be determined as a function of temperature. The thickness of the dead layer on the entrance window of the wafer, a significant factor in determining the energy resolution of the detector, can be estimated by rotating the Am source to change the angle of incidence of the radiation.

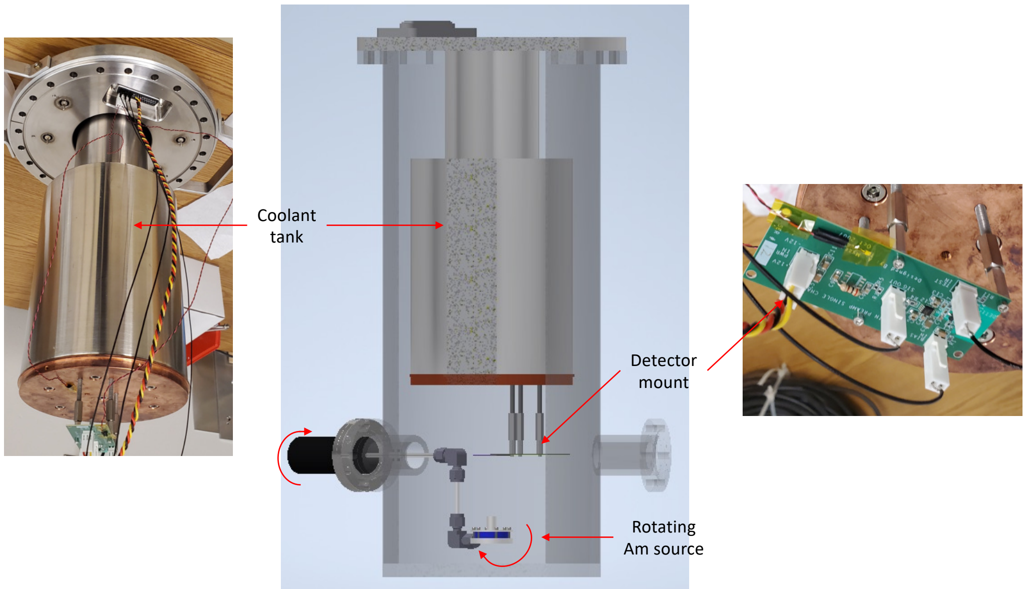

Figure 1-1. Apparatus used to test the LBNL low energy electron detector. Left and center panels show the vacuum cryostat, and the right panel the preamp. The detector is not yet mounted on the preamp.

- Background suppression: Robertson has suggested a number of innovative ideas for identifying and suppressing backgrounds. One is to develop a technique to detect single electrons and, by time of flight, reject those electrons that did not originate from the source. This technique is now being investigated by KATRIN colleagues at the University of North Carolina. The largest KATRIN background arises from thermal ionization of Rydberg atoms in the spectrometer. Another proposal is a transverse energy filter (TEF) that capitalizes on the small initial energies of Rydberg electrons to remove them while allowing the beta decay electrons to pass through to the detector. This idea is being developed by the University of Münster and KIT and will be tested in the KATRIN focal plane detector in December 2021

TRIMS and the beta decay of molecular tritium

B. Daniel*, M. Kallander, Y.-T. Lin, D. S. Parno*, R. G. H. Robertson, and A. P. Vizcaya Hernández*

The most sensitive experiments to measure neutrino mass rely on the beta decay of tritium because it has a simple atomic structure. In practice, laboratory experiments such as KATRIN make use of molecular T_2, and the initial state molecule may be thermally excited into accessible rotational states, while the final state has many possible electronic excitations, as well as vibrational and rotational excitations that are excited by the recoil momentum from the leptons. Each initial and final state corresponds to a slightly different endpoint energy,

*Carnegie Mellon University, Pittsburgh, PA.

smearing the spectrum in the region where one looks for a distortion caused by neutrino mass. The excitation energies and probabilities are determined from theory. One test of this theory is the branching ratio to the bound molecular ion THe^+. Two experiments carried out in the 1950s both gave branching ratios of $\sim 90\%$, whereas the present theoretical prediction is 57%, a striking and concerning disagreement[1].

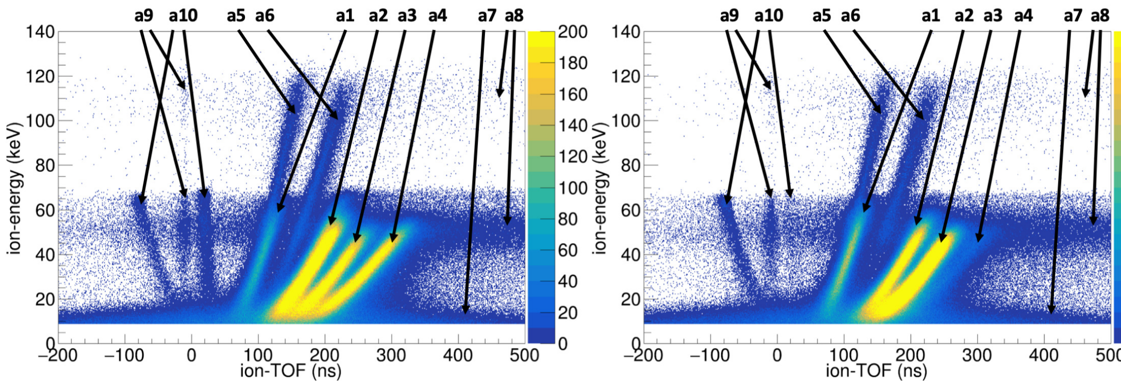

(a) (b)

Figure 1.4-2. Ion-energy versus ion-time-of-flight histogram for (a) gas rich in TT and (b) gas rich in HT. The z-axis represents the event count. The bands labeled a1–a6 represent distinct detection channels: a1) protons, a2) $^3He^+$ and T^+, a3) H^3He^+, a4) T^3He^+, a5)$^3He^{++}$, and a6) $H^+ +\ ^3He^+$. The a7–a10 bands arise from interactions with the apparatus with the associated emission of secondary electrons, or decays at the ends of the acceleration chamber.

The Tritium Recoil Ion Mass Spectrometer (TRIMS) was conceived and built at CENPA to make a comprehensive study with modern apparatus of the branching to ionic final states in the beta decay of HT and TT molecules. The apparatus construction and commissioning were completed at the end of 2017, followed by 18 months of data-taking. Fig. 1.4-2 shows the TRIMS apparatus and some of the data obtained with it.

A detailed analysis framework was built in parallel and the data analysis completed by the fall of 2019. The results, which form the thesis of Ying-Ting Lin, agree precisely with the theoretical prediction and disagree with the earlier measurements. These results have been published[2]. Lin received the Henderson Prize from the Physics Department for his thesis.

We consider that data-taking is complete, but the apparatus is in cold standby should further operation be called for. Diana Parno now holds a faculty position at Carnegie Mellon University, continuing her involvement in the experiment and her supervision of graduate students. Lin, Parno, Robertson, and two new Carnegie Mellon students are working on a long paper on the TRIMS experiment. In the past year, a quantitative explanation for the failure of the historical experiments has been discovered and will form part of the long paper. Its completion and publication is expected in 2022, and will mark the completion of the TRIMS project.

[1] L. I. Bodine, D. S. Parno, and R. G. H. Robertson, Phys. Rev. C **91**, 035505 (2015).

[2] Y. T. Lin *et al.*, Phys. Rev. Lett. **124**, 222502 (2021).

Project 8

1.5 Project 8 overview

C. Claessens and E. Novitski

The Project 8 experiment is pursuing a direct measurement of the absolute neutrino mass scale from the distortion of the tritium beta decay spectrum near the endpoint with a sensitivity goal of $\sim 40\,\mathrm{meV/c^2}$. The collaboration has successfully established Cyclotron Radiation Emission Spectroscopy (CRES), a frequency-based approach to detect electrons and determine their kinetic energy with high precision[1]. The experimental program is divided into four phases. The CRES proof of concept was carried out in Phase I by recording a high-resolution $^{83\mathrm{m}}$Kr conversion electron spectrum.

Our work this year has focused on finishing Phase II and on development work for Phase III. In Phase II, we recorded the first tritium spectrum with the CRES and have now extensively characterized the systematic effects of the technique.

Phase III is focused on demonstrating several fundamental elements of a large-scale (Phase IV) neutrino mass experiment including electron detection with an antenna array or cavity, and the use of atomic tritium as the beta-emitting source gas. One component of UW's Phase III effort is developing CRES in larger volumes, at higher gas densities, with higher efficiency, and with higher energy resolution. UW hosts the CRES platform in a 90-cm bore, 1-ppm-homogeneity patient-size medical MRI magnet. UW is also building an electron gun, the primary calibration tool for CRES demonstrators and test platform for large-volume detection concepts. On the atomic tritium side, UW hosts an atomic tritium testbed developing a high-flow cracking method with stable hydrogen isotopes. UW has also been playing an important role in developing the capstone mid-scale experiment that will be Project 8's final apparatus before proceeding to the full-sensitivity Phase IV.

1.6 Tritium spectroscopy in Phase II

C. Claessens and E. Novitski

In Phase II of Project 8, a small prototype apparatus was used to make the first CRES measurement of a continuous spectrum. Data-taking was concluded in 2020. The analysis effort since has improved our understanding of instrumental resolution, the effects of scattering, and the dependence of detection efficiency on frequency. It has also enabled a quantitative characterization of systematic contributions to uncertainty. Dual Bayesian and frequentist analyses, with the frequentist analysis led by UW, have yielded measurements of the tritium endpoint and limits on the neutrino mass. The results are expected to be finalized before the end of the year. While the mass limit from this small-volume prototype Phase II apparatus was only 185 eV/c^2, we demonstrated CRES's promise as a precision neutrino mass measurement technique: high 1.5 eV resolution, low background, and excellent understanding and control of systematic effects.

[1] D. Asner *et al.*, Phys. Rev. Lett. **114**, 162501 (2015).

In Phase II, a gas system developed by UW enabled either T_2 gas, for the main measurement, or ^{83m}Kr, a source of mono-energetic conversion electrons for calibration and systematic studies, to be fed to a cryogenic gas cell within a 1-T superconducting NMR magnet. The left panel of Fig. 1.6-1 shows an event after Fourier transformation.

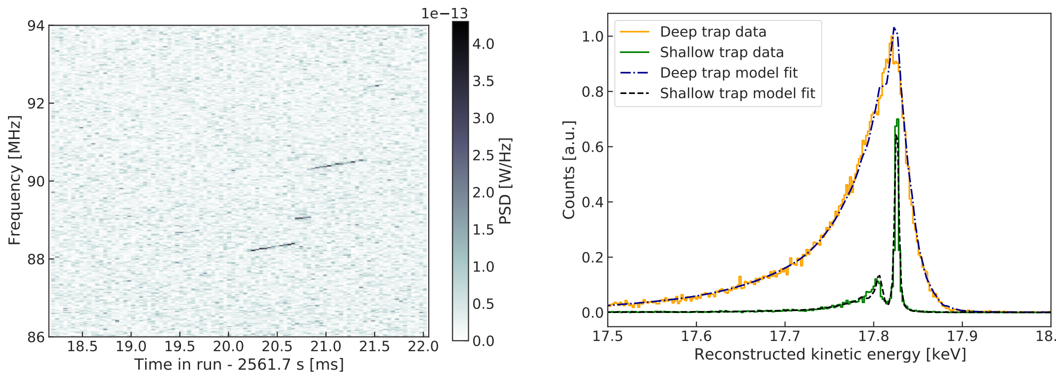

Figure 1.6-1. Left: A CRES event, showing an electron's creation, slow rise in frequency as it loses energy, and occasional sudden loss of energy due to a collision with a gas molecule, splitting the event into multiple "tracks." Right: Spectra of 17.8-keV ^{83m}Kr conversion electrons in both a shallow, high-resolution magnetic trap and a deeper, high-event-rate trap.

Using mono-energetic data from ^{83m}Kr, in Phase II the first detailed investigation was done of the response function in CRES. Fig. 1.6-1 (right) shows ^{83m}Kr data taken in both a shallow magnetic trap configured for narrow 1.5-eV resolution and in the deeper magnetic trap used for the T_2 data campaign that was configured to maximize statistics in this small apparatus. UW personnel played key roles in elucidating the several factors that contribute to the lineshape, including shake-up and shake-off,[1] the magnetic-field broadening, and scattering from residual gas molecules. To study these effects and their impact on the data, the Phase II simulation module had to be upgraded substantially and now includes

- the krypton K-line shake-up/off spectrum as start energy distribution,
- the calculation of a realistic pitch angle distribution in a provided magnetic field map,
- corrections of the received average frequency (Fig. 1.6-2 (left)) and power due to the trajectory and the resulting frequency modulation for the signal of an electron traveling in the field profile of a single powered trapping coil, and
- energy loss and pitch angle changes in scattering of electrons from hydrogen or krypton gas molecules.

The simulations were validated by comparing the simulated data to data recorded with the apparatus in the same trap configuration and processed by the same trigger and reconstruc-

[1] R. G. H. Robertson and V. Venkatapathy, Phys. Rev. C **102**, 035502 (2020).

tion algorithm. Fig. 1.6-2 (right) shows the distribution of first track SNR in a simulated and a recorded krypton K-line dataset.

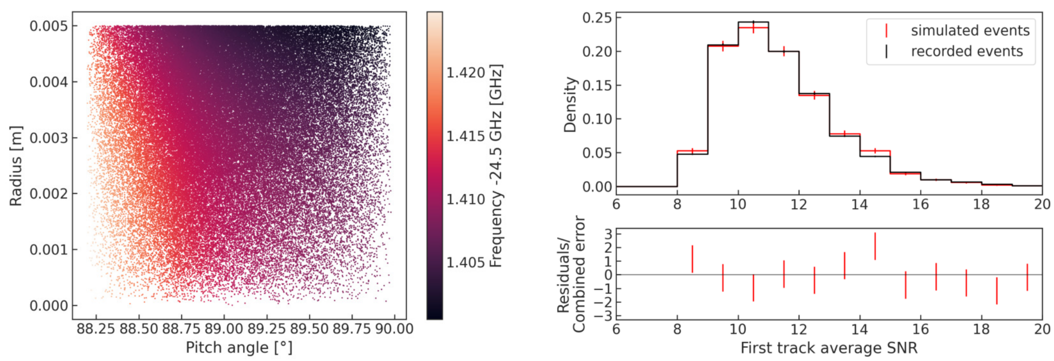

Figure 1.6-2. Left: Received main carrier frequency from electrons with a given radial position and pitch angle (angle between momentum and background field vector at the trap potential minimum) as included in the Phase II simulations. The observed frequencies are calculated from the electrons' trajectories in a map of the trapping field. Right: Comparison of the first-track-in-event SNR distribution after triggering and offline event-reconstruction for simulated data (red) and krypton K-line data recorded in the same trapping field configuration used for tritium data taking.

The good agreement between data and simulation that was achieved allowed us to use the simulations to generate the energy resolution shape and include this shape in the detector response model. With the help of the simulations we were also able to show that the pitch angle changes during scattering have a big impact on the probability for an electron to only be detected after the next scatter. An expression was found to capture this effect in the detector response model. The combination of the simulated resolution shape and empirical tail model led to the very good agreement between the full detector response model and krypton data shown in Fig. 1.6-1 (right), which increases our confidence in the model's accuracy and helped us reduce the systematic uncertainty in the tritium analysis.

The $^{83\mathrm{m}}$Kr data and response model were also used to probe the variation of detection efficiency within the frequency range of interest corresponding to the 16.2-19.8 keV energy range around the tritium endpoint. UW personnel built a long, thin solenoid that fit between the gas cell and the bore of the NMR magnet. With this, we were able to sweep the magnetic field within a $\pm 0.3\%$ range, altering the frequency at which the 17.8 keV $^{83\mathrm{m}}$Kr line appeared, without altering the ppm calibration of the superconducting magnet. After an additional correction for the dependence of signal power on electron energy, this yielded an efficiency map, shown in Fig. 1.6-3 (left), for use as an input to the tritium analysis. The observed structure is due to RF interference with reflections from waveguide components, and is consistent with expectations from analytical calculations and finite-element RF simulation software.

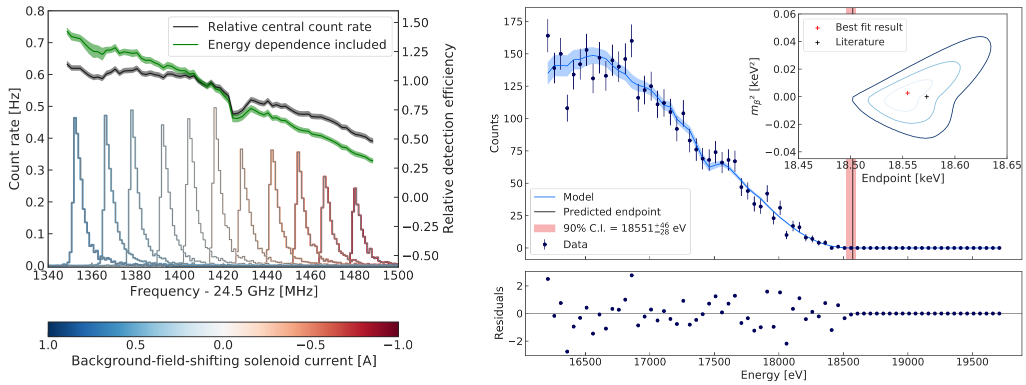

Figure 1.6-3. Left: The 17.8 keV ^{83m}Kr conversion electron line recorded in the deep trap at different magnetic background fields (red to blue). The gray curve shows the relative change of count rates at peak center ($\pm$1 MHz) vs. frequency position of the peak. The green relative efficiency curve for tritium data is produced by correcting for the difference in power dependence of the CRES signal on electron kinetic energy in the continuous tritium spectrum at constant magnetic field strength. Right: Measured tritium endpoint spectrum, with inset of neutrino mass vs. endpoint with 1σ, 2σ, and 3σ contours.

Phase II culminated in a three-month T_2 data campaign yielding 3742 events (Fig. 1.6-3). Zero events were observed above the endpoint, setting an excellent background limit of $\leq 3 \times 10^{-10}\,\mathrm{eV^{-1}s^{-1}}$, and demonstrating CRES's potential as a low-background technique. A frequentist analysis, led by UW, and a Bayesian analysis are nearly complete. The current next-to-final endpoint energy is 18550.6 (+46.1,-27.5) eV, with an upper limit on the effective neutrino mass of 185 eV.

1.7 Electron gun for CRES calibration in Phase III

E. Novitski and R. G. H. Robertson

Achieving the target resolution for Phases III and IV of Project 8 will require new calibration methods. Spatial variations in electric potential and magnetic field within order m^3 trap volumes must be understood, as must variations in detection efficiency with energy. An ideal calibration source would introduce a source of monoenergetic electrons at a known, tunable energy into the trap volume, which could then be detected using CRES.

UW has designed and built an electron gun to serve as a calibration source for Phase III and a prototype for Phase IV. It will produce a 1 μA current of electrons at an energy tunable between 18 and 30 keV, with a narrow 0.3-eV beam energy spread expected from the BaO or LaB_6 cathode. A small fraction of these electrons will Mott-scatter from low density He or Ne gas into trappable pitch angles within the trap volume and will be detected.

A schematic of the electronics for the electron gun is shown in Fig. 1.7-1. A little over 1 W of electrical power to heat the cathode to 1150 K is supplied by an LED array/solar panel setup to float the supply at up to 30 kV. A capacitively coupled ripple monitor probes voltage stability. Initial tests show ripple in the range 30 Hz to 1 MHz to be less than 70 mV p-p.

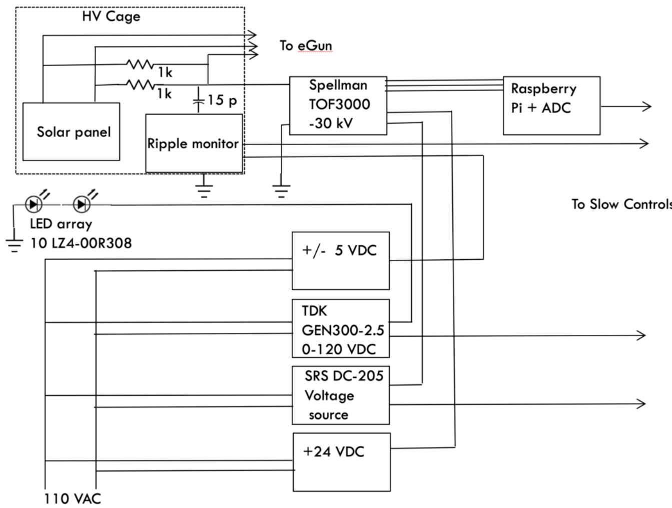

Figure 1.7-1. Electronics for the electron gun.

The electron gun electrodes (Fig. 1.7-2) have a Pierce geometry, designed with the surfaces of insulating spacers perpendicular to the magnetic field direction to prevent breakdown via secondary-emission-enhanced electron avalanches.

Figure 1.7-2. Electron gun components, clockwise from top left: vacuum test stand (also used in coaxial dissociator development for atomic tritium); cathode, Pierce electrodes, and insulating spacers; cutaway of Pierce gun design; LED/solar panel assembly for delivering power to cathode at high voltage; 3-strut pantograph.

The electrodes are mounted on a 3-strut pantograph to enable the egun to be positioned anywhere within a 5 cm radius circle, while retaining its orientation with respect to magnetic field to within the 2-degree tolerance indicated by simulations. Leads to electrodes and to the cathode are insulated within glass tubes between the vacuum feedthrough and their connections to the egun. The assembled electron gun will soon be mounted in a vacuum chamber to test its operation at full current and voltage and to measure the beam spot size using a fluorescent screen.

In parallel, we have been developing an apparatus to perform CRES using the electron gun as the electron source. This Waveguide Electron Gun Apparatus (WEGA) will use a waveguide to collect cyclotron radiation, as in Phase II of Project 8, and we will be able to re-use many techniques and pieces of equipment from that phase. The WEGA's goals are

1. to allow us to verify the electron gun's expected narrow energy resolution, and therefore its suitability as a calibration tool for future phases,
2. to do the first demonstration of CRES at sub-eV resolution, validating our understanding of systematic effects at that level, and
3. to detect cyclotron radiation from a direction perpendicular to the electrons' axial motion, which will the be the geometry used in all future phases and which we expect to reduce pernicious Doppler effects that were limiting in Phase II.

After the waveguide-based studies are complete, the apparatus will be modified to replace the waveguide with a cavity in a first test of large-volume CRES. An initial design of the WEGA is complete (Fig. 1.7-3), with a round of detailed thermal, vacuum, and mechanical studies ongoing to finalize the design.

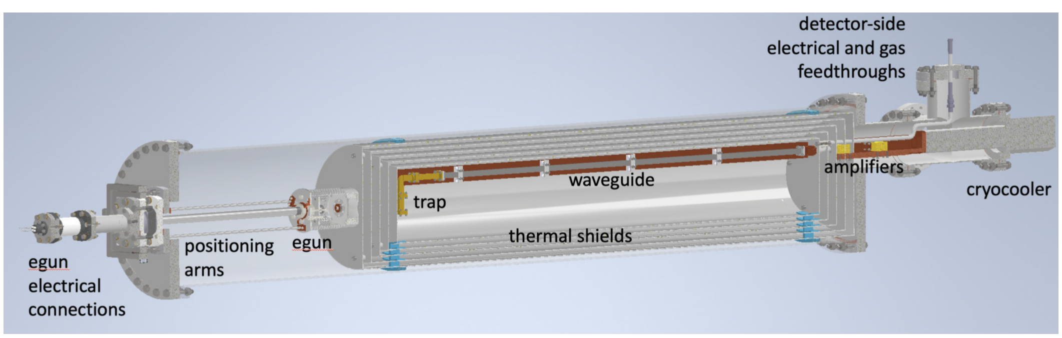

Figure 1.7-3. Design of the Waveguide Electron Gun Apparatus.

1.8 Slow-controls for atomic-source R&D

S. Enomoto

The Project-8 collaboration developed a software package of slow-controls system, called Dripline. The system provides readout and control access to various devices, and can easily integrate external systems such as databases and external Python scripts. Dripline version 2 was used for the Phase-II setup, and the development team released version 3 for use in the next phase, most importantly, for FSCD. Together with the major update to version 3 of the Dripine core, the development team plans major changes on the peripherals, including database, user-interface, visualization, and run-controls. Integration of non-simple devices, such as RGA / mass-spectrometers, is also being discussed.

The R&D of the atomic-source lies in the gap between Phase-II and FSCD, where the new version of Dripline core is ready but has not been widely used yet, and design of peripherals is still under active discussion. Consequently, the slow-controls setup for the atomic-source R&D has two contradicting aspects: as a reliable system for a running measurement, and as a test-bench for evaluation of new code and prototype designs. To fulfill the needs for immediate use, it includes a number of temporary yet working components, half of which were taken from KATRIN and the other half from prototype implementation of new designs.

In addition to the early-phase application of Dripline version 3, there are several unique challenges here: 1) the mass-spectrometer is the main apparatus for this R&D, but it has totally different scheme from all the other slow-control devices, in both controlling and data structure (i.e, time-series vs spectrum), 2) unlike Phase-II where run-controls were done by Python scripts on Linux, "runs" are defined by operation of the mass spectrometer with Windows GUI, 3) unlike Phase-II, analysis is mostly on slow-controls data, but the existing toolchain was not designed for that, 4) the atomic-source setup is ever changing and anticipated to keep growing towards the final Phase-IV setup but making predictions is almost impossible, and 5) data analysis is performed by prominent physics professors who should not be bothered by low-level software complications such as coding.

In the atomic-source setup, the Dripline 3 components are deployed on Docker containers. Official container images of the PostgreSQL database and Grafana visualizer are added to the deployment, as well as the official container image of RabbitMQ, the message hub of Dripline. The mass spectrometer is operated by a proprietary software on Windows and is currently totally independent from the Dripline - Docker system. File sharing between the mass-spectrometer Windows PC and Dripline Linux PC makes the mass spectrometer data files immediately visible on the Dripline PC after every "run". At this point, all data is stored on a Linux PC and the time-series data from Dripline, stored in PostgreSQL, is visualized with Grafana (Fig. 1.8-1).

Integration of the mass spectrometer data and Dripline data is done by the KAFFEE automation software developed for KATRIN. KAFFEE watches new mass spectrometer files and automatically performs a pre-defined chain of analysis tasks, depending on the contents. For each run, Dripline slow-controls data and mass spectrometer counts are digested and integrated by KAFFEE, and the summarized data become available for Jupyter-HUB setup for quick Python analysis on Web browsers. The BREW run table software, which was also taken from KATRIN, displays all the run data in a table form on Web browsers with editing and filtering functionality, and also provides exporting to Excel, enabling quick drawing on Excel with a few mouse clicks.

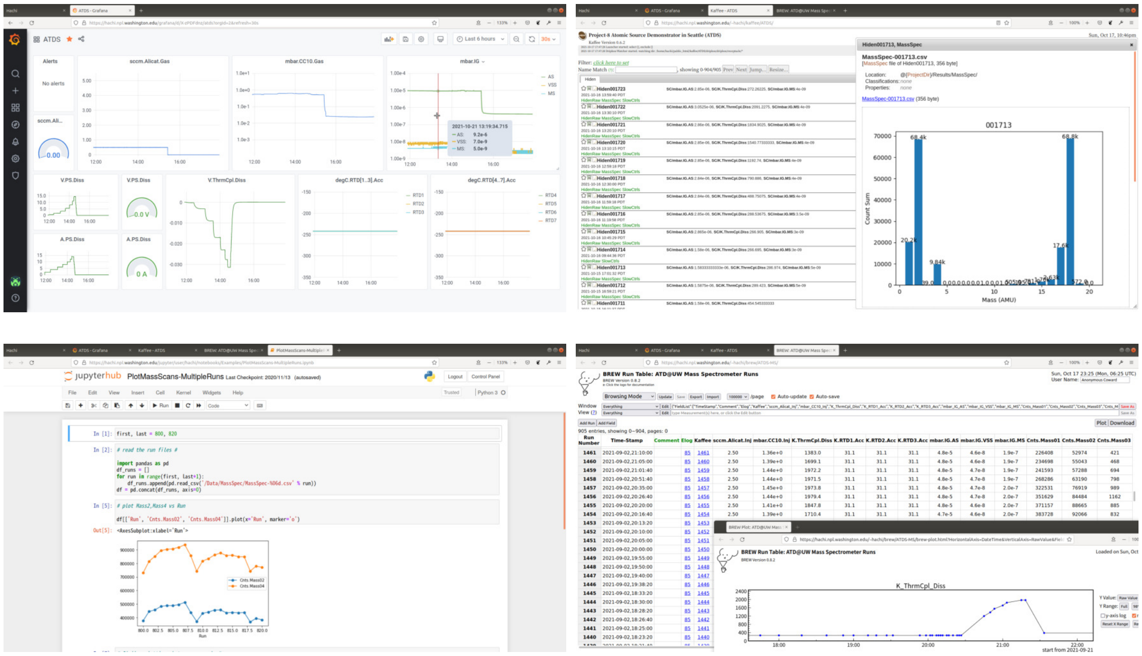

Figure 1.8-1. Screenshots of UI components. Top-left: Grafana for visualizing raw time-series data stored in Dripline database, excluding the mass spectrometer data. Top-right: KAFFEE automation to automatically detect mass spectrometer files, analyze and digest the contents, and integrate the results with time-series data from Dripline. Bottom-left: Jupyter-HUB for Python scripting with easy access to the KAFFEE-digested data. Bottom-right: BREW run table with run-average slow-controls and mass-spectrometer counts in a table form, with exporting to Excel.

Under the hood, a new C++ library was developed for slow-controls data access with managed calibrations, channel mapping, and unit conversions, with a systematic and extensible sensor naming scheme (partly visible in the data names in Fig. 1.8-1), designed for changing and growing measurement systems. The library also serves as an abstraction layer for various underlying data storages and provides simple user interface in a style similar to the Python Pandas library, with embedded resampling and data cleaning functions.

Using the new data access library, a new user interface, slow-controls dashboard (SlowDash), was developed (Fig. 1.8-2). The dashboard displays the current status of the setup in one screen, both the on/off status and good/bad status, on a schematic drawing of the setup, as well as historical plots for selected sensors. The layout and alarm settings are described in simple YAML configuration files. Currently under development is a function to control the displayed devices, possibly combined with Python scripts to define sequences, by mouse clicks on the dashboard, which will replace (at least partly) the command-line interface used for Phase-II.

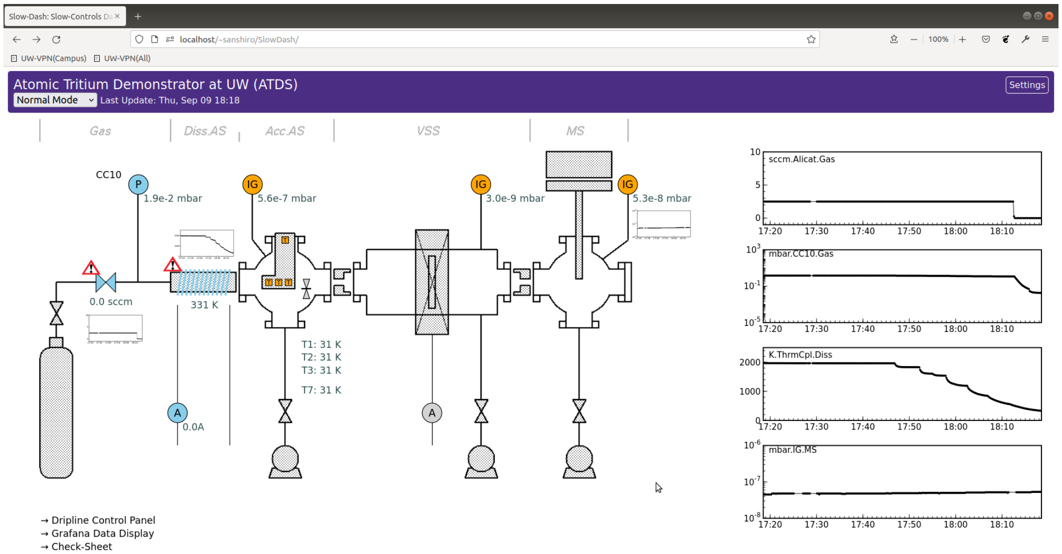

Figure 1.8-2. Screenshot of Slow-controls Dashboard. Sensors are displayed on a schematic drawing of the setup with on/off status (colors) and good/bad status (icons). The pulldown menu on the top left selects operation modes, based on which conditions for alarms are switched. By clicking a sensor symbol, a popup opens which allows operators to interactively analyze history data. Sensor control functions will be implemented on the popup. An external YAML configuration file describes the layout of sensors, binding to database entries, plot settings, and alarm conditions.

1.9 Project 8 mid-scale experiment

R. G. H. Robertson

Before the ultimate Project 8 experiment with 40-meV mass sensitivity can be realized, a mid-scale experiment that serves to demonstrate all the fundamental elements is considered to be essential. Such an experiment serves not only to test the physics and engineering principles, but it can have world-class physics reach if its scale allows measurements below 1 eV, where KATRIN is presently unique.

The path to an atomic source is defined by the reactivity of atomic hydrogen. Magnetic and gravitational trapping must replace physical walls. A benefit of this complication is that T_2 with its negligible magnetic moment will rapidly escape the confinement region. This is essential because the molecular endpoint energy is 10 eV greater than the atomic one and it would otherwise contribute a background at the atomic endpoint. A magnetic field that confines the T will also trap the electrons for observation, but the magnitudes of the appropriate fields are very different, which leads to the magnetogravitational trap solution. For the magnetic walls, two types of magnetic bottle, a Ioffe trap similar to the one used to trap anti-hydrogen in the ALPHA experiment and a Halbach array similar to those used to trap ultra-cold neutrons are under consideration. In both cases, the atomic gas being trapped must be very cold – an atom in a magnetic field of 1 T has a potential energy equal to its kinetic energy at 0.6 K. Design of the Ioffe version is being led at Mainz and MIT, while the Halbach array study has been initiated at CENPA.

In the past year, we have made substantial progress in developing a new overall concept that appears to resolve many troublesome limitations that have been encountered along the road to an atomic experiment. The central ingredients of this concept can be summarized as follows:

- Move down in frequency from the present 27 GHz to about 1 GHz or less. This reduces dipolar spin-flip losses in the trap fivefold.

- Develop in-flight evaporative cooling of atomic tritium from the source to reach mK temperatures. This approach is potentially orders of magnitude more efficient than magnetically selecting a slice of the Maxwell-Boltzmann distribution around the desired temperature.

- Capture CRES signals in a resonant cavity. The coupling of an electron in cyclotron motion to the lowest-order axial mode of a cavity is almost Doppler-free, increasing the usable range of pitch angles of trapped electrons, and thus the efficiency with which atoms from the source are used.

- Simplify the mode structure of the cavity by mode filtering, a technique that is implemented by segmenting the cylindrical walls into rings so that only TE01p modes are supported. This greatly increases the volume that can be used at a given wavelength before mode crossings complicate the response.

- Open the cavity ends for admission of atoms and pumping of molecules. Open cavity structures are known, and have Qs almost as high as the more common closed cavities.

Production of an intense, cold atomic beam of tritium entails several steps: thermal “cracking” (dissociation) of T_2 on a hot tungsten surface, cooling of the atoms to tens of Kelvin by accommodation on a cold surface of aluminum, capture and state selection in a magnetic guide, further cooling by evaporation to milliKelvin temperatures, injection into the experiment’s magnetic trap, and recycling of the molecular tritium after eventual loss from the trap and recombination. Valuable information on production and trapping of atomic hydrogen emerged from the efforts to prepare a Bose-Einstein condensate in the 1980s and 1990s. An illustration of the concept of an evaporatively cooled atomic beam coupled to a magnetogravitational trap is shown in Fig. 1.9-1.

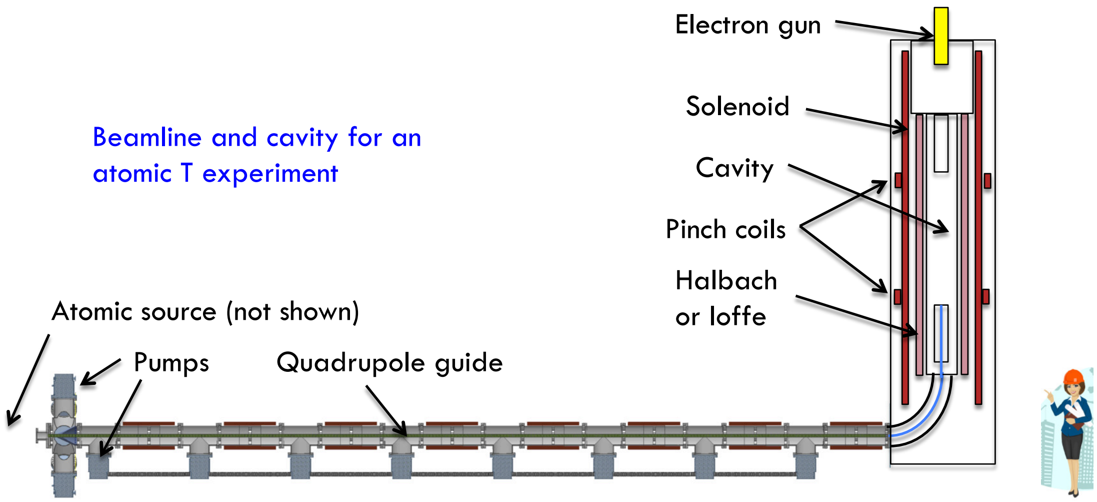

Figure 1.9-1. A midscale CRES atomic experiment sensitive to masses $\lesssim 1$ eV.

The first stage of an experiment of this nature would be the cavity, the solenoid, diagnostic devices such as the electron gun, a low-noise amplifier, data-acquisition system, and tritium handling system (i.e, the right-hand part of Fig. 1.9-1). This constitutes a standalone T_2 experiment with sub-eV sensitivity that would verify the performance of many of the novel features of the instrument and have excellent performance in the search for sterile neutrinos in the eV mass range.

1.10 Phase III atomic tritium

C. Claessens, P. J. Doe, S. Enomoto, and R. G. H. Robertson.

As noted above in Sec. 1.9, Project 8 mid-scale experiment, to realize the 40 meV potential of Project 8 will likely require a source of $\approx 10^{19}$ tritium atoms per second, of which some fraction will be cooled to a few milliKelvin in order to maintain a density of $\approx 10^{17}$ m^{-3} in the atomic trap. Commercial devices are available that can thermally dissociate, or crack, molecular tritium to provide atomic tritium beams of $\approx 10^{16}$ atoms per second. To achieve the higher flux, we are developing a cracker that consists of coaxial tungsten tubes electrically heated to > 2000 K. Molecular tritium flows down the inner tungsten tube, dissociating upon contact with the hot wall of the tungsten tube. A schematic diagram of the coaxial cracker is shown in Fig. 1.10-1 along with the test apparatus in which initial tests of the electrical performance of the cracker are made.

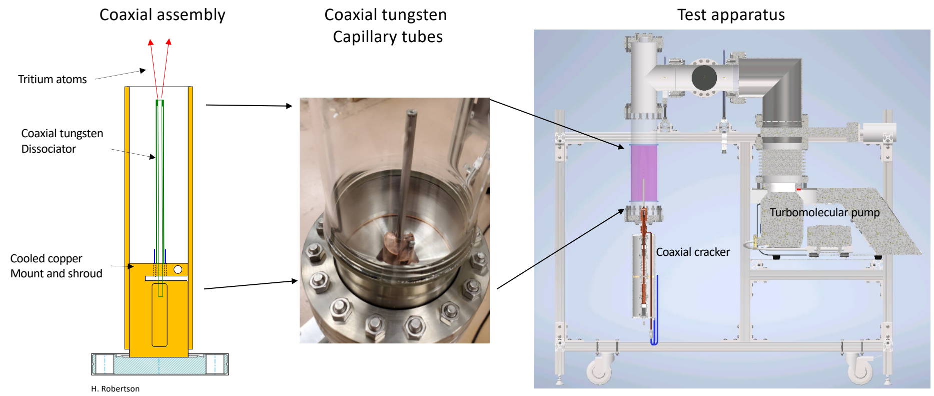

Figure 1.10-1. Left; a schematic diagram of the coaxial tungsten tubes of the cracker. Center: the tungsten tubes mounted in the test apparatus, Right: a schematic diagram of the vacuum chamber in which the electrical and thermal properties of the cracker are tested.

In order to test the dissociation and beam forming properties of the coaxial cracker, we have constructed the apparatus shown in Fig. 1.10-2. This consists of a commercial cracker, with well-defined properties, a collimation system consisting of two collinear apertures followed by a mass spectrometer, optimized for masses 2 and 4 and capable of scanning horizontally and vertically across the beam coming from the apertures. We are in the process of commissioning this apparatus. Once it is thoroughly understood using the commercial cracker, the coaxial cracker will be installed and commissioned.

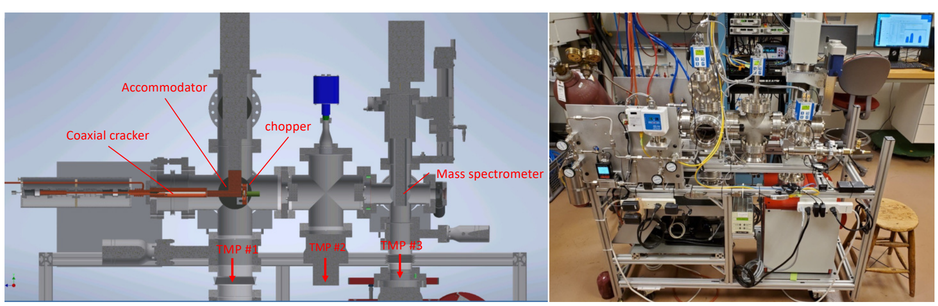

Figure 1.10-2. Left: a drawing of the apparatus for investigating the atomic beam produced by the coaxial cracker and the performance of the accommodator used to cool the beam emerging from the cracker. Right: photo of the apparatus.

The next step is to cool the atomic beam of atoms to a few 10's K. To accomplish this, we have built an accommodator consisting of an aluminum tube cooled by a pulse tube cooler to approximately 40 K. We will measure the temperature profile of the cooled beam by chopping the beam and measuring the time-of-flight between the chopper and the mass spectrometer. Further development will be directed towards tailoring the beam to meet the requirements for filling the Phase III magnetic trap, this will include magnetic state selection and evaporatively cooling the beam to milliKelvins.

Majorana

1.11 Status of the Majorana Demonstrator neutrinoless double-beta decay experiment

J. A. Detwiler, A. Hostiuc, W. Pettus†, N. W. Ruof, and C. Wiseman

The Majorana Demonstrator neutrinoless double-beta decay ($0\nu\beta\beta$) experiment has completed data taking for its search for neutrinoless double-beta decay in ^{76}Ge. The experiment consists of a modular array of p-type point contact (PPC) high purity germanium (HPGe) detectors, with most detectors enriched in the $0\nu\beta\beta$ isotope ^{76}Ge (Fig. 1.11-1). The apparatus continues data taking at the 4850 ft level of the Sanford Underground Research Facility (SURF) in Lead, SD with a smaller array of non-enriched HPGe detectors to measure backgrounds.

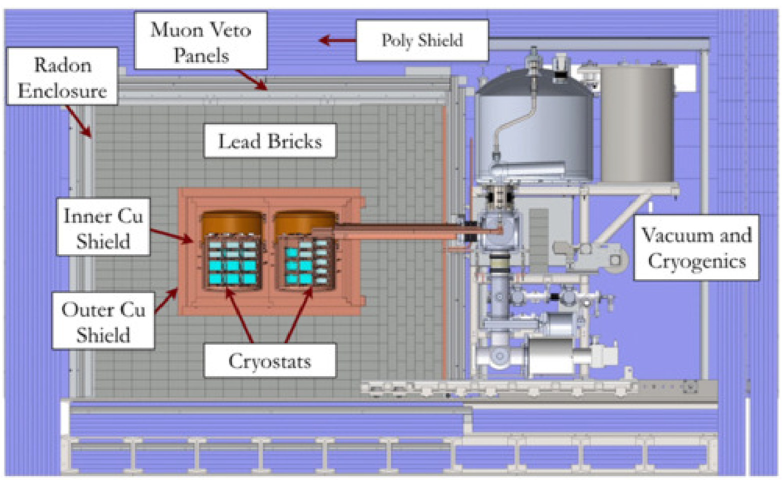

Figure 1.11-1. Schematic of the MAJORANA DEMONSTRATOR experiment. The germanium detectors (teal), enriched in the ^{76}Ge isotope of interest, are assembled with low-background materials into close-packed arrays in two cryostats inside a passive shield.

The stable operation of the detector has afforded greater emphasis on analysis efforts. In 2021, the group saw publications on the ADC Nonlinearity Correction[1], and the Search for Double-β Decay of ^{76}Ge to Excited States[2] (the latter, spearheaded by former CENPA graduate student Ian Guinn).

Beginning in March 2021, the science run was interrupted and both modules were opened for the removal of the enriched detectors in order to have them shipped to Gran Sasso, Italy, for inclusion in the LEGEND-200 experiment. The remaining natural detectors have been

†Presently at Indiana University, Bloomington, IN.

[1]N. Abgrall *et al.*, Transactions on Nuclear Science VOL. 68, NO. 3, March 2021.
[2]I. J. Arnquist *et al.*, Phys. Rev. C **203**, 015501 (2021).

put back in the modules and are now running for "Dataset 9". Graduate student Alex Hostiuc went on-site and helped with the enriched detector extraction.

The CENPA MAJORANA group had significant achievements in 2020-21. Alex Hostiuc passed his general exam for Ph.D. candidacy. Postdoc Clint Wiseman continues his leadership of the low-energy working group, with publications in preparation (Sec. 1.15). Graduate student Nick Ruof has continued his development of the AvsE analysis, while graduate student Alex Hostiuc has continued his work on the DCR surface alpha rejection and implemented a new estimator, Late Charge (LQ) (Sec. 1.12). The group operates germanium detectors in the lab at CENPA, investigating key detector response characteristics and providing involvement for undergraduates in the project, while leveraging the technical expertise at CENPA.

The group's contributions to the project are further recognized by election to leadership positions. Jason Detwiler continues service as co-spokesperson of the collaboration, being re-elected last summer. Alex was elected as one of the two young member representatives for July 2020 through June 2021, as Nick and Ian completed their term in the same position.

1.12 Pulse-Shape Analysis for the MAJORANA DEMONSTRATOR

J. A. Detwiler, A. Hostiuc, W. Pettus[‡], N. W. Ruof, and C. Wiseman

The characteristic signals produced by the p-type point contact detectors in the MAJORANA DEMONSTRATOR allow for the discrimination of background events by analyzing the shapes of the signal waveforms. The pulse shape analysis contains a delayed charge recovery cut, a multi-site cut, and a late charge cut. The delayed charge recovery cut removes events caused by alpha particles deposited on the detector passivated surface. The multi-site cut removes events that deposit energy in more than one location with in a single detector, typically due to Compton scattering. The late charge cut removes multi-site events where one of the energy depositions is in close proximity to the detector point contact, which give a signature that is not tagged by the traditional multi-site cut.

[‡]Presently at Indiana University, Bloomington, IN.

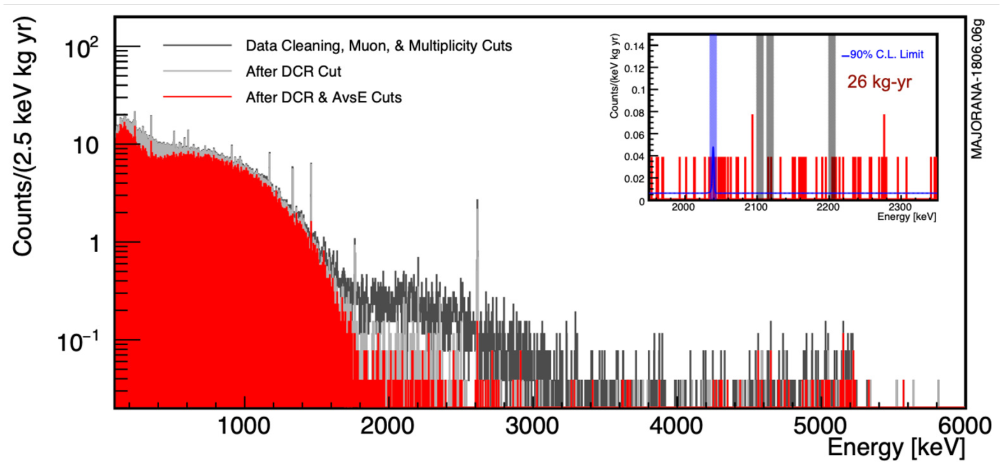

Figure 1.12-1. Energy spectrum of 26 kg-yr of exposure with successive application of cuts. The inset shows the spectrum of the background estimation window; 10 keV windows are excluded around known gamma lines (gray) and $Q_{\beta\beta}$ (blue).

In the latest result[1], after all analysis cuts the MAJORANA DEMONSTRATOR achieved a background index of 11.9 $\pm$ 2.0 cts / (FWHM t yr) and a lower half-life limit of 2.7×10^{25} yr. Fig. 1.12-1 shows the full energy spectrum before and after cuts are applied. In this analysis, the delayed charge recovery accounts for a 70% reduction of the background, and the multi-site rejection accounts for an additional 25% background reduction. In addition to the late charge cut, new improvements have been made to each element of the pulse shape analysis to make cuts that are more uniform across all detectors and include extra corrections that improve the cuts based on their dependencies on other pulse shape parameters. The MAJORANA DEMONSTRATOR has finished data-taking with enriched germanium detectors and the improved analysis is being prepared for release on the full dataset with a total combined exposure of 65 kg yr.

Multi-site background rejection in the MAJORANA DEMONSTRATOR

The MAJORANA DEMONSTRATOR p-type point contact (PPC) detectors have multi-site rejection capability by performing pulse shape analysis on waveforms originating from the detectors. The long drift times, greater than 10 μs across the detector bulk, combined with the heavily localized weighting potential near the point contact, yield charge collection waveforms with fast rising edges. Due to the waveforms' fast rise times, it is possible to distinguish waveforms with one localized event from waveforms with two or more localized events by relating the current amplitude of the waveforms to the energy deposited. A waveform originating from a multi-site event has a current amplitude that is degraded compared to a single-site event waveform's current amplitude with the same energy (Fig. 1.12-2). Since neutrinoless double-beta decay is inherently a single-site event, multi-site events can be rejected from the search.

[1] I. S. I. Alvis *et al.*, Phys. Rev. C **100**, 025501 (2019).

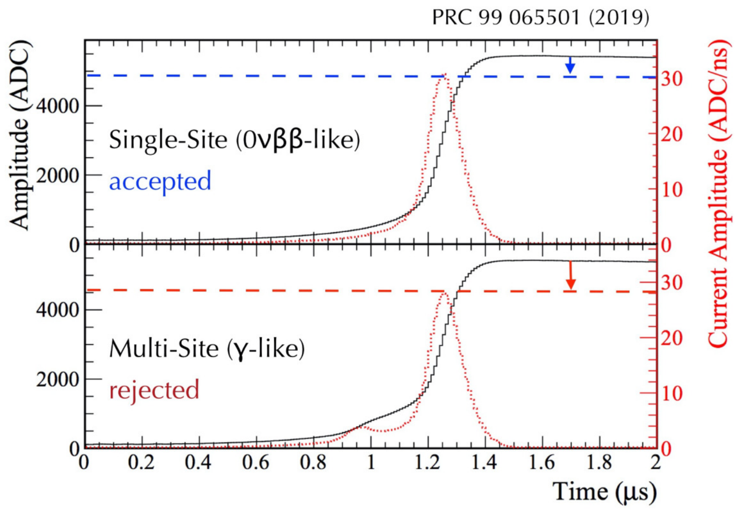

Figure 1.12-2. *Top:* A charge (black) and corresponding current (red) waveform for a single-site event in a germanium detector. *Bottom:* A charge and current waveform for a multi-site event. Comparing two waveforms of the same energy shows that multi-site waveforms are degraded in current amplitude, a distinguishing feature that can be used to remove these events from the background.

Relating the amplitude (A) of the current pulse and the total energy (E) collected, defines the $AvsE$ pulse shape parameter for multi-site rejection.

$$AvsE = -\frac{A(E_{cal}/E_{unc}) - quad(E_{cal}, a, b, c) - exp(E_{cal}, d, \tau)}{\sigma(E_{cal}) \times s} \tag{1}$$

Subtracted from the calibrated current amplitude is a quadratic function and an exponential function to correct for the amplitude's dependence on energy. $\sigma(E_{cal})$ is a scaling function that corrects for the width-energy dependence of $AvsE$ and s is a constant scaling factor that sets the multi-site cut at -1. It has also been discovered that the rate at which charge is collected, or the drift-time, also has some dependence on $AvsE$. The nature of whether a waveform is single-site or multi-site should not depend on how fast the charge is collected. To correct for this, a rotation in the (drift-time, $AvsE$) space is done before correcting for the width and tuning the constant scaling factor.

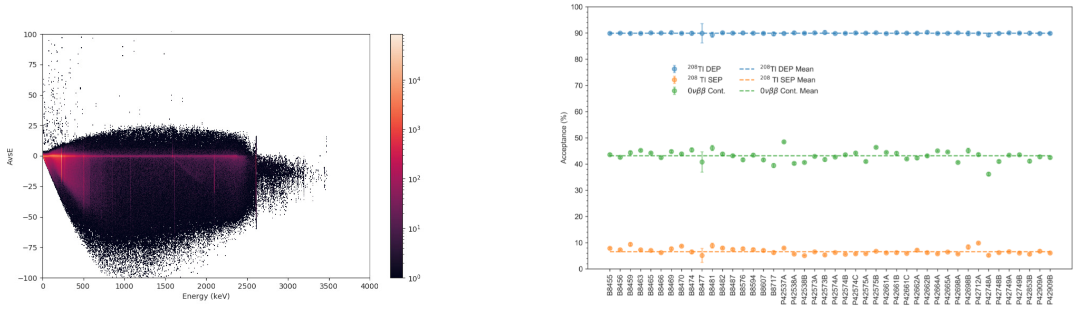

Figure 1.12-3. *Left:* An $AvsE$ spectrum for a series of long calibration runs in a ^{228}Th calibration study. A flat cut at $AvsE = -1$ represents a multi-site event cut, with 90% of events in the signal-like ^{208}Tl double escape peak still remaining after the cut. *Right:* To measure the performance of the $AvsE$ parameter, the acceptance rate in each of three energy regions (double escape peak, single escape peak, and $0\nu\beta\beta$ Compton continuum) is measured for all long calibrations from the latest dataset.

The goal of the $AvsE$ parameter is to create a parameter with a flat cut that will exclude mostly multi-site events. This is done by flattening out the distribution of current amplitudes vs energy and setting the cut value where the acceptance rate at the ^{208}Tl double escape peak in a ^{228}Th calibration is 90%. A double escape peak in an energy spectrum is a population of mostly single-site events. Additional improvements, reflected in Eq. (1), have been added: an extra residual correction to more precisely flatten the current amplitude, a drift-time correction to remove effects of variable charge collection times, and a width energy dependence correction to account for the changing width of $AvsE$ with energy. In the analysis of a ^{56}Co spectrum, it was shown that the width of the various double escape peaks is dependent on the energy, and now $AvsE$ is scaled to an empirical function that resembles the width dependence trend. The overall performance of the new $AvsE$ parameter shows a 90% acceptance for the double escape peak, 7% acceptance for the single escape peak, and 43% for the Compton continuum (Fig. 1.12-3).

1.13 Alpha particle discrimination in the Majorana Demonstrator

J. A. Detwiler, A. Hostiuc, W. Pettus, N. W. Ruof, and C. Wiseman

P-type point-contact germanium detectors like those used in the Majorana Demonstrator been observed to exchibit reduced charge collection for events occurring on or near their passivated surface. In our experiment, events have been observed in which alphas originating on the passivated surface are significantly degraded in energy, which can result in background in the region of interest (ROI) for neutrinoless double beta decay, i.e. close to the $Q_{\beta\beta}$ value for ^{76}Ge of 2039 keV.

The delayed charge recovery (DCR) parameter is used in the Majorana Demonstrator in order to reject this alpha background in the attempt to achieve the necessary low background. The physical effect behind DCR is that the charge deposited by the alpha particle does not get collected all at once. Rather, some of the charge is trapped and then released slowly, on a timescale much longer than that of the charge cloud drift. The presence of such delayed charge collection can be detected as an increase in the slope of the waveform tail.

The new implementation of DCR, or version 2.0, has been developed and is the principal discriminator for background alpha rejection. For a detailed treatment of the development of DCR, see the 2020 Annual Report[1]. A comparison of DCR version 2.0 to the original DCR, showing notable improvements in stability detector-by-detector, can be seen in Fig. 1.13-4.

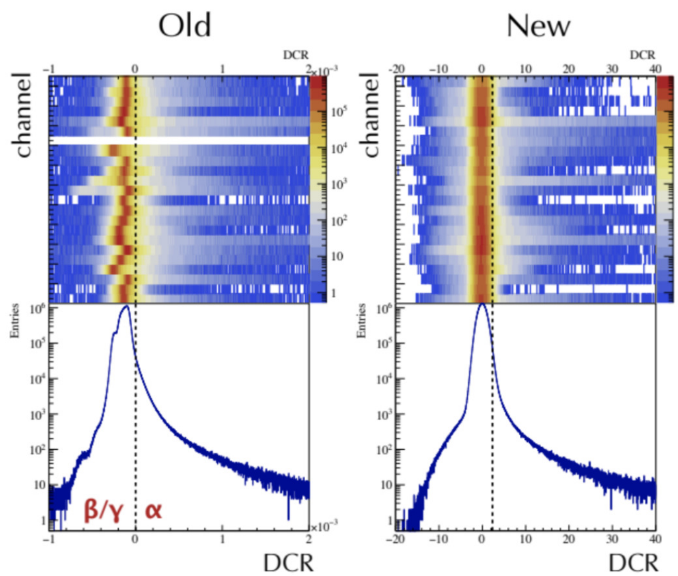

Figure 1.13-4. A comparison of the old and the new (v2.0) DCR parameters. We see more similarity between the distributions of each channel, allowing for the same cut to be applied for all channels (although the efficiency does differ). There is no more need to reprocess data when the efficiency is not as desired; an optimization study for all channels at once is on-going.

In addition, we have implemented a drift time (or charge trapping) correction to DCR. Charge trapped during bulk drift event gets released on the same timescale that DCR is being measured. Thus, we also recover delayed charge that is not associated with trapping near the passivated surface, where our alpha-contamination occurs, but rather, with trapping in the bulk. Such trapped charge in the bulk should be proportional to drift time, thus we can estimate how much extra DCR we expect from this contribution on an event-by-event basis and subtract it, reducing its contribution to the variance. This effect is detector-dependent, but we foresee improvements in our ability to identify and reject alphas very close to the DCR cut boundary.

The drift time corrected DCR distribution is described by a dominantly Gaussian shape with a mean of 0 and a standard deviation of 1, although many detectors have some high-DCR tailing. To retain $\sim$ 99% of the bulk detector events, we reject any events with a

[1]CENPA Annual Report, University of Washington (2020) p. 31-34.

DCR value greater than 2.326, equivalent to a one-sided 99% cut for a Gaussian distribution. Calculations of the efficiency in datasets 0 through 6c indicate that the new DCR parameter achieves high efficiency of 98.7%. This departure from a 99% efficiency is due to the high-DCR tailing and varies detector-by-detector. An example of a typical DCR v2.0 distribution is given in Fig. 1.13-5.

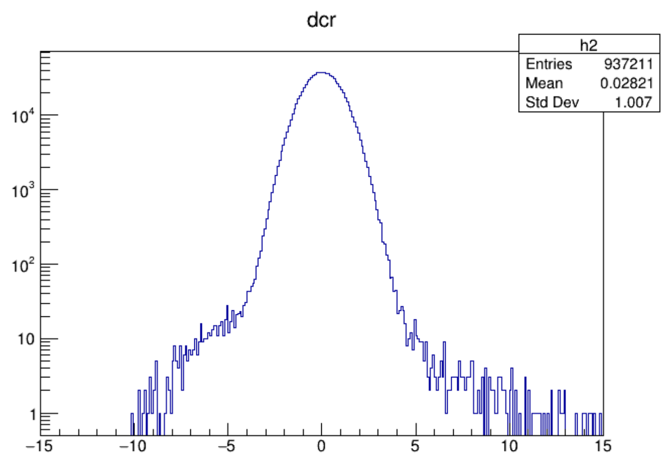

Figure 1.13-5. A typical DCR distribution, in this case for one detector during one calibration. The distribution has a Gaussian shape centered around 0 with a standard deviation of approximately 1, with some tailing visible on both sides.

1.14 Late Charge (multi-site) discrimination in the MAJORANA DEMONSTRATOR

J. A. Detwiler, A. Hostiuc, W. Pettus‡, N. W. Ruof, and C. Wiseman

While, as discussed above, the $AvsE$ discriminator is our principal multi-site discriminator, in some situations it doesn't have excellent performance. Specifically, if one of the interaction sites is close to the point contact, then the proximity to the point contact results in an enhanced current amplitude (A) whereas a typical multi-site event would normally have a reduced A for a given energy E.

‡Presently at Indiana University, Bloomington, IN.

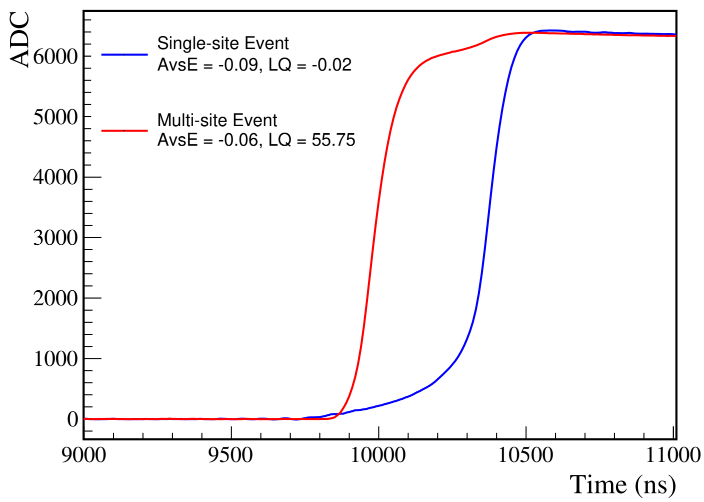

Figure 1.14-6. An example of a single-site (blue) and a multi-site (red) waveform. The MS waveform has an obviously higher LQ value.

The Late Charge (LQ) parameter is a new parameter which seeks to identify and reject multi-site events not tagged by our main multi-site cut ($AvsE$), where at least one of the sites is close to the point contact of the detector. We define a late charge (LQ80) parameter based on the charge drift of the second interaction, i.e. looking at charge drift after the 80% energy time point of signal (see Fig. 1.14-7). Near-point-contact multi-site events that evade the $AvsE$ cut have high LQ80 values.

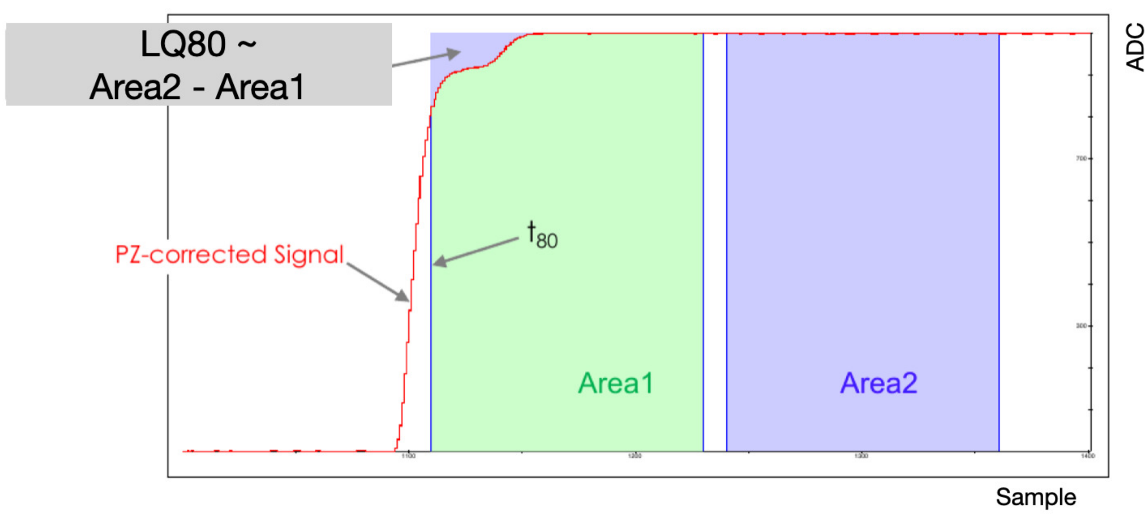

Figure 1.14-7. This plot shows how LQ80 is computed starting from a flat-top waveform. LQ80 is the starting point for defining our final LQ parameter.

LQ80 is converted into a Gaussian distribution, shifted and normalized such that its mean is 0 and its standard deviation is 1, following the same method as for DCR. We call this tuned parameter LQ. As we desire a very high single-site acceptance, a cut of $LQ < 10$ is applied in the MAJORANA DEMONSTRATOR analysis. The overall efficiency through dataset 6c is 99.74% with an uncertainty of 0.22%.

1.15 Low Energy Analysis for the Majorana Demonstrator

C. Wiseman

The MAJORANA Low Energy Working Group has made significant progress this year towards completing our analysis of the 1–100 keV region of the MAJORANA DEMONSTRATOR spectrum, collected during the primary operational period between June 2016 – November 2018. Our efforts to clean a multi-year >5 TB dataset with significant noise contamination near the energy threshold have passed internal collaboration review, and a series of publications are being drafted, including searches for bosonic dark matter, solar axions, and wavefunction collapse.

The Low-Energy Analysis Toolkit (LAT) has been developed to perform pulse shape analysis and pulse shape discrimination specifically at low signal-to-noise levels. We have developed methods to apply adaptive time-dependent energy threshold cuts, wavelet-based high-frequency noise rejection, high-rate burst cuts, slow pulse (surface event) rejection, and determination of the total fast event acceptance efficiency, which remains > 20% at 1 keV. We have lowered the overall analysis energy threshold by a factor 5 from our previous result in 2017, to a new lower limit of 1 keV. To quantify the slow pulse rejection efficiency, a novel method of determining the cut efficiency based on small-angle Compton scatters in calibration data was developed. An example of the fast waveform fit for slow pulses is shown in Fig. 1.15-1.

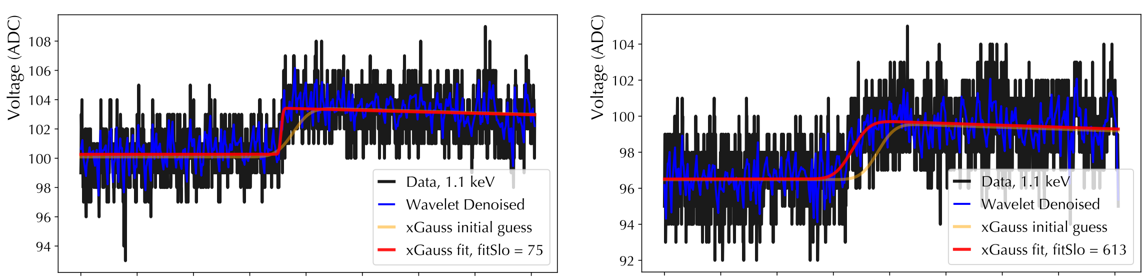

Figure 1.15-1. Two waveforms with the same evaluated energy, with distinct values of the `fitSlo` parameter. At 1.1 keV, the waveform fit shows a significant difference between a fast (bulk) signal (top) and a slow signal (bottom). (X-axis in nanoseconds.)

We have produced spectra from the ^{76}Ge-enriched and natural-abundance detectors in the DEMONSTRATOR with the LAT toolkit with a nominal 1 keV software threshold, with greater than 40% cut efficiency at all energies. The enriched spectrum from 1–5 keV, shown in Fig. 1.15-2, shows an unanticipated excess of events, in addition to the continuum from tritium beta decay. This excess is significantly larger than the similar signals recently reported by the XENON1T and PandaX-II collaborations, and is still under study. It is most likely due to radioactivity from ^{210}Pb or other contamination leading to energy deposits near the passivated surfaces of the enriched detectors, which exhibit degraded energy.

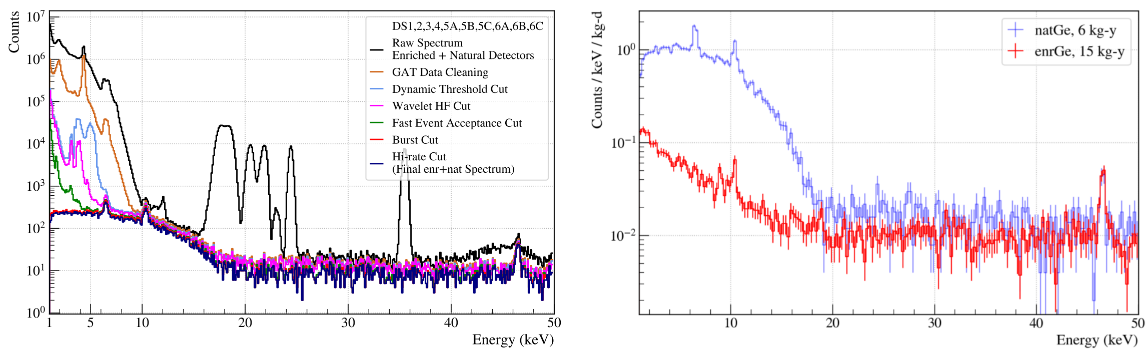

Figure 1.15-2. *Left:* The succession of cuts applied to produce the final spectrum. Large features due to noise in the raw spectrum are effectively removed by the threshold, data cleaning and burst cuts. Application of the slow pulse cut changes the spectral shape and makes the tritium feature and cosmogenic lines visible. *Right:* The *preliminary* enriched and natural spectrum from the open data analysis. The effect of the campaign to reduce the surface exposure and tritium activation of the enriched Ge detectors is apparent, and increases the sensitivity to low-statistics rare event searches.

Two background models are used in the peak search analysis. One reproduces the method used in the 2017 analysis, using a tritium PDF and a linear background function to describe the continuum part of the energy spectrum, and a set of Gaussians to describe known cosmogenic peaks. A hypothetical "rare signal" peak (also Gaussian) is scanned across the 1–100 keV energy range, using an unbinned likelihood fit to produce a 90% upper limit of counts attributable to a rare peak. A second method of performing the fit uses a low-order Chebyshev polynomial to locallay approximate the continuum background in a moving narrow window around the rare signal peak, while keeping the Gaussians for the cosmogenic lines. Both models are implemented using the `RooFit` framework, and incorporates the cleaned energy spectra, and considers systematic errors in cut efficiencies and energy resolution. We are currently pursuing unblinding, using the full DS1–6C exposure. Our data processing and peak search analysis codes have been automated to expedite this process.

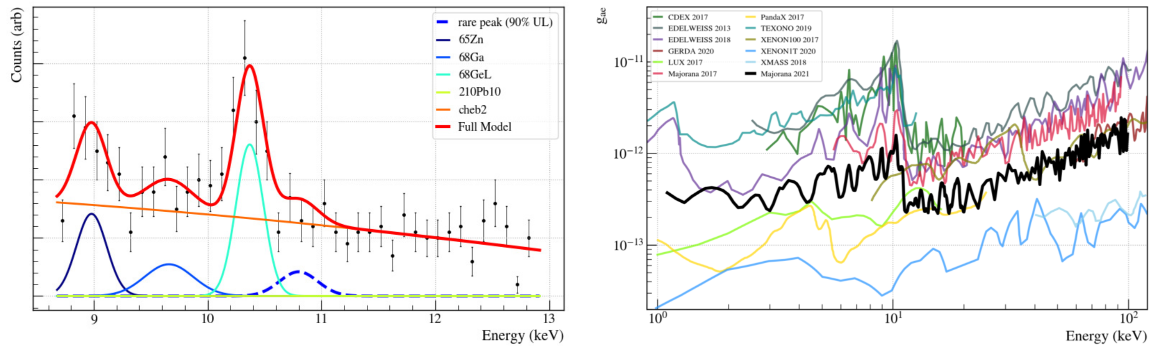

Figure 1.15-3. *Left:* Example calculation of an upper limit of counts attributable to a rare signal peak (N_U) with a 90% confidence level. The initial guesses for the cosmogenic peak fits are taken from a fit without the signal peak. When the signal peak overlaps with a cosmogenic line, the cosmogenic heights are minimized to ensure that N_U is maximized. *Right:* Exclusion limits for pseudoscalar (axionlike) bosonic dark matter. The MAJORANA curve (black) is the best limit for any Ge experiment, with the increased exposure and a factor 5 reduction in energy threshold from the previous analysis. Xe experiments (XENON1T, PandaX-II) give more stringent limits owing to their much larger active mass.

LEGEND

1.16 LEGEND: A Ton-Scale Search for Neutrinoless Double-Beta Decay in 76Ge

S. Borden, T. Burritt, J. A. Detwiler, A. Hostiuc, C. J. Nave, D. A. Peterson, R. Roehnelt, N. W. Ruof, G. Song, D. A. Sweigart, and C. Wiseman

LEGEND is a next-generation neutrinoless double-beta ($0\nu\beta\beta$) decay search in ^{76}Ge. By combining the technological expertise and experience from the MAJORANA DEMONSTRATOR and GERDA experiments, LEGEND is expected to reach a design sensitivity two orders of magnitude greater than its predecessors.

The phased program advances from the intermediate scale LEGEND-200 experiment to the future LEGEND-1000 experiment. LEGEND-200, using 200 kg of enriched HPGe detectors, is now under construction at the Laboratori Nazionali del Gran Sasso (LNGS) in Italy. LEGEND-200 reuses the cryostat vacated by the former GERDA experiment. LEGEND-1000 is a leading candidate for a future US-led tonne-scale $0\nu\beta\beta$ experiment. It leverages the advances of the ^{76}Ge program, through LEGEND-200, to retire risks in demonstrating array scalability and achievement of background goals. It will yield an additional order-of-magnitude sensitivity to the $0\nu\beta\beta$ half-life, covering the neutrino mass parameter space allowed by the inverted ordering of neutrino masses.

The CENPA LEGEND group plays a leading role in the development of the analysis framework for the project, which is actively tested on the data collected with our local test stands. Professor Detwiler is a member of the LEGEND Steering Committee, an Analysis

Co-Coordinator, and the lead of the Analysis Framework task group. Locally we are pursuing R&D efforts to understand the surface response of HPGe detectors, the light detection of SiPM detectors, and alternative readout electronics. These efforts are described in the subsequent sections.

1.17 Analysis Framework for LEGEND

S. Borden, J. A. Detwiler, I. Guinn[‡], D. A. Sweigart, and C. Wiseman

The LEGEND collaboration has made significant progress towards a set of data processing tools for the upcoming LEGEND-200 experiment, known as `pygama`. Our local CENPA group has taken a leading role in the development of these tools and performed the first multi-detector analysis using the "Post-GERDA Test" (PGT) (Sec. 1.18) and an analysis of SiPM data (Sec. 1.21). The tools are being developed to run automatically at the LNGS and NERSC computing facilities, taking the data from the output of the data acquisition system (DAQ), running and optimizing a suite of digital signal processing, and producing output files containing energy and pulse shape information for fast analysis. The pipeline is shown in Fig. 1.17-1.

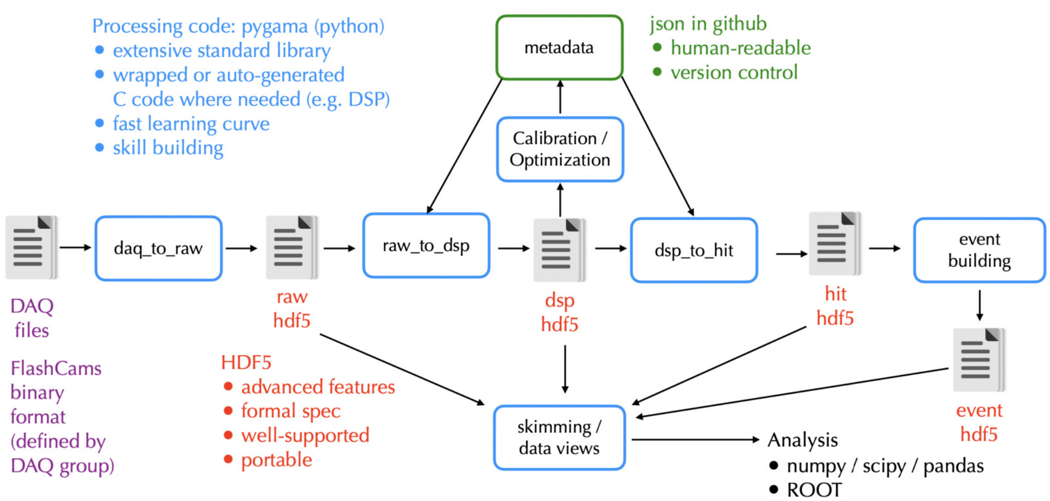

Figure 1.17-1. Illustration of the data processing pipeline for LEGEND data, extending to HPGe detectors, SiPMs, and PMTs. Data from each detector are analyzed automatically to produce pole-zero constants and other parameters necessary to optimize the energy resolution of the detectors. Data from each detector are processed separately until later stages, where timing information is incorporated to produce "events" from the full array for coincidence analysis.

Several important milestones in the development of `pygama` were completed this year. Development of LH5, a custom file format for LEGEND using HDF5 was completed, allowing fast access to all Ge data using Python and `h5py`. Waveform compression algorithms are

[‡]Presently at University of North Carolina at Chapel Hill.

being implemented to reduce file sizes, an important disk savings for a multi-year experiment. Significant effort has gone into the digital signal processing of waveform data. We have developed a framework (`ProcessingChain` and `WaveformBrowser`) which computes pulse shape parameters and waveform transforms using simple implementations in Python, accelerated with the `numba` toolkit. These calculators have been used for the PGT data, as well as for ongoing detector characterization campaigns at HADES and SURF, and also the CAGE test stand setup at CENPA (Sec. 1.19). Routines have been written to automatically optimize pole-zero constants and other parameters for each detector, minimizing the energy resolution and maximizing pulse shape discrimination capabilities of each detector. One example of this waveform optimization is shown in Fig. 1.17-2, where the RC decay of the detector signal is removed to look for events with abnormal slope in the tail, indicating if delayed charge recovery (DCR) is present in each waveform.

Construction of LEGEND-200 is ongoing, and the next milestone for LEGEND is a full-chain electronics test for LEGEND-200, for which the `pygama` framework will be ready for use.

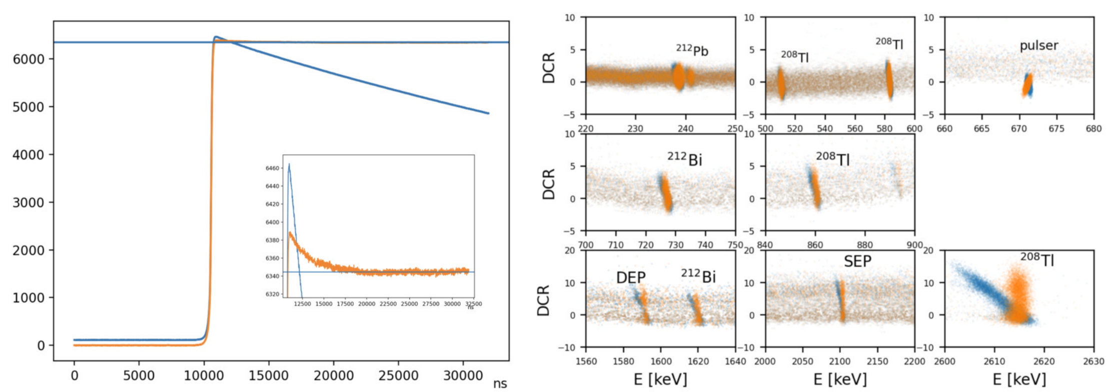

Figure 1.17-2. Optimizing the pole-zero correction for an ICPC detector in the MAJORANA DEMONSTRATOR, which will be installed in LEGEND-200. *Left:* Showing the optimization region for the PZ correction on a single waveform. *Right:* Distributions of the delayed charge recovery (DCR) parameter for regions of interest. After characterizing the response to gamma events, the DCR parameter can be used to identify and reject α particle events near detector surfaces.

1.18 Post-GERDA Test Analysis

D. A. Sweigart

The construction of the LEGEND-200 experiment is currently underway at the Laboratori Nazionali del Gran Sasso. This first phase of the LEGEND program builds upon the success of the MAJORANA and GERDA experiments, employing improved hardware such as new germanium detectors and associated electronics. In preparation, an early test of the LEGEND-200 hardware—known as the Post-GERDA Test (PGT)—was performed in July and August 2020 to identify any issues in time to remedy them before LEGEND-200's full commissioning later this year. To that end, a software suite has been developed at CENPA that characterizes the germanium detectors deployed in the PGT and has been used to flag potential problems in the hardware. Moving forward, this suite serves as a ready analysis tool for the soon-to-be-collected data from LEGEND-200.

More specifically, the software characterizes a given detector in three main stages using data taken with a ^{228}Th calibration source. First, the energy scale associated with the detector's signal amplitude is estimated. Next, the parameters used to extract each signal's energy are tuned to optimize the energy resolution at the observed lines. These parameters include those in the pole-zero cancellation, the trapezoidal filter, and the charge-trapping correction. Finally, using the optimized parameters, independent analyses are performed, studying various aspects of the detector. These studies include the signal's characteristic shape, the noise profile, crosstalk among the detectors, and the long-term stability of the clock used to digitize the signals.

This software suite has uncovered some potential issues with the hardware used in the PGT, which are being taken into account for LEGEND-200. For example, as depicted in Fig. 1.18-1 and Fig. 1.18-2, each detector's signal has a coherent, complex structure, which is largely determined by the preamplifier board to which the detector's output is connected. If not accounted for, such nonideal structure can bias the energy measurement by up to 0.13 %. Also, the pole-zero cancellation's optimal time constant surprisingly depends on energy for three detectors; the cause is still under investigation. Moreover, the signals in certain detectors were found to produce proportional signals in others, and the pattern of such crosstalk suggests that it was, in part, caused by the cable positions. For a final example, data from the data-acquisition system revealed that the sampling clock used was unstable over the long term. The clock system is being upgraded for LEGEND-200.

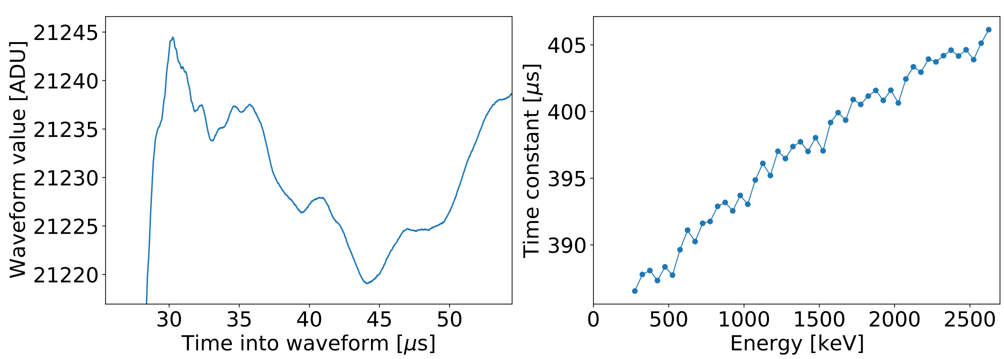

Figure 1.18-1. *Left:* The averaged, pole-zero-cancelled signal from a germanium detector in the PGT. The amplitude of the ringing was found to scale linearly with energy above 400 keV. *Right:* The energy dependence of the optimal pole-zero cancellation's time constant from another germanium detector in the PGT.

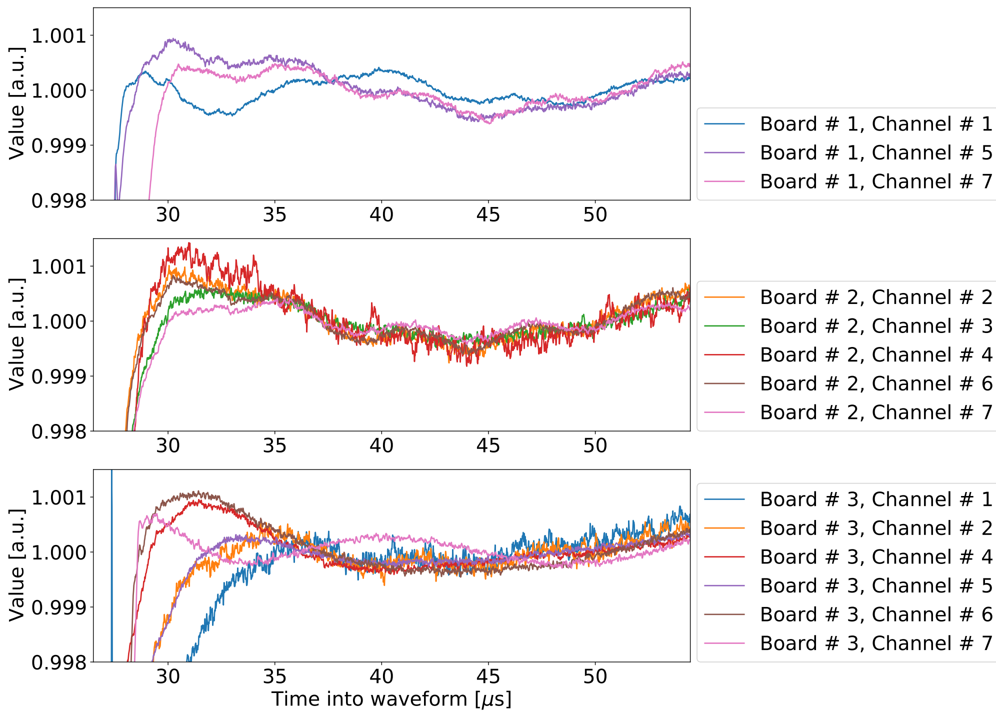

Figure 1.18-2. Averaged, normalized, pole-zero-cancelled signals from all germanium detectors in the PGT. Each plot shows the signals for those detectors connected to each different preamplifier board used in the PGT. The signal's color indicates the channel to which its corresponding detector was connected on the board.

In addition, this software was developed to analyze data sets from not only the PGT but also LEGEND-200—which will have an order of magnitude more germanium detectors. To handle $\mathcal{O}(100)$ detectors, the code can run in parallel over each detector in each data file. Written in Python, the code was sped up further by using Numba implementations wherever possible and using the digital-signal processing infrastructure in `pygama` (Sec. 1.17). Benchmarked on the PGT data, the full software suite's processing speed is currently 65 MB/s. This should be sufficient for the LEGEND-200 data to be analyzed in a reasonable amount of time at the NERSC supercomputing facility.

1.19 Commissioning CAGE: An internal-source scanning cryostat for HPGe detectors

T. Burritt, J. A. Detwiler, T. Mathew, G. Othman*, D. A. Peterson, W. Pettus†, R. Roehnelt, G. Song, T. D. Van Wechel, and C. Wiseman

CAGE is a scanning test stand designed to characterize surface events in a variety of HPGe detector geometries. The HPGe detectors used in MAJORANA and LEGEND consist of a

*Presently at University of North Carolina, Chapel Hill, NC.
†Presently at Indiana University, Bloomington, IN.

p+ point contact and an n+ surface that surrounds the sides and bottom of the detector, as shown in Fig. 1.19-1. The contacts are separated by a passivated surface made of amorphous germanium. Events near the n+ surface have been shown to be a major contributor to the background in $0\nu\beta\beta$ searches, but events near the passivated surface have not been studied in great detail. Characterizing and removing these events to help reach LEGEND-200's background goal of 0.6 cts/(FWHM t yr) is the primary goal of CAGE.

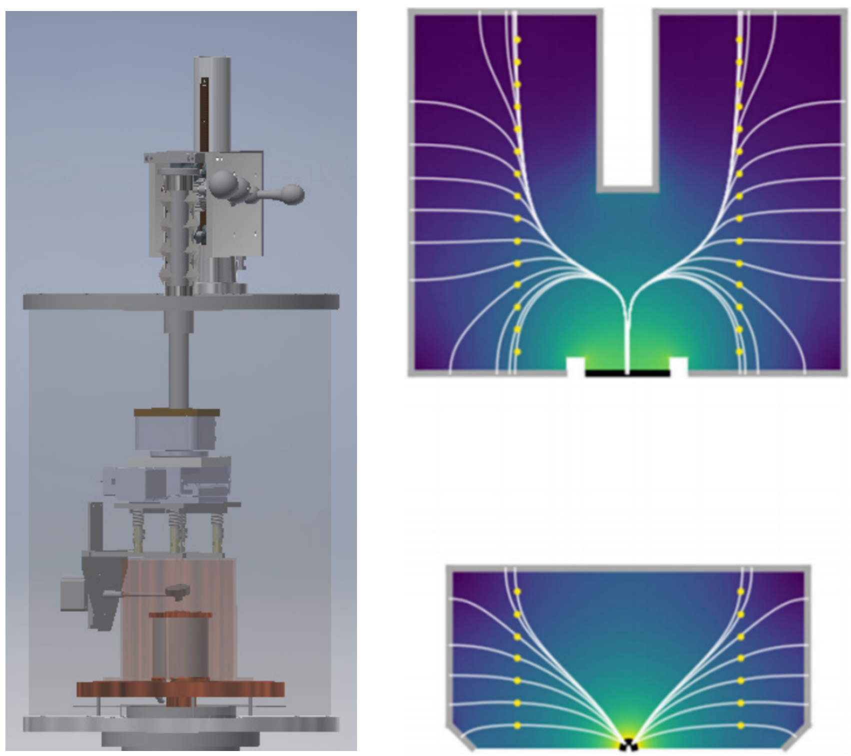

Figure 1.19-1. *Left:* 3D model of CAGE, showing the cold plate, top hat, collimator, and motor assembly and lift. *Right:* Detector geometries used in MAJORANA and LEGEND. The n+ and p+ contacts are shown on the edges of the detector in grey and black respectively. The bottom shows a MAJORANA-style, P-type point contact (PPC) detector, and the top shows an inverted coaxial point contact (ICPC) detector that will be used in LEGEND.

Inside a vacuum cryostat, the HPGe detector sits on a copper cold plate, which is connected to a liquid nitrogen dewar that is used to cool the detector to near liquid nitrogen temperatures. As shown in Fig. 1.19-1, the key feature of CAGE that distinguishes it from previous germanium detector scanners is the copper "top hat," a movable IR shield that allows us to direct the source beam's position anywhere on the detector surface. It sits on two motor stages, a linear stage that drives the source radially across the detector surface, and a rotary stage that rotates the source about the center of the detector. The collimated source inside the IR shield is mounted on another rotary stage that allows us to control the angle at which the alpha beam hits the surface of the detector. The entire top hat and motor assembly is lifted by a gear box on the atmosphere side of the cryostat before performing

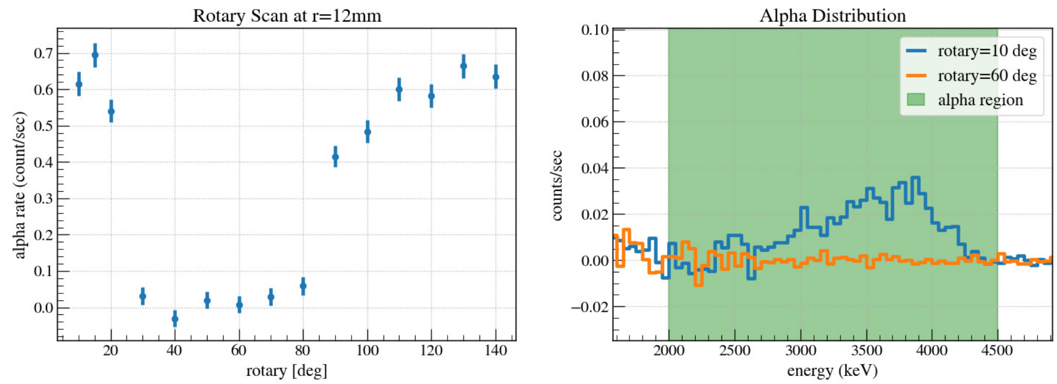

Figure 1.19-2. *Left:* Rotary scan from 10° to 140° at a radius of 12mm. We can see that the alpha rate drops in the middle of the scan as the source passes over the front-end electronics board, which the alphas cannot penetrate. *Right:* Alpha distribution for a spot showing the full alpha rate compared to a spot in the middle of the diving board, where there are no alphas.

motor motions to ensure adequate clearance of the detector.

The multiple motor stages provide additional degrees of freedom that allow us to perform scans that previous test stands are not capable of, such as a “rotary scan” that sweeps out an arc on the surface of the detector at a fixed radius, shown in Fig. 1.19-2. These scans are one method of verifying the alignment of the system, since we can see the alpha rate drop when the source beam is blocked by the PEEK diving board that holds the front end electronics. This type of scan will also be necessary in order to scan the passivated ditch of the ICPC detectors.

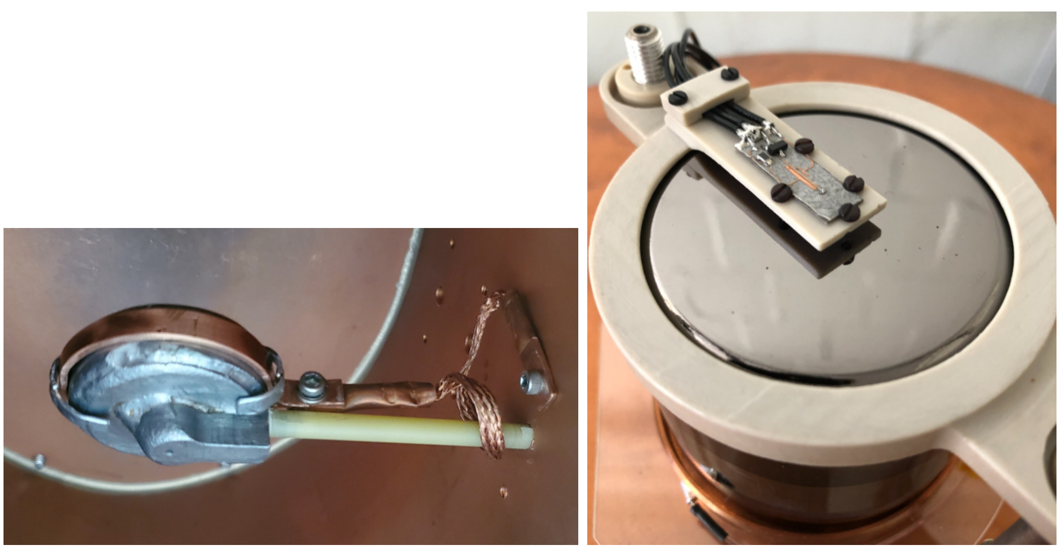

Figure 1.19-3. *Left:* New collimator design with copper band and lead tabs to secure the cap. The copper braid attached to the top hat provides cooling to the collimator. *Right:* Custom front end board designed at CENPA that replaced the reused front end from MAJORANA.

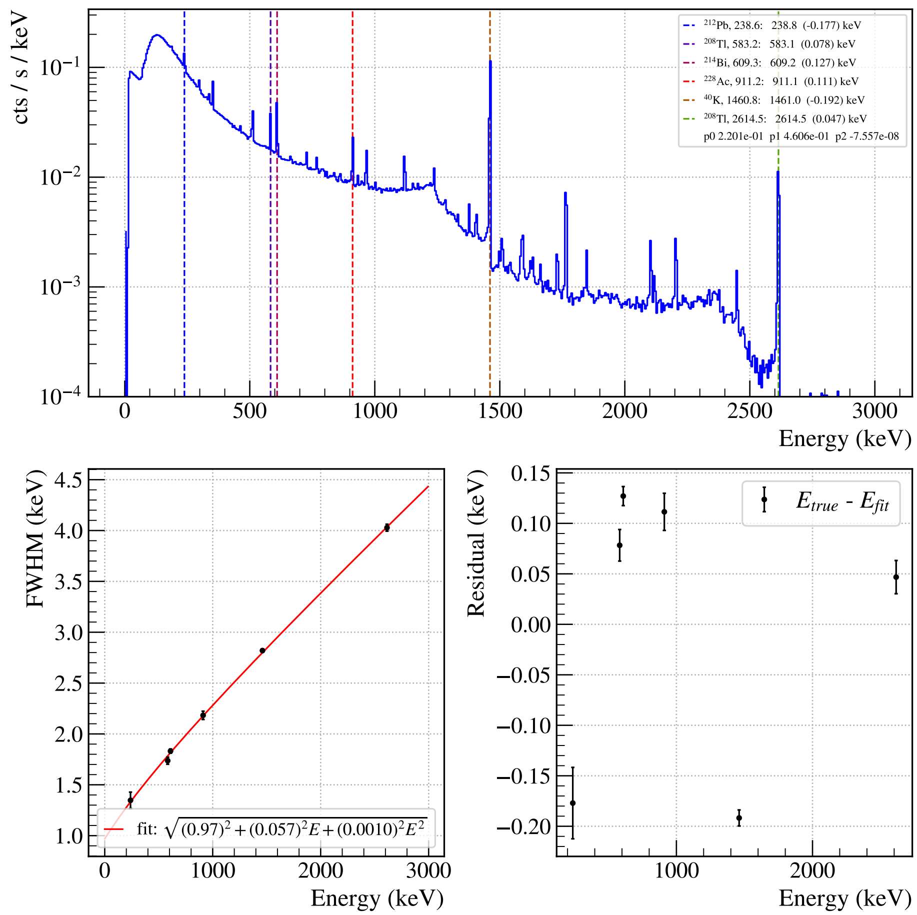

Figure 1.19-4. Energy spectrum obtained by CAGE using the new electronics designed at CENPA, showing an energy resolution of 4 keV at the thallium 2615 keV peak for an overnight background run.

Hardware improvements to CAGE over the past year, shown in Fig. 1.19-3, include the installation of a cable tray to improve wire management during rotary motions and a new collimator geometry to hold the source more securely. Simulations with the updated collimator geometry of the alpha rate show agreement with data to within the uncertainty of the source activity and collimator hole diameter. On the electronics side, we have transitioned from reusing Majorana Demonstrator amplifier electronics made at LBNL to a full electronics chain designed at CENPA. By iteratively making improvements to the design, we have achieved similar performance (in CAGE) to the low-noise MJD electronics at a significantly lower cost per unit, and we have observed the best energy resolution in CAGE to date. These electronics may be able to be used in other custom HPGe arrays and test stands where the low-radioactivity requirement can be relaxed. We have also designed an n+ readout box, that will allow us to read the signal from electrons moving to the n+ contact that complements the traditional p+ signal. We will test whether this additional information will allow us to distinguish between events that occur in the bulk of the detector and events that occur in close proximity to the point contact, which may have sufficiently different capacitance to ground to show a deviated signal.

CAGE is currently performing proof of concept scans with the OPPI1 PPC detector to verify the alignment of the system and characterize the uncertainty in the beam position, as well as to ensure the stability of the system over multiple thermal cycles. We are also designing new mounting hardware to facilitate the installation of an upgraded ICPC detector to perform scans of the passivated ditch.

1.20 Electronic characterization of silicon photomultipliers for LEGEND-1000

S. Borden, T. Burritt, J. A. Detwiler, A. Hostiuc, D. A. Peterson, W. Pettus*, N. W. Ruof, T. D. Van Wechel, and C. Wiseman

LEGEND-1000 is a future tonne-scale experiment designed to search for neutrinoless double beta decay in ^{76}Ge. For a successful measurement campaign, the background around the energy region of interest must be as low as possible; LEGEND-1000 has a background goal of 1×10^{-5} cts/(keV kg yr), a factor of 50 times lower than the completed GERDA experiment. Primary sources of background events at the $Q_{\beta\beta}$ value include gammas from the radioactive decay chains of ^{238}U and ^{232}Th. Tagging and identifying these gammas as well as other background events in the ROI allows for analysis cuts to be made, lowering the background index. To remove these events present in the background window the high purity germanium detector arrays are submerged in liquid argon (LAr), which scintillates when hit by ionizing radiation. Scintillation photons are collected by wavelength shifting fibers that shift the VUV 128 nm LAr scintillation to photons within the visible range where most photosensitive detectors have the greatest detection efficiency. The visible photons are guided through the fibers and are read out by silicon photomultipliers (SiPM). With simultaneous readout of germanium detector events and SiPM signals, an anti-coincident veto can be used to remove physics events that deposit energy in the germanium as well as in the LAr.

A test stand has been built to measure the photon detection efficiency (PDE) and characterize the noise of SiPMs at liquid nitrogen (LN) temperatures (77 K), see Fig. 1.20-1. To understand the background rejection capability of LEGEND-1000 it is important to know the photon detection efficiency of SiPMs around LAr temperature (87 K). Inside the test stand is an integrating sphere with a SiPM, photodiode, and LED light source attached. The SiPM is placed on a cold finger which can be submerged in LN. To prevent ambient light from reaching the inside of the dewar, the test stand is placed in a dark box that is internally coated with matte black paint and externally shielded with metal foil.

*Indiana University, Bloomington, IN.

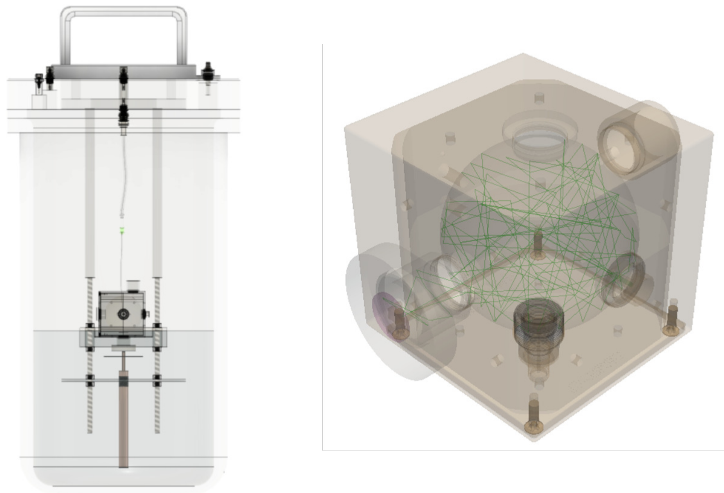

Figure 1.20-1. *Left:* A 3D model of the SiPM Testand with the integrating sphere inside a dewar. Connected to the integrating sphere are a SiPM, a clear fiber bundle fed to a photodiode, and a fiber fed to an LED light source. *Right:* A close up view of the integrating sphere with the SiPM board in purple and a photodiode in black casing connected directly to the sphere. Photon paths with in the integrating sphere are simulated with Chroma, an optical photon Monte-Carlo simulation software accelerated with GPU Ray-Tracing.

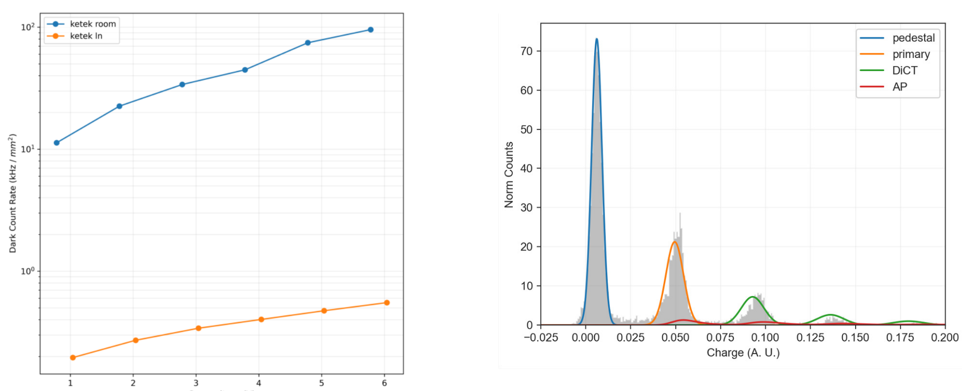

Figure 1.20-2. *Left:* A measurement of the primary dark count rate for a KETEK 3 $\times$ 3 mm SiPM at room temperature and at liquid nitrogen temperature. The primary dark count rate is measured by histogramming the time spacing between each waveform and fitting an exponential where the dark count rate is the inverse of the time constant. *Right:* A pulse charge spectrum where waveforms passing through an integration window are counted. The SiPM dark noise is comprised of the pedestal (integrating the baseline), primary dark counts, direct cross-talk (when a primary dark count fires a neighboring cell in the SiPM), and afterpulsing (delayed charge collection).

A full characterization of the dark noise for a KETEK PM3325-WB-D0 has been done and initial room temperature photon detection efficiency data have been taken, see Fig. 1.20-2.

Hardware improvements to this setup from the past year include a two stage preamplifier for the SiPM and the installation of an avalanche photodiode. The SiPM two stage pre-amplifier includes a first stage which is close to the SiPM board and uses a LMH6629 Op Amp, in order to be operational at liquid nitrogen temperature, and a second stage outside of the dewar for further amplification. The avalanche photodiode, used as a reference in comparison to the SiPM, has an internal gain that improves the strength of the signal when estimating the photon rate inside the integrating sphere.

To measure the photon rate uniformity inside the integrating sphere, the CAD model of the integrating sphere is simulated in Chroma, an optical photon Monte-Carlo accelerated with GPU ray-tracing. Preliminary studies show there is a slight non-uniformity in photons arriving at each of the integrating sphere ports, which is somewhat expected since the integrating sphere doesn't have perfect spherical symmetry. This results in a systematic uncertainty on the total number of photons incident on the SiPM.

1.21 Data processing and analysis of silicon photomultipliers for LEGEND

S. Borden, J. A. Detwiler, I. Guinn*, N. W. Ruof, D. A. Sweigart, and C. Wiseman

The LEGEND Collaboration is in the process of assembling and commissioning LEGEND-200. As part of that effort, a test strand of silicon photomultipliers (SiPMs) attached to a curtain of wavelength-shifting (WLS) fibers were submerged in liquid argon (LAr) and operated at the Gran Sasso laboratory in Italy. The WLS fibers transmit the scintillation light in the LAr to the SiPMs. Characterization of the test array's dark noise, signal stability, and energy reconstruction are crucial before the full installation of the remaining arrays in LEGEND-200.

Due to the high volume of raw data from the 64 SiPMs installed on the test strand, fast data processing is required. The Python-based `pygama` software package is being developed by the Collaboration to achieve this. In a first step, `daq_to_raw`, the files generated by the FlashCams DAQ are converted into a collaboration-designed HDF5 format called LH5.

After the `daq_to_raw` step, the raw signals are then processed using a suite of digital signal processing routines (`raw_to_dsp`). Using SiPM data available from the post-GERDA test (PGT), a Python script was developed to process the raw waveforms and extract parameters relevant for measuring the dark noise, the signal stability, and energy reconstruction. First, the raw waveforms are baseline subtracted. Then the waveforms are Gaussian filtered before the integrated charge, the maximum energy, and the time of maximum energy are finally stored. Fig. 1.21-1 shows the pulse height spectrum generated by running the `raw_to_dsp` script, with Gaussian fits overlaid from a later analysis step. The dark count rate and energy reconstruction can be characterized from this plot.

*University of North Carolina, Chapel Hill, NC.

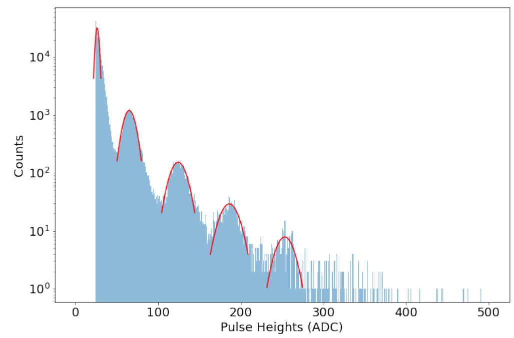

Figure 1.21-1. Pulse height spectrum of SiPM channel 21 from run 30 of the LEGEND PGT. The histogram shows the counts of pulse heights identified in all the filtered, baseline subtracted waveforms analyzed with the `raw_to_dsp` script. The "five-finger" shape of this plot, the presence of five distinct photo-electron peaks, shows that the SiPMs are operating normally.

Speed is also of the essence in the `raw_to_dsp` scripts. Leveraging the code developed by Sweigart for performant processing of PGT data, the `raw_to_dsp` processes were multi-threaded and run in parallel on multiple nodes. This achieved a factor of ∼8 speeadup. This script will be used in the commissioning of LEGEND-200 to process data from its numerous SiPM arrays.

In order to get these scripts into **pygama**, several new processing functions had to be implemented. For the sake of speed, all processors in **pygama** are guvectorized functions, compiled using the Numba package. A one-dimensional Gaussian filter was deployed, as well as a peak finding function. A processor called `multi_t_filter` was also coded to find multiple initial rise times in waveforms with multiple pulses—this function is the first of its kind to return an arbitrary number of outputs in **pygama**. An example of the `multi_t_filter` is shown in Fig. 1.21-2.

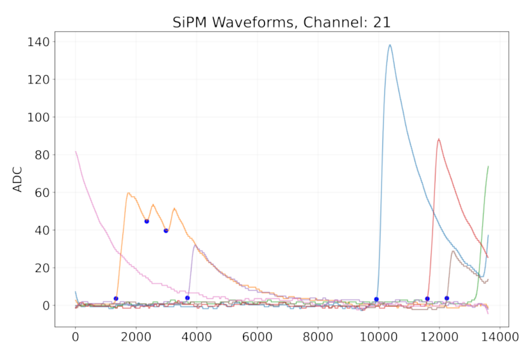

Figure 1.21-2. Example of the `multi_t_filter` applied to a PGT SiPM waveform from run 30, SiPM channel 21. The blue dots show where the processor has identified the start times of multiple puleses in a waveform. This filter will help characterize the cross talk in the SiPMs. It will also be used for energy reconstruction and tagging of multiple events.

1.22 Forward-biased JFET-based Option for R&D: alternative preamplifier design for HPGe detector readout

T. Burritt, J. A. Detwiler, A. Hostiuc, C. J. Nave, D. A. Peterson, N. W. Ruof, T. D. Van Wechel, and C. Wiseman

The high-purity germanium (HPGe) detectors used by the LEGEND experiment are reverse-biased diodes, with small amounts of charge deposited on their p+ contact when an ionization event occurs. This charge is typically converted into an output signal by a “front-end” circuit board placed very close to the detector. In typical designs, the signal is amplified by a reverse-biased JFET. However, this configuration requires the use of either a feedback resistor or additional circuits (e.g., an optoelectronics board), to discharge the feedback capacitor. At low temperatures, the required resistance is usually on the order of GΩ, meaning the resistor generates significant electronic noise. To avoid this, and for simplicity, one can design a circuit using a forward-biased JFET. This allows the detector’s and JFET’s leakage current to flow through the gate-source junction. This also provides a path for continuous discharge of the feedback capacitor.

A charge sensitive preamplifier with forward biased reset is currently under testing at CENPA under the umbrella of the LEGEND project. This device is referred to as the Forward-biased JFET-based Option for Research and Development (FJORD). The classic charge-sensitive preamplifier circuit uses a feedback resistor for stabilizing the operating point and providing a path for the detector leakage current. The forward biased reset preamplifier eliminates the feedback resistor, which is a major source of noise especially when using a detector that features low leakage current. In LEGEND, this also eliminates the need to find a low-background resistor that can survive repeated Liquid Argon (LAr) immersion, and thus represents an attractive alternative to the baseline technology[1].

CENPA Engineers have made changes to the test stand and the previous version of the FJORD device, to minimize the effects of external sources of noise, such as microphonics. This allows us to optimize the output (i.e., minimizing the threshold and using the optimal energy estimator) from the CAEN CoMPASS software when using a radiation source, and to characterize the performance of both low-gain and high-gain output from the CENPA built post-amp box.

A new front-end board has been fabricated and tested with a pulser. Some noise was observed but the amplifier still provided amplification of the signal well above the noise. A test on a HPGe detector in a vacuum cryostat is planned. Fig. 1.22-1 shows the new board being test-mounted on a HPGe detector blank.

[1]CENPA Annual Report, University of Washington (2018) p. 27.

Figure 1.22-1. FJORD front-end board mounted on a Germanium detector blank. The detector holder parts were sonicated and cleaned in preparation for data taking in the KrSTC cryostat.

Issues with our vacuum system interrupted operations for a short time. Repairs were made in-house on the diaphragm pump and a vacuum gauge. Both the pump and the vacuum gauge are now in working order and the cryostat has been pumped down to vacuum. A ^{83m}Kr source has been connected to the cryostat as we begin preparations to take data with a MJ60, a HPGe R&D detector from the MAJORANA DEMONSTRATOR project.

1.23 Neutrino-Electron Elastic Scattering Backgrounds in LEGEND-1000

J. A. Detwiler and C. J. Nave

LEGEND-1000 is a leading candidate for a future US-led tonne-scale $0\nu\beta\beta$ experiment. For that to be the case, the LEGEND collaboration must have a deep understanding of the backgrounds in the detector, specifically those that fall in the region of interest (ROI), or close to the $Q_{\beta\beta}$ value for ^{76}Ge of 2039 keV. The dominant backgrounds expected in LEGEND-1000 are from the ^{238}U and ^{232}Th decay chains, ^{42}K in the liquid argon (LAr), alpha decays on detector surfaces, and cosmogenics. One background that is expected to be negligible in the ROI comes from external neutrino interactions with ^{76}Ge. As a cross-check, we performed calculations to confirm that the background rate from ν-e^- neutral current elastic scattering is expected to be significantly lower than our expected background rate in the ROI in LEGEND-1000.

To perform this calculation, we first computed the differential cross section of the elastic scattering (ES) interaction $\nu + e^- \rightarrow \nu + e^-$. This differential cross section is plotted versus electron recoil energy in Fig. 1.23-1.

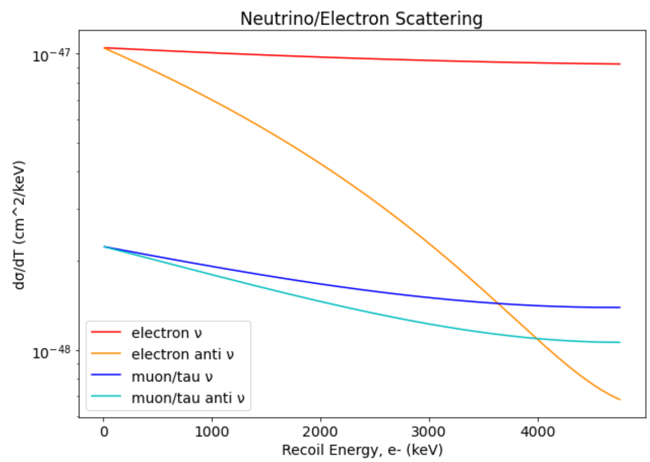

Figure 1.23-1. Differential cross section of ν-e^- elastic scattering for a neutrino of energy $E_\nu = 5$ MeV. Note that $\frac{d\sigma}{dT}$ for ν_μ and ν_τ is equivalent, as is $\frac{d\sigma}{dT}$ for $\overline{\nu}_\mu$ and $\overline{\nu}_\tau$.

The differential cross section is dependent on T, the recoil energy of the outgoing electron, E_ν, the energy of the incident neutrino, and multiple known constants dependent on neutrino type. This means we must take into consideration oscillations from electron (anti)neutrinos to muon and tau (anti)neutrinos. The expression also involves a kinematically-limited maximum recoil energy, $T_{\max} \equiv \frac{2E_\nu^2}{2E_\nu + m_e}$, where $T_{\max}$ depends on neutrino energy and the mass of the electron (the mass of the neutrino is considered negligible in this case).

The other crucial aspect of this calculation is finding the neutrino flux for whichever neutrino source we are considering. In total, we looked at the following neutrino sources: atmospheric neutrinos, supernovae neutrinos, geoneutrinos, reactor neutrinos, and solar neutrinos. For all of these except the solar neutrinos, the flux was either too low or too far from our ROI to be considerable. Therefore, we need only worry about the contributions from solar neutrinos. The solar neutrino flux from the top contributing sources are shown in Fig. 1.23-2.

While there are a number of different solar neutrino reactions, only four of them have high enough energy to contribute to the background rate in the ROI: hep (^{3}He + p$^+$ $\rightarrow$ ^{4}He + e$^+$ + ν_e), ^{8}B (^{8}B $\rightarrow$ ^{8}Be* + e$^+$ + ν_e), ecCNO O (^{15}O + e$^-$ $\rightarrow$ ^{15}N + ν_e), and ecCNO F (^{17}F + e$^-$ $\rightarrow$ ^{17}O + ν_e). We find the recoil rate per kg-year per keV by folding the differential cross section with the neutrino flux—taking into account neutrino oscillations—and multiplying by the necessary constants. Performing a numerical integration, we found the number of electron recoils per kg-year per keV in our ROI to be 1.3×10^{-7} (see Fig. 1.23-2), about two orders of magnitude less than our background goal of 1×10^{-5} counts/(keV kg yr).

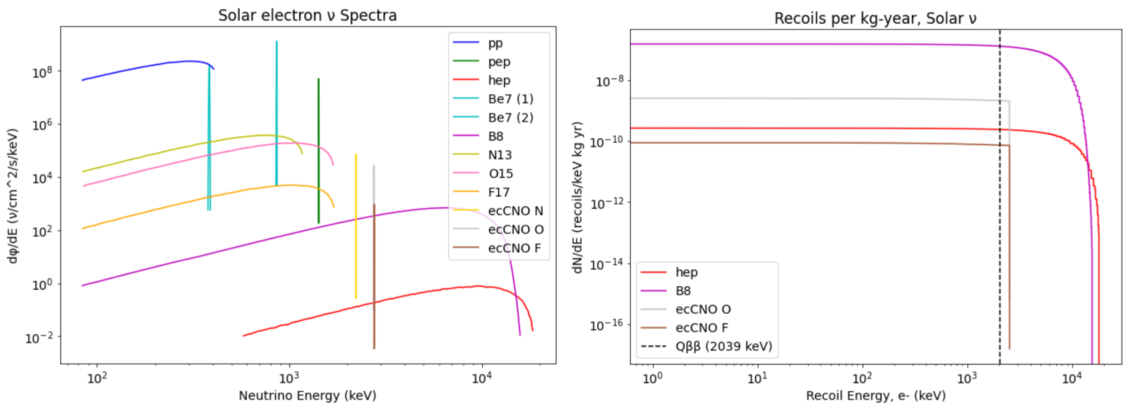

Figure 1.23-2. *Left:* Solar neutrino flux spectrum from all sources considered. Monoenergetic neutrino sources were converted to Gaussians with ^{76}Ge energy resolution. *Right:* Solar neutrino differential recoil spectrum per kg-year as a function of electron recoil energy. ^{8}B neutrinos are the dominant background source in ROI near 2039 keV.

The impetus for this study was to confirm the results of a paper by Klimenko[1] that estimates the background in the ROI through the use of GEANT Monte Carlo simulations. Klimenko found the background rate from ^{8}B solar neutrinos (the dominant contributor) in a Germanium experiment ROI to be 4.6×10^{-7} counts/(keV kg yr). This is still an insignificant background rate but is larger than our calculated rate by a factor of ~ 3.5. There are a number of approximations made to calculate this background rate and investigation into the source of the difference between our result and Klimenko's is ongoing.

Elastic scattering is only one of the neutrino interactions that can pose a background for LEGEND. We must also consider inverse beta decay (IBD), in particular $\nu_e + {}^{76}\text{Ge} \rightarrow {}^{76}\text{As} + e^-$. The calculation for this interaction is ongoing but again not expected to be a large source of background in the LEGEND-1000 ROI. Other neutrino interactions such as neutrino-nuclear scattering are to be studied as well.

[1] A. A. Klimenko, arXiv:hep-ph/0407156v1 [hep-ph] 14 Jul 2004.

Selena

1.24 Solar neutrino spectroscopy with Selena

A. E. Chavarria

The Selena experiment was proposed to search for the neutrinoless $\beta\beta$ decay of ^{82}Se with unprecedented sensitivity[1]. The detector consists of towers of imaging modules made from amorphous selenium (aSe) deposited on a CMOS active pixel charge sensor (APS). Free charge generated by ionizing particles in the aSe is drifted by an applied electric field and collected by the pixels resulting in high resolution images. From these images, Selena can *i)* measure the deposited energy, *ii)* identify the type and number of ionizing particles (electrons, α's, etc.) from the track topologies, and *iii)* identify radioactive decay sequences by spatio-temporal correlations. This strategy has been realized to some extent in the context of dark matter searches by the DAMIC experiment to constrain the activities in the silicon target of every β-decay isotope in the ^{238}U and ^{232}Th decay chains[2]. When applied to the search for neutrinoless $\beta\beta$ decay with Selena, this strategy may achieve background rates at $Q_{\beta\beta} = 3\,\mathrm{MeV}$ below 6×10^{-5} per keV per ton-year.

Recently, we expanded the scientific case for Selena after noting that solar ν_e capture in ^{82}Se, considered a background for neutrinoless $\beta\beta$ decay searches[3], can be tagged on an event-per-event basis with high efficiency. This would allow us to perform solar ν spectroscopy together with the search for neutrinoless $\beta\beta$ decay. Fig. 1.24-1a shows the two nuclear processes of interest for Selena. The threshold for ν_e capture is remarkably low at 172 keV, sensitive to all solar ν species, and leads to a decay sequence. The first step with $\tau_{1/2} = 7.2\,\mathrm{ns}$ is too fast to be distinguished from the electron with energy $E_\nu - 172\,\mathrm{keV}$ emitted following ν_e capture. Together they constitute the "prompt" event, whose spectrum is shown in Fig. 1.24-1b. The prompt event is followed by a sequence of two decays, which are expected to occur at exactly the same spatial location with time delays of $\sim$5 min and $\sim$1 day, respectively. Although these time separations may seem large, the probability of any two accidental events occurring at exactly the same pixel (*i.e.*, in $\sim 10\,\mu$g of aSe) is negligible. Furthermore, any charged particle reaction to produce ^{82m}Br (2^- state) from ^{82}Se would have remarkably different prompt event topology. Additionally, no background isotope has been identified that could mimic the ν_e capture sequence in time separation, event energies and topologies. So far, it appears that zero-background solar ν spectroscopy with a large Selena detector may be possible.

---

[1] A. E. Chavarria, C. Galbiati, X. Li, and J. A. Rowlands, JINST **12** (2017) P03022.
[2] A. Aguilar-Arevalo *et al.* (DAMIC Collaboration), JINST **16** (2021) P06019.
[3] H. Ejiri, and S. R. Elliott, Phys. Rev. C **95**, 055501 (2017).

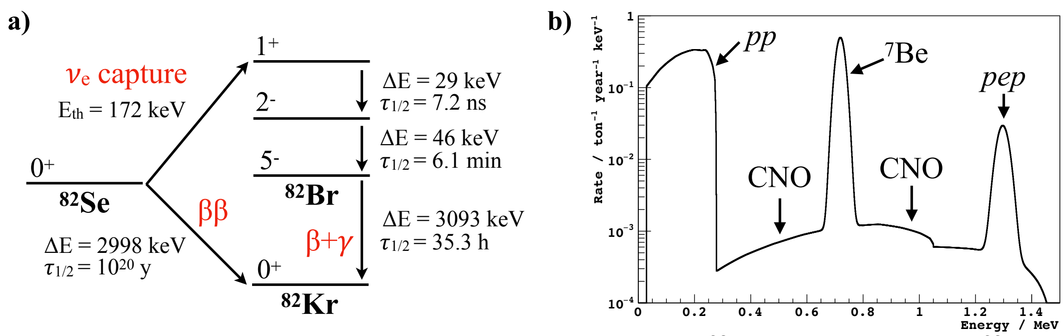

Figure 1.24-1. **a)** Diagram showing two natural channels for ^{82}Se to transmute into ^{82}Kr. Both $\beta\beta$ decay and solar ν_e capture will be detected with high efficiency by Selena for nuclear physics studies. **b)** Spectrum of the prompt event from solar ν_e capture. The neutrino species from different solar-fusion reactions are labeled.

In recent proceedings[1], we explore the scientific potential of a large Selena detector with a 100 ton-year exposure of ^{82}Se. Besides a limit of $\tau_{1/2} > 10^{28}$ y for neutrinoless $\beta\beta$ decay, the detector is expected to measure the *pp* rate to $\sim$1% for a <3.5 % constraint on the neutrino luminosity, the *pep* rate to $\sim$8% to probe the onset of the Mikheyev-Smirnov-Wolfenstein (MSW) effect for solar neutrinos[2], the CNO-cycle rate to $\sim$10% to measure solar metallicity[3], and the mean energies of the *pep* and ^{7}Be lines for a $\sim$25% estimate of the solar core temperature[4].

1.25 Hybrid aSe/CMOS sensor characterization

A. E. Chavarria, X. Ni, A. Piers, and outside collaborators[1]

Following a successful campaign of measurements with a single-pixel sensor to determine the intrinsic energy response of amorphous selenium (a-Se)[5 6], we proceeded with the characterization of a pixelated a-Se sensor based on Topmetal-II$^-$: a low noise CMOS pixelated direct charge sensor[7]. We setup a working installation of the detector, and induced tracks in the detector under radiation. We were able to achieve a noise performance of 22.7 ± 0.4 electrons. The optimal operating parameters are still under investigation. Meanwhile, we are actively designing and fabricating new prototypes of the detector based on our findings.

Our detector consists of a 500 μm thick layer of a-Se deposited on the Topmetal-II$^-$ CMOS pixelated sensor. The deposition of the selenium was done by Hologic Corporation, and the

[1]X. Li, and Y. Mei (Lawrence Berkeley National Laboratory); C. Galbiati (Princeton University); S. Bogdanovich, and B. Polischuk (Hologic Corporation).

[1]A. E. Chavarria (Selena Collaboration), arXiv:2111.00644 (2021).
[2]S. P. Mikheev, and A. Y. Smirnov Sov. Phys. Usp. **30** 759 (1987).
[3]A. Serenelli, S. Basu, J. W. Ferguson, and M. Asplund, Astrophys. J. Lett. **705** L123 (2009).
[4]J. N. Bahcall, Phys. Rev. D **49** 3923 (1994).
[5]CENPA Annual Report, University of Washington (2020) p. 50.
[6]X. Li, A. E. Chavarria, S. Bogdanovich, C. Galbiati, A. Piers, and B. Polischuk, JINST **16** (2021) P06018.
[7]M. An *et al.*, Nucl. Instrum. Methods Phys. Res. **A810**, 144 (2016).

Topmetal-II^{-} chips were provided by Dr. Yuan Mei from Berkeley National Laboratory. Hologic's deposition of selenium includes a proprietary hole-blocking layer in order to reduce the dark current and a gold electrode on top of the selenium for the high voltage. The Topmetal-II^{-} chip contains a 72 by 72 array of 83 μm-size square pixels. Each pixel has an exposed electrode directly connected to a low-noise charge-sensitive preamplifier (CSA). Surrounding the electrode, there is an isolated ring electrode known as the Guard Ring (Gring). With a high voltage applied across the a-Se, electron-holes generated in the selenium are drifted across the a-Se and onto the Topmetal-II^{-} pixels, where they can be read out.

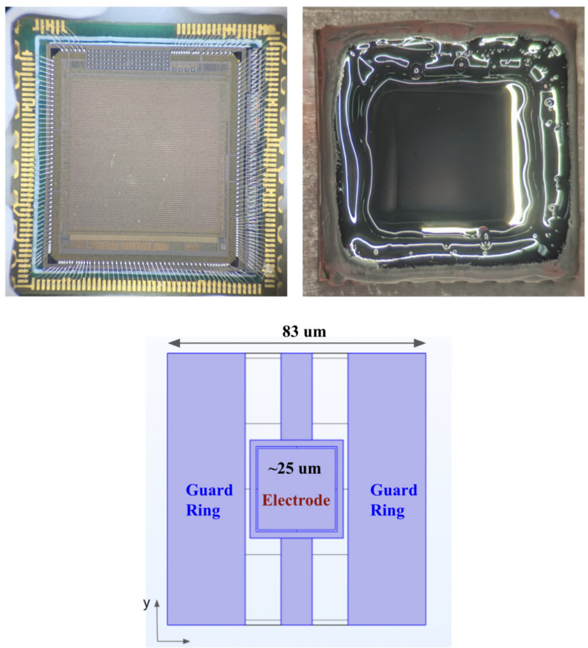

Figure 1.25-1. *Top Left:* Bare Topmetal-II^{-} chip. *Top Right:* 500 μm a-Se applied to Topmetal-II^{-}. *Bottom:* Individual pixel structure

The detector was wired bonded and placed on a carrier board, which allowed us to provide the Topmetal-II^{-} chip with the required reference voltages and read the chip's output. The detector is hosted in a vacuum chamber in order to withstand high voltages up to 10kV and isolate the system from noise. We used a CAEN HV power supply to apply a high voltage to the selenium layer through a wire attached to the gold electrode via a conductive carbon paint. Digital logic signals such as the clock and reset pulses for the Topmetal-II^{-} chip were provided via a Digilent Basys-3 FPGA. All the connections were attached via vacuum feedthrough.

In addition, we developed a digital trigger on our FPGA in order to reduce the data storage and analysis requirements of the chip readout. After splitting the chip output, we used an ADC to provide digital pixel values to the FPGA. The FPGA stores each pixel value along with its pixel index for an individual image of the chip, and compares it with the previous pixel value for the same index, which was stored in memory If the difference is larger than the set threshold, the FPGA sends out a trigger to our CAEN digitizer to readout the digitizer's buffer.

We provided ionization signals in two ways: β particles from ^{90}Sr and γ-rays from ^{57}Co. An example image of a β track is shown in Fig. 1.25-2. The 122 keV γ tracks are admittedly less interesting since they only show up in a single pixel. Yet, the mono-energetic nature of the γ tracks should provide us with a peak in the spectrum of event amplitudes. We are actively working on tuning the parameters of our system in order to produce a spectrum that we fully understand. Fig. 1.25-3 shows a histogram of pixel values for 5 Co-57 induced triggers. Initial results indicate that we can achieve a pixel distribution with a σ of 22.7 ± 0.4 electrons, while events outside the distribution show pixels with an excess of charge due to ionization in the a-Se.

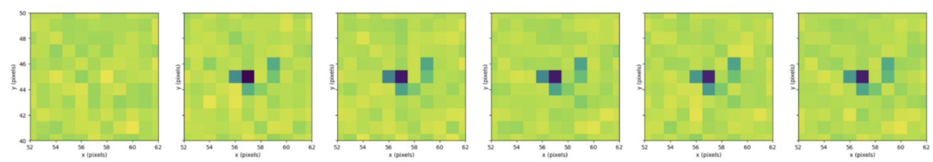

Figure 1.25-2. An example of a β track from our Sr-90 source. Moving left to right represents images taken at consecutive time steps, showing the appearance and slight decay of the track.

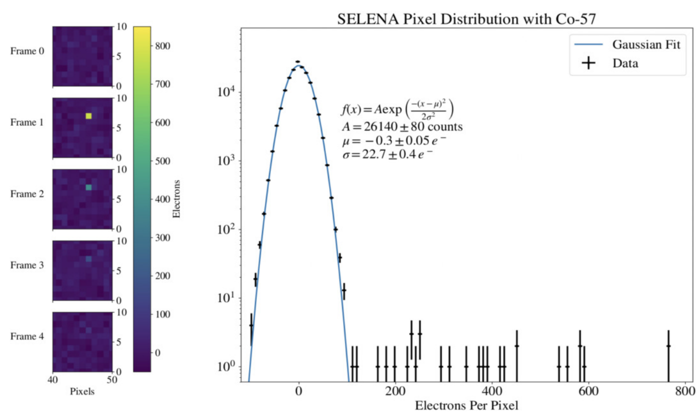

Figure 1.25-3. *Left:* The arrival and decay of a Co-57 122 keV γ in our detector. *Right:* A histogram of pixel values under Co-57. The fitted Gaussian shows the baseline distribution of pixels, while the higher electron pixels show the pixels illuminated by the 122 keV γ tracks.

We have created a new design for the deposition of the a-Se and packaging of the current prototype, which is being done by collaborators at Princeton University and Hologic. In addition, we are currently designing a new prototype of the Topmetal-II$^-$ chip, which well be uniquely suited to the needs of our detector. Based on simulations of the Topmetal-II$^-$ geometry in COMSOL and GEANT, we have identified a pixel geometry which will optimize our collection efficiency. These new prototypes will allow us to further demonstrate the imaging capabilities of the a-Se/Topmetal-II$^-$ detector.

COHERENT

1.26 Characterization of NaI(Tl) Crystal Scintillators for the NaI(Tl) Detector Subsystem for COHERENT

T. Burritt, J. A. Detwiler, M. R. Durand, J. Librande, D. A. Peterson, N. Chen, O. McGoldrick, T. D. Van Wechel, D. I. Will*, and C. Wiseman

The COHERENT project is a collaborative effort to measure coherent elastic neutrino-nucleus scattering (CEνNS), a Standard-Model process whose precision measurement will allow searches for non-standard interactions of neutrinos with matter and a deeper study of nuclear structure. CEνNS is also key process in core-collapse supernova events (Type II SNe), and therefore its study will aid in the understanding of supernova dynamics. CEνNS can also be used to detect the neutrinos produced in the core collapse. The CEνNS process is also important for understanding the "neutrino floor" background for direct searches for dark matter, arising from CEνNS interactions of solar and atmospheric neutrinos.

The COHERENT experiment is based at the Spallation Neutron Source (SNS) at Oak Ridge National Laboratory in Tennessee. The sodium iodide (NaI[Tl]) group at the University of Washington has worked with collaborators at Duke University to characterize roughly two tons of thallium-doped sodium iodide (NaI[Tl]) crystal scintillators, including roughly 120 7-kg crystals at UW, to deploy in one of the next detector phases of the multi-phase approach of the COHERENT collaboration.

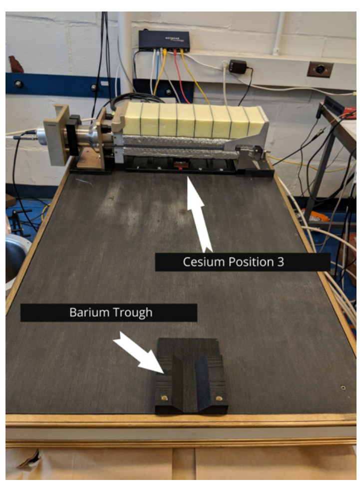

Figure 1.26-1. Experimental setup for the crystal characterization campaign.

The characterization effort aimed to assess the performance of each crystal by identifying the ideal voltage to which each crystal's PMT base should biased such that the gain across all crystals is consistent. A secondary goal was to identify and reject defective crystals with

*Retired July 1, 2019.

any sort of damage or impurity. To characterize each NaI[Tl] crystal, we run two sets of five 10-minute trials exposing the crystal to both a ^{137}Cs source directly below the crystal and a ^{133}Ba source roughly 73 cm off perpendicular to the detector's side (Fig. 1.26-1). The first set of measurements determined the relationship between detector gain and bias voltage by varying the supply voltage to the PMT in 100V intervals from 600V to 1000V. The second set looked for differences in the measured energy of the Cs-137 peak by placing the ^{137}Cs source at five different equidistant positions beneath the crystal.

The campaign to characterize all of the crystals is now complete. Summary plots of the detector gains, ^{137}Cs peak widths, and ^{137}Cs peak energy sensitivity to source position are shown in Fig. 1.26-2 The detectors selected to ship to ORNL all passed the selection criteria of less than 20-keV variation in the energy of the Cs peak as the Cs source "scanned" underneath the crystal, and less than 34-keV resolution of the Cs peak when it was directly underneath the center of the crystal. 100 detectors passing these criteria (Fig. 1.26-3) have been shipped to ORNL, where they away detector array assembly and commissioning.

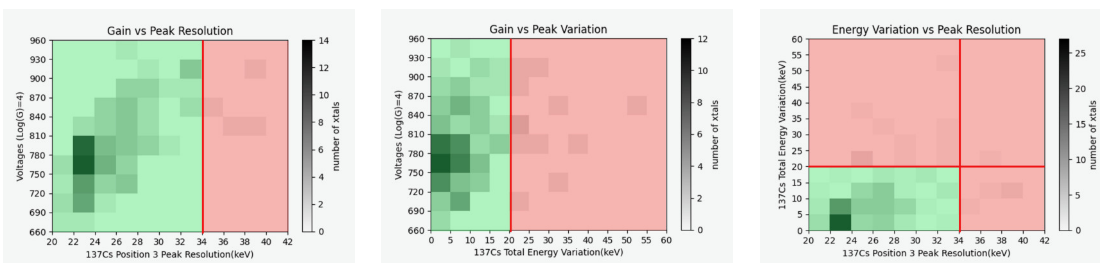

Figure 1.26-2. These plots show the gain of each of our crystals versus their respective peak variations and peak resolutions as well as the energy variations versus peak resolution. The green regions show crystals that met our selection criteria, and those in red did not and will not be sent to ORNL.

Figure 1.26-3. Fully characterized crystals. The three stacks in the foreground of the image are to be sent to ORNL, and the stack in the background is to stay at UW.

An additional study performed with the crystals looked at their gain variation with temperature. The light yield of NaI scintillating crystals is sensitive to temperature. Thus temperature data are recorded during data collection to be taken into account in the analysis. Typically there's a linear relationship between the gain and temperature, as shown for example in Fig. 1.26-4. However, many factors can cause uncertainty, including intrinsic gain differences between the bases, discrepancies in collected temperature data measured by different devices, and gain variation with respect to time. The goal of the temperature study was to determine whether temperature variation was a dominant component. It was ultimately found to be subdominant to temporal variations in the gain.

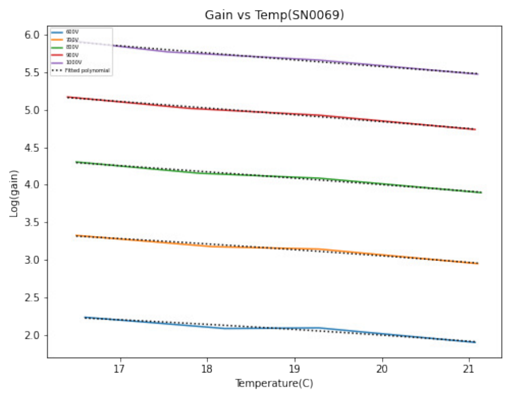

Figure 1.26-4. Linear dependence of gain on temperature in crystal SN0069. This crystal is used in both the temperature study and absolute efficiency and stability study and will remain at UW for further use.

Another study being finalized in the interest of crystal characterization is measuring the absolute detection efficiency of our NaI[Tl] crystal scintillators and testing our Monte Carlo models of the light collection. To measure this experimentally, a data run of standard length (10 minutes) at a bias voltage of 800 V was taken, during which time the detector was only exposed to our ^{137}Cs source. A background run was then taken to be subtracted from the source run, after each had had their energy scales calibrated and number of pulses scaled with respect to their relative live times. The final spectra for data taken when the Cs source was a standard distance from the crystal (roughly 51.50 mm) are shown in Fig. 1.26-5. Using an estimated Cs source activity of (13110 ± 130) Bq, the absolute efficiency of our detector was calculated to be $(10.06 \pm 0.10)\%$.

To determine our expected count efficiency, a background-free run was simulated multiple times using the software g4simple, a Geant4-based simulation application. The simulations differed in location of the Cs source to account for uncertainty in measured distance to the crystal. These simulations help illuminate possible problems in the detection efficiency and allow us to calculate the efficiency degradation. The expected absolute efficiency was calculated from the simulations to be $(11.6^{+0.8}_{-0.7})\%$, which is slightly outside of the measured value and its uncertainty. At the time of writing, this discrepancy is still under investigation.

In addition to the detection efficiency, this study was extended to investigate the stability of the crystals' detection efficiency over time. Using data taken over the course of the aforementioned temperature study, the count rate in the Cs peak over time (including background counts and ^{133}Ba pileup counts) was calculated and compared to the expected decay rate of our sources. The count rate of the crystals appears to fall off faster than the decay rate of our sources, indicating degrading efficiency. To verify this, two new runs were taken on which the absolute efficiency and stability routines are to be repeated: both at a bias voltage of 800 V with the ^{137}Cs in position 3, one with the ^{133}Ba source present (stability estimation) and one shielded from the ^{133}Ba source (affording a more rigorous efficiency calculation). The repetition of these routines on these runs is currently underway to investigate this possible degradation in counting efficiency.

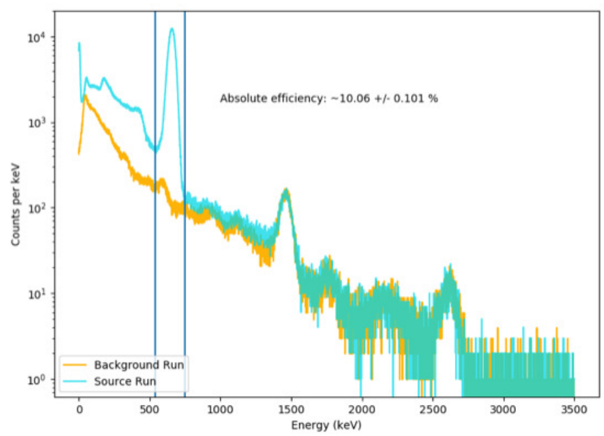

Figure 1.26-5. The energy-calibrated and deadtime-corrected measured energy spectra of crystal SN0069, also used in the temperature study, with (aqua) and without (orange) our ^{137}Cs source present.

An additional study that is currently ongoing is an investigation of the background intrinsic to the NaI[Tl] detectors, primarily due to potassium impurities in the crystals. As the detectors were not initially produced with the intention of executing precision measurements, they are contaminated with varying amounts of potassium from the growth process. CEνNS is a rare signal that will show up in the low-energy region of our data. The background due to the potassium in the crystals cannot be shielded or removed in any way, so it is important that we understand it well. To investigate this intrinsic background, four detectors have been placed into a box of lead bricks to shield from environmental background. Test data has been taken and its analysis is underway. The measurement will also be simulated using the g4simple software for comparison.

2 Fundamental symmetries and non-accelerator-based weak interactions

Torsion-balance experiments

2.1 Gravitational Calibration of the LIGO Hanford Observatory

E. G. Adelberger, J. H. Gundlach, M. P. Ross, E. A. Shaw, and C. M. Weller

Precise calibration is paramount to the accurate interpretation of gravitational wave events record by the LIGO gravitational wave observatories. Previously, calibration of the LIGO observatories has been achieved with the Photon Calibrator (PCal) system[1] which applies a known force via radiation pressure. We have developed and deployed a complementary calibration system, the Newtonian Calibrator (NCal). This system uses an aluminum rotor with two-fold and three-fold symmetric tungsten masses inserted into it to apply a time varying gravitational force. The two mass configurations inject calibration lines at twice and three-times the rotation frequency of the rotor.

The NCal rotor was installed at the LIGO Hanford observatory during LIGO's most recent observing run, after which we conducted a series of test injections with the rotor spinning at 4-10 Hz, injecting calibration lines into the observatory at 8-30 Hz. The injected forces were extracted from the observatory's strain readout with an uncertainty ranging from 1-12%. In order to predict the gravitational force imparted by the NCal, we developed three methods to calculated the force: an analytical point-mass approximation, a finite-element analysis, and a multipole calculation. All three methods were consistent with each other and yielded an force prediction uncertainty of $< 1\%$.

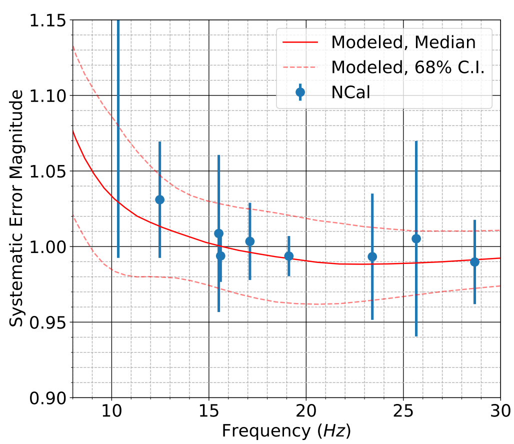

Figure 2.1-1. Systematic error of the LIGO Hanford strain readout measured by the NCal as well as the model using the existing calibration system.

The observatory's readout is recorded in pre-calibrated strain units. However, to ensure

[1] S. Karki et. al., *Review of Scientific Instruments* **87**, 11 (2016).

the accuracy of this calibration over time, calibration lines are periodically injected with the PCal system to measure the multiplicative error in this pre-calibrated pipeline (i.e. the systematic error). During operation these calibration lines are swept through the sensitive band of the observation to yield a model of the systematic error for a given time. As a initial proof of concept, we used the ratio of the predicted and measured NCal force amplitudes to calculate the observatory's systematic error, shown in Figure 2.1, and compared it to the modeled systematic error for the correspond time of the NCal injection. Our measurements are consistent with the existing system and exceeds or matches the precision of the model at most frequencies. This is the first precise, independent cross-check of the existing LIGO calibration system and shows the promise of gravitational calibration for the LIGO observatories. For more information see our recent paper[1].

With future injections and improvements, we hope to achieve sub-percent precision calibration with the NCal system. This system will be able work in concert with the existing PCal system to decrease the uncertainty of the low-frequency calibration of the LIGO observatories and thus increase our knowledge of gravitational wave systems.

2.2 Search for ultra low-mass dark matter

E. G. Adelberger, J. H. Gundlach, M. P. Ross, and E. A. Shaw

Torsion balances are exquisitely sensitive instruments for measuring differential accelerations. With a composition dipole on the balance, they are sensitive to a variety of new theorized fundamental forces mediated by bosons coupled to quantum numbers related to electrically neutral atoms: baryon number (B), lepton number (L), B-L, etc. B-L is a particularly interesting charge as it is a conserved in many unified theories. Recent theoretical work has highlighted that dark matter could be composed of such ultra low-mass bosons (ULMBs)[2]. Recently, we have put out new constraints on ULMBs as a pre-print that is in the review process[3]. The most interesting constraints on B-L coupled ULDMs are shown in Figure Fig. 2.2-1.

The main developments in the analysis over the past year have been improving the accuracy of our torque estimation and adding daily drift parameters to our fits to model the effect tilts have on our analysis. The equation of motion of a torsion balance is $\tau = I\ddot{\theta}(t) + \kappa\,(1 + i/Q)\,\theta(t)$ where τ is the torque, I is the moment of inertia of the balance, κ is the torsion constant of the torsion fiber, Q is the Quality factor, and θ is the angle. The imaginary term, which was previously left out of the analysis, introduces frequency-dependent amplitude and phase shifts that can be accurately accounted for by introducing a frequency-dependent first-derivative term $\kappa\dot{\theta}(t)/(\omega Q)$. To model the drift related to tilt we fit for sinusoidal signals with 24-hour and 12-hour periods. We worked on a number of injection tests and calculated the correlation between these new fit parameters and the science signal

[1] M.P.Ross et. al., *Phys. Rev. D* **104**, 082006 (2021).
[2] P.W.Graham et. al., *Phys. Rev. D* **93**, 075029 (2016).
[3] E.A.Shaw et. al., *arXiv* 2109.08822 (2021).

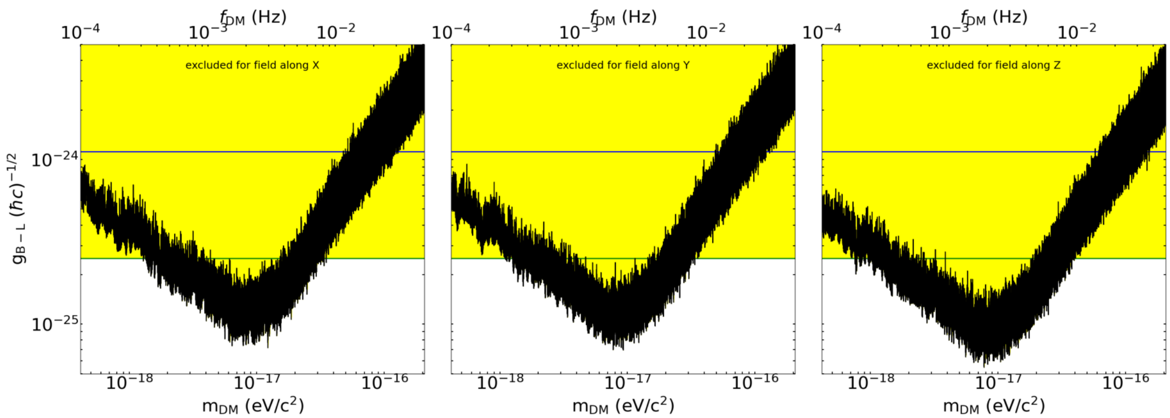

Figure 2.2-1. Upper limits on B-L coupled dark matter ULMBs. The exclusion regions are indicated in yellow. The black lines show the 95% confidence limits on the amplitudes of fields along X, Y, and Z in geocentric coordinates. The horizontal blue lines are the upper limit from the Eöt-Wash EP test[1]. The green lines are the upper limits from the initial MICROSCOPE result[2]

of interest to show that these modifications to our analysis introduce no bias in our improved results.

2.3 Progress toward equivalence principle test for superconductors

E. G. Adelberger, C. Gettings, J. H. Gundlach, M. P. Ross, and E. A. Shaw

There are very few experimental avenues to explore the intersection of quantum mechanics and gravity. One avenue is conducting gravitational experiments with materials that exhibit macroscopic quantum effects. Specifically, testing whether superconductors follow the equivalence principle (EP). There have been suggestions [3] that Cooper pairs violate the EP due to breaking of gauge-invariance inside superconductors. Additionally, previous measurements of the Cooper pair inertial mass found a deviation[4] which seems to violate the EP.

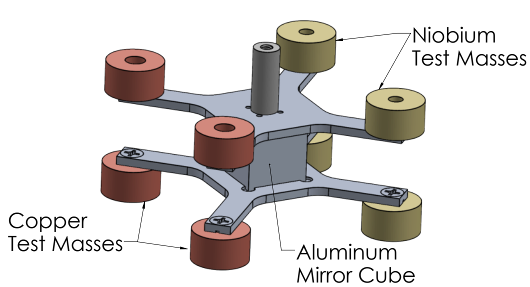

Figure 2.3-1. CAD rendering of pendulum we plan to use for an equivalence principle test for superconductors.

[3]C.J. de Matos, *Journal of Superconductivity and Novel Magnetism* **23**, 8 (2010).

[4]J.Tate, S.B.Felch, and B.Cabrera, *Phys. Rev. B* **42**, 13 (1990).

We have begun construction on a torsion balance experiment with a pendulum, shown in Figure 2.3, with test bodies made of superconducting niobium and copper. This pendulum will be installed in our existing cryogenic torsion balance apparatus which was originally built to decrease thermal noise in traditional gravitational experiments. Once installed, we will search for anomalous daily signals in the exterior torque applied to the torsion balance. If the EP is not violated for superconductors, we would expect the sun to apply no net torque on the balance. If the converse is true, then the sun would apply a torque on the balance which would modulate once per day as the earth rotates.

In a previous proof-of-concept experiment, we were able to operate a torsion balance with superconducting test bodies (confirmed by a magnetic coil placed near the pendulum) in a 1.2 μTorr helium environment but were unable to constrain a variety of environmental systematics (temperature variations, apparatus tilts, etc.). However, this showed that such an experiment is readily possible with the existing equipment.

2.4 Update on rotating equivalence principle experiment

E. G. Adelberger, C. Gettings, J. H. Gundlach, M. P. Ross, and E. A. Shaw

The equivalence principle (EP) is formulated in Newtonian physics, where $F = m_i a = G m_g M_g / r^2$, as the equivalence between inertial (m_i) and gravitational (m_g) mass. In general relativity (GR) this equivalence becomes a consequence of the geometry of spacetime and how all particles move along geodesics in an equivalent way. Ephraim Fischbach highlighted[1] that in addition to EP tests precisely testing GR, they have potential as a search for a fifth-force of nature mediated by hypothetical bosons. Our group tests EP with a rotating torsion balance experiment designed to be sensitive to the full range of theoretical possibilities of EP tests on length scales from those typical in a laboratory (≈ 1 m) all the way out to the center of the galaxy (10^{20} m).

The experiment is currently undergoing improvements prior to a new scientific data run. One critical component of the experiment that is to be updated is the data acquisition system (DAQ) and eddy-current motor software, and associated hardware, for controlling the turntable that rotates the experimental apparatus. Precise control and logging of the turntable speed is required as it directly influences the frequency of the signals the torsion balance is exposed to. The current setup consists of a C# program running on a Windows computer combined with custom-built electronics for acquiring input voltage signals from the experiment detailing the position of the turntable in real-time, and outputting a voltage signal calibrated to drive the turntable motor to a specific rotational velocity. The custom-built electronics for this process have become antiquated and overly complex due to many past revisions, and the program suffers from occasional crashes that can disrupt measurements. To that end, a quality-of-life improvement is required.

The custom-built electronics are to be replaced with a commercially sourced cRIO-9040 CompactRIO FPGA Controller in conjunction with 16-bit NI 9205 ADC and NI 9263 DAC

[1] E. Fischbach et. al., *Phys. Rev. Lett.* **56**, 1 (1986).

modules, all made by National Instruments. The C# program will be replicated within a new LabVIEW FPGA program compiled directly to the CompactRIO controller. Simplifying the electronics down to a single piece of integrated hardware greatly reduces the risk of failure points and removes the possibility of time-consuming diagnostic searches. Compiling the LabVIEW program onto the controller itself, which uses a Linux operating system, removes the time-keeping and hardware synchronization issues inherent within Windows operating systems. In this configuration, the DAQ and turntable's three-phase eddy-current motor will be processed by the CompactRIO's embedded controller, with a Windows host computer simply acting as the user-interface for inputting the required DAQ and turntable eddy-current motor settings via the LabVIEW program. These changes will improve the precision and reliability of the experiment's turntable, which in turn should increase the quality of future scientific measurements.

Following a successful integration of this new system to the experiment, more of the experiment's I/O processes may be moved to the CompactRIO controller. The advantage then being that all the critical real-time aspects of the experiment will be controlled from one centralized piece of hardware, facilitating synchronization across the board.

2.5 The Fourier–Bessel expansion: applications to experimental probes of gravity and feeble short-range interactions

E. G. Adelberger, B. R. Heckel, J. G. Lee, F. V. Marcoline*, and W. A. Terrano† and

Experimental probes of new short-distance physics often probe the interaction between two parallel flat plates (rather than, say, between two spheres) as this maximizes the amount of test-body mass that can be placed in close proximity. In this case, the conventional spherical multipole expansion does not converge but the Fourier-Bessel expansion converges rapidly, providing a powerful analytic technique for designing and analysing such instruments. Two recent Eöt–Wash torsion balance instruments exploited optimized Fourier–Bessel cylindrical geometries to test the short-distance properties of gravity[1] and to constrain exotic dipole–dipole and monopole–dipole interactions[2]. We discuss in detail the efficient analytic techniques for computing the expected torques in those instruments arising from Newtonian and Yukawa interactions between unpolarized test bodies and dipole–dipole and monopole–dipole torques on polarized test-bodies. We consider systematic effects induced by weak external magnetic fields on the nominally unpolarized test-bodies. We also present a new Fourier–Bessel expansion for inverse-power-law (IPL) potentials and use this to calculate the expected IPL signals in our recent short-distance test of the gravitational inverse-square law[3]. Our results slightly improve limits on inverse-5th-power law potentials. This work was published in Classical and Quantum Gravity[3].

*Cardiovascular Research Institute, University of California, San Francisco CA.
†Department of Physics, Princeton University, Princeton NJ.

[1] J.G.Lee et. al. *Phys. Rev. Lett.* **124**, 101101 (2020).
[2] W.A.Terrano et. al. *Phys. Rev. Lett.* **115**, 201801 (2015).
[3] J.G.Lee et. al. *Classical and Quantum Gravity* **38**, 085020 (2021).

3 Accelerator-based physics

^{6}He-CRES

3.1 ^{6}He Overview

W. A. Byron, W. Degraw, B. Dodson, M. Fertl[*], A. García, B. Graner, E. Hanes, H. Harrington, L. Hayen[†], X. Huyan[‡], S. Hightower, M. E. Higgins[§], N. C. Hoppis[¶], M. Kimsey-Lin, K. Knutsen, D. McClain[‖], D. Melconian[‖], P. Mueller[**], N. S. Oblath[‡], R. Roehnelt, G. Savard[**], E. B. Smith, D. Stancil[†], D. W. Storm H. E. Swanson, R.J. Taylor[†], J. Tedeschi[‡], B. A. VanDevender[‡], F. Wietfeldt[††], and A. R. Young[†],

He6-CRES aims at measuring with high precision the ^{6}He, ^{14}O and ^{19}Ne beta spectra. The motivation is a high-sensitivity search for chirality-flipping interactions, which would signal physics beyond the Standard Model. Using an effective Lagrangian for the charged weak current with additional scalar and tensor interactions with couplings ϵ_S and ϵ_T[1]

$$\begin{aligned}\mathcal{L}_{\rm CC} = -\sqrt{2}G_{\rm F}^{0}V_{\rm ud}\ \Big[&\bar{e}^{L}\gamma_{\mu}\nu_{e}^{L}\cdot\bar{u}\gamma^{\mu}(1-\gamma^{5})d \\ &+\epsilon_S\,\bar{e}^{R}\nu_{e}^{L}\cdot\bar{u}d \\ &+\epsilon_T\,\bar{e}^{R}\sigma_{\mu\nu}\nu_{e}^{L}\cdot\bar{u}\sigma^{\mu\nu}(1-\gamma^{5})d\Big]\end{aligned} \tag{1}$$

the beta spectra, $\frac{dN}{dE}$, are expected to present a distortion with respect to the Standard Model prescription, $\frac{dN_{SM}}{dE}$, proportional to m/E (the ratio of the mass to total relativistic energy of the beta):

$$\frac{dN}{dE} = \frac{dN_{SM}}{dE}\ \left(1 + b\,\frac{m}{E}\right). \tag{2}$$

The so-called Fierz interference coefficient, b, is directly proportional to the couplings ϵ_S and ϵ_T.

Fig. 3.1-1(left) exemplifies the type of expected distortion, and Fig. 3.1-1(right) gives the sensitivity for $b < 10^{-3}$ measurements in comparison to other determinations[2]. Significantly, we are aiming for searches that are beyond the level of sensitivity of any previous experiment.

---

[*]Johannes Gutenberg University Mainz.
[†]Department of Physics, North Carolina State University, Raleigh, NC.
[‡]Pacific Northwest National Laboratory, Richland, WA.
[§]Presently at Duke University, Durham, NC
[¶]Presently at University of Maryland, College Park, MD
[‖]Texas A&M, College Station, TX.
[**]Argonne National Laboratory, Lemont, IL.
[††]Department of Physics, Tulane University, New Orleans, LA.

[1] Bhattacharya et al., Phys. Rev. D **85**, 054512 (2012).
[2]M. Gonzlez-Alonso, O. Naviliat-Cuncic, and N. Severijns, Prog. Part. Nucl. Phys. **104**, 165 (2019).

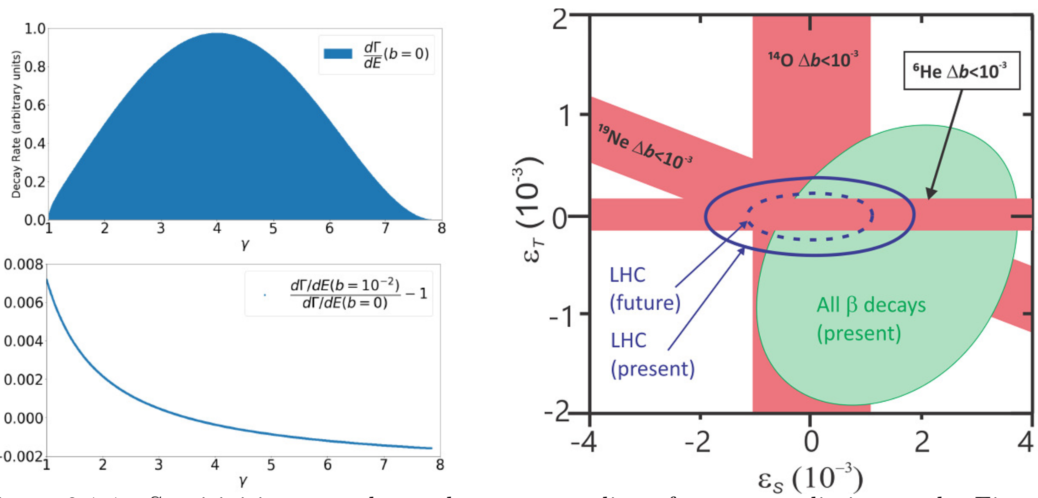

Figure 3.1-1. Sensitivities to scalar and tensor couplings from upper limits on the Fierz interference coefficient, b, expected from the He6-CRES nuclei in red. In green, we show the result of a combination of all beta decay measurements up to date, including neutron decays. The blue lines indicate limits from the LHC.

We use the technique called Cyclotron Radiation Emission Spectroscopy (CRES), developed by the Project8 collaboration for the tritium endpoint. The basic idea is to arrange for the beta decays to occur in a magnetic field. Betas undergo cyclotron motion with frequency

$$f = \frac{qBc^2}{2\pi\ E}. \tag{3}$$

For $E \approx 1$ MeV in a ≈ 1 T field, the frequency is ≈ 20 GHz. Letting the radioactive decays occur within an RF waveguide generates RF excitations with the cyclotron frequency. Typically, we digitize RF waves in slices of ≈ 30 μs, calculate FFTs, and produce spectrograms, called 'waterfall' plots, which allow extraction of E at the point of decay, before any energy loss takes place. The latter feature, combined with a lack of significant backgrounds, and a first-principles connection between the measured frequency and the energy, are very attractive for a method aimed at probing for new physics.

The He6-CRES experiment is different than the Project8 in some main aspects:

- In order to measure the beta spectra of up to several MeV, we use a much larger bandwidth than the Project8 collaboration. But even at that, due to RF-bandwidth limitations, we are forced to 'stitch together' spectra taken at different B fields. Fig. 3.1-2 shows a sketch of the ^{6}He spectrum and the coverage for different B-field values.
- Control is needed over any effect that can distort the beta spectra over a wide range of energies.
- Statistics are not a main concern. With the production rates at CENPA and a DAQ acquiring events at ≈ 1 kHz, we would achieve statistics for $b < 10^{-3}$ in ≈ 1 day of counting.

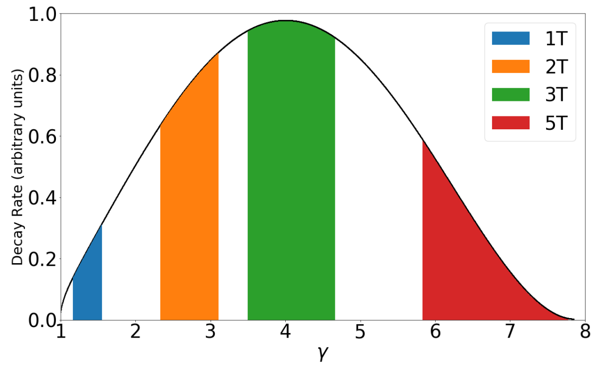

Figure 3.1-2. Sketch of ^{6}He beta spectrum with bands indicating the regions measured simultaneously by a $18-24$ GHz RF-bandwidth system.

Fig. 3.1-3 shows the main RF components. We had to pay careful attention to the distribution of heat in our design to allow for optimal temperatures at the Low Noise Amplifiers (LNAs), while keeping the decay cell at above 100 K to avoid freezing ^{83m}Kr, which is an important calibration source.

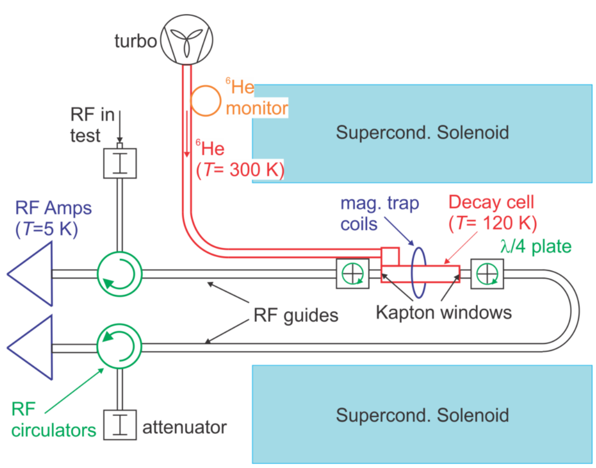

Figure 3.1-3. Sketch of components for He6-CRES. The radioactivity is compressed by a turbo pump into a decay cell, which is part of an RF guide. The guide is connected on both ends to RF Low Noise Amplifiers (at ≈ 5 K) to minimize issues related to Doppler effects. An ambient receiver box, not shown, mixes down the LNA signals to be digitized at several GHz. The "^{6}He monitor" measures beta rates in a manner insensitive to magnetic fields, and allows for normalizing spectra taken at different field values.

He6-CRES is organized into phases with milestones that are presented in Table 3.1-1. We are in Phase I, and moving into Phase II.

Phase I: *proof of principle*;
Observe ^{83m}Kr lines;
Understand RF issues and spectra;
Study RF power distribution;
Develop ^{19}Ne source.
Show detection of cycl. radiation from ^{6}He;
Phase II: *first measurement ($b < 10^{-3}$)*;
^{6}He and ^{19}Ne measurements;
Develop ^{14}O source.
Develop design of ion-trap systems.
Phase III: *ultimate measurement ($b < 10^{-4}$)*;
^{14}O measurements;
Use ion-trap for no limitation from geometric effect.

Table 3.1-1. He6-CRES phases with proposed milestones.

We report here on progress since March 2020. At that point, we had assembled the hardware needed to detect signals from a ^{83m}Kr source. But then we lost access to our laboratory, due to the Covid-19 crisis. We organized ourselves to continue to make progress on software analysis tools, particularly in finding ways to organize the data so as to produce spectrograms and identify tracks of events due to beta particles. As soon as we gained some access to the laboratory, around October 2020, we prioritized activities so as to achieve detection of CRES events from a ^{83m}Kr source. Work concentrated on:

- a campaign to map magnetic fields, of which there is more detail in (Sec. 3.3);
- measurements of RF properties (noise and gain) and improvements and tests on the DAQ system, of which there is more detail in (Sec. 3.6).

The ^{83}Rb source arrived in early 2021, and in April we saw first CRES events, of which there is more detail in (Sec. 3.2). The confirmation of expectations to observe CRES events was a very important milestone for He6-CRES. This observation gave us a much more secure footing for progressing towards our goal. Significantly, we were able to observe signals on a broad bandwidth of ≈ 1.4 GHz.

One issue that became clear with the CRES data, is that we needed improvements in our vacuum systems. A big challenge for He6-CRES, is that when radioactivity is being produced by the accelerator system and driven toward the CRES apparatus, no turbo vacuum pump can be set up at the decay cell itself. Any small leak into the system plus evaporation from the walls is compressed toward the decay cell, where we can afford to use only getter vacuum pumps. The wanted radioactivity needs to be compressed into the decay cell, which imposes a tight constraint on usually negligible leaks and wall evaporation rates. Much work was dedicated during the summer of 2021 for improvements, of which there is more detail in (Sec. 3.4). A particular section of the vacuum systems with cryo surfaces (controlled at

≈ 40 K to avoid freezing ^{19}Ne) had to be given special attention, and is described in (Sec. 3.5). Except for a remaining issue with the latter, that should be fixed in the near future, vacuum systems have now been optimized and they are ready for radioactivity data.

Fig. 3.1-4 shows a photo of part of the He6-CRES team near the CRES apparatus.

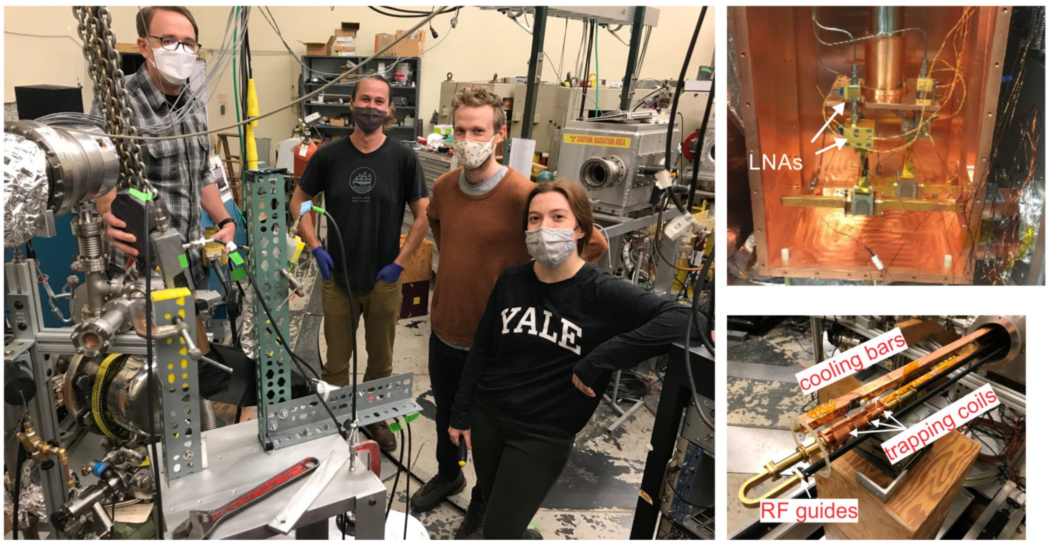

Figure 3.1-4. Left: photo of some members of the team near the CRES setup; from left to right: Brent Graner, Winston Degraw, Drew Byron, and Heather Harrington. Right, top: photo of the insides of the cryo-cooler box, showing some of the LNAs. Right, bottom: photo of decay cell and RF guides, showing the coils used for the beta magnetic trap.

By the end of May the ADMX He liquefier broke down and we switched to work on the vacuum systems and on optimizing production and transport of ^{19}Ne and ^{6}He to the CRES decay cell. More detail on the latter can be found in (Sec. 3.8) and (Sec. 3.7).

As mentioned above, an important element to yield beta-decay spectra is the ability to 'stitch together' measurements performed at different values of the magnetic field. Details on this are presented in (Sec. 3.9).

With our emphasis focused on hardware development and achieving observation of CRES signals, we were not able to make much progress in needed simulations. But we have started efforts in that direction and (Sec. 3.10) gives more details.

In summary, CRES signals from a ^{83m}Kr source have been obtained. This has illuminated our path forward. Except for a few, relatively small remaining issues, the challenging vacuum-system constraints seem to be resolved. Production and transmission of ^{6}He and ^{19}Ne seems on secure footing. So we should be able to observe CRES events from ^{6}He and ^{19}Ne as soon as we are able to cool down the magnet again.

3.2 First CRES events from ^{83m}Kr

W. A. Byron, W. Degraw, M. Fertl*, A. García, B. Graner, E. Hanes, H. Harrington, L. Hayen†, X. Huyan‡, S. Hightower, M. Kimsey-Lin, K. Knutsen, D. McClain§, D. Melconian§, P. Mueller¶, N. S. Oblath‡, R. Roehnelt, G. Savard¶, E. Smith, D. Stancil†, R.J. Taylor†, H. E. Swanson, J. Tedeschi‡, B. A. VanDevender‡, F. Wietfeldt‖, and A. R. Young†,

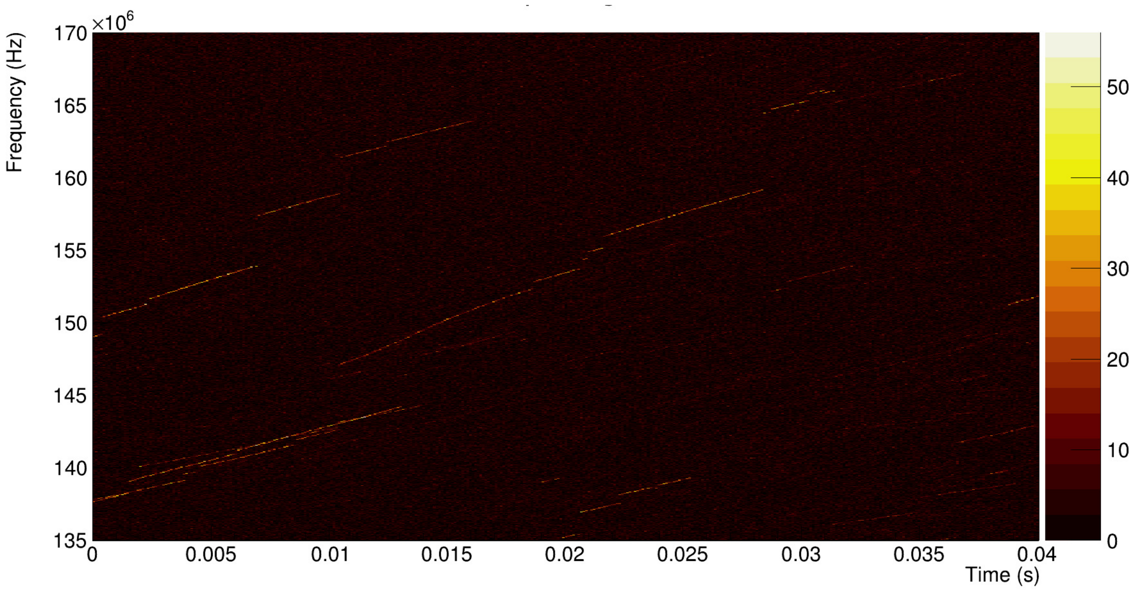

Figure 3.2-1. Power spectrogram zoomed in to show tracks from 31.9 keV M line conversion electrons from ^{83}Kr, taken at a background field of 0.6846 T and a relative trap depth of 4×10^{-3}.

In April of 2021 we succeeded in taking our first CRES data. This was achieved using a source of ^{83m}Kr prepared at PNNL and shipped to CENPA. Excited ^{83}Kr is let into our decay cell. Here it is trapped in harmonic magnetic trap where it decays through a cascade of two gamma transitions with the energies of 32.2 and 9.4 keV. Both transitions are highly converted to electrons. These almost-monoenergetic conversion electrons undergo cyclotron motion in a 0.7T background field with better than 20ppm/cm uniformity and the resulting cyclotron radiation couples into the propagating TE_{11} mode in our waveguides. This signal is amplified and a room temperature ambient receiver at 17.9 GHz is used to mix down the signals. For example: 30 keV $\rightarrow f_c = 18.1$ GHz $\rightarrow 0.2$ GHz $= 200$ MHz.

*Johannes Gutenberg University Mainz.
†Department of Physics, North Carolina State University, Raleigh, NC.
‡Pacific Northwest National Laboratory, Richland, WA.
§Texas A&M, College Station, TX.
¶Argonne National Laboratory, Lemont, IL.
‖Department of Physics, Tulane University, New Orleans, LA.

Time domain data from each side's amplifiers are sent to two ADCs. An FPGA on the ROACH then performs a Fast Fourier Transform on each 23.41 μs time slice of data. For more information on the DAQ, refer to (Sec. 3.6). The resulting frequency spectra have a resolution of 42.7 kHz. Two time slices are averaged by the ROACH, and then another factor of two are averaged by the Katydid analysis. This results in a time resolution of 93.64 μs.

We have analyzed our data using the Katydid Analysis Framework created by Project8 for processing CRES data. First, we accumulate many time slices to form a power spectrogram. Fig. 3.2-1 shows a frequency vs time spectrogram of data taken in our first week of CRES data collection. The upward tracks are the result of electrons. When an electron begins to propagate freely in the magnetic field, a signal with the resulting down-mixed cyclotron frequency appears in the data. The frequency is in fact the average over many axial periods as the electron oscillates back and forth in the trap, sampling an average magnetic field that depends on the pitch angle. As energy is radiated away, the electron loses kinetic energy causing it to form tighter cyclotron orbits resulting in the cyclotron frequency increasing over time. This is the cause of the upwards slope of the tracks in the data. When an electron undergoes elastic or inelastic scattering with residual gas, that results in a change in energy and/or pitch angle that results in a jump up or down in measured frequency. We observed many instances of both although it is more likely for the electron to lose energy.

We then apply a frequency dependant threshold. Assuming the noise is white noise, we extract the frequency dependent gain of our system based on the variation of the mean power of the noise. We then only accept data with a given SNR or number of standard deviations above that mean. In the case of the data shown here, an SNR > 4.2 to the mean noise was required. Fig. 3.2-3 shows the so called 'sparse spectrogram' of bins above threshold for the same data as is shown in Fig. 3.2-1.

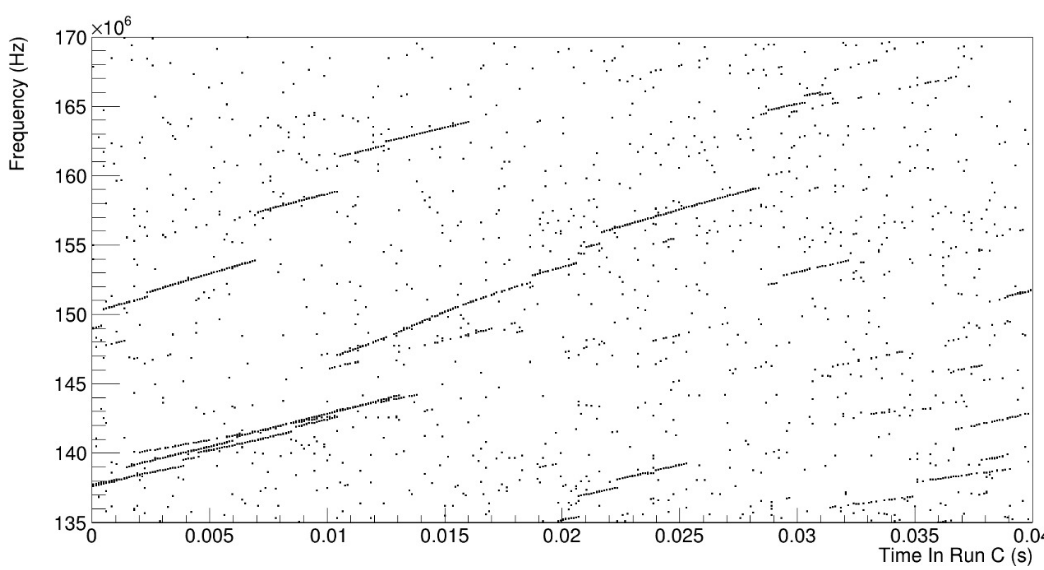

Figure 3.2-2. Sparse spectrogram of points above the threshold of SNR > 4.2.

Next, we cluster the bins over threshold into tracks. A guess is given for the average slope of tracks in the data. Then for each point above threshold, Katydid looks for a point in the next time slice that is at the frequency expected from that initial guess of slope plus or minus some frequency range. If an over threshold point is found there, it is added to the track. As this continues the slope used to project to later time bins is calculated from the points already grouped into the track.

A time gap chosen for the analysis is also permissible due to a track often dipping bellow threshold due to a combination of noise and power leakage across frequency bins in the FFT. After all tracks are found, another processor clusters tracks that overlap or are collinear. Fig. 3.2-3 shows the tracks identified in the same data as above.

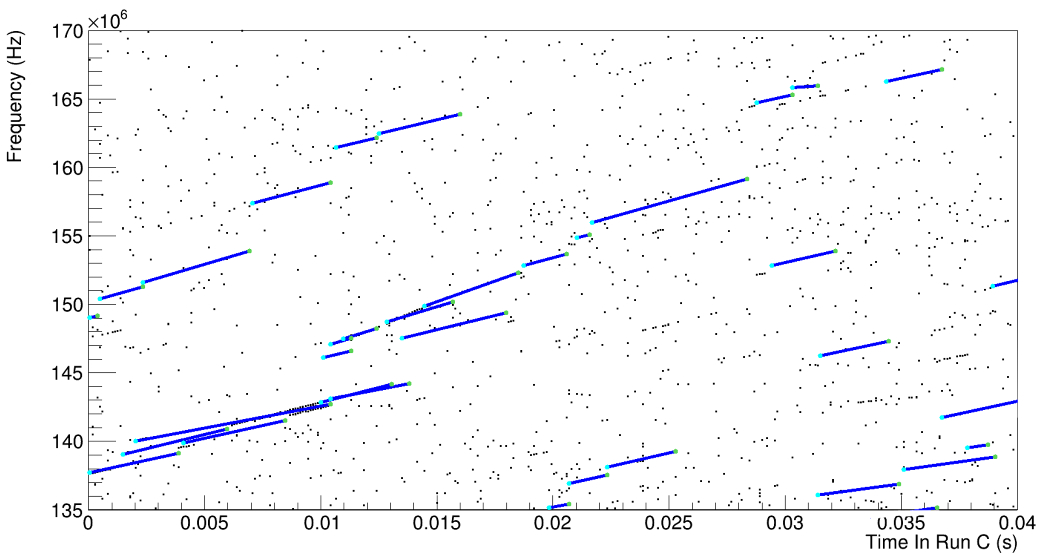

Figure 3.2-3. Tracks identified by Katydid. The start frequency and time are marked with a light blue dot and the end frequency and time is marked with a green dot.

For our first round of analysis, we have just considered the start frequencies of all identified tracks. In our first round of data collection this year we had such high event rates that we have not yet implemented sideband identification or event reconstruction over scatters into our analysis. Due to the scattering, this results in a line shape with a sharp rise and a tail from scattered tracks at higher energies. Fig. 3.2-4 shows a frequency spectrum of track start frequencies for the same dataset as above. As we could not yet simultaneously measure the magnetic field during CRES data-taking in April, we extracted the strength of the field from the leading edge of the 30.5 keV L line. With our large frequency bandwidth we were able to observe many of the lines from ^{83m}Kr simultaneously.

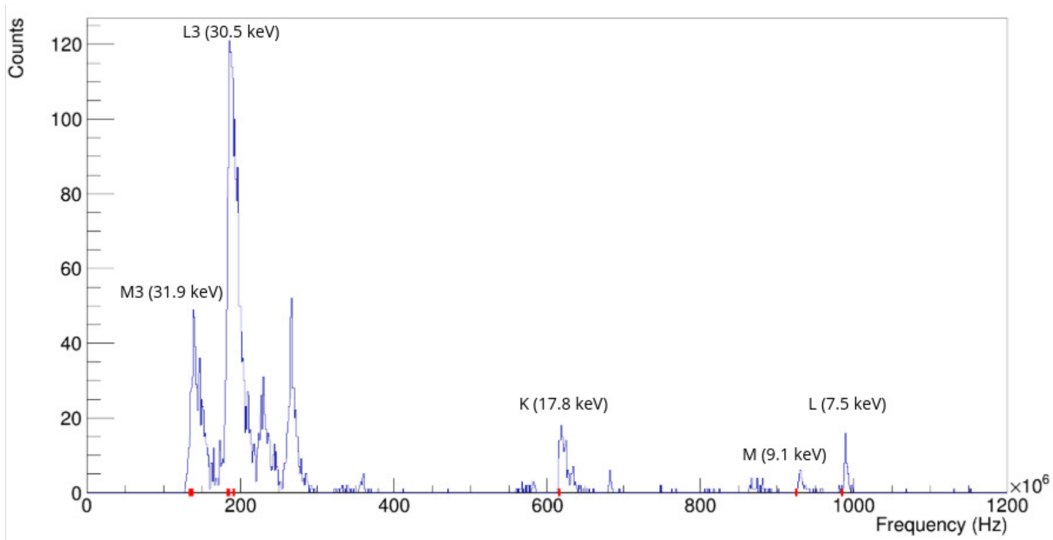

Figure 3.2-4. A frequency spectrum from just one second of CRES data. Red ticks on the frequency axis mark the expected frequencies of the indicated CE lines given the extracted magnetic field of 0.6846 T. Only tracks with SNR > 30 are included.

This is the first simultaneous observation of the K-L-M lines from ^{83m}Kr. The Project8 bandwidth is a factor of ≈ 14 in each of three 100-MHz bandwidth DAQ channels.

Although we were very happy with the observation of CRES events, there are features that remain to be understood, once we can get more data:

- In addition to the expected ^{83m}Kr lines, there are several unexplained ones. We attribute these to artifacts created by the large residual gas pressure and the high event rates.
- Despite some effort to identify sidebands due to Doppler effect, we have not found clear examples in our data. We attribute this to low SNR in our initial data.

3.3 Mapping and shimming the magnetic field

W. A. Byron, W. Degraw, M. Fertl*, A. García, B. Graner, E. Hanes, H. Harrington, L. Hayen†, X. Huyan‡, S. Hightower, M. Kimsey-Lin, K. Knutsen, D. McClain§, D. Melconian§, P. Mueller¶, N. S. Oblath‡, R. Roehnelt, G. Savard¶, E. Smith, D. Stancil†, R.J. Taylor†, H. E. Swanson, J. Tedeschi‡, B. A. VanDevender‡, F. Wietfeldt‖, and A. R. Young†,

*Johannes Gutenberg University Mainz.
†Department of Physics, North Carolina State University, Raleigh, NC.
‡Pacific Northwest National Laboratory, Richland, WA.
§Texas A&M, College Station, TX.
¶Argonne National Laboratory, Lemont, IL.
‖Department of Physics, Tulane University, New Orleans, LA.

The ^{6}He-CRES experiment uses a 1-7 Tesla superconducting magnet to generate the background field for the experiment. The magnet is a liquid nitrogen-shielded, horizontal bore superconducting magnet from American Magnetics, Inc. (AMI), serial number 8946. This magnet is quoted at being able to achieve 1ppm/cm homogeneity near the center of the bore. It comes equipped with eight active superconducting shims that may be used to cancel any inhomogeneity on the field up to sextupole order.

We have made significant progress mapping the magnetic field within the region of interest at 0.7 T, the field used to take CRES data with the ^{83m}Kr calibration source. For this we are using a PT2025 NMR Precision Teslameter system from Metrolab. This Teslameter system achieves 5 ppm absolute accuracy and 0.1 μT resolution for measurements and mappings of magnetic fields in the range 0.043 T to 13.7 T. An NMR probe is positioned within the bore using a mount that has three degrees of freedom. One of these degrees of freedom is a rotation about an axis, which is driven by a computer-controlled stepper motor. Theodolite data were taken to check the positioning of the probe provided by this mount. The un-shimmed field was found to be homogeneous to 14 ppm/cm, with the largest gradient being that in x. Shimming is thus necessary to achieve our target of 1 ppm/cm homogeneity.

Shim Coil	Calculated	Measured at AMI	Measured at CENPA	Units
Z	20.5	26.0	21.7	ppm/cm
X	19.0	21.6	Not Working	ppm/cm
Y	19.0	21.6	18.7	ppm/cm
Z^2	2.0	4.37	Untested	ppm/cm^2
ZX	2.77	2.5	3.1	ppm/cm^2
ZY	2.77	2.5	3.3	ppm/cm^2
XY	2.3	2.0	3.7	ppm/cm^2
$X^2 - Y^2$	2.3	2.0	Not Working	ppm/cm^2

Table 3.3-1. Measured and calculated strengths of the shims per Amp with ppm relative to 0.7 T.

To shim the field, we first had to measure the strength of each shim coil on site at CENPA and check that they all worked as expected. Table 3.3-1 shows the strengths of all the measured shims, and Fig. 3.3-1 shows the fields due to two of the working shims.

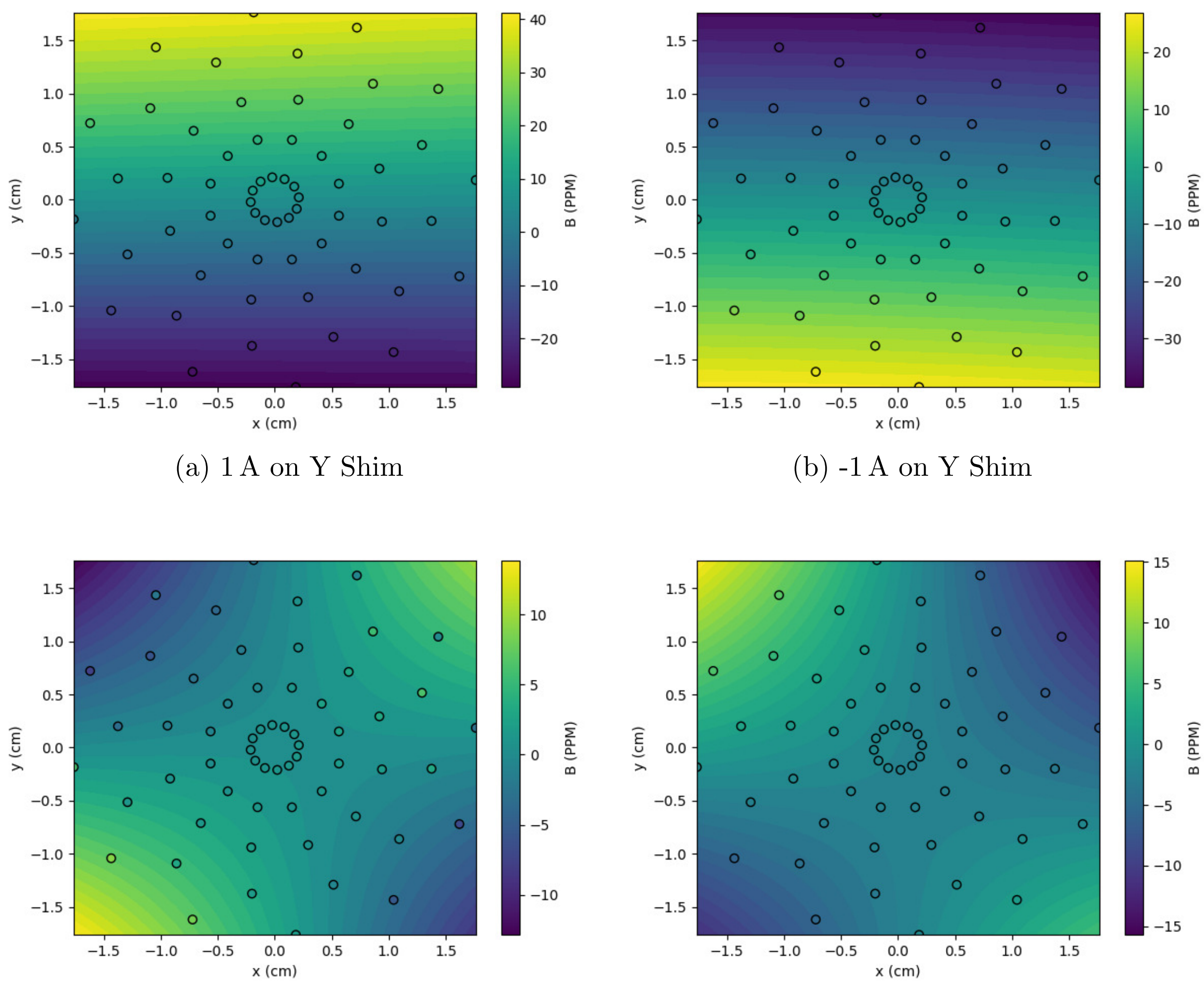

(a) 1 A on Y Shim

(b) -1 A on Y Shim

(c) 1 A on XY Shim

(d) -1 A on XY Shim

Figure 3.3-1. Fields due to two shim coils in ppm of the main field in the rotated frame. Values found by subtracting the un-shimmed field from the shimmed field at each probe location. Left plot is due to 1 A through the shim, right is due to -1 A through the shim. All taken at z=0.

We found that two of the shims (X and $X^2 - Y^2$) do not seem to be working as expected. Additionally, the shim geometry in our magnet was rotated 45° relative to the lab frame. All field maps shown here are after correcting for this. Finally, we have modified our apparatus to allow real-time magnetic field monitoring with an NMR probe while taking CRES data. The mapping data fit to a multipole expansion will allow us to extrapolate the field in the decay volume from that measured nearby.

3.4 Cryo and vacuum systems

W. A. Byron, W. DeGraw, M. Fertl[*], A. García, B. Graner, H. Harrington, L. Hayen[†], X. Huyan[‡], K. Knutsen, D. McClain[§], D. Melconian[§], P. Mueller[¶], N. S. Oblath[‡], R. Roehnelt, G. Savard[¶], E. Smith, D. Stancil[†], R.J. Taylor[†], H. E. Swanson, J. Tedeschi[‡], B. A. VanDevender[‡], F. Wietfeldt[‖], A. R. Young[†],

In 2021 the ^{6}He CRES collaboration observed its first ^{83m}Kr CRES events. In 2022 we plan to observe our first ^{6}He and ^{19}Ne CRES events. To that end we have implemented many improvements to our vacuum system over the past year. The two main accomplishments, decreasing the pressure of residual gas in the CRES decay cell and configuring our vacuum system in order to introduce ^{6}He and ^{19}Ne to the decay cell, will be discussed.

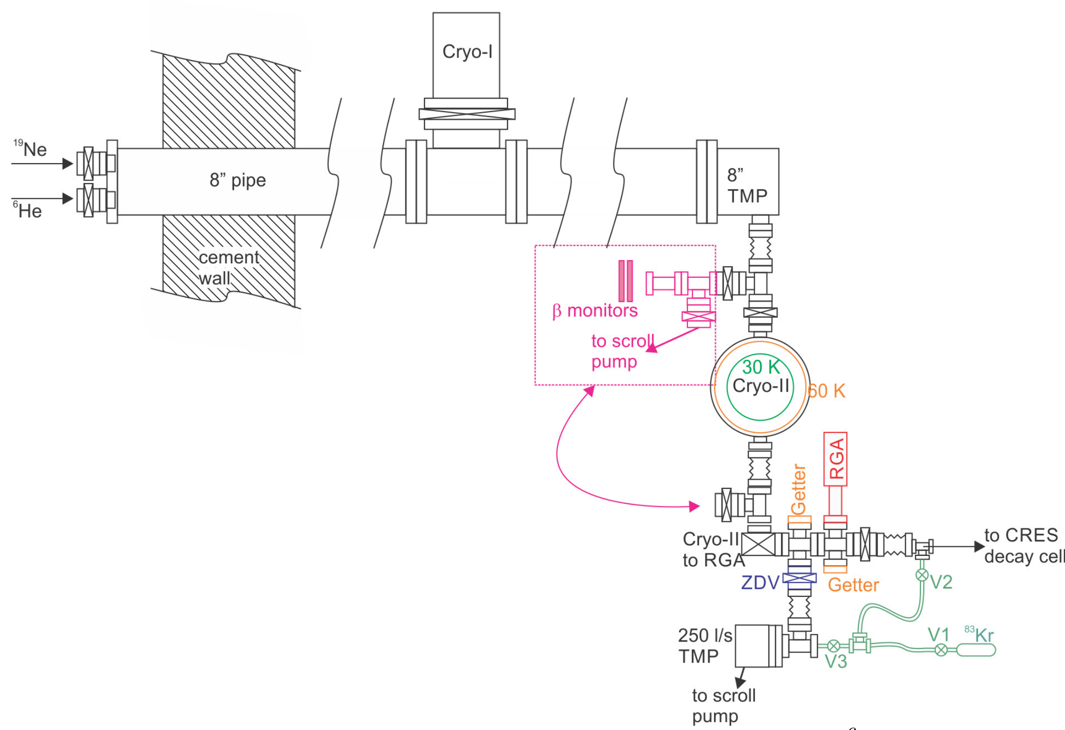

Figure 3.4-1. Vacuum configuration for introducing radioactivity to the ^{6}He CRES decay cell.

In our first campaign of acquiring CRES data we discovered that for RGA pressures[1] above roughly 10^{-6} Torr the CRES track lengths became shorter than 5 ms. A track ends

*Johannes Gutenberg University Mainz.
†Department of Physics, North Carolina State University, Raleigh, NC.
‡Pacific Northwest National Laboratory, Richland, WA.
§Texas A&M, College Station, TX.
¶Argonne National Laboratory, Lemont, IL.
‖Department of Physics, Tulane University, New Orleans, LA.

[1]Note that the RGA is not inside the decay cell, but the pressure it measures is proportional to the pressure in the decay cell. See Fig. 3.4-1

when a CRES electron scatters off of a residual gas particle. As such, the CRES track length is inversely proportional to the pressure in the decay cell. Long tracks, ideally longer than 10 ms on average, are immensely important to our analysis because longer tracks are easier to differentiate from noise.

When we take CRES data the only pumping on the decay cell region is via getter pumps because a turbo would pump the radioactive gas of interest. Since there is minimal pumping during data taking we are very sensitive to air leaks of any size. Argon, being inert, is not pumped by the getter pumps. During our first campaign of acquiring CRES data in March 2021 we discovered that the pressure of Ar as measured by the RGA rose to mid 10^{-6} Torr after 5 minutes. This meant that all of our data acquisition had to take place in the five minute window in which the pressure was low enough that our track lengths would be of reasonable length. Thus a large priority for this year was to eliminate the air leaks in our vacuum system.

Ryan Roehnelt and Drew Byron redesigned a problematic flange, and we replaced all vacuum seals with conflat flanges. With the improvements, the air leak was fully resolved and the Ar is no longer problematic. We can now sustain a pressure of $< 10^{-7}$ Torr with only the getters pumping the decay cell. This should greatly improve the CRES track lengths we observe.

Over the past year we also configured our vacuum system such that we can now introduce radioactivity (^{6}He or ^{19}Ne) created in Cave 2 into our decay cell (see Fig. 3.4-1). In the process we added two cryopumps (CRYO-I and CRYO-II in Fig. 3.4-1) that help clean up the large 8 inch pipe that is used to transport the radioactivity from Cave 2 to Cave 1. We also added a second getter pump in order to increase the pumping power while we are taking data.

3.5 Second stage cryotrap

W. A. Byron, W. Degraw, M. Fertl*, A. García, B. Graner, E. Hanes, H. Harrington, L. Hayen†, N. C. Hoppis‡, X. Huyan§, S. Hightower, M. Kimsey-Lin, K. Knutsen, D. McClain¶, D. Melconian¶, P. Mueller‖, N. S. Oblath§, R. Roehnelt, G. Savard‖, E. Smith, D. Stancil†, R.J. Taylor†, H. E. Swanson, J. Tedeschi§, B. A. VanDevender§, F. Wietfeldt**, and A. R. Young†,

The goal of the second stage cryotrap (Cryo-II) is to clean up the gas supply to the He6-CRES experiment. The Cryo-II is one of the last components of the gas supply system, with only a getter and an RGA between it and the decay volume. The Cryo-II is built onto a

*Johannes Gutenberg University Mainz.
†Department of Physics, North Carolina State University, Raleigh, NC.
‡Presently at University of Maryland, College Park, MD
§Pacific Northwest National Laboratory, Richland, WA.
¶Texas A&M, College Station, TX.
‖Argonne National Laboratory, Lemont, IL.
**Department of Physics, Tulane University, New Orleans, LA.

modified CRYO-Torr-8F Cryopump with the 80K condensing array removed. The gas passes through a torus shaped region defined by the "spool" and the 80K heat shield. The spool is attached to the second stage cold head of the cryopump. These make good thermal contact, and lacking additional load comes into thermal equilibrium at 12K when the cryopump is on.

The temperature of the spool is raised to and held at a set point temperature (in the range of 30K to 40K) using a PID controller and active heating. The heating element is a 150 Ω heater from Cryocon. The temperature of the spool and heat shield are monitored using S950 silicon diodes that are read out through an electronic feedthrough to custom electronics boxes that display the transition voltage from a 10-µA excitation current. The temperature of the second stage is monitored using a built in silicon diode of different model. This is also read out with a calibrated electronics box. We are in the process of testing and redesigning portions of this cryotrap for better efficiency of gas transport.

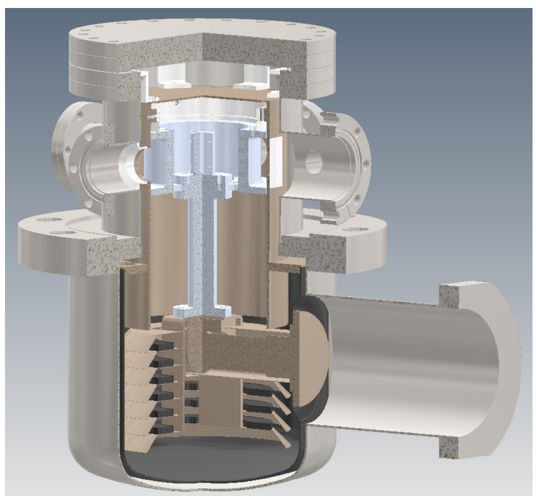

Figure 3.5-1. Design of the first iteration of the second stage cryotrap.

3.6 ^{6}He CRES waveguide systems and data acquisition (DAQ)

W. A. Byron, W. DeGraw, M. Fertl[*], A. García, B. Graner, H. Harrington, L. Hayen[†], X. Huyan[‡], K. Knutsen, D. McClain[§], D. Melconian[§], P. Mueller[¶], N. S. Oblath[‡], R. Roehnelt, G. Savard[¶], E. Smith, D. Stancil[†], R.J. Taylor[†], H. E. Swanson, J. Tedeschi[‡], B. A. VanDevender[‡], F. Wietfeldt[‖], A. R. Young[†],

Because the microwave power coupled to the TE_{11} mode of a cylindrical waveguide for individual beta-decay electrons is on the order of femtowatts (10^{-15} W), the amplification system

[*]Johannes Gutenberg University Mainz.
[†]Department of Physics, North Carolina State University, Raleigh, NC.
[‡]Pacific Northwest National Laboratory, Richland, WA.
[§]Texas A&M, College Station, TX.
[¶]Argonne National Laboratory, Lemont, IL.
[‖]Department of Physics, Tulane University, New Orleans, LA.

of any CRES-based experiment is critical to achieving acceptable sensitivity. Furthermore, the loss of kinetic energy to radiation causes the beta's cyclotron frequency to increase with time, which can yield valuable information about the kinematics if and only if one can achieve high frequency resolution on these femtowatt-level signals with short time-averaging windows. In the last year, our collaboration has demonstrated that our apparatus is capable of both minimizing thermal noise and amplifying these femtowatt-level signals above the threshold of detectability with good resolution in both frequency and time.

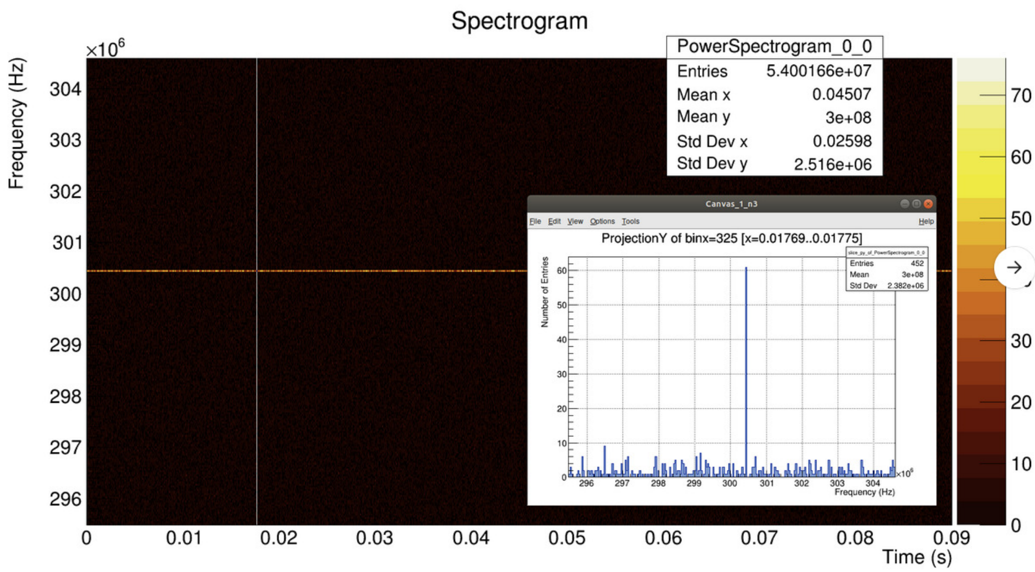

Figure 3.6-1. Observation of a 18.2004 GHz tone (300.4 MHz above baseband) introduced into the He6-CRES apparatus waveguides at -123 dBm (≈0.5 fW). Inset: an individual 50 μs power spectrum approximately 18 ms into the spectrogram (which corresponds to the white vertical line), with the input -123 dBm signal This indicates that signal-to-noise ratios on the order of 20 are achievable in 0.05 ms time on sub-femtowatt signals.

The frequency resolution of a CRES experiment is critical because the cyclotron frequency is directly coupled to the beta's kinetic energy at any given time. Fig. 3.6-1 shows a spectrogram with an injected signal at 18.2004 GHz, with a single power spectrum inset. The frequency resolution of our FPGA-based DAQ system is ≈40kHz as currently configured, or about 2 ppm on a typical 20 GHz CRES signal.

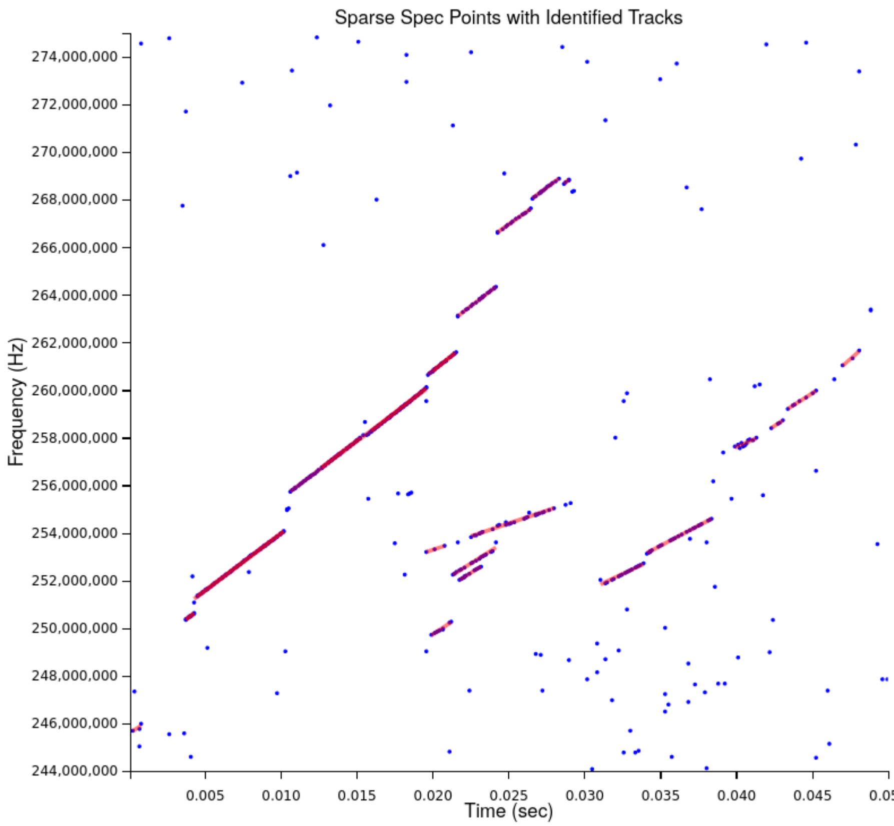

Figure 3.6-2. Observation of ^{83m}Kr decay electrons on a 'sparse spectrogram', where each data point (in blue) is a frequency bin within a given time slice with power above a predetermined threshold. Red lines are the preliminary CRES track reconstructions, indicating that the changing cyclotron frequency of the electrons can be clearly reconstructed with the current He6CRES DAQ system.

In addition to the need for high frequency resolution, it is important to be able to resolve CRES signals within a short time window to extract information from the time-varying cyclotron fequency of the beta. Fig. 3.6-2 shows that the slope of CRES signals for electrons ejected in the internal conversion decay of ^{83m}Kr is well-resolved, and will enable us to reconstruct the electron's pitch angle and displacement from the central axis of the waveguide with high precision.

Finally, it should be noted that the best signal-to-noise ratio (SNR) on a time-changing frequency signal is achieved when the signal occupies a single frequency bin in the fast Fourier transform (FFT) for the entire FFT sample window, and that the slope of CRES signals (in frequency per unit time) will increase for higher-energy CRES events involving the beta decay of ^{6}He and ^{19}Ne. The reconfigurability of the FFT parameters on our FPGA-based DAQ system provides the flexibility to optimize SNR for dynamic signal properties, and we intend to work on leveraging this flexibility in our DAQ system as we move towards gathering CRES data with ^{6}He and ^{19}Ne decays in the coming year.

3.7 ^{6}He production

W. A. Byron, W. DeGraw, M. Fertl*, A. García, B. Graner, H. Harrington, L. Hayen†, X. Huyan‡, K. Knutsen, D. McClain§, D. Melconian§, P. Mueller¶, N. S. Oblath‡, R. Roehnelt, G. Savard¶, E. Smith, D. Stancil†, R.J. Taylor†, H. E. Swanson, J. Tedeschi‡, B. A. VanDevender‡, F. Wietfeldt‖, A. R. Young†,

Having a reliable ^{6}He source is immensely important to our intermediate term goal of obtaining the first CRES measurement of the beta decay energy spectrum of ^{6}He. The ^{6}He source in Cave 2 had not been used or maintained since the last ^{6}He production run in early 2018. Over the last several months we have successfully refurbished the Li target. By the end of August we produced ^{6}He, albeit with minimal production, and delivered it to the ^{6}He CRES apparatus in Cave 1 for the first time.

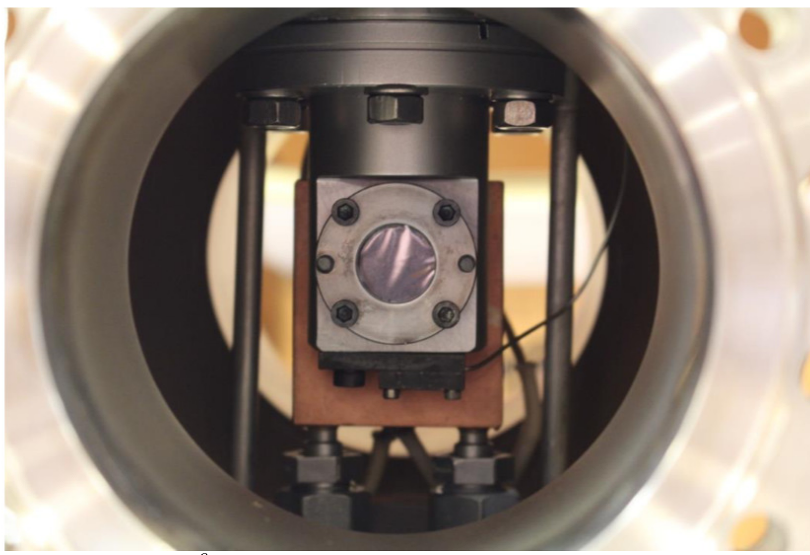

Figure 3.7-1. A photo of the ^{6}He target assembly. The tantalum window can be seen within the circular aperature. The target heater is embedded within the copper block behind the tantalum window.

The tantalum window on the old target assembly was broken and the Li inside had been exposed to air so we reinstalled a new target assembly on the ^{6}He beam line and replaced the Li in the trap. Fig. 3.7-1 shows a photo of what the tantalum window looks like from the perspective of the incoming deuteron beam. We rewired the thermocouples that monitor the temperature of the Li target as well as the heater that enables us to melt the Li. We also rewired and tested the stepper motors that enable us to stir the molten Li during ^{6}He production.

*Johannes Gutenberg University Mainz.

†Department of Physics, North Carolina State University, Raleigh, NC.

‡Pacific Northwest National Laboratory, Richland, WA.

§Texas A&M, College Station, TX.

¶Argonne National Laboratory, Lemont, IL.

‖Department of Physics, Tulane University, New Orleans, LA.

During our single ^{6}He production run in August 2021, due to difficulty putting high current on target, we were unable to produce enough ^{6}He for a CRES measurement. Over the next few months we will work to improve our production to the point where a CRES measurement of ^{6}He will be possible.

3.8 ^{19}Ne source

W. A. Byron, W. DeGraw, B. Dodson, A. García, B. Graner, H. Harrington,
M. E. Higgins*, N. C. Hoppis†, E. B. Smith, and D. W. Storm

As described in last year's Annual Report[1] we built a gas handling system and target in order to use the ^{19}F$(p,n)^{19}$Ne reaction with a beam from the Tandem accelerator at around 12 MeV. The source design is similar to the ^{19}Ne source developed at Berkeley[2,3] and used later at Princeton,[4] but without the difficulties related to getting polarized atoms.

The gas flows continuously through the target, and the activated gas passes through a cold trap to freeze out the SF_6, leaving the ^{19}Ne free to be compressed by a turbo pump. We plan two alternating cold traps to permit continuous operation, but so far we have one.

In 2019-2020 we completed and tested most of the gas handling system illustrated in Fig. 3.8-1. We also "cleaned" 33 moles of SF_6 by freezing the gas from the supply tank while pumping off the non-condensable gas impurities and then sublimating the SF_6 back into our storage tanks. However a residual gas analyser (RGA) showed there was a significant background of air in the SF_6 that we had already cleaned once, so we repeated the process, freezing the entire contents of each storage tank while pumping. This repeated step removed most of the air, but there was still a significant amount of CF_4 in the vacuum over the cold trap. The vacuum registered around 5×10^{-5} Torr while the SF_6 was flowing into the trap. The RGA indicated this was mostly CF_4 and SF_6. The indicated pressure is consistent with an extrapolation to 80K of published values[5] of the vapor pressure of SF_6 at low temperature. In order to remove gas that does not freeze out at 80 K, we built a second cold trap, inserted after the Cave 1 turbo pump. See (Sec. 3.5).

This year we added taps (labeled B on Fig. 3.8-1) for connecting a Baratron[6] gauge to measure the pressure drop in the line following the needle valve, as well as a gauge in the line right ahead of the target. The Baratron pressures enable us to determine the stream velocity,

*Presently at Duke University, Durham, NC.

†Presently at University of Maryland, College Park, MD.

[1] CENPA Annual Report, University of Washington (2020) p. 77.

[2] D. Dobson, *The beta-decay asymmetry and nuclear magnetic moment of Neon-19,* Ph. D. Thesis, U. C. Berkeley (1963).

[3] D. C. Girvin, *Test of time-reversal invariance in ^{19}Ne beta decay,* Ph. D. Thesis, U. C. Berkeley (1972).

[4] M. B. Schneider, F. P. Calaprice, A. L. Hallin, D. W. MacArthur, and D. F. Schreiber, Phys. Rev. Lett. **51**, 1239 (1983).

[5] https://encyclopedia.airliquide.com/sulfur-hexafluoride

[6] MKS Instruments, Inc., Andover, MA

since we know the mass flow rate. For example, for 3-atmosphere SF_6 at a volume flow rate of 5.4 cc/sec through the target, we found 74 Torr after the needle valve and 50 Torr at the manifold; for the 3/8" copper tube, these correspond to an average stream velocity of 4 m/s and a transit time of only 2 sec from the target to the manifold. Thus we don't expect much decay of the 17-sec half-life ^{19}Ne after the gas exits the target. The new gauge just before the target confirms that the pressure drop in the supply line between G2 and the target is negligible. Finally, we connected the third storage tank to the system.

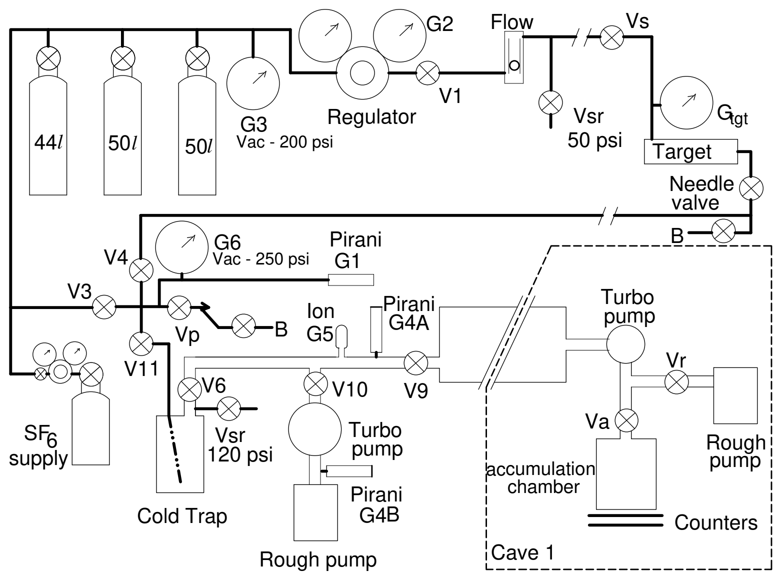

Figure 3.8-1. The gas handling system as described in the text. The target and SF_6 handling system is in Cave 2, near the ^{6}He production system. Both systems connect to a 6-inch pipe running through the wall into Cave 1, where the activities will eventually be fed into the ^{6}He-CRES device. The heavy lines indicate either 3/8" or 1/4" copper refrigeration tubing for gas transport.

We did 4 runs producing ^{19}Ne both to study the half-life and to study the effectiveness of our production system. (We did an additional 8 runs, without beam, testing the gas system.) Using the cross sections of Jenkin[1] in a repeated version of the calculation described previously[2], we find that 7.8×10^8 s$^{-1}\mu$A^{-1} should be produced in the target. We expect to lose about half of these due to decay before the chamber, leaving about 4×10^8. Measurements to date have given a figure an order of magnitude smaller, which is still sufficient for our needs. The measurements should be considered a lower limit on the production rate, as the efficiency of the detectors we have been using is questionable. We plan to do a careful determination of the efficiencies of our detection systems to finish up characterizing the source.

We studied both varying the pressure and the flow rate to see the impact on the production rate. Initially we operated at a flow rate of 5.4 cc/sec with 3-atmosphere gas (mass flow rate

[1] J. D. Jenkin, L. G. Earwaker, and E. W. Titterton, Nucl. Phys. **44**, 453 (1963).
[2] CENPA Annual Report, University of Washington (2020) p. 82.

2.44 mole/hr). The volume flow rate compares with the 57-cm^3 target volume, and the 3 atmospheres was chosen since at room temperature SF_6 at 2 atmospheres should stop the beam within the target length. Eventually, with high beam currents, the gas will be quite hot, hence the extra pressure. The decay in transit from the target is small, whereas we are only changing the gas in the target once in about 10 sec, so we could lose significant activity there.

Besides noting the relative activity per unit beam current for various pressures and flow rates, in order to understand how much decay was occurring before the sampling chamber, we measured the time from turning the beam on until the activity appeared in the measuring apparatus for various conditions. For these measurements both V_a and V_r (Fig. 3.8-1) were open, so we were monitoring the gas that was passing from the turbo to the rough pump. A typical cycle is shown in Fig. 3.8-2. We used the time from "beam on" to the midpoint of the rise to characterize the passage time of the activity. This "delay" was found to be weakly dependent on the flow rate (about 16 sec for 5.4 cc/sec and 20 sec for 2.7 cc/sec). The amount of activity obtained did appear to vary with delay as one would expect for the 17-sec half life. As the delay is about one half-life, transit time of the activity is not the source of our apparently low production rate.

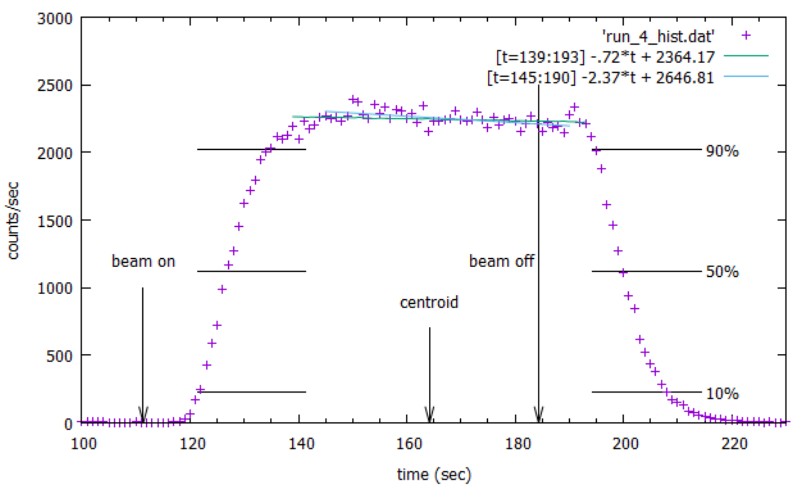

Figure 3.8-2. Count rate vs time when the beam is turned on and off. Note the delay between the beam and the arrival of the activity, as well as the rise and fall times.

3.9 Monitor detector for relative normalization

W. A. Byron, W. DeGraw, M. Fertl*, A. García, B. Graner, H. Harrington, L. Hayen†, X. Huyan‡, K. Knutsen, D. McClain§, D. Melconian§, P. Mueller¶, N. S. Oblath‡, R.

*Johannes Gutenberg University Mainz
†Department of Physics, North Carolina State University, Raleigh, NC.
‡Pacific Northwest National Laboratory, Richland, WA.
§Texas A&M, College Station, TX.
¶Argonne National Laboratory, Lemont, IL.

Roehnelt, G. Savard[¶], E. Smith, D. Stancil[†], R.J. Taylor[†], H. E. Swanson, J. Tedeschi[‡], B. A. VanDevender[‡], F. Wietfeldt[‖], A. R. Young[†],

Since the ^{6}He-CRES data is taken in a finite band width ($\approx$ 18-20 GHz) that covers a small portion of the beta spectrum, we take data at different values of the magnetic field to span the whole beta spectrum. In order to stitch together these different parts, we use a monitor beta detector (shown in Fig. 3.4-1, right after the turbo pump, at the top of the diagram). Thus, this monitor detector has to have stability at the level required for the experiment.

Along with the silicon detector monitor that we reported on last year, we have developed a monitor system using plastic scintillators with PMT readout, a schematic of which can be seen in Fig. 3.9-1.

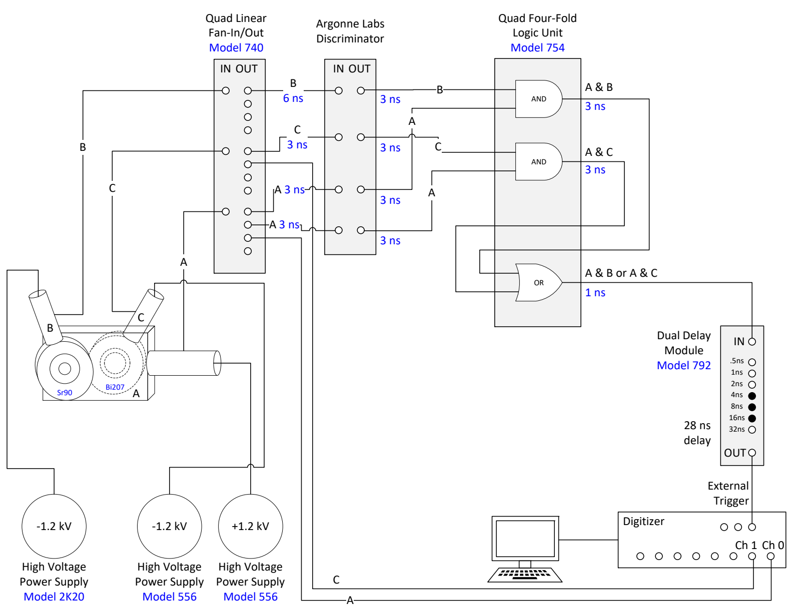

Figure 3.9-1. Schematic of scintillator arrangement.

We have three scintillators in total, two thin "delta E" (B and C in schematic) scintillators and a thicker "E" (A in schematic) scintillator in order to fully stop the beta and get an energy measurement. The two thin scintillators will have separate sources shining on them. One will have the radioactivity that we ultimately aim to measure with the CRES technique (^{6}He, ^{19}Ne) directed on it, the other will have a small ^{207}Bi source. The purpose of the separate sources is to be able to observe any variations in gain of the scintillator/PMT arrangement as we continuously monitor the radioactivity of interest. We use the combined logic of (A and B) or (A and C) to trigger our digitizer, and take data for the output of the A and C scintillator. This way we get the ^{207}Bi spectrum for controlling gain variation, as well as the full spectrum of the radioactivity of interest + ^{207}Bi to ultimately be used for normalization of the spectrum achieved with the CRES technique.

[‖] Department of Physics, Tulane University, New Orleans, LA.

In order to measure the stability of the scintillators + PMT monitor we used an ^{90}Sr source in place of ^{6}He/^{19}Ne. We took data continuously for 48 hours in order to determine the Allan deviation of the system, which is shown in Fig. 3.9-2.

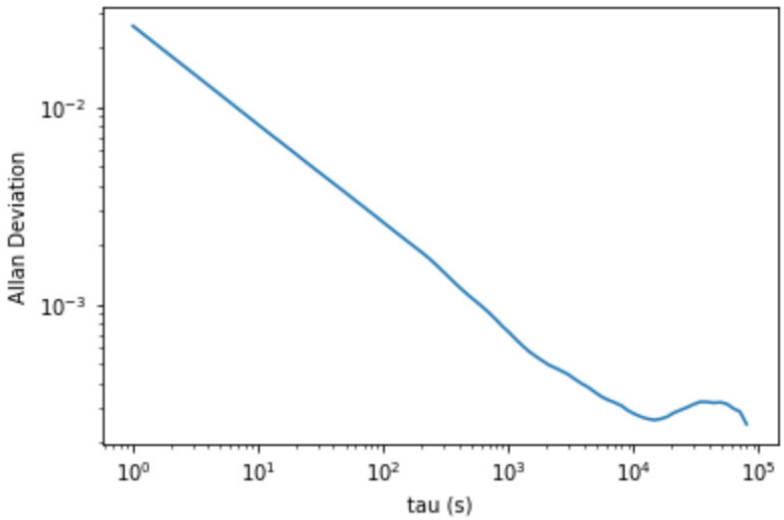

Figure 3.9-2. Allan deviation of scintillators + PMT beta monitor.

The monitor achieved a stability of $\sim 2.5 \times 10^{-4}$, which is adequate for our monitor purposes in the short term. A cause for concern with this system is the PMT's efficiency dependence on external magnetic fields. Despite the monitor being placed outside of the bore of the magnet there will still be fringe fields present. In order to decrease our sensitivity to these fields we plan on using Silicon Photomultipliers (SiPM's), which are immune to the effects of magnetic fields, for the readout of our scintillators. In the coming months we will be exploring this option for our monitor system.

3.10 Simulations

W. A. Byron, W. DeGraw, M. Fertl*, A. García, B. Graner, H. Harrington, L. Hayen†, X. Huyan‡, K. Knutsen, D. McClain§, D. Melconian§, P. Mueller¶, N. S. Oblath‡, R. Roehnelt, G. Savard¶, E. Smith, D. Stancil†, R.J. Taylor†, H. E. Swanson, J. Tedeschi‡, B. A. VanDevender‡, F. Wietfeldt‖, A. R. Young†,

An accurate and reliable simulation will be integral to the interpretation of our future CRES data. Over the past few months we have begun to build a simulation package in python.

*Johannes Gutenberg University Mainz.
†Department of Physics, North Carolina State University, Raleigh, NC.
‡Pacific Northwest National Laboratory, Richland, WA.
§Texas A&M, College Station, TX.
¶Argonne National Laboratory, Lemont, IL.
‖Department of Physics, Tulane University, New Orleans, LA.

The intention is that the simulation package will construct realistic CRES data that can be analyzed via the same Katydid pipeline we use for real data.

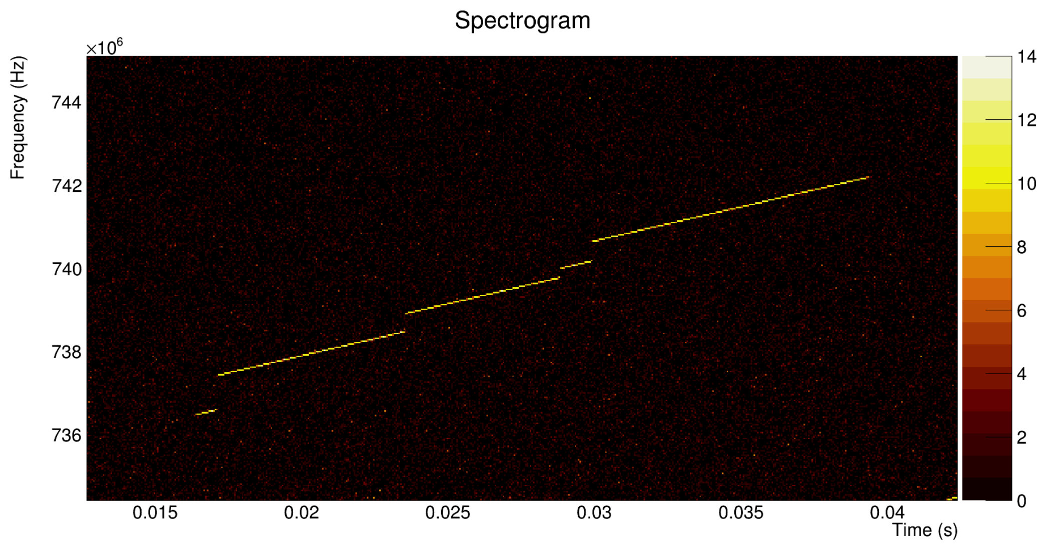

Figure 3.10-1. The power spectrogram of a simulated event consisting of 5 tracks.

On a high level this entails modeling a beta decay within the decay cell, deciding if the beta is trapped, modeling the axial motion of the beta, and modeling scattering off residual gas in the decay cell. The power and slope of tracks are calculated based on the pitch angle and radial position of the beta. The measured gain and noise floor of our system is used as an input to construct simulated tracks that are written to .spec files, the same file type output by our Roach (an FPGA board).

The simulation is organized into different classes we are referring to as blocks (Physics, Hardware, Kinematics,..). Each block is responsible for a concrete part of the simulation. For example the Hardware block is responsible for determining if a beta is trapped, based on the beta pitch angle and proximity to the guide walls. The simulation package is still in development but we currently have the ability to write very simple tracks overlaid on top of simulated noise to a spec file. Fig. 3.10-1 shows a simulated event.

For validation we will compare the simulation to data acquired with a ^{83m}Kr monoenergetic conversion electron source. Once we have the simulation working we will be able to use it to conduct systematic studies. We will also be able to use it to investigate the details of our full measurement pipeline, from acquiring data to presenting an energy spectrum, without needing to take real data.

4 Precision Muon Physics

4.1 Overview

The Precision Muon Physics Group's scientific program is based on experiments that determine fundamental Standard-Model parameters, low-energy effective-field-theory constants, or provide sensitive tests for new physics. We are involved presently in three efforts that are all at different life-cycle stages. We present overviews and individual articles that represent just some of the technical work we have been doing on the MuSun, Muon $g-2$, and PIONEER experiments. It is but a small sample of the actual work accomplished of course, but should provide a flavor for the variety of UW work in the past year.

4.2 Muon capture and the MuSun experiment

D. W. Hertzog, P. Kammel, E. T. Muldoon, and D. J. Prindle

Muon capture is a powerful tool to study the properties and structure of the nucleon and few nucleon systems as predicted by effective field theories (EFT) founded on Quantum Chromodynamics. Our program focuses on capture from the simplest muonic atoms, namely on the proton (MuCap experiment) as well as on deuterium (MuSun experiment). Substantially improved precision is enabled by a novel active-target method based on the development of high-pressure time-projection chambers (TPC) filled with hydrogen/deuterium gas, which our collaboration pioneered.

The goal of the MuSun experiment is a first precise measurement of a weak process in the 2-nucleon (2N) system. These reactions include muon capture on the deuteron, $\mu + d \to n+n+\nu$, together with two astrophysics reactions of fundamental importance, solar *pp* fusion and νd reactions, where the latter provided the evidence for solar neutrino oscillations. The extremely small rates of these processes do not allow their cross sections to be measured precisely; they must be calculated by theory, with information derived from the more complex three-nucleon system. These interactions all involve the same axial-vector coupling at a four-nucleon vertex, characterized by a single poorly known low-energy constant (LEC) d^R in the EFT description. This LEC is also an essential ingredient in the construction of chiral three-nucleon forces and in other weak and strong dynamics. MuSun plans to determine the rate Λ_D of muon capture on the deuteron to 1.5%, where Λ_D denotes the capture rate from the μd doublet hyperfine state. Current experiments are at the 6-10% level, and the most precise one disagrees with the latest theory calculations[1,2] $\Lambda_D = 399 \pm 6\,\mathrm{s}^{-1}$ by more than 3 standard deviations.

The MuSun experiment uses the so-called "lifetime method" consisting of a precision measurement of the muon disappearance rate $\lambda_{d\mu}$ in deuterium. As $\lambda_{d\mu} \approx \lambda_{\mu^+} + \Lambda_d$ and the free muon decay rate λ_{μ^+} is known[3] to 1 ppm, a 13 ppm measurement of $\lambda_{d\mu}$ is required.

[1] L.E. Marcucci et al., Phys. Rev. Lett. **108**, 052502 (2012).
[2] B. Acharya et al., Phys. Rev. C **98**(6), 065506 (2018).
[3] V. Tishchenko et al., Phys. Rev. D **87**(5), 052003 (2013).

Muons are stopped in a cryogenic time projection chamber (cryo-TPC) filled with ultra-pure deuterium gas (Fig. 4.2-1). Decay electrons are detected in two cylindrical wire chambers and a segmented scintillator barrel. The experiment must simultaneously meet several stringent requirements. i) The target conditions (T=31 K and density 6.5% of liquid-hydrogen density) are optimized for an unambiguous extraction of Λ_D, and the suppression of muonic atomic physics complications that arise when muons stop in deuterium, such as muon-catalyzed fusion. ii) Muons are tracked in three dimensions in the active target TPC, which eliminates most muon stops in wall material. iii) Muon transfer to impurity elements is suppressed by keeping and monitoring the gas contamination at the 10^{-9} level. The CENPA team was responsible for numerous hardware systems in MuSun, including TPC construction, custom built cryo-preamplifiers and the electron detector. After several technical developments and upgrades, MuSun collected its full statistics of 1.4×10^{10} events in two main production runs R2014 and R2015 at PSI, followed, in 2016, by a shorter systematic run.

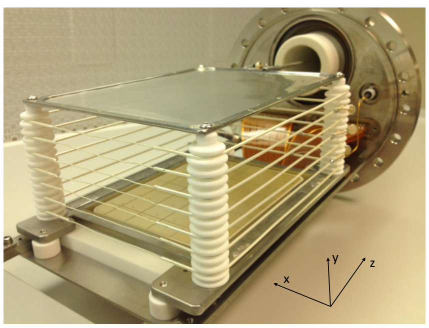

Figure 4.2-1. MuSun cryo-TPC with 6×8 anode pads. The grid frame has a composite construction to withstand thermal cycling.

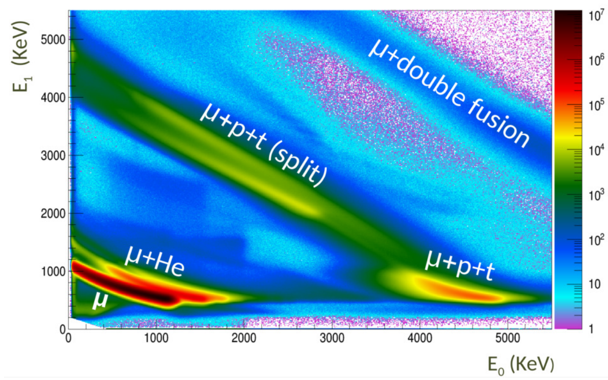

Figure 4.2-2. Energy in the penultimate pad E_1 vs. the stop pad E_0. Pure muon stops and muon-fusion pile-up areas are clearly identified.

In order to achieve the required precision in Λ_D both statistical and systematic uncertainties $\delta\Lambda_D$ should not exceed $\pm$ 4 s^{-1}. Such a precision requires careful attention to systematics from physical as well as instrumental effects. In particular early-to-late effects within the fit range of 1-24 μs must be tightly controlled. Additional analysis challenges were introduced by the poorer beam quality of the new beamline, where the experiment had to relocate after the development phase. The final analysis at the required level is performed by the UW group. The muon stop definition is critical, as there is a $\approx$ 5% chance that the muon track overlaps with fusion recoils, generated by muon-catalyzed fusion in $dd\mu$ molecules, potentially leading to misreconstruction of the muon stopping point (see see Fig. 4.2-2). This issue is discussed in detail in the contribution by Muldoon, where a new method to correct for it is presented.

At the operating temperature T=31 K of MuSun, all relevant impurities have frozen out except for nitrogen. MuSun determined the sensitivity to trace nitrogen contamination as $\partial\lambda_{d\mu}/\partial c_N \approx 4\,\mathrm{s}^{-1}$ per ppb. During R2015 the MuSun chromatography was able to limit c_N to about 1 ppb. A more direct method applied to all runs is the detection of the capture recoil from $\mu + N \to C^* + \nu$ in the TPC. The result of this challenging analysis is presented in the report by Prindle. The *in-situ* analysis agrees with the chromatography result, yielding an associated $\delta\Lambda_D < 2$ s^{-1}.

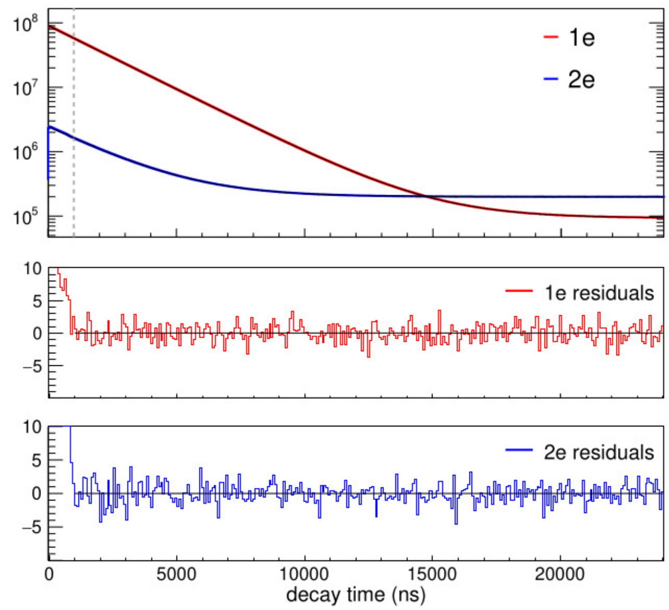

Figure 4.2-3. Muon decay spectra from scintillators observed in R2014 requiring one (1e) or two (2e) electrons in the region of interest. The data is fitted to a single exponential and an accidental component with a small linear term in the range 1-24 μs.The normalized residual plots demonstrate consistency once early kicker induced background has subsided.

The muon decay spectra, see Fig. 4.2-3, are built by histogramming the electron scintillator barrel hits against the entrance scintillator time for muons that were tracked to stops inside the fiducial volume of the TPC. For decay electrons the signals in the scintillator are used or, alternatively, this information is combined with tracking in the electron wire chambers. The time spectra shown in the figure are sorted depending whether only one (1e), or two (2e) electrons were detected in the region of interest 0-24 μs after muons stop, which suppress and enhance accidentals, respectively. With this method, a slight time-dependent decrease of the background is observed, which is probably related to the fast kicker, and accounted for in a simultaneous fit of both spectra (work by Muldoon). The linear correction term induced an uncertainty $\delta\Lambda_D \approx 3$ s^{-1}.

The analysis of R2014 is well advanced, focusing on a single significant remaining systematic issue and quantifying subdominant systematic effects. We plan to unblind and publish these results during the next months. The statistics are sufficient to clarify the existing 3-sigma discrepancy between experiment and theory. Most systematic issues are identical for the larger second dataset R2015, but further data quality and consistency checks are required. The final analysis will include both data sets to obtain a capture rate with 1.5% uncertainty, commensurate with the current precision in theoretical calculations.

4.3 Early time fusion analysis

D. W. Hertzog, P. Kammel, E. T. Muldoon, and D. J. Prindle

One of the most challenging systematic effects in the MuSun experiment has always been TPC tracking errors caused by the presence of muon-catalyzed fusion. After the muon stops in D_2 there is a $\sim$6% probability for formation of a muonic molecule $dd\mu$, which spontaneously fuses into either $({}^3He+n)$ or $(p+t)$. These reaction products can overlap with the original muon track and produce a mis-reconstructed stop position, a process known as *fusion interference*. Our standard tracking algorithm tends to mis-reconstruct muon stops upstream, producing a significant stop position dependence in the fusion fraction. This is not a problem in itself, but if fusion interference occurs across the fiducial volume boundary it can lead to fusion events being cut in a biased way. Muon decay times for a fusion event follow a non-exponential distribution, shown in the left panel of Fig. 4.3-1, and a 1% loss of fusion events corresponds to a 6 Hz shift in the MuSun Λ_d capture rate.

Several previous analyses have attempted to correct for fusion interference, either by creating alternative trackers or by tagging fusion events by the extra energy deposition from the fusion products. These methods have all struggled to produce fully consistent results at the required level of accuracy. One challenge common to all of these methods is that they have focused only on TPC information to correct the tracking errors. A new independent approach developed this year instead estimates fusion interference using only lifetime information.

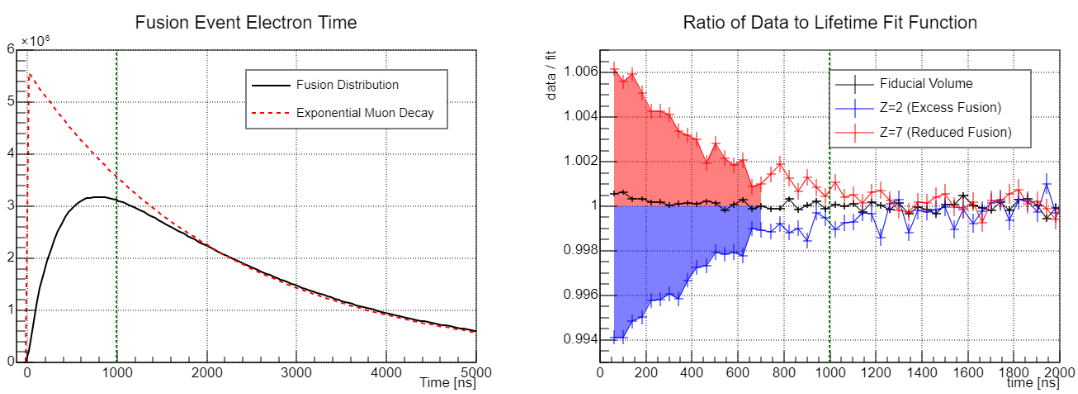

Figure 4.3-1. *Left*: Time distribution of muon decays following fusion events. The vertical green line indicates the standard fit start time. *Right*: Ratio of data to exponential fit for fiducial volume and for Z bins with high and low fusion fractions. The shaded regions indicate the integration range for quantifying the deviation.

The standard fitting procedure for MuSun uses a 1 μs start time to avoid beam background effects[1], at which point the fusion produces a relatively small effect. At earlier times however the effect becomes much more significant as there is too little time for many fusions to occur before the muon decay. For more realistic fusion fractions we can see this effect more clearly by taking the ratio of the data to the fit function to cancel out the decay component, shown

[1]CENPA Annual Report, University of Washington (2019) p. 5.

in the right panel of Fig. 4.3-1. Integrating over this histogram gives us a numeric deviation value which we can relate to the fusion fraction and lifetime shift.

Using this deviation measurement to monitor fusion events has several advantages. First, assuming the fit is correct the deviation value is proportional to the difference in fusion fraction from the correct value. This means that we can directly see the fusion gains or losses, unlike previous fusion tagging approaches which required careful analysis to determine the true fusion fraction. A second advantage is that this method is completely insensitive to fusion tagging efficiency and will even work for muon stops outside the active TPC volume. Finally, an independent analysis lets us compare the results and gain a better understanding of this difficult systematic.

The new method also has its own challenges. First, the fit function must accurately model the beam background in the first microsecond where the beam is switched off by a fast kicker. This has been avoided in the past, but at this point we have a good understanding of the background structure. Our integration window from 40 to 720 ns was chosen to pick out a period of constant background between the muon entrance and the kicker gate at 800 ns. The background rate here is different than in the normal fit window, but we can determine it by fitting the beam background shape before the muon entrance.

Another challenge is that this analysis assumes the lifetime distortion always follows a universal form. The muon kinetics do produce a fusion time distribution satisfying this requirement, but in order to cause interference the fusion must also overlap with the muon track. This introduces dependence on the clustering algorithm which can alter the time distribution somewhat for specific track configurations. Several other processes could also produce entirely separate distortions, including muon capture in high-Z wall materials or TPC interference effects caused by other particles such as the decay electron itself. These issues have each been studied and found to be within acceptable bounds, so this method seems capable of constraining fusion interference to within our target uncertainty budget.

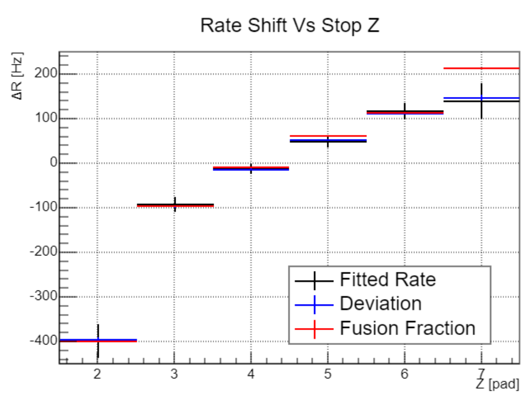

Figure 4.3-2. Rate shift versus muon stop pad. The predictions from the early time deviation and the fusion fraction estimates agree with the observed rate shift, except on the last pad where the fusion tagging loses efficiency and therefore predicts a higher rate.

The new early time deviation method agrees well with the previous fusion fraction analysis except near the back of the TPC where fusion products can leave the active volume and cause the fusion tag to lose efficiency, as shown in Fig. 4.3-2. The agreement between these two methods is a positive in that it increases our confidence in the overall analysis, but it also means that the new method confirms an issue evident in the previous analysis. In particular, we can make energy cuts on the incoming muon energy deposition to alter the stop distribution. When using a low energy cut to select downstream stops we see an excess of fusions too large to be accounted for by migration, which persists even when the downstream fiducial volume cut is removed in an attempt to eliminate migration as a factor. This unexpected behavior is not reproduced in simulation and requires additional study.

4.4 Impurities in the MuSun TPC gas

D. W. Hertzog, P. Kammel, E. T. Muldoon, and D. J. Prindle

The purity of the gas in the MuSun cryo-TPC is extremely important. The tighter binding energy of higher-Z elements causes muons to rapidly transfer to impurities, and once bound there is a Z^4 enhancement of the capture rate. The main impurities of concern are oxygen and nitrogen[1], requiring levels below 3 ppb O_2 and 1 ppb N_2 to achieve our uncertainty goal for the deuteron capture rate. The vapor pressures in the MuSun production target are such that oxygen should be frozen out of the gas, but the equilibrium nitrogen concentration is over 10 ppb. Our Circulating Hydrogen Ultrahigh Purification System (CHUPS) continuously purifies the deuterium gas to near the required level, but it is still necessary to precisely measure and correct for any residual impurity.

To quantify the purity level of the deuterium gas, the MuSun experiment uses a dual approach. A custom gas-chromatography system, developed by our collaborators from the Petersburg Nuclear Physics Institute, is directly connected to our TPC and CHUPS. After a careful calibration procedure and an upgrade of the readout system, the gas-chromatography reached a sensitivity of ≈1 ppb in R2015. The uncertainty is dominated by the uncertainty of nitrogen and gas impurities introduced by the room-temperature gas system and sampling lines. Due to the complexity of the measurement procedure, samples were taken relatively infrequently and must be interpolated to estimate the impurity throughout production.

A complementary in-situ method of measuring the N_2 impurity levels in the TPC gas was developed to verify the R2015 gas-chromatography results as well as check on the R2014 data which was taken before the gas-chromatography system had reached the 1 ppb sensitivity. Carbon recoils from muon capture on nitrogen are visible in the TPC, with a wide energy distribution peaked near 150 keV. This partially fills a gap between low energy electron and noise pulses and the peak from muon-catalyzed ^{3}He fusion recoils, as shown in the left panel of Fig. 4.4-1. Most of the ^{3}He recoils will have an associated electron, since the muon is usually recycled and decays normally. The impurity captures consume the muon and therefore cannot have an associated decay electron. Subtracting electron tagged events from electron veto events therefore isolates the muon capture signal. We also use a delayed time window to suppress the dominant fusion background, which proceeds with a lifetime of ≈300 ns while the peak of the impurity capture doesn't occur until ≈2 μs. Integrating

[1]CENPA Annual Report, University of Washington (2015) p. 87.

the background subtracted histogram over our optimized time and energy windows results in the observed capture yield (Y_c). For the production data we observe fairly consistent yields below 10^{-6} per muon stop, as shown in the right panel of Fig. 4.4-1.

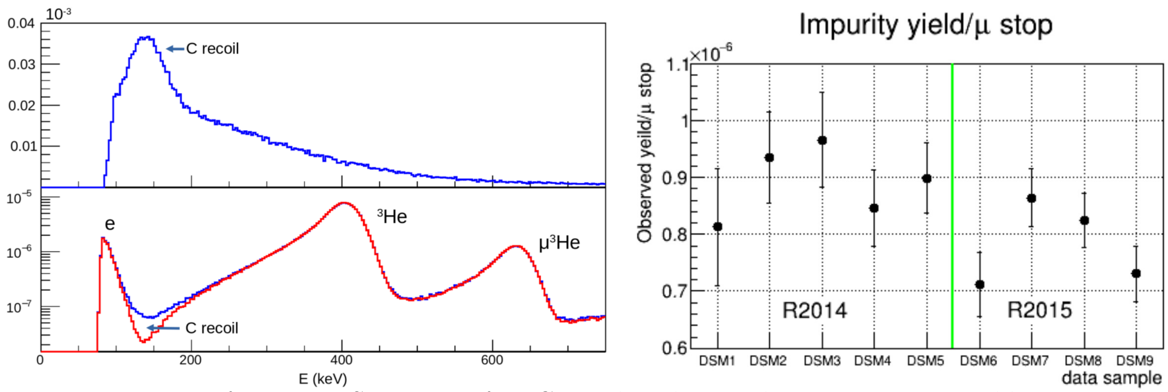

Figure 4.4-1. Left: Energy Spectrum of TPC recoils. The top shows a N capture calibration spectrum, while the bottom shows signal (blue) and background (red) spectra from R2015 production. Right: Observed impurity yields for subsets of R2014 and R2015, selected by run conditions. The observed yield is reasonably constant over each run, with a slightly smaller yield for R2015 than R2014.

To calibrate Y_c to the impurity level in the TPC we use data from R2013 and R2016 where N_2 was injected into the TPC. In R2013 we had periods with N_2 impurity levels of ≈500 ppb and ≈1750 ppb, which produced large distortions to the lifetime and allowed us to determine the muon transfer rate to nitrogen. The effect depends on our fit window, with fits starting near 1μs having their decay rate shifted by $4s^{-1}$ per ppb of N_2. For R2014 we switched to an upgraded TPC with a slightly different energy response, limiting the accuracy of the calibration for the yield itself to 10%. In R2016 we injected N_2 at a much lower level, achieving about 13 ppb and 30 ppb periods. This calibration is limited to about 5% accuracy because of the statistical uncertainty on the background subtraction. Combining both calibrations we find that a Y_c of 10^{-6} corresponds to 2 ppb N_2.

In addition to muon capture on N_2, Y_c is also sensitive to deuteron recoils from neutron scattering. These neutron scattering events occur throughout the TPC, and can be seen clearly by selecting isolated pulses away from the muon stop pad. We observe neutrons from both the μdd $\rightarrow$ n^{3}He fusion channel and μd $\rightarrow$ νnn capture, but the fusion contribution is removed by our background subtraction. To estimate the neutron contribution to Y_c we use Monte Carlo to extract the neutron yield on the stop pad. In the Monte Carlo we can directly select capture events using the truth information, which we then match to the data as shown in Fig. 4.4-2. Off the stop pad the Monte Carlo and data match very well, except below 200 keV where noise and electron pulses dominate. On the stop pad we see that between 150 and 250 keV, where we measure Y_c, about one third of the yield is due to recoils from neutrons. Correcting Y_c for neutrons we find a N_2 level of 1.2 ppb, for a correction to our measured capture rate of 4.8 s^{-1} with an uncertainty of less than 2 s^{-1}.

We are currently working on verifying the Monte Carlo neutron response by studying the neutrons from the n^{3}He channel in more detail. Then we will check the capture neutron

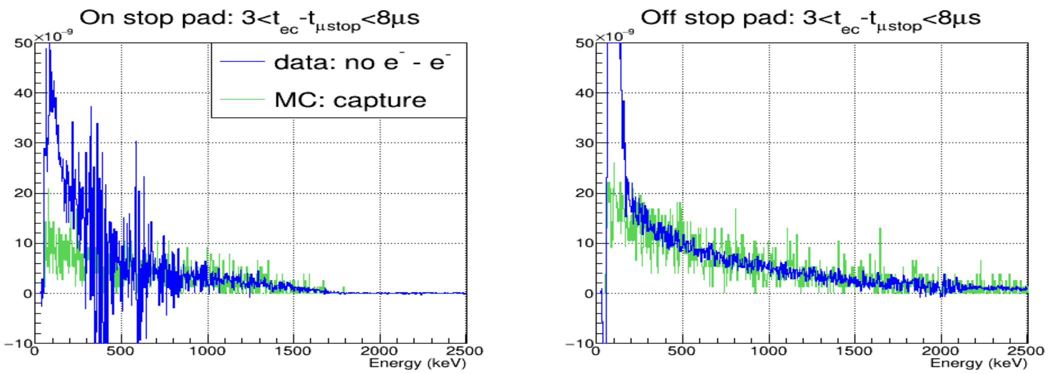

Figure 4.4-2. Neutron recoils in the TPC for pulses on (left) and off (right) the muon stop pad. Monte Carlo deuterium capture events are shown in green, and background subtracted data is shown in blue. Both data histograms show an excess at low energies due to electron and noise pulses, but on the stop pad there is an additional excess at higher energies due to N_2 capture.

contribution for stability during R2014 and R2015 to produce a final adjustment to Y_c and corresponding correction to the measured muon capture rate on deuterium.

4.5 The Muon $g-2$ Experiment

H. Binney, A. García, J. B. Hempstead, D. W. Hertzog, Z. Hodge, P. Kammel, J. Kaspar, J. LaBounty, B. MacCoy, and H. E. Swanson

Physics and motivation

The muon's anomalous magnetic moment, $a_\mu \equiv (g-2)/2$ is a special quantity because it can be both measured and predicted to sub-ppm precision, enabling a test for new physics defined by $a_\mu^{\rm New} \equiv a_\mu^{\rm Exp} - a_\mu^{\rm SM}$. As a flavor- and CP-conserving, chirality-flipping, and loop-induced quantity, a_μ is especially sensitive to new physics contributions. During the recent grant period, the *Muon $g-2$ Theory Initiative* published its first comprehensive summary of the Standard Model prediction for the muon anomaly [2] providing a benchmark against which our experimental results can be compared. This work was the result of a series of Workshops focused on the hadronic contributions, in particularly the 2019 meeting hosted by El-Khadra, Hertzog, and Hoferichter at the Institute for Nuclear Theory on our campus.

The SM contributions to the muon anomaly include electromagnetic, strong, and weak interactions that arise from virtual effects involving photons, leptons, hadrons, and the W, Z, and Higgs bosons. The recommended value

$$a_\mu(\mathrm{SM}) = 116\,591\,810(43) \times 10^{-11} \qquad (0.37\,\mathrm{ppm})$$

[2] Phys.Rept. 887 (2020), 1-166.

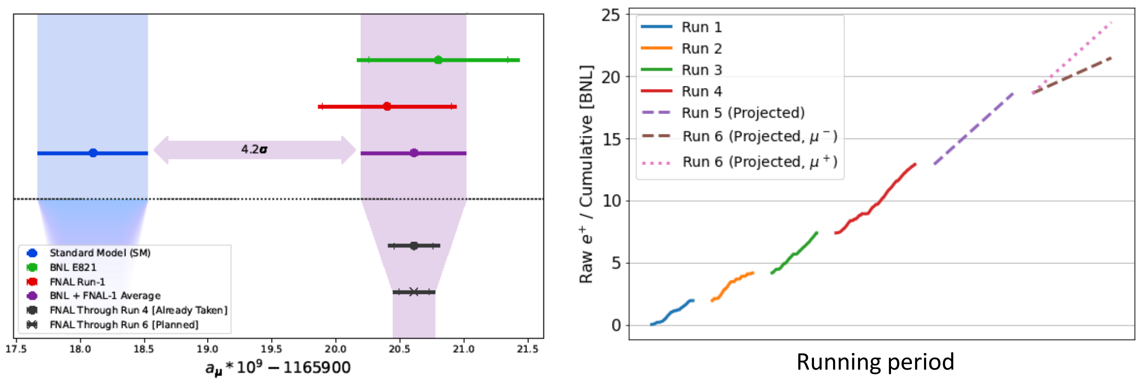

Figure 4.5-1. Left: The SM prediction for a_μ is compared to the previous BNL E821 final result, the new FNAL Run-1 result, and the world average. The SM uncertainty will reduce in the coming years as will our experimental uncertainty based on already existing and anticipated data. The placement of the future data points is, of course, purely arbitrary. Right: The Nearline summary of data accumulation for the existing Runs 1-4, and the anticipated data taking for Run-5 and Run-6, where the slope in Run-6 depends on whether μ^+ or μ^- running is carried out.

is based on contributions from QED to tenth order, hadronic vacuum polarization via $e^+e^- \to$ hadrons data, hadronic light-by-light, and electroweak processes. A comparison of experiment to theory at high precision represents a highly sensitive test of the completeness of the Standard Model. Our collaboration unblinded the Run-1 data set in early 2021 and published 4 papers [3] in April, 2021. Our result,

$$a_\mu(\text{FNAL}) = 116\,592\,040(54) \times 10^{-11} \quad (0.46\,\text{ppm}),$$

is in excellent agreement with (and thus confirms) the BNL-E821 measurement [4] from nearly 20 years ago. Averaged together, the new world average is

$$a_\mu(\text{Exp}) = 116\,592\,061(41) \times 10^{-11} \quad (0.35\,\text{ppm})$$

and when compared to the Standard Model gives

$$a_\mu(\text{Exp}) - a_\mu(\text{SM}) = (251 \pm 59) \times 10^{-11} \quad (4.2\,\sigma).$$

The results are shown graphically in Fig. 4.5-1. Run-1 represented slightly more than 1 BNL equivalent in statistics and $\sim 6\%$ of our goal of a $\sim$ 20-fold overall increase. With Run-4 recently completed, we have approximately 12 BNL sized data sets stored on tape as shown in Fig. 4.5-1. We expect to complete the data taking in Runs 5 and 6, with the priority at this time to target Run-6 for negative muon running.

[3] Phys.Rev.Lett. 126 (2021) 14, 141801, Phys.Rev.A 103 (2021) 4, 042208, Phys.Rev.D 103 (2021) 7, 072002, and Phys.Rev.Accel.Beams 24 (2021) 4, 044002.

[4] Phys.Rev.D 73 (2006), 072003.

Experimental concept and status

When a muon with charge q is circulating in the horizontal plane of a magnetic storage ring, its cyclotron frequency is $\vec{\omega}_c = -q\vec{B}/m\gamma$. The muon spin precesses at frequency $\vec{\omega}_s = -(gq\vec{B}/2m) - [(1-\gamma)q\vec{B}/\gamma m]$. Assuming a negligible muon electric dipole moment, the anomalous precession frequency can be expressed simply

$$\vec{\omega}_a \equiv \vec{\omega}_s - \vec{\omega}_c = -\left(\frac{g-2}{2}\right)\frac{q\vec{B}}{m} = -a_\mu \frac{q\vec{B}}{m}. \tag{1}$$

Parity violation associates the decay positron energies in the laboratory frame with the average spin direction of the muon at the time of the decay, such that the highest-energy positrons are preferentially emitted when the muon spin is aligned with its momentum, and lower-energy positrons are emitted when the spin is reversed. The UW system of electromagnetic calorimeters is used to measure the decay positron times and energies, and from these data determine the anomalous spin precession frequency ω_a.

The magnetic field B is measured in terms of the proton's Larmor precession frequency ω_p. The pNMR system developed at UW is critical to this effort. It is further necessary to know the muon distribution in the storage ring for the muon population that contributes to the ω_a data. This distribution is folded with similarly determined azimuthally averaged magnetic field moments to give the effective magnetic field seen by the muons, $\tilde{\omega_p}$ below. One obtains a_μ through the relation

$$a_\mu^{\mathrm{Exp}} = R\frac{g_e}{2}\frac{m_\mu}{m_e}\frac{\mu_p}{\mu_e}, \quad \text{where} \quad R \equiv \omega_a/\tilde{\omega_p} \tag{2}$$

is measured by our collaboration. The electron g_e factor, the muon-to-electron mass ratio, and the proton-to-electron magnetic moment ratio are known to sufficient precision.

Briefly, the experimental data taking proceeds as follows. Compact bunches of 3.1 GeV/c polarized muons are delivered into our 1.45 T superconducting storage ring at a fill rate of $\sim$ 11 Hz. Their intensity, timing, and spatial profiles are measured with UW built T0 and IBMS counter systems. Once inside the ring, muons are deflected on the their first turn onto stable orbits within a defined storage volume by a magnetic outward, pulsed kick. A system of electrostatic quadrupole plates that are charged prior to vertically contain the particles. The positrons from muon decay curl inward where their hit times and energies are recorded in one of the 24 UW-built electromagnetic calorimeter stations. Two calorimeter stations include in-vacuum tracking chambers just upstream of the detectors in order to provide an indirect tomography of the stored muon distribution from tracing the positron trajectories into the storage volume. The magnetic field is monitored continuously by 378 fixed NMR probes built at UW and placed above and below the vacuum chamber. The azimuthally dependent multipolarity of the field is mapped in detail in the storage volume every $\sim$ 3 days using a 17-probe NMR trolley. Representative figures for a subset of the UW-built hardware are shown in Fig. 4.5-2.

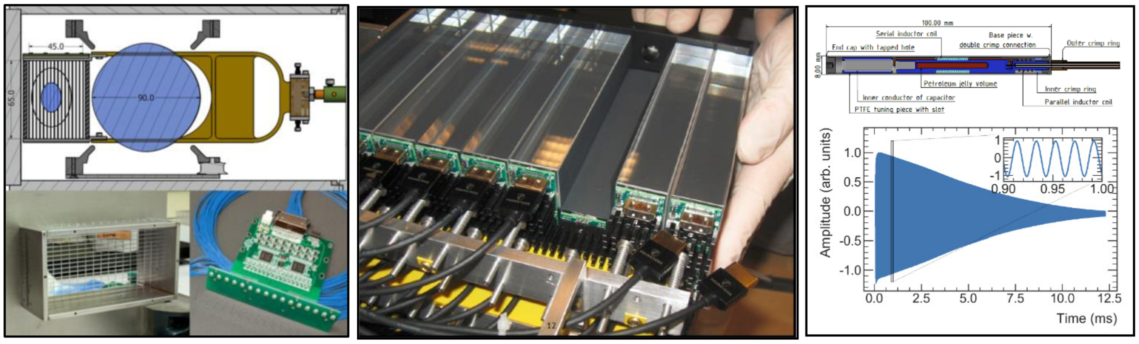

Figure 4.5-2. Representative UW-built hardware images. Left-top: IBMS-3 design; bottom: IBMS-1 detector and electronics. Three IBMS detectors measure the incoming beam intensity, trajectory, and spatial profile. Inner error bars are statistical; outer are total. Middle: Photo of an opened calorimeter showing crystals and SiPM readout. 24 such stations measure the decay positron times and energies. Right-top: An NMR probe used in the fixed and trolley systems; bottom: a typical free induction decay signal (Ref. [16]. 378 probes form the fixed-probe system and 17 are embedded in the in-vacuum trolley.

Notable news and developments

We note that Hertzog led the overall publication process, was lead editor of the PRL and the PR-AB papers, and presented the main results at a special plenary session during the APS April 2021 meeting. Almost all group members have given invited talks, press interviews, or participated in various outreach efforts as a consequence of the result's international interest. Our group's role in the analyses of Run-1 was significant, ranging from the muon precession analyses (Fienberg, Hertzog, Hempstead) to the field analysis (MacCoy, Kammel, Swanson) and to determinations of several of the key corrections to beam dynamics (Binney, Hertzog, LaBounty) and to field transients (Swanson).

The group has had important transitions since our last Annual Report. Jason Hempstead, who was central to the construction, installation, and operations of the calorimeters, finished his Ph.D. in June, 2021. Postdoctoral scholar Zach Hodge joined our group just as the Covid shutdown began. Zach is located at Fermilab and has been an essential personnel there, along with very few others, who are operating the experiment onsite. Research scientist Jarek Kaspar, who contributed enormously to all hardware issues in $g-2$, led the calorimeter development, and was the "go to" trouble shooter on site, was recruited to an exciting position at Siemens Medical Systems. Christine Claessens joined CENPA and is spending 50% of her postdoc time working with Brynn MacCoy and Peter Kammel on the development of a new in-ring, nearly transparent, scintillating fiber based mapping system aimed at providing new insight into beam dynamics issues.

4.6 Updated Clustering Algorithm

H. Binney

Pileup occurs when two positron hits arrive within a short time window in the same calorimeter, leading them to be incorrectly clustered together as a single event. Pileup causes a pull on ω_a, because an incorrectly reconstructed pileup event enters into the ω_a histogram as a single event with energy $E_1 + E_2$, rather than two events with $E1$, $E2$. It is also a rate-dependent effect, meaning that there is more pileup at the beginning of the fill when there are more muons. Therefore, all ω_a analyses apply a pileup correction to subtract as much pileup as possible. Fig. 4.6-1 (left) shows a sample decay positron energy spectrum before and after the pileup correction. Because the stored muons are 3.1 GeV, any decay positron energy above that value is nonphysical and must be pileup.

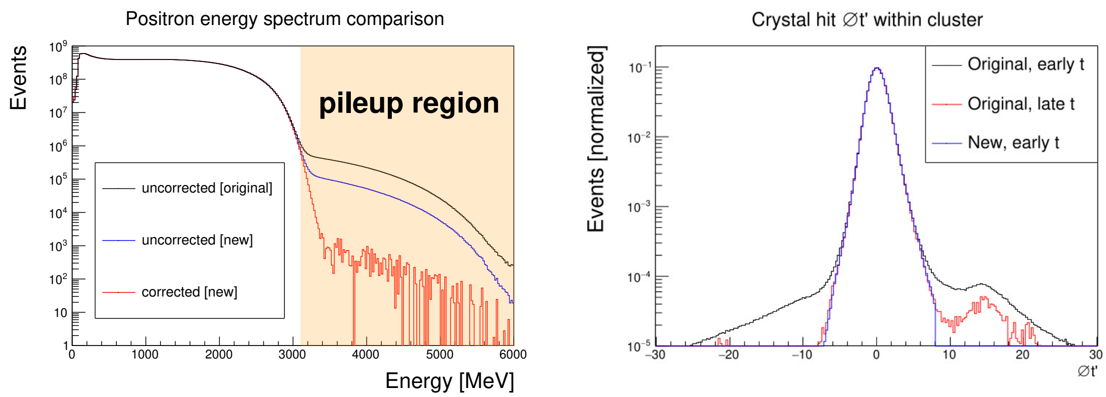

Figure 4.6-1. Left: Comparison of decay positron energy spectra with original clustering (black), new $\Delta t'$ clustering (blue), and a pileup-corrected spectrum (red). Right: $\Delta t'$ distribution within clusters at early times, when pileup is present (black), at late times, when there are singles only (red), and at early times with new $\Delta t'$ clustering (blue).

However, there is still a systematic uncertainty associated with the accuracy of the size and shape of the pileup correction. For the Run-1 UW analysis performed by Aaron Fienberg, the systematic uncertainty due to the pileup was $\approx$50 ppb, higher than the 40 ppb goal set for the final analysis. As more statistics are collected and the statistical uncertainty decreases, improvements should be made to decrease the pileup systematic uncertainty in tandem.

The strategy for decreasing the statistical uncertainty involves improving the time discrimination of the clustering algorithm. The clustering algorithm groups crystal hits together in time in order to gather the full energy deposited by the decay positron. The new algorithm leverages the inherent energy dependence of the time resolution of the crystal hits, which had not previously been incorporated. The timing of low energy hits is known less precisely than the timing of high energy hits, so the former should be given more leeway to be in a cluster than the latter. The original algorithm used a straight Δt metric to determine whether crystal hits should be included in a cluster, where $\Delta t \equiv t_h - t_c$, with t_h the crystal hit time and t_c the cluster time. A new empirical metric was created, $\Delta t'(E_{\text{eff}}) \equiv \frac{\Delta t}{\sigma_{\Delta t}(E_{\text{eff}})}$, where $E_{\text{eff}} \equiv \frac{E_h E_c}{\sqrt{(E_h^2+E_c^2)/2}}$, the effective energy of the crystal hit energy and the cluster energy. The denominator $\sigma_{\Delta t}(E_{\text{eff}})$ weights Δt by an energy-dependent pseudo-time resolution, which is empirically extracted from the time distributions of crystal hits within a cluster.

The effect of replacing Δt with $\Delta t'$ can be seen in Fig. 4.6-1 (right). At early times, there is a high level of pileup, which is evident in the long tails in the high $\Delta t'$ regions outside of the more Gaussian center. At late times, when the distribution is pure singles, the distribution is concentrated towards the center. A $\Delta t'$ window for clustering was chosen to replicate this singles distribution even at early times (in blue). The high $\Delta t'$ bump in the red distribution is due to a small fitting error and is unrelated to pileup.

The new clustering algorithm successfully reduces the pileup in the pileup region by 4x, visible when comparing the black and blue spectra in Fig. 4.6-1. Because of a small spatial dependence induced by the low cluster dead time, the original pileup subtraction routine was no longer as successful. As a result, a new type of pileup correction has to be applied. The pileup subtracted spectrum using the new clustering and new pileup correction can be see in Fig. 4.6-1 (left), in red. This new clustering algorithm is expected to significantly reduce the pileup systematic uncertainty for the ω_a analysis. Calculation of that uncertainty is ongoing.

Using the new clustering and pileup algorithms, a fit can be applied to the full Run-2 dataset, which includes seven sub-datasets (Fig. 4.6-2). This fit is preliminary, but it shows that a good fit can be performed with the new algorithms. The final analysis of the Run-2 and Run-3 datasets will likely be performed using these improvements.

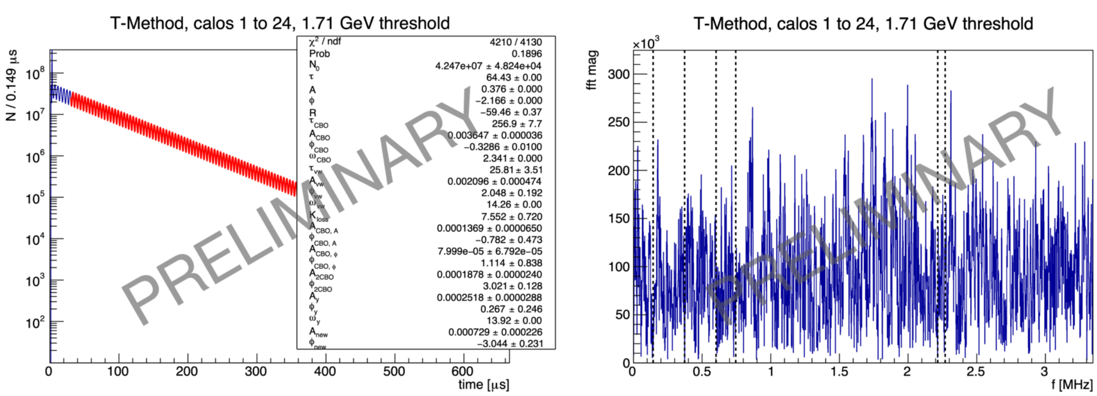

Figure 4.6-2. Left: preliminary fit to full Run-2 statistics using the new clustering and pileup algorithms. Right: FFT of residuals showing flat spectrum.

4.7 Recovering Laser Fills in Run 2+ Data

J. LaBounty

The laser calibration system for the Muon g-2 experiment provides excellent timing stability and gain calibration over the course of the experiment. It is used to correct for in-fill (i.e. O(millisecond)) gain sag due to particle flash at injection, as well as long-term (i.e. day/month) gain drifts due to ambient temperature differences. Special laser configurations are also used to determine extremely short-term (i.e. sub-microsecond) effects due to the recovery time of individual pixels in the SiPMs. Long term effects present a negligible concern to the g-2 analysis. Short term changes in the gain, however, could couple with an energy-dependent phase and introduce a direct bias to our extraction of ω_a and thus to our measurement of $g-2$.

The calibration system measures the in-fill gain dependance for each crystal by firing laser pulses of a known energy into the calorimeters at various times while muons are in the ring. By comparing the known laser energy to what is reconstructed at time t in the 700 μs fill, the gain response for each one of the 1296 PbF_4 crystals can be mapped. For a subset of fills (1/9 of them in Run 1, 1/11 in Runs 2-3, and 1/11 - 1/22 in Run 4), 3 laser pulses separated by $\approx 200\mu s$ are fired into each of the crystals. A diagram of this pulse structure can be seen in Figure Fig. 4.7-1.

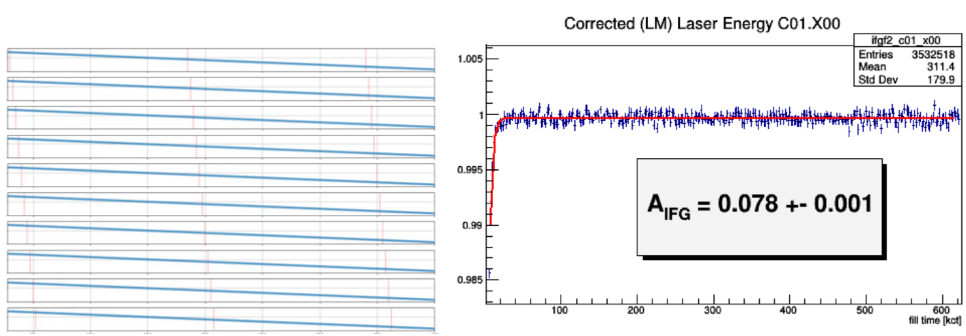

Figure 4.7-1. Left: Schematic showing the structure of the in-fill laser pulses for various fills. The 3 laser pulses per fill walk forward coherently to map out the gain function for the entire $700\mu s$. Right: Measured gain sag for one crystal.

During the Run 1 analysis, it was decided that the subset of fills "contaminated" with laser pulses would be excluded from the analysis. The reason for this was the worry that measurement of the gain at time t could introduce some perturbation to positron energies measured at $t+\delta$. The purpose of this study was to determine whether such an effect existed, and if so to quantify the magnitude of the effect and develop a strategy for mitigation.

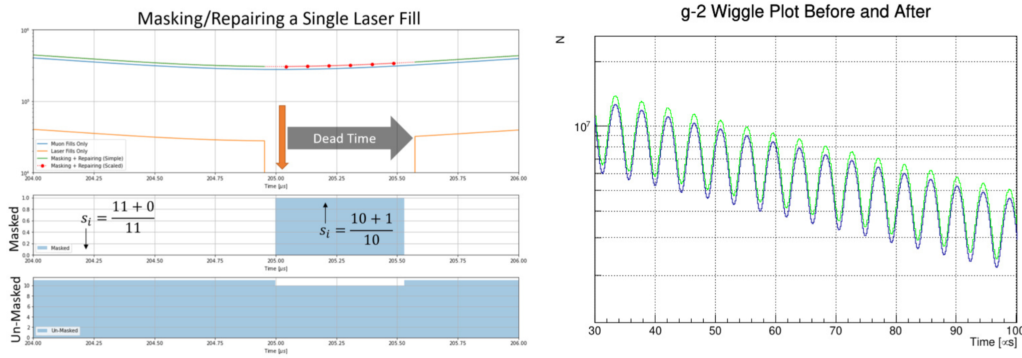

Figure 4.7-2. Left: Diagram showing the masking/repair strategy for including laser pulses in the main g-2 analysis. The scale factor gets diluted as more fills with different laser timings are combined. Right: Wiggle plot before and after this correction, showing the increase in statistical power including these fills affords us: 4,604,947,699 positrons vs. 4,186,732,387.

Since only 3 laser pulses were introduced into each "contaminated" fill, the subset of data which might be affected by the laser in any given sample is quite small. Even if we assume the worst case scenario that the data for the entire 50 $c.t. \approx 62.5\ ns$ SiPM pixel recovery time is untrustworthy, that leaves the vast majority of the 700 μs fill uncontaminated. However, since this window of suspect data moves through the fill, we cannot simply mask the region of data in the final fit. Instead, we adopt a fill-by-fill masking and repairing procedure. For each fill, we identify the time of the laser pulse on a calo-by-calo basis. We then mask, for that fill, any bin which overlaps with our chosen artificial dead time. The number of fills in which bin i is masked (N_{i-m}) and un-masked (N_{i-um}) are tracked and used to construct a scale factor to repair the main analysis histogram like so:

$$s_i = \frac{N_{i-m} + N_{i-um}}{N_{i-um}} \tag{1}$$

$$N_i^{'} = s_i * N_i \tag{2}$$

$$\delta N_i^{'} = s_i * \sigma N_i = s_i * \sqrt{N_i} \tag{3}$$

where N_i are the bin contents and δN_i are the bin errors, which are each inflated beyond their nominal Poissonian value by the same scale factor. Figure Fig. 4.7-2a shows a diagram of this procedure being applied to a single 11-fill laser cycle and Figure Fig. 4.7-2b shows a wiggle plot before and after the application of this procedure. The increase in statistics corresponds to the additional fills (for Run-2, we increase our statistical power by a factor of 11/10).

Since this procedure is designed to identify the presence of a bias to the extraction of ω_a, it is important that we first verify that it does not itself introduce such a bias. We do this by applying this procedure to data which does not contain any laser pulses and performing a comparison to the fit results and FFTs from the un-altered data. We can also increase the size of any bias to the fit by changing the artificial pre-scale factor from 1/11 to 1/2. We did not identify any bias to the fit parameters from applying this procedure to uncontaminated data. We record an increase in the errors on the fit parameters due to the inflation of the errors on the masked bins.

Comparisons were made to the laser fill data in Runs 2C and 2D, representing a combined 11878603 muon fills and $\approx$ 108000 laser fills (the final amount included in fits will be altered by data quality control). For these datasets, a typical scale factor was: $s_i \approx 1 + O(10^{-3})$. Fits for ω_a were performed to:

- Muon Fills Only (this was the configuration used for the published Run-1 results)

- Muon + Laser Fills (Masked + Repaired)

- Muon + Laser Fills (Un-Masked, Naively Combined)

Results of these fits can be seen in Fig. 4.7-3. From this figure, we can see that the addition of the laser fills changes the extracted R value by ≈ 0.4 *ppm* and decreases the uncertainty on the extracted value from ≈ 0.632 *ppm* $\rightarrow 0.603$ *ppm* in the case of Run 2C. We can also compare the masked (orange) and naively combined (green) points for both of these datasets. In both cases, we identify no biases in the extracted R value of the combined muon+laser fills out to a dead time of $300c.t. \approx 375$ *ns*, well past the short term recovery time of the crystals from a single hit. We also observe that, while the shift in R is large from the blue points to the green/orange, the direction of the shift is different for Runs 2C and 2D. Plotting the R value extracted from the laser fills alone (1/11 of the total data) vs. random subsets of the muon fills of the same size also indicates that this difference falls within the spread of reasonable R values. Because of this, we conclude that there is no systematic bias from including the laser fills. It is our recommendation to the g-2 collaboration as a whole that the muon fills be included in an analysis without this masking procedure, with the masking employed as a cross check to place a limit on any systematic error. From this study, we estimate the size of such a systematic error to be < 5 *ppb* per dataset. A full analysis of the Run-2+ data will yield a final number before publication.

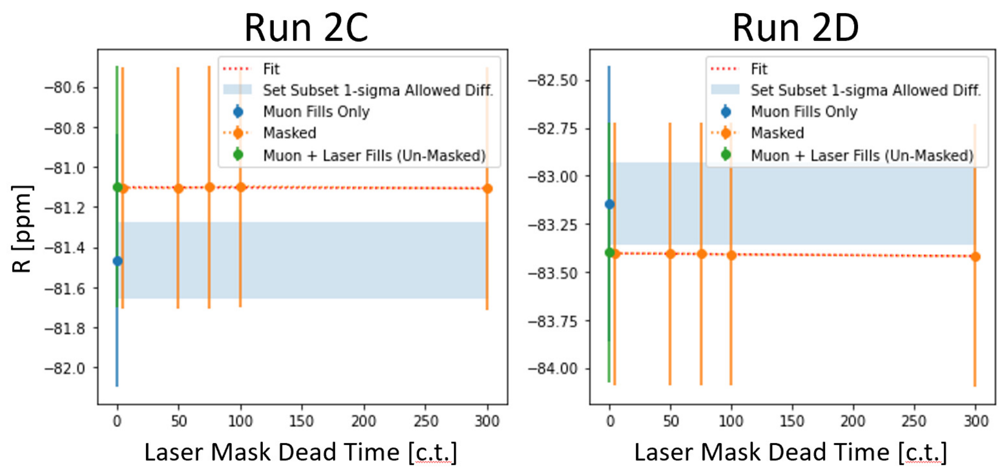

Figure 4.7-3. Fit results for the muon fill only data (blue), un-masked laser data (green), and masked/repaired laser data (orange). A sweep of the laser mask dead time shows no significant bias to the extracted R value from this procedure.

4.8 The muon weighted magnetic field in Run 1

P. Kammel and B. K. H. MacCoy

The anomalous precession frequency for magic-momentum muons with no vertical betatron oscillation is $\omega_a = -\frac{q}{m} a_\mu \tilde{B}$. ($\omega_a$ is corrected for these assumptions separately.) $\tilde{B}$ is the magnetic field experienced by the muons which enter the ω_a measurement. The muon-weighted field $\tilde{B}$ is calculated by weighting the field map by the muon distribution and averaging over space and time. For a given time interval, $\tilde{B} = \int_V B(x, y, \theta) M(x, y, \theta) dx\, dy\, d\theta$, where the field map B and the muon probability density M are expressed in ring coordinates; x is radial relative to the ring design radius, y is vertical relative to the ring midplane, and θ is the ring azimuth. Because M can drift on timescales of hours, $\tilde{B}$ is calculated in time intervals $T \approx 3\,\text{h}$ before taking the decay-positron-weighted average over longer run periods.

Magnetic field: The magnetic field B is measured with CENPA-built NMR probes. The field inside the muon storage region is periodically mapped with a probe trolley, and the field drift is monitored with fixed probes just outside the storage region. The field drift is then used to interpolate the field map to intermediate times. B is considered constant during each fill and is interpolated in 2 s intervals, then weighted by decay positron count and averaged over each T interval. The 2D field map $B(x, y)$ (Fig. 4.8-2) is expanded in a multipole basis parameterized by multipole moments m_n; the azimuthal map consists of θ-binned 2D moments.

Muon distribution: The muon distribution varies as a function of θ due to the ring guide fields. Trackers reconstruct the beam at two azimuthal locations. Tracker profiles are treated as constant and integrated over the time of the fill ($\sim 1\,\text{ms}$), then accumulated over each T interval. The muon distribution is extrapolated around the ring (Fig. 4.8-1) by shifting and scaling the tracker profiles using θ-dependent beam dynamics information. The equilibrium radius is off-center due to the under-performing kicker (Fig. 4.8-2), and varies with θ due to the dispersion (the off-momentum muon trajectory). Closed orbit distortions due to a θ-varying magnetic dipole moment shift the radial mean away from equilibrium. The vertical mean position is zero in the absence of a radial magnetic field. The RMS widths are determined from beam optics functions obtained from a model of the ring fields.

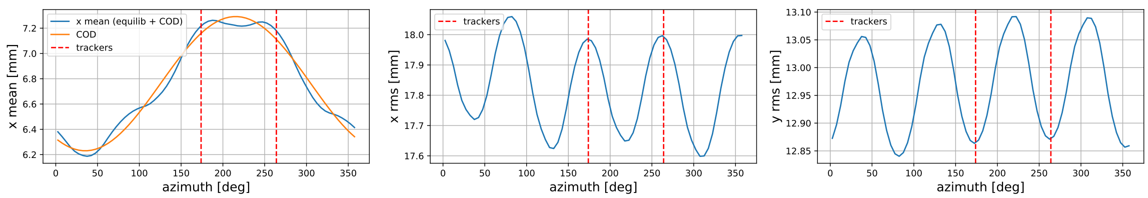

Figure 4.8-1. Example reconstructed muon distribution as a function of ring azimuth. Red dashed lines indicate the two tracker locations. Left: The x mean (blue) is distorted away from equilibrium by the closed orbit distortion (orange). Middle and right: The x and y RMS widths vary with azimuth due to beam optics.

<u>**Muon weighted field**</u>: The muon-weighted field $\tilde{B}$ is calculated by weighting the field multipole moments m_n by the beam multipole projections k_n, which give the fractional contribution of each moment.

$$\tilde{B} = \sum_{n=0}^{4} m_n k_n \tag{1}$$

Because the Run 1 standard field analysis produced θ-averaged moments, $\tilde{B}$ was calculated from θ-averaged moments, then corrected for azimuthal interference between the field map and the muon distribution. The dominant contributions to $\tilde{B}$ were from the normal quadrupole (m_1, corresponding to a radial gradient) and normal sextupole (m_5, corresponding to a quadratic distribution) moments due to the characteristic radial asymmetry of the muon distribution. Typical beam projections were $k_1 = 0.15$ and $k_5 = 0.10$.

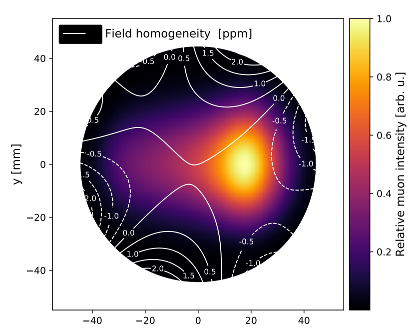

Figure 4.8-2. Example azimuth-averaged muon distribution overlaid with azimuth-averaged field map contours.

Muon weighting systematics were evaluated in several categories related to the muon distribution, shown in Table 4.8-1; these exclude field-specific systematics. The dominant source of uncertainty was tracker misalignment, which may be reduced in future runs with smaller multipole moments and improved alignment verification.

	correction [ppb]	uncertainty [ppb]
Tracker and calo effects	-	9 to 20
Closed orbit distortion effects	+1 to +2	5
In-fill time dependence effects	−1 to −4	-

Table 4.8-1. Run 1 systematic corrections and uncertainties on the muon-weighted field. Ranges are given when values vary among the four Run 1 datasets.

4.9 In-vacuum NMR probes

T. Burritt, S. Charity*, S. Corrodi†, P. Kammel, B. Kiburg*, B. MacCoy, D. Peterson, R. Roehnelt, and H. E. Swanson

The fixed probe system continuously monitors the magnetic field in the muon g-2 storage ring at Fermilab. It includes 378 NMR probes embedded in the storage ring vacuum chambers in groups spaced each 5 degrees in azimuth around the ring. Some probes in the inflector vacuum chamber experience large field gradients with reduced precision in field measurements. Moving these probes to lower gradient regions requires removing the vacuum chamber and physically extending the grooves in which the probes are mounted. We decided instead to add 13 additional probes inside the chambers where the field is more homogeneous. Our NMR probes were designed to operate at atmosphere and need to be enclosed in hermetically sealed containers when placed in the high vacuum storage ring volume. This article describes the design of these in-vacuum containers.

Materials were chosen for both low outgassing and low magnetic susceptibility properties. The field measurement trolley passes in close proximity to the added probes and any increased field perturbations interfere with trolley measurements. In addition sealed in-vacuum probes need to spend many months in the storage ring vacuum without loss of air in the enclosed volume. Spare trolley NMR probes were used without modification so they could be retrieved intact if needed as replacements. This motivated a design with non-destructive access to the probe.

The outer shell uses a 12 inch length of $\frac{1}{2}$ inch diameter PEEK tubing. This was bored out to $\frac{3}{8}$ inch diameter to accommodate the NMR probe and signal cable. Each end of the tube has a machined o-ring surface and threads for end caps which seal the enclosed volume. The end caps are made from aluminum and have an o-ring groove and threads to attach to the shell. One of these is shown in Fig. 4.9-1 which also has the signal feedthrough for connecting to the NMR probe. A campaign was undertaken at the precision test magnet at

*Fermi National Accelerator Laboratory.
†Argonne National Laboratory.

Argonne National Laboratory to determine magnetic properties of connectors and adaptors commercially available that were specified as non-magnetic. Parts were moved past an NMR probe with closest approach matching the trolley's path at Fermilab and field perturbations were measured. Of the many bulkhead feedthrough adapters tested we were unable to find any that had small enough magnetic footprints. Only a few connectors meant for coax cables were deemed acceptable to be in close proximity to the trolley.

Custom feedthrough adapters were constructed using the SMA and SMB cable connectors found to be sufficiently non-magnetic. A short length of copper semi-rigid coax was inserted in a hole drilled in the aluminum end cap and sealed with TorrSeal epoxy. The connectors were soldered on each end of the copper coax. The feedthroughs were Helium leak tested and those with leak rates below 1.0×10^{-8} Atmosphere $\cdot$ cm^3/sec were used in assembling the probe shells. The complete feedthrough adapter is shown in Fig. 4.9-1 connected to an NMR probe within the PEEK shell.

Figure 4.9-1. Photo of our custom end cap showing the signal feed through connected to an NMR probe within the PEEK tube. A short length of semi-rigid coax epoxied in the aluminum end cap with TorrSeal has connectors soldered on each end. The end cap screws into threads machined in the tube and seals the enclosed volume with an o-ring. A second end cap without the feedthrough seals the other end of the tube.

4.10 Muon g-2 experiment operations

Z. Hodge

Run4 Operations

The Muon g-2 experiment over the last year has continued with operations and the collection of high quality physics data thanks to support from laboratory management and collaboration members. The beginning of Run4 in late 2020 saw the fastest ever startup for the experiment, with first beam achieved on 4 December and the official start of production data taking on 15 December. Run4 operations began with shift members splitting responsibilities between onsite and remote personnel, but due to ongoing pandemic safety concerns, this quickly transitioned to an all remote operation of the experiment. Luckily, the experiment was well prepared from previous improvements to the DAQ and hardware device control being already remote operable, along with a robust web-based data quality monitoring suite. In mid February, a power supply module for the inflector magnet failed, leading to a two-week downtime for inspection and repairs. Additionally, the cryogenic cooling system for the experiment's superconducting magnets experienced significant reliability issues throughout Run4, limiting the number of days between trolley runs and requiring the main ring magnet to be ramped down for cryo-system maintenance. Nevertheless, Run4 achieved the most number of decay positrons collected from any single run in Muon g-2 history, with a total across all four runs now over 12 times that collected by the Brookhaven experiment. The fraction of BNL equivalent collected in Run4 and the total collected over the last four runs are shown in Fig. 4.10-1.

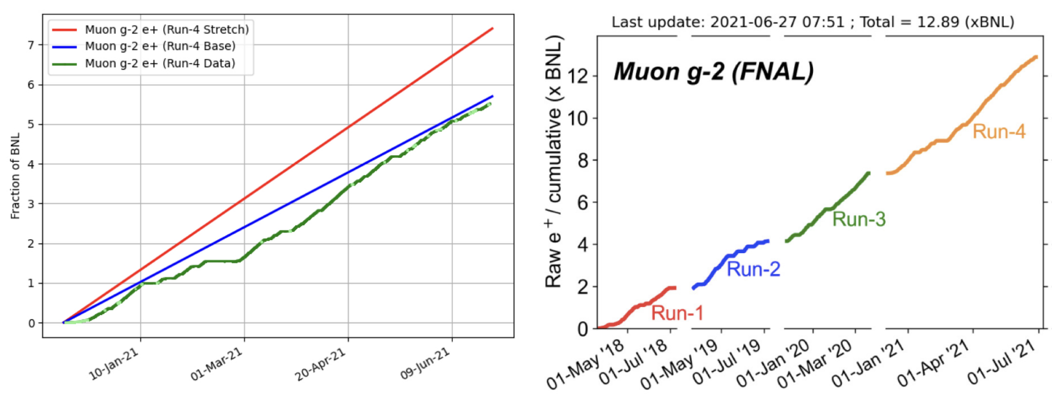

Figure 4.10-1. Left: The fraction of BNL positrons collected during Run4. Right: The cumulative fraction of positrons collected over all runs.

DAQ Upgrades

The summer 2020 shutdown provided the opportunity to update and upgrade much of the data acquisition system's computing software. This included an operating system update from SLF6 to SLF7 for all computer systems, transition of python scripts from v2.7 to the now standard v3.6, and an upgrade to the latest version of MIDAS with an increased use of C++ . The fast frontend programs for all AMC13s have been multi-threaded, providing each frontend their own independent execution thread. The slow control frontends for all of the 24 calorimeters and μTCA crates have been consolidated to a single multi-threaded frontend for each. New diagnostics pages were created to monitor thread activity and buffer management for the AMC13, CaloSC, and μTCA frontends. All of these upgrades and improvements led to a increased DAQ stability and reliability, achieving a better than 96% up-time for the whole of Run4. The DAQ uptime throughout Run4 is shown in Fig. 4.10-2

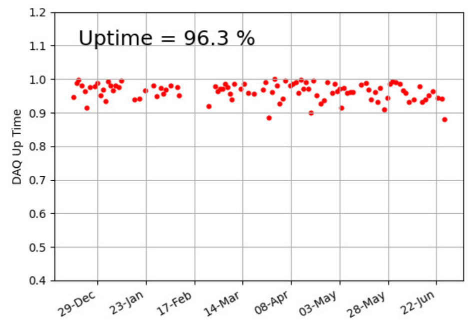

Figure 4.10-2. Muon g-2 DAQ uptime throughout Run4.

Detector Maintenance

During Run4, some components of the calorimeters systems began to show their age. In particular the HDMI cables delivering slow control communication and bias voltage to the SiPMs in several detectors experienced intermittent or complete connection loss. This often required intervention in the form of opening the calorimeter enclosure and either reseating the connector or replacing the cable completely. In mid February 2021, calorimeter 5 lost all signal to a SiPM located in a critical region of the detector, ultimately requiring a tear-down and replacement of that PbF_2 crystal+SiPM assembly during an opportune downtime. During the shutdown period following Run4, additional debugging was conducted on calorimeter 9, which had been exhibiting slow gain drifts during the run. This was found to be due to a faulty Megabox (RC-circuit for bias voltage recovery), that was subsequently replaced. Also during the shutdown, calorimeter 11 required the replacement of a crystal assembly due to complete signal loss. The crystals that were necessary to remove during the repair are shown in Fig. 4.10-3. In September 2021, a position survey of the crystal faces and parting planes on the radially outer most side of six calorimeters (upstream and downstream of both tracker stations and calorimeters 1 and 2) was conducted by Fermilab's Alignment and Metrology Department. Photographs taken during this survey measurement campaign are shown in Fig. 4.10-4. The analysis of this data is still on-going, but it will hopefully provide better insight on beam dynamics in the storage ring.

Figure 4.10-3. Left: PbF_2 cystal+SiPM assemblies removed from calorimeter 11. Right: Remaining crystals during calorimeter 11 replacement operation.

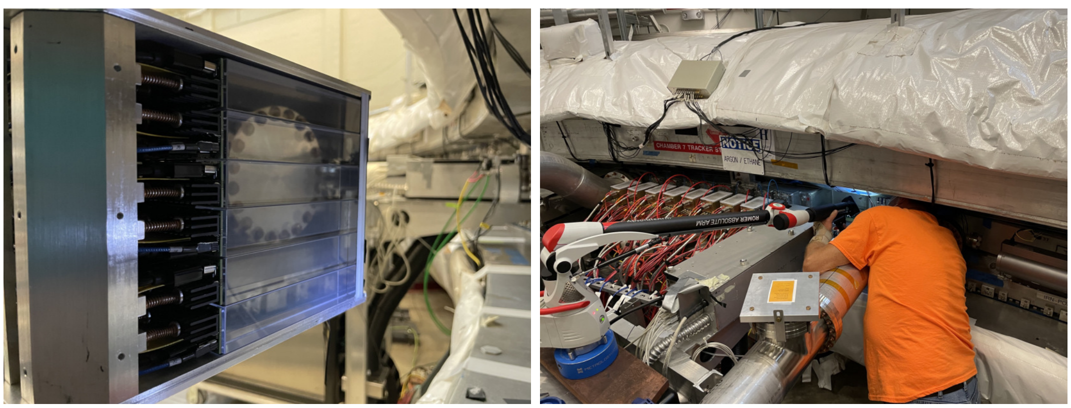

Figure 4.10-4. Left: Radially outer crystal faces as measured during the survey. Right: Alignment and Metrology team surveying calorimeter crystal faces.

Run5 Startup

The experiment is currently at the start of Run5, which will begin in early November 2021. This is following a delayed start due technical complications involving the experimental hall building's electrical infrastructure. The automatic transfer switch that is responsible for switching the building's electrical connection from the Fermilab site's electrical network to a local backup generator in the event of power loss failed during a routine test. Repair and replacement of this device has been problematic, resulting in nearly a month of downtime. During this period, studies for the beam delivery to the Mu2e experiment have taken place that were otherwise scheduled for later in the run, with hopefully no significant loss of beam time for Muon g-2 data production. As Run5 at Muon g-2 begins, we are planning for a successful data taking period, bringing us even closer to achieving the experiment's ultimate sensitivity to the anomalous magnetic moment of the muon.

4.11 Rare Pion Decays: PIONEER

D. W. Hertzog, Z. Hodge, P. Kammel, J. LaBounty, and R. Roehnelt

Lepton flavor universality (LFU) simply requires that the weak force is the same for e, μ and τ leptons. Our MuLan experiment [5] measured the muon lifetime to a precision of 1 ppm, which determined the Fermi Constant G_F to 0.5 ppm, through the understanding that G_μ is identical to G_F because of LFU. It is fair to ask, how solid is this assumption? In 1999, Marciano raised the issue [6] and more recently Crivellin and Hoferichter [7] explored how LFU violation might be the root cause of the $> 3\sigma$ tension in the Cabibbo-Kobayashi-Maskawa (CKM) quark-mixing matrix first-row unitarity relation. A persistent pattern of large LFU violations in B decay channels also exists beyond Standard Model expectations, perhaps with a different underlying cause. Finally the $> 4\sigma$ significance between the measured and calculated values for the muon anomalous magnetic moment is yet another hint at new physics that might be related to lepton flavor. Our group has been working with others to develop a next-generation rare pion decay experiment that can contribute significantly to both LFU violation tests and CKM unitarity. We call this new collaboration "PIONEER."

Our first priority is to measure the charged-pion branching ratio to electrons vs. muons, $R_{e/\mu}$, which is extremely sensitive to new physics at high mass scales. The proposed detector system – appropriately upgraded for rate – can also be used to measure pion beta decay, $\pi^+ \to \pi^0 + e^+\nu_e(\gamma)$, and other rare decays. Order of magnitude improvements in sensitivity to these reactions will probe LFU at an unprecedented level, determine V_{ud} in a theoretically pristine manner, and test CKM unitarity at the quantum loop level.

Regardless of specific new-physics models, these experiments are well motivated. The $R_{e/\mu}$ ratio,

$$R_{e/\mu} = \frac{\Gamma\left(\pi^+ \to e^+\nu(\gamma)\right)}{\Gamma\left(\pi^+ \to \mu^+\nu(\gamma)\right)} \tag{1}$$

was calculated to extraordinary precision within the Standard Model by Cirigliano and Rosell [8], obtaining $R_{e/\mu}\,(\mathrm{SM}) = (1.2352 \pm 0.0001) \times 10^{-4}$. The PDG experimental average $R_{e/\mu}\,(\mathrm{Exp}) = (1.2327 \pm 0.0023) \times 10^{-4}$ is in fair agreement with the SM but more than 20 times less precise. The $R_{e/\mu}$ ratio can be interpreted as a test of e–μ universality; the current ratio leads to the relation $g_e/g_\mu = 0.9990 \pm 0.0009$. The large gap in precision between experiments and theory represents a discovery opportunity.

Basics for a new measurement of $R_{e/\mu}$

At rest, the pion lifetime is 26 ns and the muon lifetime is 2197 ns. The monoenergetic positron from $\pi \to e\nu$ has an energy of 69.3 MeV. Positrons from ordinary muon decay form the Michel

[5] Phys. Rev.Lett. 106, 041803, Phys. Rev.D 87, 052003, and previous Annual Reports.
[6] Phys. Rev.D 60, 093006.
[7] Phys. Rev. Lett. 127, 071801.
[8] Phys. Rev.Lett. 99, 231801.

spectrum from 0 to an endpoint of 52.3 MeV. The monoenergetic e^+ is well above that Michel endpoint and can be easily identified using a high-resolution, hermetic calorimeter. However, counting all $\pi \to e$ events with a precision at a few parts in 10^4 requires determining the low-energy tail of the shower that hides under the Michel spectrum from the $\pi \to \mu \to e$ chain, which has several orders of magnitude higher rate. That challenge was critical to previous generations of these experiments and is responsible for the leading systematic uncertainty in the most recent complement – PIENU at TRIUMF and PEN at PSI – for different, but related technical reasons. We are designing an experiment that follows the PEN approach with a 3π geometric acceptance calorimeter, but with a much greater radiation length, 28 compared to their 12. Simulations show this alone reduces the tail fraction by several orders of magnitude. At present, we are exploring a high-resolution liquid xenon calorimeter, following the work of the MEG Collaboration. We are also examining various crystal geometries involving L(Y)SO and possibly reusing PEN CsI crystals as an outer tail-catching layer.

A better calorimeter alone is not enough. It is important to be able to create triggers that can isolate $\pi \to e$ from $\pi \to \mu \to e$ chains within the stopping target, including pion and muon decays in flight, as well as identify pileup from long-lived muons remaining in the target from earlier pion stops. To achieve these goals we will use an active target (ATAR) that can provide 4D tracking (at the level of 150 μm in space and 100 ps in time) and energy measurements from the 30 keV (MIP) signals for electrons to the 4000 keV Bragg peaks of stopping pions and muons. Our collaboration is focusing on the new LGAD (low-gain avalanche diode) sensors as a centerpiece of the experiment.

The experiment will require a 75 MeV/c continuous wave pion beam with different characteristics for the two physics channels: 0.3 MHz with $\delta p/p \sim 1\%$ for $\pi \to e\nu$, and $\geq$10 MHz with $\delta p/p \sim 3\%$ for $\pi \to e\pi^0\nu$. These beams exist at PSI. We will need to deploy detector systems to image and trigger the arrival of pions into the ATAR. Because of the high data rate, state-of-the-art triggering, fast digitizing electronics, and high bandwidth data acquisition will be required.

The developing PIONEER Collaboration is drawn from physicists having considerable experience in experimental precision physics, together with leading theorists who are carefully articulating the goals to maximize scientific impact. Member groups led previous generation rare pion decay experiments (PIENU, PEN and PiBeta), rare kaon decay experiments (BNL-E787/E949 and CERN NA62), stopped muon experiments (MEG, MuLan, MuCap and MuSun), and Fermilab Muon $g-2$. The group has expertise in all of the technical areas listed above.

Hertzog and Kammel hosted the pion/muon session at the Developing New Direction in Fundamental Physics workshop[1] at TRIUMF in 2020 This session led to the formation of a larger working group, initiated design work at UW, simulation studies by various group members, and provided a physics motivation for the UCSC group who had been exploring new LGAD detector technology. In Spring 2021 we submitted a detailed Letter of Intent (S2127LOI, Bryman, Hertzog, Mori spokespersons) to TRIUMF's Experimental Evaluation Committee outlining the program described in this section. Although well received scientif-

[1] https://meetings.triumf.ca/event/89/

ically, there is no technical path at TRIUMF to the realization of the needed intense pion beamline that now does not exist. Our focus has turned to PSI where two beamlines already exist and where many of us have considerable experience.

On the technical side, Kammel and Roehnelt designed the complex stopping target region and a conceptual LXe calorimeter for the LOI; both are shown in Fig. 4.11-1. Hertzog is exploring the L(Y)SO options based on our lab's experience in building the PbF2 calorimeter arrays for $g-2$. Our group is hosting weekly collaboration working meetings. We are devoting a fraction of our group's research time to simulation studies and plans going forward for component prototype tests and to the preparation of a proposal for PSI. Kammel has been working closely with the UCSC group to help direct their unique ATAR R&D targeted toward the specific PIONEER requirements. He is also developing plans for test beam measurements at CENPA using our Van de Graaff's Rutherford Backscattering (RBS) technique, which can provide heavy, slow protons into the ATAR planes to mimic stopped pions or muons.

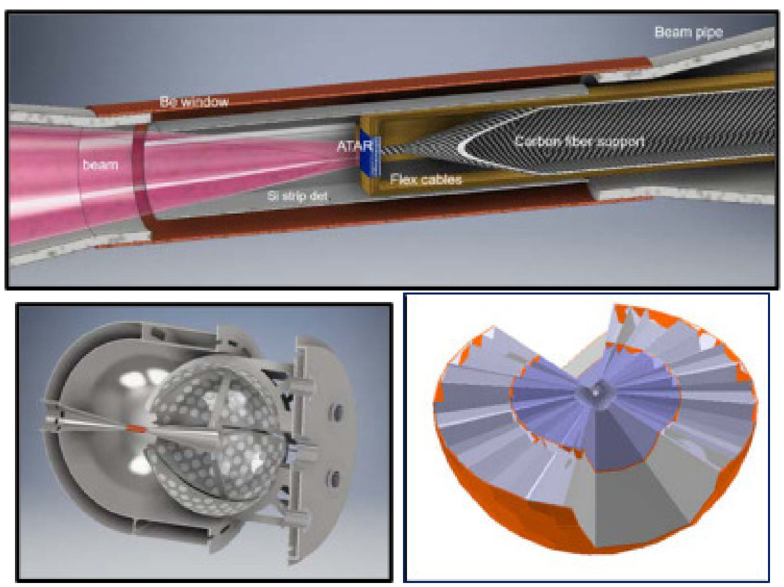

Figure 4.11-1. UW engineering designs of the pion stopping region (top) including the active target (ATAR), flex cable signal transport, carbon structural support, and a Be beam pipe. This region mates with the UW preliminary design concept for a LXe calorimeter with SiPM readout, as seen is an exploded view (bottom left). The bottom half of an alternative crystal calorimeter (bottom right) made of an inner L(Y)SO layer (blue) and an outer CsI layer (gray) from the existing PEN detector is shown.

As an example of recent simulation work, LaBounty built a `Geant4` model to evaluate the performance of the LXe and L(Y)SO calorimeters with respect to pileup, based on our experience with $g-2$. Using the `CENPA-Rocks` computing cluster, large numbers of simulated decays are stored and analyzed. These scintillation time spectra are histogrammed and used to build an average pulse template, Fig. 4.11-2(left), whose shape has been shown to be independent of energy. The middle panel of Fig. 4.11-2 shows a fit to a single event using the template, while the right panel shows examples of successful fits to a variety of pileup events.

This template fitter is robust against pileup over a broad range of energies. Initial results show that the energy and timing reconstruction is very good for pulses where $\delta t_{peak} \geq 5\,\mathrm{ns}$ without any spatial information being incorporated into the fit. Peak amplitudes are reconstructed to the sub percent level. Further studies are underway to determine the impact of noise on the reconstruction, robustness with respect to more realistic geometry effects, and to eventually incorporate spatial information into the pileup identification algorithm.

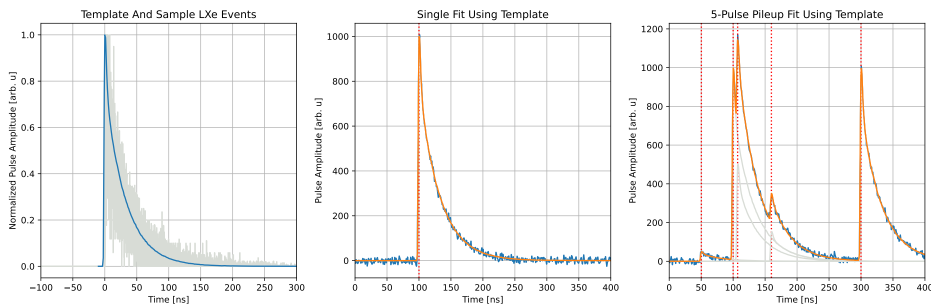

Figure 4.11-2. Template fitting in the simulated LXe calorimeter. Photons arriving on the photosensitive outer shell are used to construct a pulse shape template (left). This template is used as part of an iterative χ^2 fitting procedure to determine the energy deposition in the calorimeter and identify pileup events. Fits with a single pulse (center) and multiple pulses (right) can be seen.

5 Dark matter searches

ADMX (Axion Dark Matter eXperiment)[1]

5.1 The ADMX Experiment

C. L. Bartram, T. Braine, R. Cervantes*, N. Crisosto, N. Du†, M. Guzzetti, C. Hanretty, S. Kimes‡, G. Leum, T. Nitta, L. J Rosenberg, G. Rybka, J. Sinnis, and J. Yang§

In recent years, the Axion Dark Matter eXperiment (ADMX) has become the most sensitive axion haloscope: an experimental technique first proposed by Pierre Sikivie in 1983[2] as a method of detecting "invisible" axion dark matter in the galactic halo. Axions are a particularly well motivated dark matter candidate, due to their ability to "clean up" two outstanding problems in physics.

The first of the two has to do with particle physics: the strong CP problem. The Quantum Chromodynamics (QCD) Lagrangian has a term[3] (Equation 1) which explicitly violates CP-symmetry for a non-zero value of θ.

$$L_\theta = \theta \frac{g^2}{32\pi^2} F^a_{\mu\nu} \tilde{F}^{\mu\nu a} \tag{1}$$

One consequence of CP-violation should be the observance of the neutron electric dipole moment (nEDM). However, experimental results[4] have shown a nearly non-existent nEDM ($\mathcal{O}(10^{-26})$ e·cm). This requires θ to be unnaturally small ($\theta < 5 \times 10^{-11}$), presenting an example of a "fine-tuning" problem.

A popular solution to the strong CP problem was presented by Peccei and Quinn in 1977[5] in the form of a new $U_A(1)$ symmetry. Under this new symmetry θ is a dynamic field, as opposed to a tunable parameter, which naturally relaxes to zero. The spontaneous breaking of this symmetry (in addition to a small, explicit symmetry violation) leads to the production of a pseudo-Goldstone boson, namely the axion[6,7].

---

*Presently at Fermilab, Batavia, IL

†Presently at Lawrence Livermore National Laboratory, Livermore, CA

‡Presently at Microsoft Quantum, Microsoft, Redmond, WA

§Presently at Pacific Northwest National Laboratory, Richland, WA

[1] ADMX is supported by the DOE Office of High-Energy Physics and makes use of CENPA resources by recharge to the cost center.

[2] P. Sikivie, Phys. Rev. Lett. **51**, 1415 (1983).

[3] B. Brubaker, arXiv:1801.00835.

[4] C. Abel et al., Phys. Rev. Lett. **124**, 081803 (2020).

[5] R.D. Peccei and H. Quinn, Phys. Rev. Lett. **38**, 1440 (1977).

[6] S. Weinberg, Phys. Rev. Lett. **40**, 223 (1978).

[7] F. Wilczek, Phys. Rev. Lett. **40**, 279 (1978).

The second of the two problems is, of course, the dark matter problem. Dark matter comprises the vast majority ($\sim 85\%$) of the matter content in the universe[1], yet its true nature remains a mystery. There are a number of candidates for solving the dark matter problem, including astrophysical objects such as primordial black holes, other theorized particles such as WIMPs, as well as modified theories of gravity. Axions, in addition to solving the strong CP problem, naturally account for the entire observed dark matter density given an appropriate mass. In the scenario where PQ symmetry breaks after cosmological inflation, the mass range of interest[2] is $\mathcal{O}$ (1 - 100) μeV.

ADMX searches for dark matter axions within the lower end of this mass range using a microwave resonant cavity inside a large magnetic field, that is to say, an axion haloscope. Axions themselves are very weakly coupled to matter, however they naturally decay into two microwave photons, which are much easier to observe. However, the lifetimes of dark matter axions with masses on the order of $\mathcal{O}$ (1 - 100) μeV have been found to be greater than the age of the universe itself[3], which is problematic for taking advantage of this decay process. This is where the haloscope design becomes useful.

Maxwell's equations, after being modified to include the axion-photon interaction, show that in the presence of an external static magnetic field, this decay process is stimulated, producing microwave photons of frequency E/h. Here, E is the sum of the axion rest mass (m_a) and its (relatively small) kinetic energy, and h is the Planck constant. When the cavity resonator is tuned to match the axion's frequency of oscillation, the axion to photon conversion signal strength is greatly enhanced, allowing us to detect so-called "invisible" particles.

The two primary models for the axion are the Kim-Shifman-Vainshtein-Zakharov (KSVZ)[4,5] and the Dine-Fischler-Srednicki-Zhitnitsky (DFSZ)[6,7] models. While many find the DFSZ axion to be more compelling due to its compatibility with Grand Unified Theories, it is an order of magnitude more weakly coupled to photons than its counterpart, making it more elusive to experimentalists. To date, ADMX is the only experiment of its kind to reach DFSZ sensitivity.

The ADMX haloscope (Fig. 5.1-1) is comprised of a 136 liter cylindrical, copper-plated, resonant microwave cavity embedded inside a superconducting solenoid that produces a magnetic field of $\sim$ 7.6 T. Inside the cavity are two copper plated tuning rods which can rotate from the walls to the center of the cavity, altering the cavity's geometry and thus its resonant frequency.

---

[1] P.A.R. Ade et al., Astron. Astrophys. **571**, A16 (2014).
[2] E. Berkowitz, M. I. Buchoff, and E. Rinaldi, Phys. Rev. D **92**, 034507 (2015).
[3] I.Stern, AIP Conf. Proc. **1604**, 456 (2014).
[4] J.E. Kim, Phys. Rev. Lett. **43**, 103 (1979).
[5] M.A. Shifman, A.I. Vainstein, and V.I. Zakharov, Nucl. Phys. **B166**, 493 (1980).
[6] M. Dine, W. Fischler, and M. Srednicki, Phys. Lett. **B104**, 199 (1981).
[7] A.R. Zhitnitsky, Sov. J. Nucl. Phys. **31**, 260 (1980).

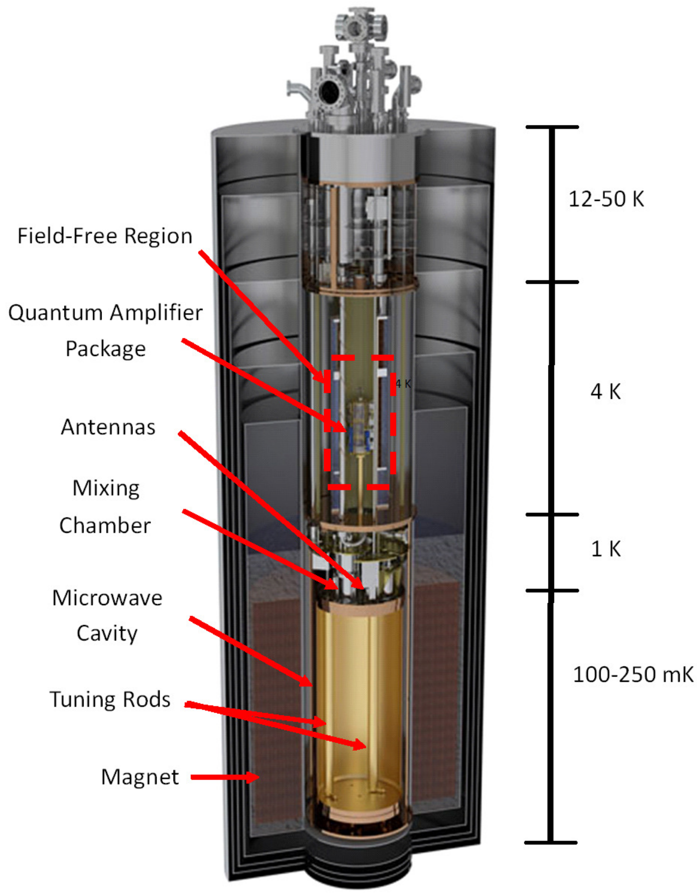

Figure 5.1-1. Cut-away diagram of the ADMX cryostat. The resonant cavity rests in the bore of a superconducting solenoid which can reach up to ~ 7.6 T and is tuned with two independent tuning rods. The system is kept cool ($\mathcal{O}(100)$ mK) with the help of a dilution refrigerator. The signal is extracted from the cavity by antennas and is amplified using the quantum amplifier package (namely a Josephson Parametric Amplifier (JPA)), which is kept in a magnetic field-free region.

The expected power of a signal when the cavity is on resonance with the axion frequency is given by Equation 2.

$$\begin{aligned} P_{\mathrm{axion}} = 7.7 \times 10^{-23}\ \mathrm{W} \left(\frac{V}{136\ \mathrm{L}}\right) \left(\frac{B}{7.5\ \mathrm{T}}\right)^2 \left(\frac{C}{0.4}\right) \left(\frac{g_\gamma}{0.36}\right)^2 \\ \times \left(\frac{\rho_a}{0.45\ \mathrm{GeV\ cm^{-3}}}\right) \left(\frac{f}{1\ \mathrm{GHz}}\right) \left(\frac{Q}{80000}\right) \end{aligned} \tag{2}$$

In this equation, V is the cavity volume, B is the magnetic field strength, C is the form factor (amount of overlap between the cavity resonant mode and the external magnetic field), g_γ is the model-dependent axion-photon coupling constant, ρ_a is the local dark matter density, f is the frequency of the microwave photon, and Q is the loaded quality factor of the cavity.

The axion signal to noise ratio (SNR) is defined by Equation 3.

$$\frac{S}{N} = \frac{P_{\text{axion}}}{k_B T_{sys}} \sqrt{\frac{t}{b}} \tag{3}$$

Here, P_{axion} is the axion signal power, k_B is the Boltzmann constant, T_{sys} is the system noise temperature (dominated by physical temperature of the cavity and the noise temperature of the amplifiers), t is the time over which the signal is integrated and b is the detection bandwidth. The strength of the axion signal is expected to be extremely small, especially for coveted DFSZ axions. In order to reach the required sensitivity, we try to keep our system noise temperature as low as possible. We achieve this by cooling the cavity with a dilution refrigerator to reduce its physical temperature to $\mathcal{O}(100)$mK, and by using ultra low noise quantum amplifiers. These two features of the experiment are what enable ADMX to reach unprecedented levels of sensitivity, in addition to our larger cavity volume.

To date, ADMX has searched for and excluded axions for both KSVZ and DFSZ between 645-800 MHz (2.66-3.3 μeV) through multiple data taking runs[1,2]. Over the course of the last year, ADMX has searched for axions between 800-1020 MHz (3.3-4.2 μeV). This run has been named Run 1C, and data taking lasted from October 2019-May 2021. The first iteration of ADMX searched up to an axion mass of 3.7 μeV, but did not reach the level of sensitivity required to detect DFSZ axions[3]. Until this most recent run, ADMX has been rescanning previously searched parameter space (albeit with significantly increased sensitivity). That makes Run 1C the first run in ADMX G2 (Run 1A onward) that is looking at parameter space which has been unexplored by any other axion haloscope experiment.

In addition to ADMX, there is a second experiment run in parallel with ADMX known as ADMX Sidecar. ADMX Sidecar consists of a smaller 0.588 liter copper cavity, shown in Fig. 5.1-2, mounted directly above the ADMX cavity. ADMX Sidecar utilizes the same superconducting magnet and dilution refrigeration system as ADMX but possesses its own microwave receiver and data taking channel.

[1]N. Du et al., Phys. Rev. Lett. **120** 151301 (2018).
[2]T. Braine et al., Phys. Rev. Lett. **124** 101303 (2020).
[3]J. Hoskins et al., Phys. Rev. D. **84** 121302(R) (2011).

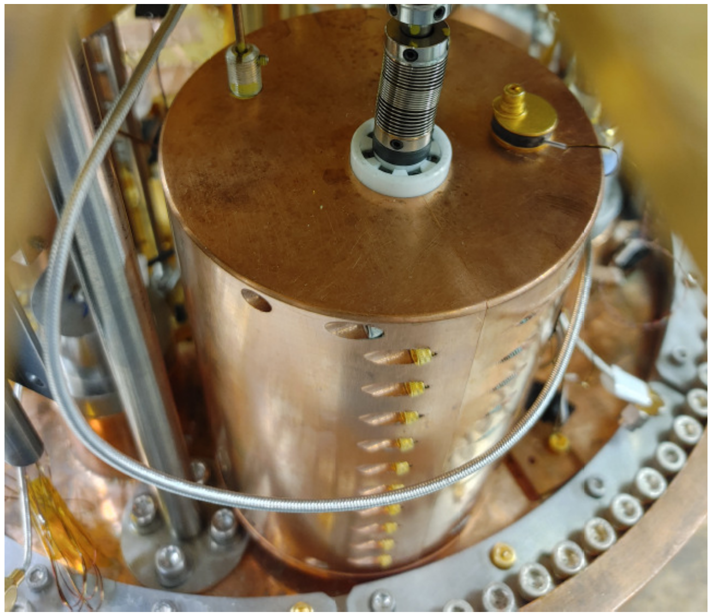

Figure 5.1-2. A bird's eye view of the ADMX Sidecar cavity mounted above the ADMX cavity.

ADMX Sidecar functions as both a test system for research and development into technologies for higher mass axion searches and is sensitive higher mass axion searches in its own right. During run 1C, ADMX Sidecar deployed piezo-electric rotors and a new 'clamshell' cavity design that may be featured in future multi-cavity operations planned by the ADMX collaboration. Most importantly, this most recent data-taking run represented the first implementation of a Josephson traveling wave parametric amplifier (JTWPA) in an axion search. Compared with the JPA used by ADMX, the JTWPA provides low noise power gain over a significantly larger bandwidth of 3 GHz. Such a wide bandwidth improves the prospects for those aiming to perform broadband axion searches. While this data-taking run achieved sensitivity in only a narrow bandwidth due to technical difficulties, the results of this pathfinder experiment will advise future axions searches that seek to leverage the full potential of the JTWPA.

Due to difficulties in maintaining a low noise temperature, (T_{sys} was around 600 mK for this run), DFSZ sensitivity was not achieved for a portion of the frequency range looked at in Run 1C. After making some upgrades to the insert during the summer of 2021 (Fig. 5.1-3), we will be performing another data taking run to increase our sensitivity in the region of parameter space where we were unable to reach DFSZ sensitivity during the initial Run 1C data taking. Preliminary results indicate that we will be able to rule out KSVZ (DFSZ) axions with 90% confidence in the 800 - 1020 MHz (970 - 1020 MHz) mass range, as shown in Fig. 5.1-4.

Figure 5.1-3. Removal of the ADMX insert from the magnet bore following the completion Run 1C It was removed to perform upgrades that will help lower the system noise temperature.

In addition to keeping the experiment up and running during the COVID-19 pandemic, ADMX released in-depth analysis[1] and hardware[2] papers. The former goes into the detail of the Run 1B (680-790 MHz) analysis procedure. The latter discusses the specifics of the technical improvements made to the insert in recent years, including the aforementioned dilution refrigerator and quantum amplifiers. In the near future, papers will also be submitted detailing the results of ADMX and ADMX Sidecar from the past run.

[1] C. Bartram et al. (ADMX Collaboration), Phys. Rev. D., **103** 032002 (2021).
[2] R. Khatiwada et al., arXiv:2010.00169.

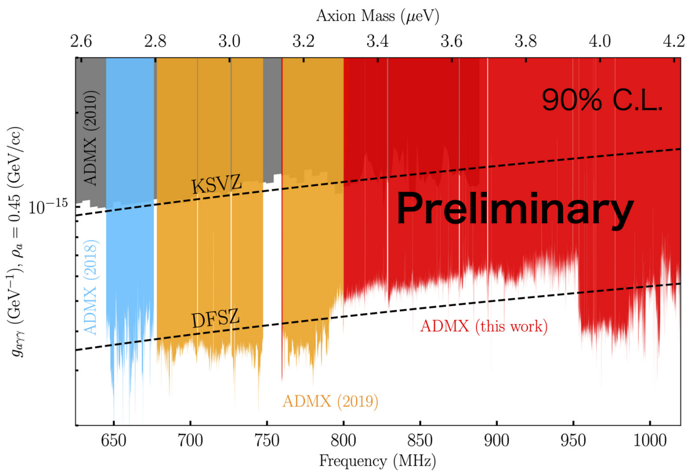

Figure 5.1-4. 90% confidence level upper limits on $g_{a\gamma\gamma}$ as a function of axion frequency. The blue and yellow portions represent limits found during Run 1A[1] and Run 1B[2] respectively. The grey underlay represents limits found as part of the initial ADMX experiment[1]. The red portion represents preliminary limits found during Run 1C, the most recent data taking run.

5.2 Higher-frequency axion searches with Orpheus

R. Cervantes, G. Leum, C. Hanretty, P. Mohapatra, G. Rybka and J. Sinnis

The ADMX Orpheus experiment aims to search for axion-like particles with masses approaching 75 μeV/c^2. This mass range corresponds to an electric field frequency that is more than an order of magnitude greater than that of the resonant modes used in the main ADMX haloscope. At such high frequencies, traditional resonant cavity haloscopes are not well-suited for use in axion detection. This is due to the reliance of traditional haloscopes on low-order modes, which require smaller cavity volumes at higher frequencies, thus decreasing the sensitivity. To search with higher order modes, a cylindrical Fabry-Perot resonator with dielectric plates placed at regular intervals along its length is used. The dielectric plates are placed so that they suppress the electric field where it is anti-aligned with the external magnetic field (to be supplied by a superconducting dipole magnet), increasing the form-factor for higher-order resonant modes (figure Fig. 5.2-2). Unlike a traditional resonant cavity, a Fabry-Perot cavity has no sidewalls. This reduces dissipation of the electric field of the resonant mode and thus increases the quality factor of the cavity.

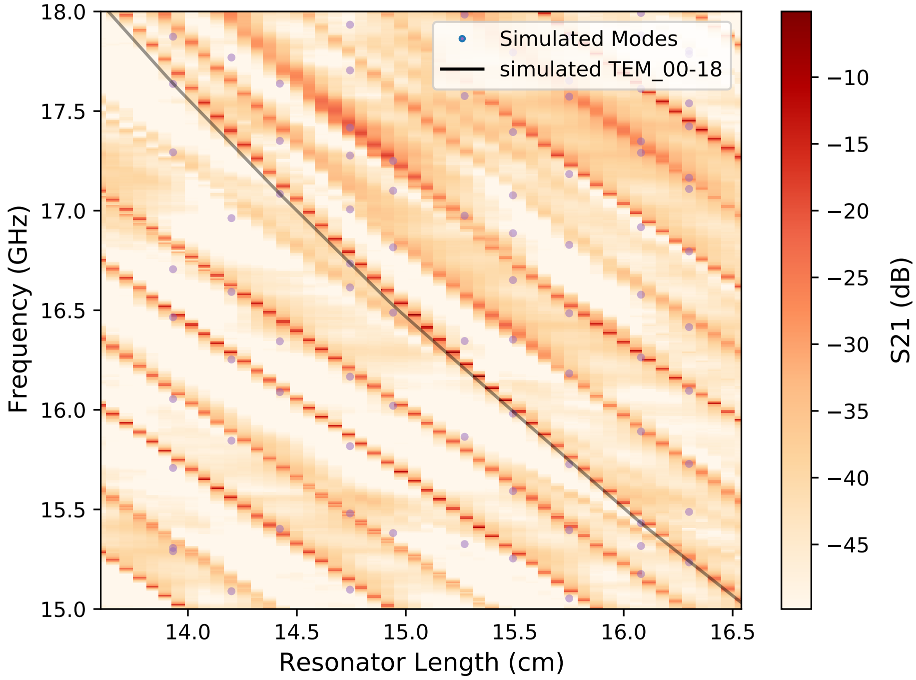

Figure 5.2-1. Modemap of the Orpheus cavity. The resonant frequency is modulated by the resonator length. The TEM_{00-18} mode goes from the upper left corner to the lower right corner of the plot.

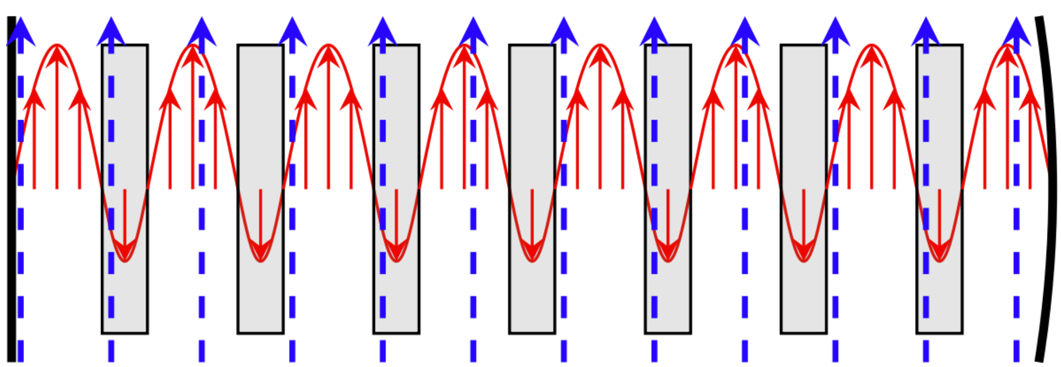

Figure 5.2-2. Illustration of the Orpheus design concept. Dielectric plates (gray) suppress the electric field (red arrows) where it is anti-aligned with the external magnetic field (blue dashed arrows). The black lines on the left and right are the flat and curved mirrors of the Fabry-Perot cavity.

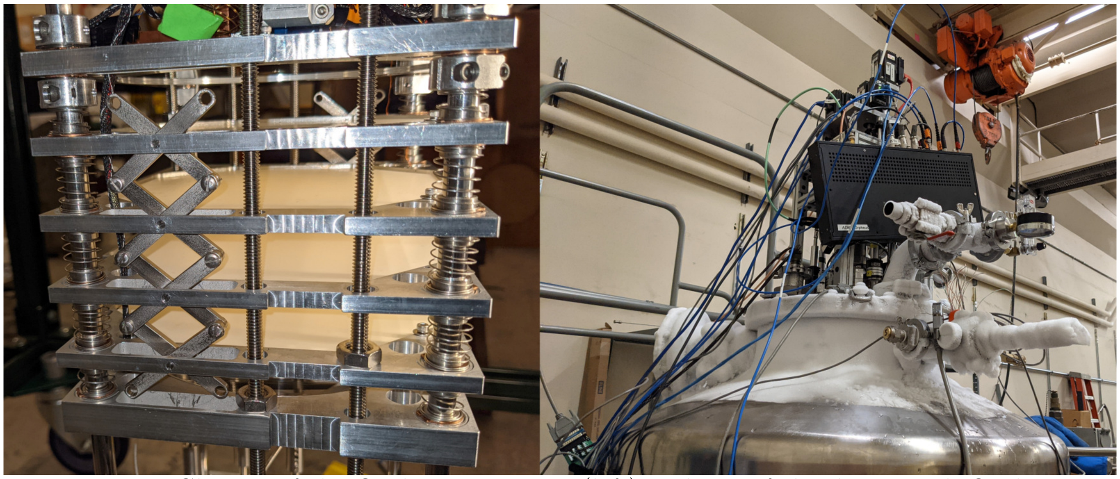

Figure 5.2-3. Closeup of the Orpheus resonator (left) and top of the dewar with Orpheus inserted during a cool-down (right). The dielectric plates are beige, and the flat and curved mirror (on the top and bottom, respectively) are visible. The scissor bridges, which regulate the spacing of the dielectrics, are visible in the foreground and background.

The experiment consists of the aforementioned cavity enclosed in a vacuum space which is inserted into a dewar. The cavity is held at liquid Helium temperatures (4.2K), and both transmission and reflection measurements of the cavity are taken (figure Fig. 5.2-4). A cryogenic amplifier that is thermally coupled to the cavity is used in these measurements. A room-temperature electronics box (which was designed and built in the last year) then down-mixes and filters the signal, then samples the signal with a digitizer. The data acquisition system of the experiment is controlled and accessed through Dripline.

The dielectric plates are made of alumina and placed at every fourth half-wavelength of the electric field of the TEM_{00-18} mode. To tune the resonant frequency, the distance between the mirrors of the cavity is controlled by a stepper motor held at room temperature and coupled to the curved mirror of the cavity. The top and bottom dielectric plates are then moved independently of each other by two other stepper motors (also at room temperature) so that the dielectric plates continue to suppress the anti-aligned electric field. A scissor bridge connects all four dielectric plates to maintain even spacing between them as the top and bottom plates are moved by the motors.

Difficulties were caused by the mechanical tuning mechanism once it had been inserted in the dewar and brought down to liquid helium temperatures. Prior to this, the tuning mechanism and motor stage had been found to work smoothly when the resonator was submerged in liquid nitrogen. However, once the insert was assembled, inserted into the dewar, and cooled down to liquid helium temperatures, one of the motors started to stall. Due to the earlier success of the tuning mechanism at low temperatures, we believe that the current issues are caused by misalignments of the motor vacuum feedthroughs of the insert leading to increased friction. This issue may be alleviated in future runs by a different choice of coupler for the motor shafts and by improving the alignment of the feedthroughs.

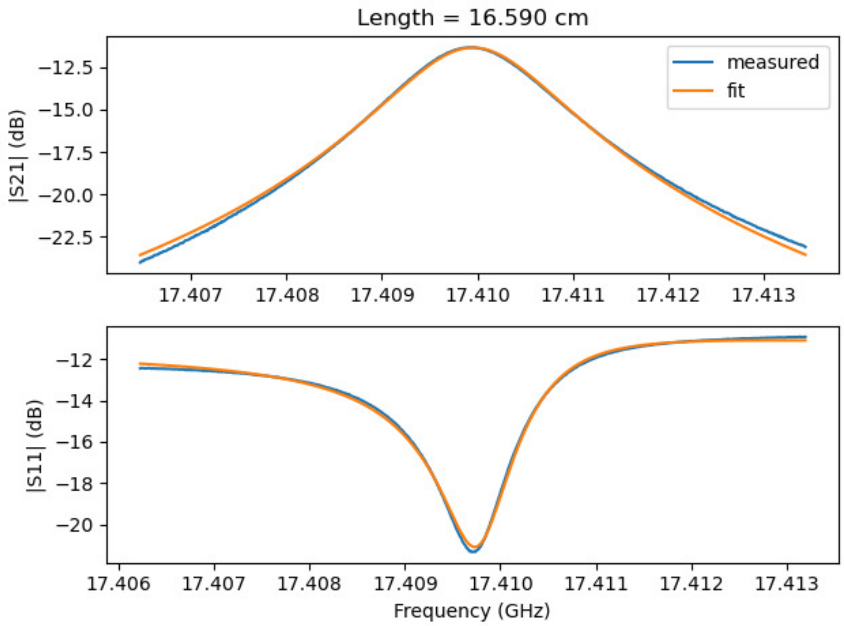

Figure 5.2-4. The fitted transmission (top figure) and reflection (bottom figure) measurements of the cavity around resonance at a given cavity length. The resonant frequency is that at which the transmission is maximized. The fit is used to estimate the quality factor of the cavity.

In September of 2021, the experiment ran for the first time at liquid helium temperatures (4.2-4.8K), scanning from $15.8 - 16.8$ GHz over two days. Because the magnet has not been made yet, the data taken will not be applicable to axion searches, but may be used for dark photon searches[1]. In the future, data applicable to axion searches will be conducted at similar temperatures with the use of a superconducting dipole magnet, which is currently being fabricated by the group and is expected to have a field strength of about 1.5 T.

DAMIC

5.3 WIMP search results from DAMIC at SNOLAB

A. E. Chavarria, P. Mitra*, A. Piers, and outside collaborators†

DAMIC (Dark Matter in CCDs) at SNOLAB is a low noise, low threshold dark matter experiment located 2 km underground in the Vale Creighton Mine near Sudbury, Ontario. The experiment consists of a tower of seven science grade, 675 μm thick, fully depleted silicon charged coupled devices shielded by layers of electroformed copper, ancient and regular

*Presently at ASML, San Diego, California.
†DAMIC Collaboration.

[1] S. Ghosh et al., arXiv:2104.09334.

lead, and polyethylene. DAMIC at SNOLAB operates with extremely low levels of electronic noise (< 2 e$^-$), leakage current ($< 5 \times 10^{-4}$ e$^-$pix^{-1}day^{-1}), and background rate (< 11 counts kg^{-1}day^{-1}keV$_{\mathrm{ee}}^{-1}$), yielding an effective search for dark matter candidates in the form of weakly interacting massive (WIMPs) or hidden-sector dark matter particles.

The seven CCDs were commissioned in 2017 and collected data until early 2019 resulting in ~ 11 kg day of total exposure after all cuts. The heart of the analysis involved developing a background model of all radioactive contaminants within the detector to realistically predict the energy spectrum in the WIMP region of interest. We simulated the full detector geometry and contaminants in Geant4, pasted the events on blank (noise only) CCDs images with an added Poissonian dark current, and ran the images through our data processing chain. With a direct comparison between data and simulation, including detector and reconstruction effects, we performed a template fit to the data > 6 keV$_{\mathrm{ee}}$ (where we do not expect a WIMP signal since other experiments have already explored this "high energy" region). We extrapolated the results of the best-fit to low energies to use it as our background expectation for the WIMP search. We considered several systematic uncertainties including the position of radioactive contaminants on the surfaces and the detector response of a previous unknown partial charge collection region on the backside of the CCDs.

We completed our analysis by performing a profile likelihood ratio (PLR) test between the global minimum (background + signal model) and the null (background only) hypothesis. We found, accounting for systematic uncertainties due to the CCD structure and the location of specific surface background components, an excess of ionization events in the bulk of the CCD that disfavor the null hypothesis at the 3.7σ level (Fig. 5.3-1). This excess (17.1 ± 7.6 events) can be characterized by a decaying exponential with decay constant of 67 ± 37 eV$_{\mathrm{ee}}$. The origins of the ionization events are unknown, including whether they are nuclear or electronic recoils, so we do not claim this as a dark matter discovery. Regardless of its origin, this excess is of great relevance for the next generation of CCD experiments that aim to probe a lower energy regime with less background.

Despite the presence of an unexplained excess of ionization events at low energy, we can still set a limit on the WIMP-nucleon scattering cross section. Fig. 5.3-2 shows the published limit from the recent DAMIC at SNOLAB run[1]. This limit represents the strongest constraints for WIMPs with $m_\chi < 9$ GeV/c^2 in a silicon target and disfavors the WIMP-signal interpretation of a previous CDMS-II Silicon result[2] with the same nuclear target.

---

[1] A. Aguilar-Arevalo *et al.* (DAMIC Collaboration), Phys. Rev. Lett. **125**, 241803 (2020).
[2] R. Agnese *et al.* (CDMS Collaboration), Phys. Rev. Lett. **111**, 251301 (2013).

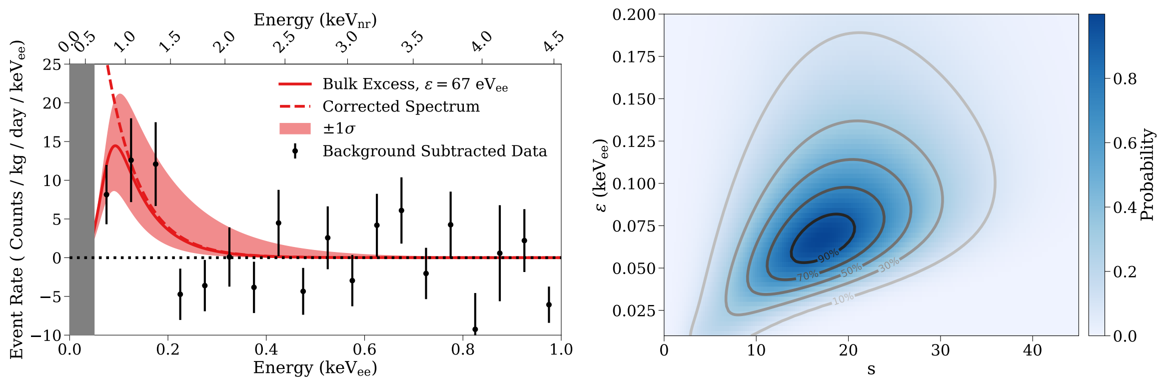

Figure 5.3-1. Left: Background-substracted data spectrum and the best-fit bulk decaying exponential. Above 200 eV$_{ee}$ the data are consistent with the background model, but below, we find an unexplained excess of ionization events. Right: p-value contours on the number of events (s) and spectral decay constant (ϵ).

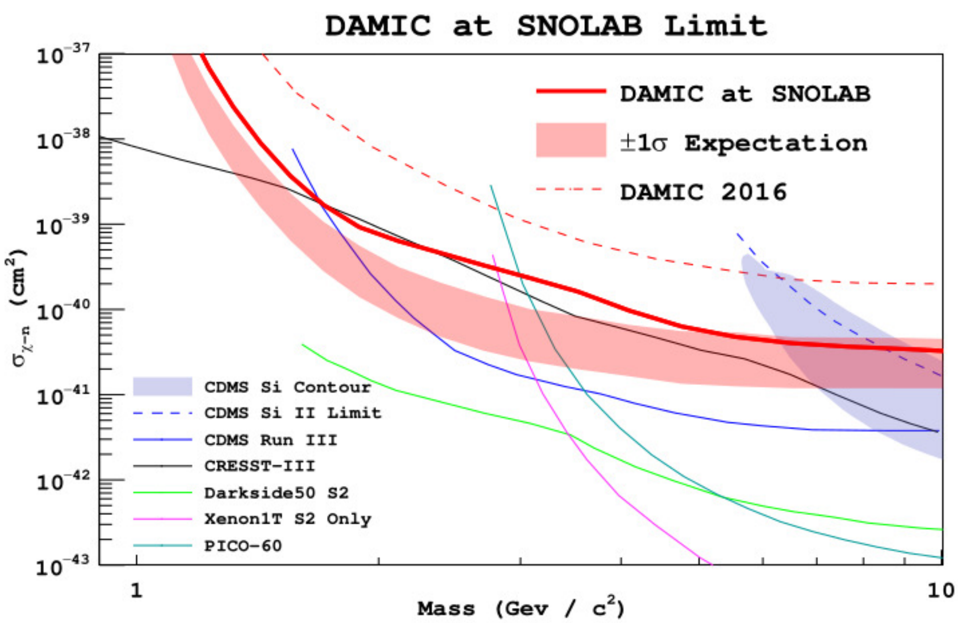

Figure 5.3-2. 90 % C.L upper limit on the WIMP-nucleon spin-independents scattering cross section (solid red) for 10.93 kg day exposure with DAMIC at SNOLAB (other experiments shown for reference). The deviation of the limit from its initial projected sensitivity (shaded red) at low masses is due to the presence of the bulk excess.

5.4 Background studies with DAMIC

A. E. Chavarria, M. Conde, M. Huehn, M. Kallander, P. Mitra*, D. Peterson, A. Piers, R. Roehnelt, T. D. Van Wechel, and outside collaborators†

Backgrounds from natural radioactivity dominate the spectrum of ionization events measured by DAMIC. It is crucial to understand these backgrounds for both credibly reporting a spectral excess as a possible dark matter signal, and to inform the background mitigation strategies for next generation detectors, e.g., DAMIC-M.

Recently, we released a long paper[1] detailing the construction of the background model used for the WIMP search (Sec. 5.3). The background model is built from the contribution of radiocontaminants throughout the DAMIC detector, whose activities were constrained by an extensive radioassay program. The resulting background spectrum is statistically consistent with the data for electron-equivalent energies >200 eV, with a conspicuous exponential excess of events at lower energies. The dominant components in the DAMIC spectrum are tritium from cosmogenic activation of the CCD bulk silicon, and ^{210}Pb on the surfaces of the CCDs from exposure to radon during device installation, fabrication and storage. The tritium activity in DAMIC is consistent with the expectation from the cosmogenic activation rate that we measured with a CCD exposed to an intense neutron beam[2,3], and the history of the CCD silicon before deployment at SNOLAB. An independent analysis[4] that exploits DAMIC's exquisite spatial resolution to identify individual radioactive decay sequences demonstrated that other backgrounds in the bulk silicon of the CCDs, e.g., ^{32}Si, ^{238}U, and ^{232}Th, provide subdominant contributions to the background spectrum. Background sources external to the CCDs are dominated by radioactive decays in the CCD holders made from commercial copper, and the Kapton flex cables that carry the signals to drive and read the CCDs.

Skipper CCDs tested at CENPA are being deployed underground to perform further background studies (Sec. 5.5). The DAMIC detector at SNOLAB was upgraded by CENPA with skipper CCDs in November 2021 to perform a more precise measurement of the spectrum at low energies and shed light on the origin of the unexplained event excess. Skipper CCDs, which can count with high resolution the number of charges collected per pixel, will allow us to lower the energy threshold from $\sim 15\,e^-$ to $5\,e^-$, and significantly improve the discrimination between surface and bulk events. Skipper CCDs will also be deployed in December 2021 in the Low Background Chamber (LBC), a new test system at Modane Underground Laboratory (LSM) designed to address some of the main background sources in DAMIC at SNOLAB. The LBC will serve as a demonstrator for the background mitigation strategies of the DAMIC-M program (Sec. 5.6). In addition, the presence (or absence) of the low-energy excess in a second detector with lower background will provide further information on its origin. Fig. 5.4-1 shows the progress in the installation of the two detectors.

---

*Presently at ASML, San Diego, California.
†DAMIC and DAMIC-M Collaborations.

1. A. Aguilar-Arevalo *et al.* (DAMIC Collaboration), arXiv:2110.13133 (2021).
2. CENPA Annual Report, University of Washington (2020) p. 131.
3. R. Saldanda *et al.*, Phys. Rev. D **102**, 102006 (2020).
4. A. Aguilar-Arevalo *et al.* (DAMIC Collaboration), JINST **16** (2021) P06019.

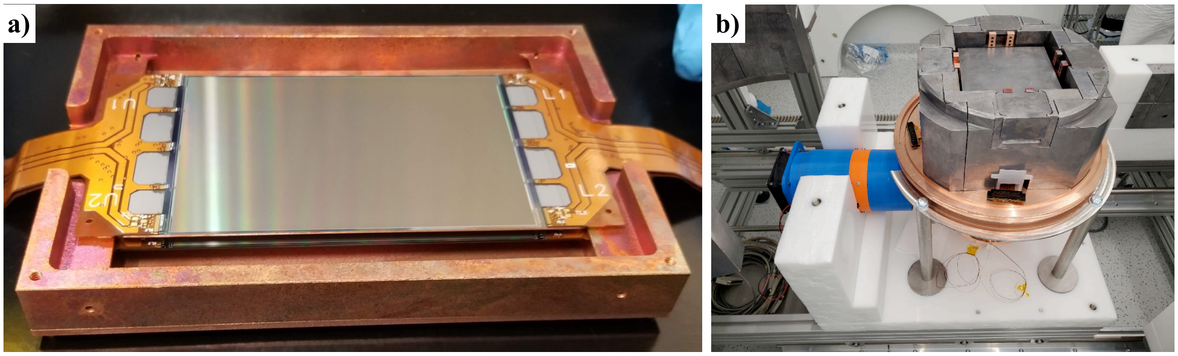

Figure 5.4-1. **a)** Two 6k x 4k CCDs installed in the new copper box in DAMIC at SNOLAB. **b)** Installation of the internal lead shield of the LBC underground at LSM. The square pocket for the copper box with skipper CCDs is visible.

5.5 Skipper CCDs for low-background detectors

A. E. Chavarria, K. McGuire, P. Mitra*, A. Piers

The DAMIC group at CENPA made major progress in 2021 in testing and characterizing sub-electron resolution "skipper" CCDs. These devices offer a promising probe for light dark matter due to the typical benefits of a solid state silicon detector (low bandgap, low leakage current, and scalability) coupled with a significantly lower noise threshold. CCDs tested and characterized at UW will soon be deployed underground for dark matter science runs. The successful operation of skipper CCDs will broaden DAMIC's science reach and act as a demonstrator for the large CCD array experiments of DAMIC-M and Oscura (with proposed 3 and 30 kg-year exposures, respectively).

Skipper CCDs have a modified output stage where the charge of an individual pixel can be repeatedly and non-destructively measured. Fig. 5.5-1 shows the schematic of how charge is measured by moving the charge in and out of a capacitively coupled output gate. We can measure the charge an arbitrarily high number of times, constrained only by the readout time of a given pixel, and average all the values measured by the amplifier to suppress any uncorrelated readout noise by $1/\sqrt{N}$, where N is the number of measurements. We have achieved noise of $< 0.1e^-$ at UW with skipper CCDs, a significant improvement over the $\sim 2e^-$ noise of the previous generation of DAMIC CCDs.

*Presently at ASML, San Diego, California.

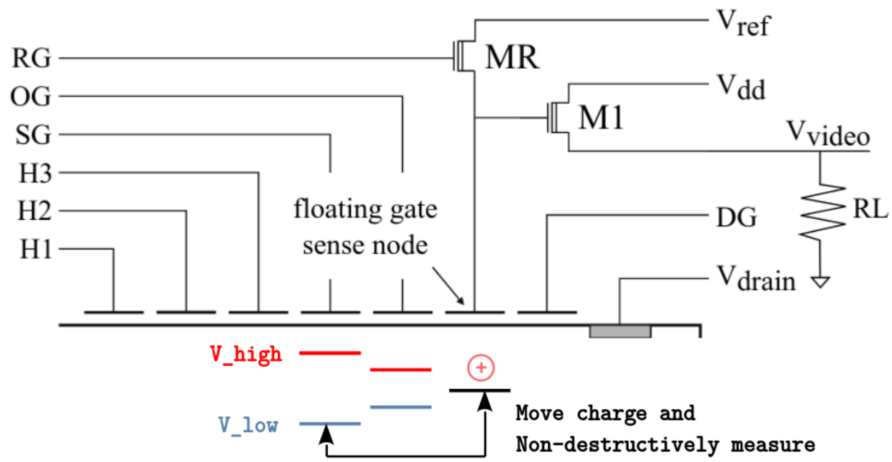

Figure 5.5-1. Schematic of a skipper output amplifier. By the relative voltages of the Summing Gate (SG) and Output Gate (OG) the charge can be moved in and out of the sense node, which is capacitively coupled to the output amplifier. This allows for repeated, uncorrelated, and non-destructive measurement of the charge, thereby suppressing the readout noise. The Dump Gate (DG) potential prevents the charge from escaping the sense node until we are done reading that pixel.

Four sizes of CCDs, denoted by the number of pixels in each dimension (1k x 6k, 6k x 4k, 6k x 1k, and 6k x 1.5k), have been packaged and operated in our test chambers located in PAB B059 and NPL 165. Despite the differences in CCD size and overall package style, we have successfully run each type at cryogenic temperatures and achieved noise $< 0.1e^-$ (Fig. 5.5-2). Additionally, we used ^{241}Am and ^{55}Fe sources for spectral measurements and CCD characterization.

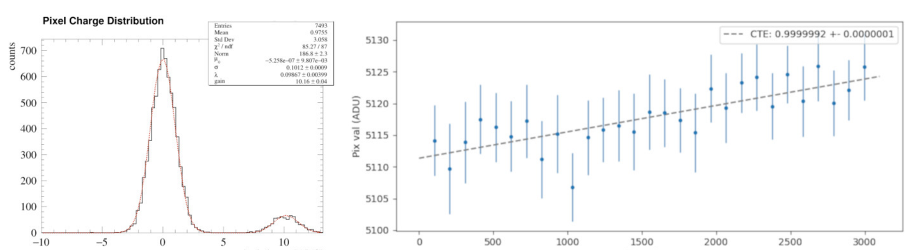

Figure 5.5-2. Performance of a DAMIC 6k x 4k skipper CCD packaged and tested at CENPA. Left: Histogram of pixel values with RMS noise of $0.1e^-$. Shown here are the zero- and one-electron peaks. Right: Charge transfer efficiency in the CCD's serial register, showing a charge loss ratio of less than 10^{-6} per pixel transfer.

One critical activity that we performed was selecting the CCDs to be deployed underground for science runs. Currently two different experiments are being set up to run skipper CCDs. The DAMIC at SNOLAB detector is being upgraded to support two 6k x 4k DAMIC-M style CCDs (and two CCDs from another collaboration, SENSEI) in a low-background environment ~ 2 km below the surface. Another system at Laboratoire Souterrain de Modane

(LSM) is currently under construction and will also run two 6k x 4k CCDs in a Low Background Chamber (LBC) that is the precursor to the larger DAMIC-M experiment. Characterization of these CCDs at CENPA includes performing detailed measurements of the charge resolution and noise performance over thousands of skips, generating pixel-level maps to search for subtle defects in the pixel array and inhomogeneities in leakage current, and measuring charge loss per skip and charge transfer efficiency. The results of some of these measurements are included in Fig. 5.5-3 and Fig. 5.5-4. Due to our increased efficiency in packaging and testing, we have found several candidate CCDs for dark matter searches.

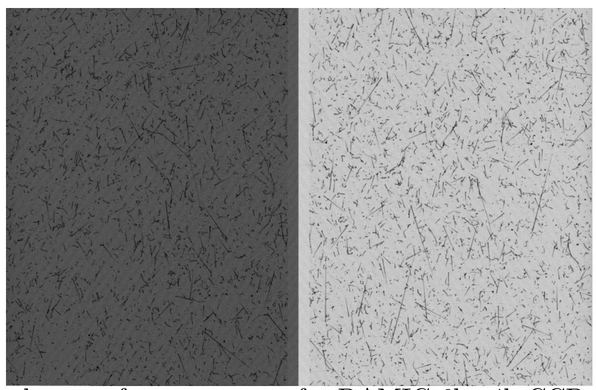

Figure 5.5-3. An hour-long surface exposure of a DAMIC 6k x 4k CCD featuring electron, muon, and γ-ray tracks. The pixel array, plus overscan region, is read out concurrently by two skipper amplifiers located at the bottom corners of the CCD.

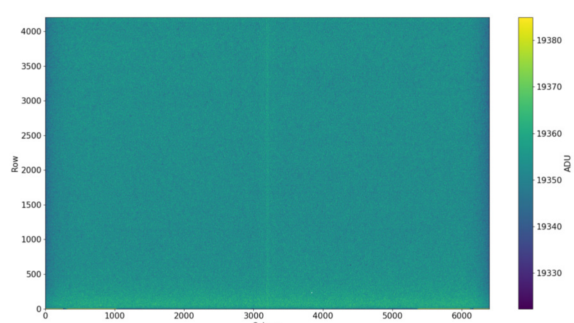

Figure 5.5-4. A composite image of 15 20-minute exposures taken with the same CCD as above. The image was generated by selecting the median value of each pixel across all images, after omitting outliers (i.e., values falling outside 1σ of the median).

The work undertaken by the DAMIC group at CENPA has been critical for the next generation of CCD experiments. As the experiments grow in mass the CCD testing will need to scale up, and the experience gained in the past year will prove extremely valuable.

5.6 DAMIC-M CCD Array

A. E. Chavarria, M. Conde, B. Elmer, M. Huehn, P. Mitra*, R. Roehnelt, A. Trevino, and outside collaborators†

The DAMIC-M detector will search for the interactions between dark matter particles and silicon atoms with unprecedented sensitivity[1]. The heart of the detector is an array of skipper CCDs with single-electron resolution deployed in an ultra low-radiation environment in the Modane Underground Laboratory (LSM) in France. The CCD array, which is the main responsibility of CENPA, underwent a significant redesign in the past year. Instead of 50 large-format 6k x 6k CCDs in a horizontal orientation[2 3], the new design features 52 modules of four 6k x 1.5k CCDs each in a vertical orientation (Fig. 5.6-1). The change in the design was motivated by concerns on the low yield ($\sim$10%) of such large devices in previous fabrication runs. For reference, out of the 22 6k x 4k CCDs packaged at CENPA (Sec. 5.7), four were deemed of sufficient quality to be deployed underground for science (Sec. 5.5).

The new design has the same 0.7 kg target mass and number of readout channels as previously but the silicon target is broken up into four times as many sensors. A pitch adapter is employed to distribute the signals between the four CCDs in a module so that the devices can be driven and read out with the same electronics controller as one large-format CCD. The pitch adapter consists of aluminum traces patterned on a 150-mm diameter silicon wafer, which is then cut into the appropriate shape. Four CCDs and a flex cable that carries the signals to and from the electronics controller are glued to the pitch adapter. The electrical connections are made with wire bonds. We designed the pitch adapter, and fabricated the first single-CCD prototypes at the Washington Nanofabrication Facility (WNF) on UW campus. Concurrently, we fabricated mock modules, with bare silicon for the CCDs and pitch adapter, for thermal and mechanical testing. The testing of the prototype pitch adapters and the mock CCD modules were the summer projects of LSAMP[4] students Benito Elmer and Areesa Trevino, respectively.

We are finalizing the design of the four-CCD pitch adapter and revising the fabrication process to decrease the impedance of the traces (signal lines). Once we confirm that the pitch adapter electrical specifications meet the requirements for DAMIC-M, we will proceed to package the first complete module. In parallel, we are integrating the design of the CCD array in the DAMIC-M cryostat while performing the relevant thermal and radioactive-background simulations[5]. These activities are carried out within DAMIC-M's Detector Task, which is led by CENPA.

*Presently at ASML, San Diego, California.

†DAMIC-M Collaboration.

[1] N. Castello-Mor (DAMIC-M Collaboration), Nucl. Instrum. Methods Phys. Res. **A958**, 162933 (2020).

[2] CENPA Annual Report, University of Washington (2020) p. 217.

[3] CENPA Annual Report, University of Washington (2019) p. 142.

[4] NSF's Louis Stokes Alliances for Minority Participation (LSAMP): `https://beta.nsf.gov/funding/opportunities/louis-stokes-alliances-minority-participation`

[5] C. De Dominics and M. Settimo (DAMIC-M Collaboration), PoS **ICRC2021** (2021) 553.

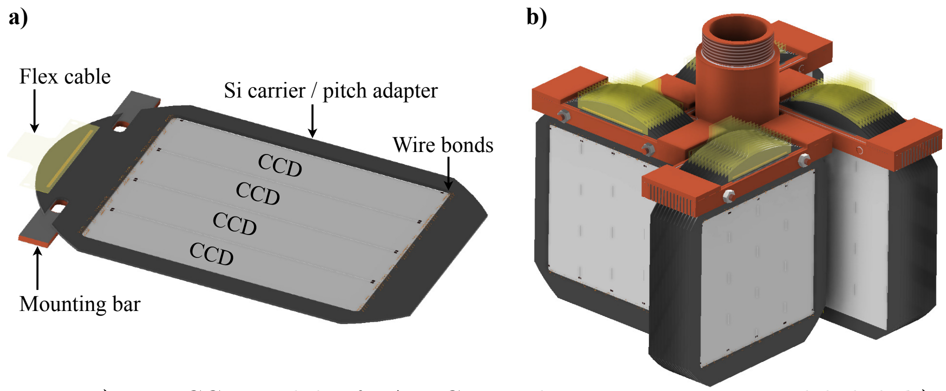

Figure 5.6-1. **a)** Four-CCD module of DAMIC-M with its main components labeled. **b)** The full DAMIC-M array of 52 CCD modules installed around a cold finger in four groups of 13.

5.7 CCD Packaging

A. E. Chavarria, M. Conde, P. Mitra*, A. Piers, and R. Roehnelt

CENPA is responsible for packaging the CCDs for the DAMIC-M program. Prototype CCDs are packaged on UW campus and distributed to collaborating institutions around the world. The packaging of the final CCDs for DAMIC-M will be performed underground at LSM to mitigate the cosmogenic activation of the CCD silicon.

Before packaging starts, all components are thoroughly cleaned and electrical connectors installed on the cables. The packaging process for most CCDs (formats: 1k x 6k, 6k x 1k and 6k x 1.5k) starts with mounting a silicon carrier on a vacuum chuck. A flex cable and a CCD are glued to the carrier with epoxy. Flex cables are plasma etched beforehand at the WNF to roughen their surfaces and increase the bond strength to the silicon. The epoxy is cured by heating the chucks to 80° C for five hours. The last step is to connect the CCD pads to the flex cable pads with wire bonds. For the 6k x 4k CCDs there are no carriers. Instead, the CCD has areas on the sides where shims of unpolished silicon are glued between the CCDs and the flex cables in a "sandwich" structure, in order to increase adhesion. Fig. 5.7-1 shows CCDs of two different formats during the epoxy curing step. At the end, the packaged CCDs are safely stored in aluminum boxes.

*Presently at ASML, San Diego, California.

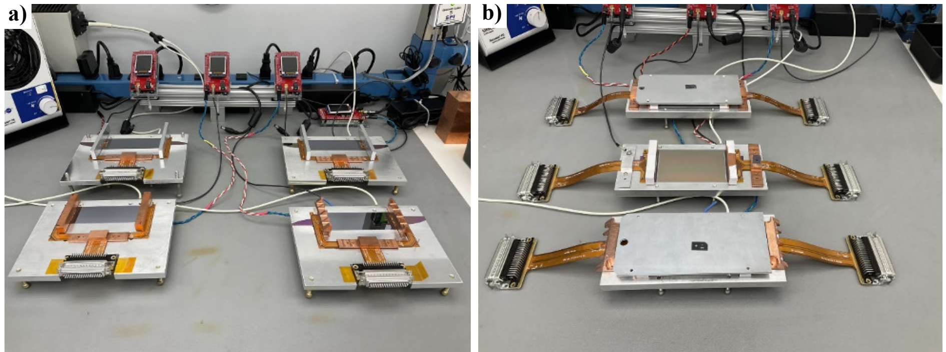

Figure 5.7-1. Four 6k x 1k CCDs (**a**) and three 6k x 4k CCDs (**b**) during the epoxy curing step of the packaging procedure in the clean lab in PAB B059.

In the past year, we implemented improvements for CCD packaging: a cleaner and better equipped cleanroom, but also a new approach for the packaging process. We now clean the area on a weekly basis, use proper personal protection equipment (ISO Class 4 compatible coveralls) and monitor the cleanliness of the area on a regular basis. We also monitor and control the humidity in the cleanroom so that it is high enough to prevent electrostatic discharges that may damage the devices. These represent important steps toward insuring high-quality packaging. A new microscope was purchased to increase the visual inspection area. The wedge wire bonder (Kulicke & Soffa 1470)—the most specialized equipment that we use in the packaging process—is in better shape now since maintenance was performed in September 2021. We are able to package multiple CCDs at a time and better manage the consumables for packaging. CCDs in four different formats are regularly packaged: 1k x 6k, 6k x 4k, 6k x 1k and 6k x 1.5k. Table 5.7-1 shows the number of CCDs packaged of each type. We note that one of the 6k x 1k CCDs was packaged with a pitch adapter (Sec. 5.6).

CCD format (col.s x rows)	Fabrication run	No. packaged
1k x 6k	UW prototype (2019)	5
6k x 4k	UW prototype (2019)	10
6k x 1k	UW prototype (2019)	13
6k x 1.5k	Preproduction (2021)	16

Table 5.7-1. Format, fabrication run, and number of prototype DAMIC-M CCDs packaged at CENPA in the last year.

Organization is extremely important when packaging a large number of devices, especially as we improve and fine-tune the packaging process. Detailed packaging records are kept using the `eLabFTW` platform while a full inventory of packaging and clean lab components is managed with the `Grocy` platform.

6 Other research

6.1 Atmospheric monitoring for radionuclides

J. Alferness, J. H. Burkett*, J. A. Detwiler, C.A. Hagedorn, S-C. Hsu, S. T. Jones, J. O'Leary*, D. B. Pengra, S. Pruitt*, D. Salvat†, C. W. Watson*, C. Wiseman, and Z. J. B. Wuthrich

In response to 2017 nuclear-weapons testing and tension on the Korean Peninsula, we restarted CENPA's nuclear atmospheric-monitoring program[1],[2]. We began prior to any known release of radioactivity in order to have instrumentation, process, and backgrounds understood before they might be needed. In addition to providing a potential public and scientific service, this project has proven to be accessible for undergraduate research and nuclear-physics education.

As in previous CENPA programs, we collected samples from HVAC air filters located at UW's Physics and Astronomy building. Each filter samples $140,000\ \mathrm{m}^3/\mathrm{d}$ of ground-level air. We initially sampled weekly, and have, with the cooling of Korean tensions, reduced our counting cadence. In addition, we explored a rainwater monitoring program and sampled water from the university power plant cooling tower, which filters an enormous volume of air.

After exposure, the filters are transported in bags to CENPA where they are disassembled, trimmed (effective volume $60,000\ \mathrm{m}^3/\mathrm{d}$), compressed, repackaged, and placed into a counting facility consisting of a 100%-efficiency germanium detector (detector-dependent resolution of 3-8 keV) surrounded by a 10 cm layer of lead bricks. Counting durations are ≥ 2 days.

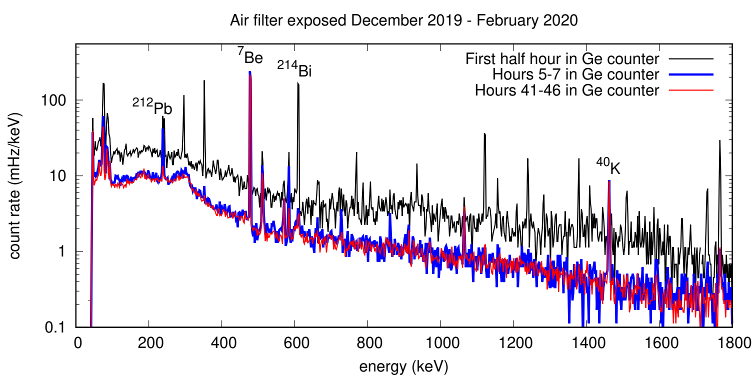

Figure 6.1-1. Example spectra from a recent filter. We plot three spectra, showing time-evolution of the sample's spectrum. ^{222}Rn and ^{220}Rn decay chains are clearly observed, with sub-hour and sub-day half-lives. Radioactivity arriving from overseas must have a half-life of a day or more. The cosmogenic ^{7}Be peak is a reliable and dominant feature.

*Now serving in U.S. Army.
†Presently at Indiana University.

[1]CENPA Annual Report, University of Washington (1986) p. 59.
[2]J. D. Leon, D. A. Jaffe, J. Kaspar, A. Knecht, M. L. Miller. J.Environ.Radioact. 102 (2011) 1032-1038

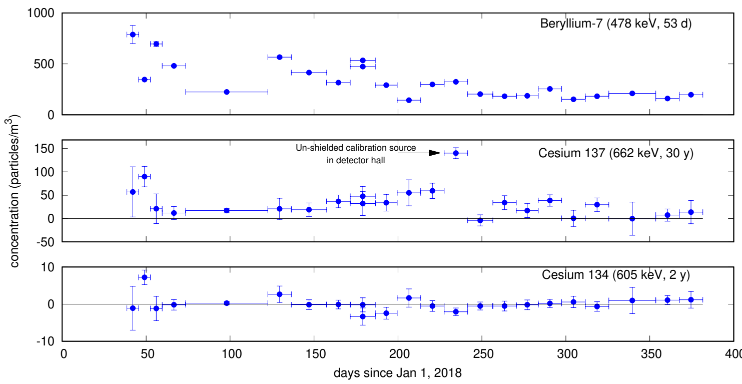

Figure 6.1-2. Time-series of inferred atmospheric radionuclide concentration of ^{7}Be, ^{137}Cs, and ^{134}Cs in our filters. Uncertainties are statistical-only; combined systematic uncertainty in filter and detector efficiency is as large as 10x. Horizontal errorbars denote exposure duration. We have not observed any significant unexpected activity in any filters from October 2017 to February 2020.

We have monitored continuously since October 2017. Recent spectra are shown in Fig. 6.1-1. A subset of the data, with constant systematic uncertainties, is shown in Fig. 6.1-2. We clearly identify short-lived cosmogenic ^{7}Be in atmospheric dust. Sensitivities for other isotopes is at the 0.1-10 Bq/m^{3} level. We have developed analysis strategies to understand and mitigate the radon-daughter background intrinsic to near-surface atmospheric sampling.

Streamlining of the analysis is underway to allow results on radionuclides of interest within a day. Detector upgrades and `g4simple`[1] simulations are underway to characterize and reduce muon-induced backgrounds that may dominate the continuum in the spectrum. We upgraded and characterized a four-scintillator-coincidence muon counter and used it to assay alternative locations with lower cosmic ray flux that may be available at CENPA or elsewhere at UW. Should a convenient location be identified, we may move the counting facility to take advantage of the lower background.

Our ready-to-go facility and process allowed us to aid UW's Radiation Safety Office in responding to a major ^{137}Cs accident. Not only could we place an upper bound on Seattle's atmospheric exposure to the radionuclide, but we were immediately able to perform assays that aided the incident response and cleanup.

With the continuing impact of COVID the monitoring activities are currently on hold. Should a event of interest occur, we will resume filter collection and counting.

[1] https://github.com/legend-exp/g4simple

7 Education

7.1 Crane Rigging & Hoisting Safety Training

B. W. Dodson

This year, engineer and qualified rigging instructor Brittney Dodson offered a training course for safe rigging practices and techniques to CENPA personnel for overhead & gantry crane use. The course material was provided by Overton Safety Training[1] and was adapted for typical crane use at CENPA. Attendees obtained a comprehensive understanding of safe rigging and hoisting practices – including OSHA regulations and guidelines, general hazards and associated responsibilities working around cranes, basic crane dynamics, and understanding and calculating load weight and center of gravity.

Attendees were instructed on general information regarding proper application, use, and inspection of various rigging hardware and slings—with practical examples of unsafe rigging equipment and hoisting configurations provided. Each student completed a written exam knowledge check and an hour-long practical exam requiring various test loads to be assessed and rigged appropriately. Each student received a workbook with detailed information and references to the instructed material to keep. The class qualified 8 CENPA personnel to safely hoist loads using overhead & gantry cranes in various lab spaces around CENPA, improving CENPA's safety awareness and management practices broadly.

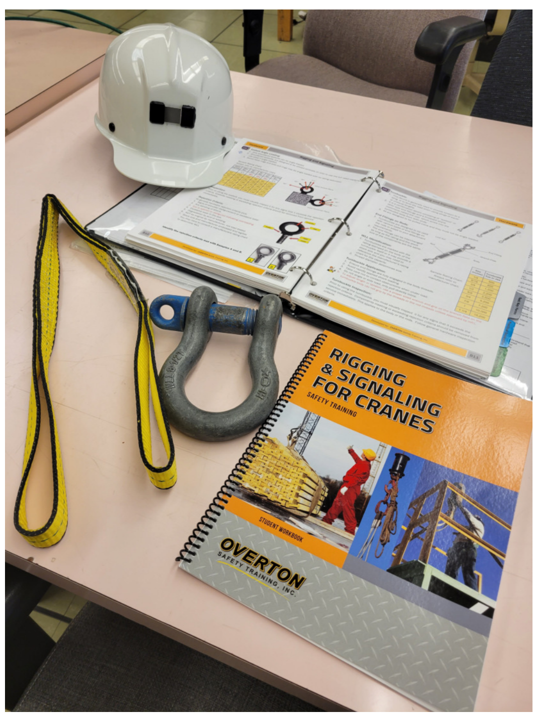

Figure 7.1-1. Crane Rigging Safety training course material.

[1]Overton Safety Training, Inc., https://www.overtonsafety.com/

8 Facilities

Accelerator

8.1 Van de Graaff accelerator and ion-source operations and development

B. W. Dodson, K. Hansen, D. A. Peterson, E. B. Smith, and T. D. Van Wechel

This annual reporting period saw very low tandem accelerator and direct extraction ion source (DEIS) demand due to operations shut-down for COVID-19 restrictions. The tandem accelerator was entered one time to investigate failed terminal computer communictions and low enegy (LE) column resitor sparking. Although the optical fibers used for terminal computer communications are subject to x-ray, neutron, and gamma radiation damage, which in turn results in signal light intensity loss, the simple uncoupling and recoupling at the fiber junctions elimiated the communications failure. It is our desire to fabricate or aquire an instrument that can measure the optical loss in the fibers, in order to document fiber damage and determine when the effort should be made to replace fibers in the tandem accelerator.

The supply hose delivering 5 MΩ-cm resistivity deionized (DI) water, for power supplies and magnets cooling, to the ion sources deck developed a pinhole leak for first time since construction in 1987, resulting in a shorting of the deck high voltage (HV) bias of -150 kV to ground. The supply and return hoses, each approximately 130' long 3/4" ID braided PVC hose, are very neatly coiled in a large PVC can to provide a very high resistance path. The PVC can is continuously purged with 4 CFM of boil-off nitrogen gas from the liquid nitrogen (LN2) storage system. However, the poly-flo tube delivering nitrogen purge gas to the PVC can was broken, resulting in corona formation of ozone in the air of the PVC can. The ozone degraded the DI water hoses, both of which had "gummy" outer texture, leaving an odor of ozone, and ultimately a pinhole leak in the supply hose. Supply and return hoses were removed, lengths measured, and new ones carefully coiled in parallel and concentrically into the PVC can. The broken nitrogen purge gas line was replaced.

The control system CAVE 1 GORDO satellite computer experienced a failed CPU in February 2020. Detailed inspection in September 2020 revealed that conductor(s) within the P1 and P2 ribbon cables running from the PC-DIO120 interface card had possibly shorted to the grounded aluminum foil rf shielding that was wrapped around each ribbon cable, and the resulting current may have damaged the CPU or motherboard. Images of melted insulation and fusing of those ribbon cables were recorded. The interface card and hard drive were transferred to a replacement PC. New P1 and P2 ribbon cables were fabricated and connected to the interface card. The re-assembled, fully functional CAVE 1 GORDO satellite restored full accelerator system controls.

During the annual reporting period from April 1, 2020, to March 31, 2021, the tandem pelletron chains operated 110 hours, the sputter-ion-source (SpIS) operated 0 hours, and the duoplasmatron direct-extraction-ion source (DEIS) operated 159 hours. Additional statistics for accelerator operations are given in Table 8.1-1. The only Tandem accelerator produced beam of ions originated from the DEIS, and was a 12 MeV $^{2}H^{+}$ for the ^{6}He-CRES ^{19}Ne experiment.

ACTIVITY SCHEDULED	**DAYS SCHEDULED**	**PERCENT of TIME**
Nuclear-physics research, accelerator	7	1.9
Development, maintenance, or crew training	47	12.9
Grand total	54	14.8

Table 8.1-1. Tandem Accelerator Operations April 1, 2020, to March 31, 2021.

CENPA Engineering

8.2 Overview

B. W. Dodson, K. Hansen, M. Huehn, M. Kallandar, and R. Roehnelt

Behind every CENPA project there is work done to ensure parts fit together and experimental requirements are achieved. How do you design a CCD detector array to minimize background, minimize mass, and maximize thermal conductivity in a 110K vacuum cryostat? How do you generate 30kV with <70mV ripple and then feed it into an electron gun in a vacuum system that happens to be inside an MRI? These are the sort of questions asked of the CENPA engineering group by every project. The CENPA engineering team that answers these questions consists of a multi-disciplinary group of engineers and physicists collaborating to design and fabricate the hardware needed to make CENPA projects function.

Starting in Q4 of 2020 the project engineering group has been standardizing on a common set of tools and processes. The most common sense of these standardizations was to consolidate multiple years of CAD product data management (PDM) software into a single repository on a single server. This simplified IT support, brought all hardware engineers to use a single version of software, and improved the frequency and quality of data backups. With an aim to improve engineering processes a weekly meeting was started where select tenets of the Toyota manufacturing system are shared, design modeling philosophy is discussed, and work in progress is presented.

8.3 Dark matter in CCDs (DAMIC)

K. Hansen and R. Roehnelt

DAMIC LN2 Automatic Control System Update

Significant effort has gone into the DAMIC project this year. The largest effort, literally, is the construction of a cleanroom inside NPL. A key system to make this cleanroom useful is the delivery of liquid nitrogen (LN2) to the DAMIC cryostat. Initially the supply was a single dewar with a solenoid for flow control. We are now in the process of updating this sytem with the goal of having a system that can recognize when the supply LN2 dewar is empty and switch over to a new dewar without interrupting the intended detector temperature.

The current set up has the supply dewar outside the Lead Lab with the liquid nitrogen line running up the outside wall of the Lead Lab, through the wall, over the front of the cleanroom frame, and back down to the detector dewar. Fitting the liquid nitrogen line into this space required a couple hard 90 degree turns. The welcomed side effect of these sharp corners is a restricted flow resulting in the final liquid nitrogen delivery rate being moderate to slow. The supplying dewar is controlled by a solenoid. The solenoid state is determined by a PID control system that consists of four algorithms that either cool down, warm up, maintain cold, or maintain warm. These PID algorithms get temperature data points from resistance temperature detectors (RTD) epoxied directly onto the detector dewar wall from inside the cryostat chamber.

One problem with the current design is that the solenoid state is determined by the temperature of the detector dewar and if the liquid nitrogen supply runs out, the PID control system won't recognize it until the detector dewar starts to warm up. To solve this problem, a manifold with two dewars controlled by separate solenoids with an RTD attached to the pipe after the solenoids will be installed. If the RTD reads that the pipe is approximately at liquid nitrogen temperature and the PID control system is asking the solenoid to be open, then the dewar still has liquid nitrogen. If the temperature of the pipe is not near liquid nitrogen temperature even though the RTD control system is asking the solenoid to be open, then the dewar is empty and that solenoid needs to be closed and a second solenoid to the backup dewar should open. This gives us time to change the empty dewar out and the process repeats. The new manifold incorporates pressure relief valves. Each side of the manifold has its own 20 psig relief valve, matching the relief valves on the supply dewar. For the case when both solenoids are closed there is a 1 psig relief valve that is connected to the overflow system.

Figure 8.3-1. Current liquid nitrogen supply setup. The uni-struts are the mounting structure for the new manifold.

Figure 8.3-2. The new manifold for the two supply dewars. The RTD will be attached to the pipe that connects to the middle flared fitting.

The other problem DAMIC wants to address at the same time is that when the solenoid closes the gas in the liquid nitrogen line warms up and when the solenoid opens again the detector will rise in temperature from this burst of warm gas that has built up. This results in spikes in temperature in the cryostat dewar. The solution we are going to install is simply a solenoid that diverts the flow in the liquid nitrogen line into a waste dewar for a given amount of time until the warm air has been purged and the liquid nitrogen starts to flow properly, then the solenoid will divert the flow back to the dewar.

CCD Packaging

In the prior year, the CCDs that were to be tested at UW (PAB, NPL) and U. Chicago were in short supply and became the bottleneck in project progress. Recognizing this issue, project management took several steps to remedy the situation. One of these steps was to request a redesign of the CCD packages to streamline fabrication and assembly. Using simplicity of design and commonality of hardware as a guide, the CCD packaging effort went from 1 or 2 CCDs packaged per month to being able to package 1 CCD per day.

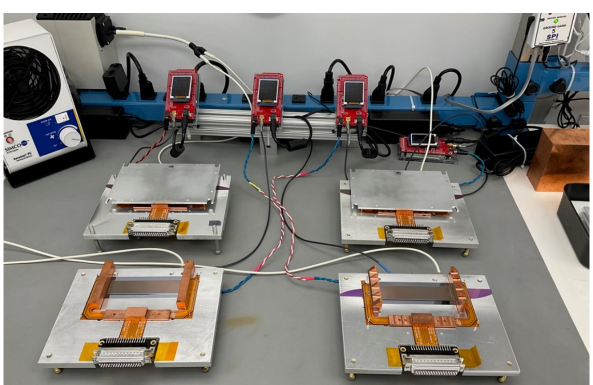

Figure 8.3-3. CCD Packaging Production Line in PAB. (Picture: Marcel Conde)

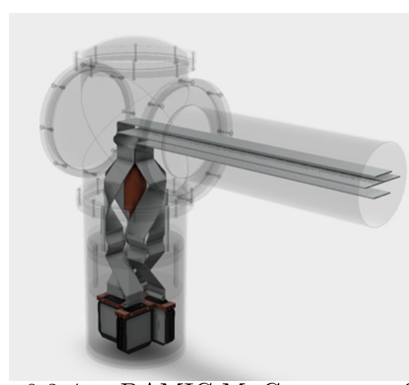

Figure 8.3-4. DAMIC-M Cryostat. Original design from T. Burritt and J. Amsbaugh. Shown is a result of collaboration of R. Roehnelt, B. Stillwell (U. Chicago), and A. Cadiou (Subatech).

As the project moves away from low mass single CCD detectors to higher mass array detectors, the design gets more complicated. Constraints include use of only radio pure materials, good thermal conductivity, and low stress. This larger detector is slated to be installed at Modane.

8.4 ^{6}He CRES improvements

B. W. Dodson and R. Roehnelt

This project requested some hardware changes to achieve better signal in the experiment. The most critical change involved a reconfiguration of the NMR probe in a more homogeneous region of the magnetic field. The existing magnet bore inner vacuum shell required modification so the NMR probe could sit as close to the waveguide as possible—with the previous configuration placing the probe outside the vacuum shell. This required reimagining the endplate of the vacuum shell with a 'probe reentry' tube at atmosphere that fit the tight space constraints of the inner waveguide and supporting hardware. Additionally, the experimenters desired a design that could accommodate future hardware insertions into the inner vacuum shell region. The solution was to design a custom CF flange fitting at the end of the vacuum shell with a welded probe entry tube analogous to a blank CF flange. With this design, custom flanges can be installed to fit new experiment configurations without further modifying the vacuum shell.

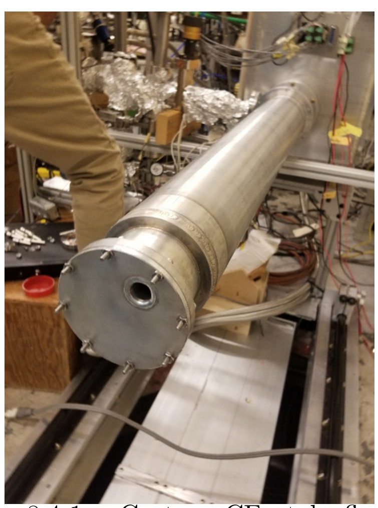

Figure 8.4-1. Custom CF style flange with welded probe reentry tube

Figure 8.4-2. Waveguide hardware created tight space constraints

To improve the magnitude of the signal and reduce the background noise the project also requested the injector line diameter be increased and to eliminate a vacuum leak resulting from a design choice made for a vacuum flange.

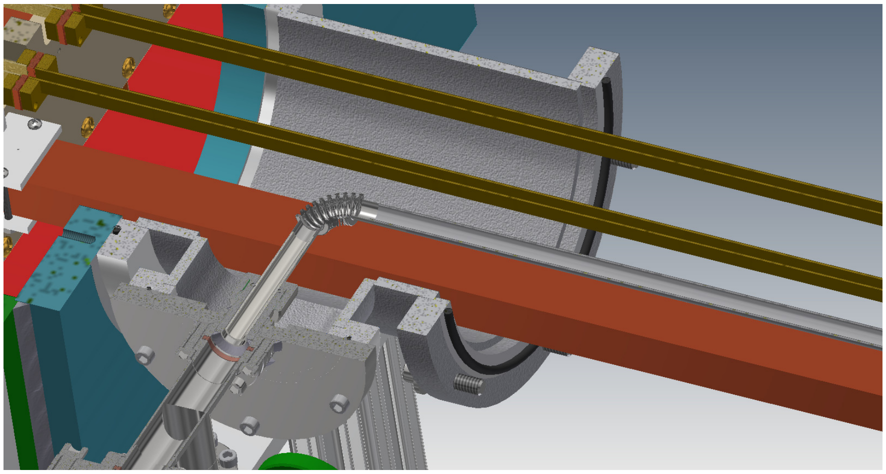

Figure 8.4-3. Cross section of vacuum flange and waveguide

8.5 Legend shipping containers

R. Roehnelt

As the Legend project moves to Legend-200 and then to Legend-1000, there will be more and more transport of Ge detectors around the world. As the number of shipments increase, so do the odds of something untoward happening, such as the poor shipping and handling which resulted in a fractured detector. That detector was a total loss, needing to be scrapped and recycled. The shipping container that was used on that shipment was elegantly designed to be simple and flexible – but it only works if there are no transverse shocks.

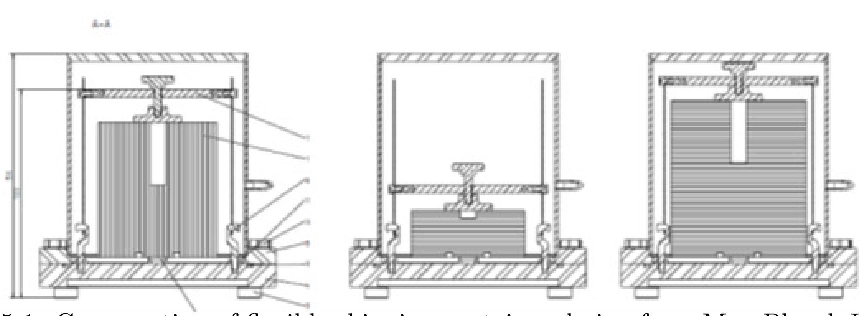

Figure 8.5-1. Cross section of flexible shipping container design from Max-Planck Institute drawing 015448.001.

Keeping the general shipping container outline and entire upper portion, an ESD compliant shipping container was developed to protect these detectors from shocks up to at least 200g in arbitrary directions.

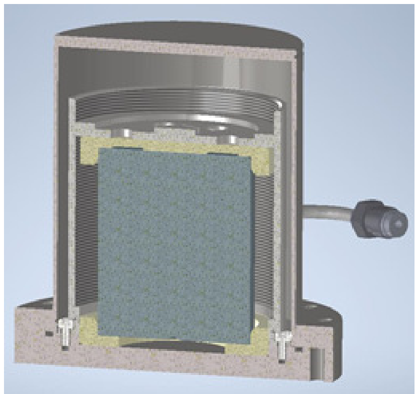

Figure 8.5-2. CAD Cross Section of Assembly.

Figure 8.5-3. As fabricated (Picture: J. Detwiler).

8.6 Majorana

B.W. Dodson, S.J. Meijer, M. Stortini, and C. Wiseman

This experiment is part of the Majorana Collaboration, which searches for neutrinoless double-beta decay ($0\nu\beta\beta$) using an array of high-purity germanium detectors. Data from the Majorana Demonstrator shows that an expected 10.8 keV X-ray line from ^{210}Pb is missing, but that its 46.5 keV line is present. To improve background models, and to better understand our low-energy limits, we aim to understand why this peak is missing and at what energy we can expect to start seeing peaks. It is hypothesized that passivated surface effects are the cause of the missing ^{210}Pb peak in our data. The objective here is to design an X-ray fluorescence (XRF) source that will allow us to study the passivated surface, and observe its effect on X-ray peaks over a range of low-energy values.

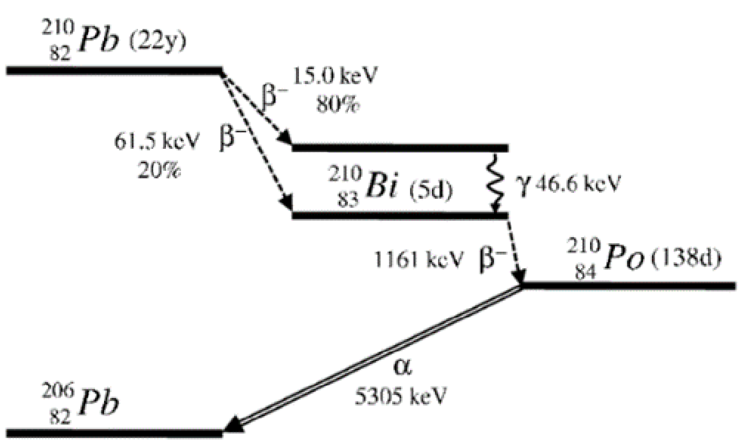

Figure 8.6-1. ^{210}Pb Decay Chain.

The apparatus will be fixed inside a cryostat and uses beta source ^{99}Tc in conjunction with a collection of foils selected so X-rays ranging from ∼8-70 keV can be observed. In choosing these foils, we searched for energies of interest in the material's kα1 line, as this line has the highest rate of production. The foils we use are Zn (kα1= 8.639), Nb (16.615), Ag (22.163), Nd (37.361), and Au (68.804). This configuration requires the apparatus have a motorized foil selection mechanism so the source will not have to be removed from the cryostat when switching foils for data acquisition.

To limit the backgrounds created by this configuration, a graded Z disk to separate the source and the foils was an imperative selection. Material near the source is required to limit bremsstrahlung and block betas, and the following material needs to be higher Z to mute the bremsstrahlung created. Aluminum was selected as the low Z material encasing the source, tungsten as the higher Z material for shielding. Figure 8.6-2 is shown to better describe the limiting parameters of this experiment. In this figure, the upper geometry represents the XRF apparatus, and the lower geometry is the PPC germanium detector that is used at UW. In this depiction d2 is chosen such that a beta that just passes through the upper hole, d1, will also just pass through the lower hole, d2. The equation relating d2 and d1 to make this true is shown, consequently d1 and d2 will be different for each foil, so that counting rates can be controlled.

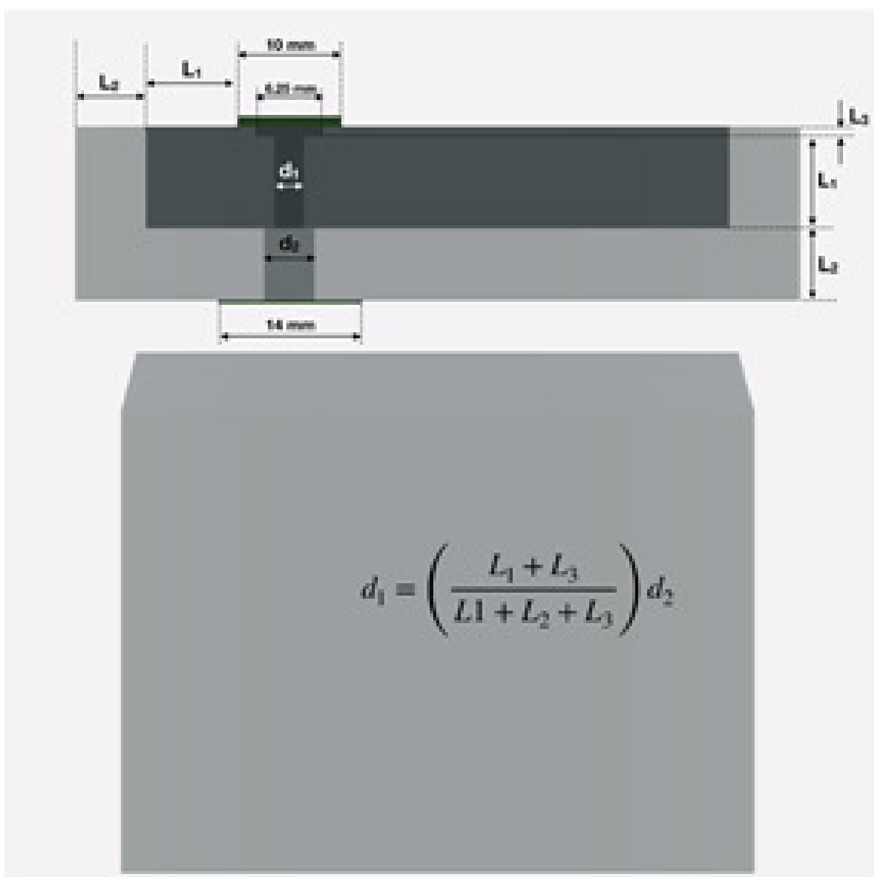

Figure 8.6-2. Shows design parameters to fit experiment objectives.

The resulting design consists of a series of disks, with the top two aluminum "source holder" disks encasing the source fixed to the cryostat lid with short bolts, allowing the rest of the assembly to rotate via a center staff attached to a stepper motor. The shaft includes several coupling pieces, starting with a g10 fitting to thermally isolate the stepper motor from the rest of the aluminum shaft. At the bottom of the center shaft is a tungsten dowel pin mated via solder to the bottom tungsten "foil holder" disk encasing the five foils. The dowel pin was selected to be the same material as the foil holder to minimize possible joint failures via differing thermal expansion coefficients. The bottom foil holder has six bolt tabs for aligning the source above each foil in a testing environment that can be encoded to the stepper motor; inside the cryostat during data acquisition these tabs are not used. There are two shielding disks with that fit together between the bottom foil holder and top source holding disks with the described d2 and d1 holes for controlled beta passage. The outer disk, denoted D2 is made of tungsten and the inner disk, D1, is made of aluminum. The tungsten foil holder is fixed to the tungsten D2 disk with small screws, and the aluminum D1 disk sits inside the D2 disk. This arrangement allows for free rotation of the center shaft, bottom foil holder, and both shielding disks as the top aluminum source holding disks are fixed to the encasing cryostat as described. The XRF apparatus has been fully designed and fabricated and has been sent to LANL to have the Tc Source and incident foils installed. Testing and data acquisition will begin once the apparatus is sent back to CENPA.

Figure 8.6-3. Preliminary design of assembly.

Figure 8.6-4. As fabricated design. The thin aluminum plate above the source holding disks is a shield to protect the stepper motor from any reflected radiation.

8.7 Project-8

M. Kallandar and R. Roehnelt

This project has an amazing number of moving pieces. In one experiment we have white hot Tungsten, vacuum, the intense magnetic field of a MRI, and temperatures approaching 10K in the center of the magnetic field.

Electron Gun

Once the magnetic field is mapped, it is important to understand the behavior of the of the CRES detector and how it will interact with that field. Some calibration method is required. Since the experiment signal will be electrons spiraling in a magnetic field, the natural method of performing the calibration is to fire known energy electrons into the detector and see what the output signal is. The initially provided sketch from Hamish Robertson was simply presented but contained a richness of detail.

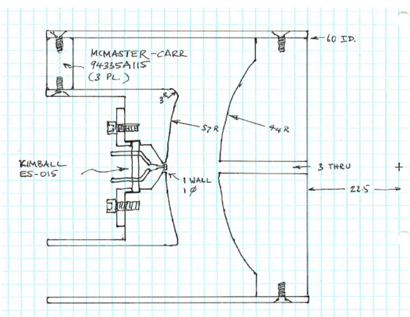

Figure 8.7-1. Design Sketch: R. G. H. Robertson.

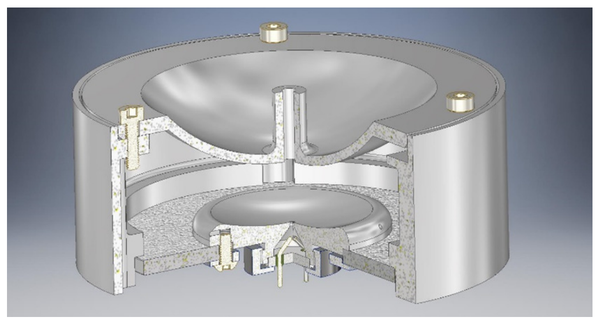

Figure 8.7-2. Initial CAD design.

From this stage, it became more complicated as this Pierce electron gun needed to be mounted in vacuum, in the homogeneous region of the MRI magnetic field, as well as be moved from field line to field line. After some discussion it was determined this would be done with piezo actuators outside of the vacuum chamber, using a flexible bellows to enable the motion. But before we can get to that point, we need to mount it on a test stand and show this e-gun design works.

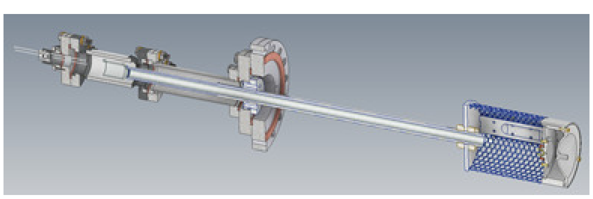

Figure 8.7-3. Test stand configuration.

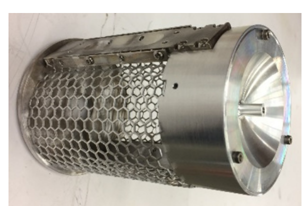

Figure 8.7-4. Fabricated e-gun.

Coaxial Hydrogen Cracker

In its end design, Project 8 will use atomic tritium as its neutrino source, eliminating uncertainties arising from the molecular final states. To produce atomic tritium, some form of dissociation is required to separate the normally diatomic molecule. CENPA is investigating a thermal cracker as a possible option. The cracker consists of two coaxial tungsten tubes, joined at one end by electron beam welding. Current is passed through the thin-walled inner tube, then flows to ground through the thicker-walled outer tube, resistively heating the inner tube. Gas flowing through the inner tube dissociates upon contacting the hot walls. Recombination is kinematically disfavored, resulting in a beam of single atoms. Only a custom built dissociator can provide the high intensity atomic beam required for the final measurement. To study the beam, we have built a differentially pumped vacuum chamber with a Hidden Analytical brand quadrupole mass spectrometer inserted in the beamline. Testing and calibrating the mass spectrometer is done with a lower intensity hydrogen atom beam source provided by Dr. Eberl MBE-Komponenten GmbH. The atomic source test stand is being upgraded to include a rotating beam chopper and cryogenically cooled accommodator stage. When complete, the atomic source test stand will be used to make time of flight measurements and determine the velocity distribution of the beam when it enters the later cooling and trapping stages.

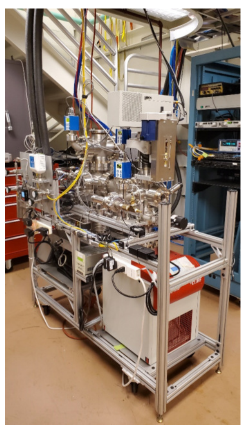

Figure 8.7-5. Atomic source test stand.

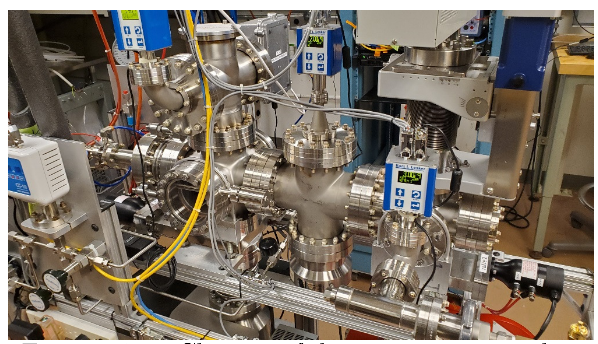

Figure 8.7-6. Close up of the atomic test stand beam line.

Auxiliary Test Stand

CENPA engineering constructed a second vacuum system to test components while the atomic source test stand is in use. This stand features a gated Leybold Turbolab 450 turbomolecular pump, electrical feedthrough flange, an adjustable linear translation arm and a Larson Scientific glass nipple for attaching test articles, all mounted to a lightweight, mobile frame. The stand has been used to test the coaxial cracker and will be used for future tests of the electron gun.

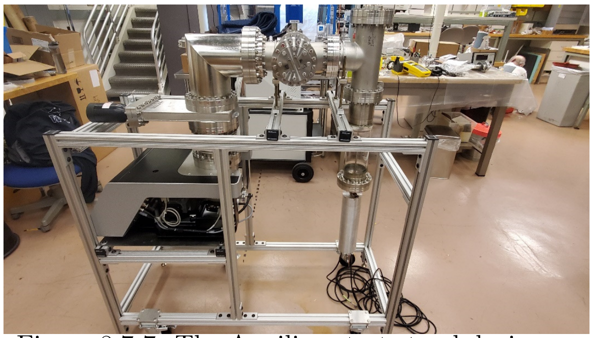

Figure 8.7-7. The Auxiliary test stand during assembly.

Figure 8.7-8. The coaxial cracker mounted in the auxiliary test stand.

CENPA electronics shop

8.8 CENPA electronic shop

D. A. Peterson and T. D. Van Wechel

The electronics shop is responsible for the design and construction of new laboratory electronic equipment as well as the maintenance and repair of existing CENPA electronics. Projects undertaken by the electronics shop in the past year include the following:

1. Several amplifiers were designed and constructed for the LEGEND collaboration. These include a charge sensitive amplifier for the CAGE OPPI detector tests, and an avalanche photodiode amplifier. Also an improved version of the charge amplifier with forward biased reset was constructed and will undergo testing with the MJ60 detector.
2. The electronics shop is involved in the setup and control of the 30 kV HV bias power supply, and the implementation of the solar cell based filament power for the Project 8 electron gun. A ripple monitor circuit was designed and constructed for observing any noise or ripple present on the HV bias at the cathode of the electron gun.

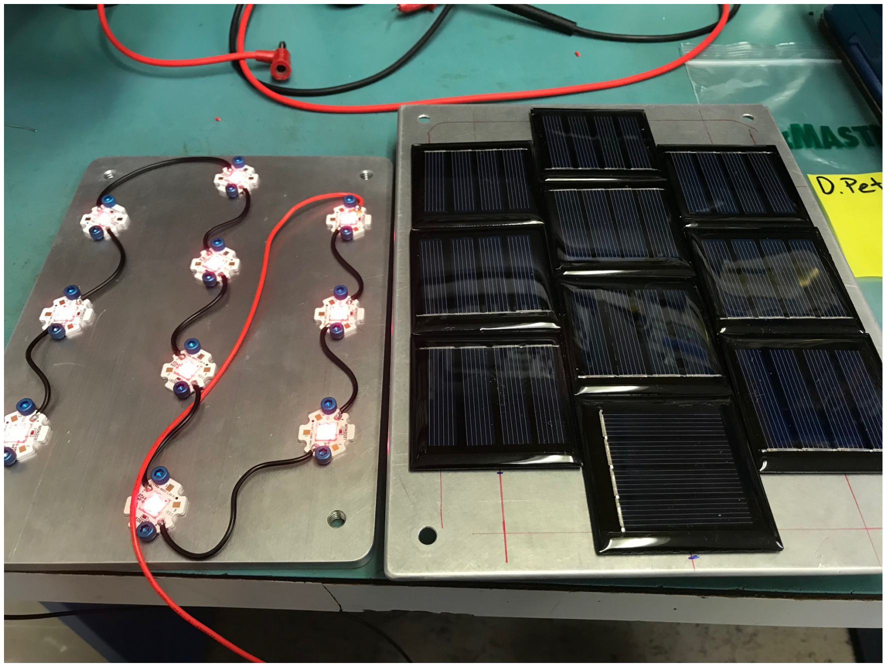

Figure 8.8-1. LED and solar panels for Project 8 electron gun filament supply isolation.

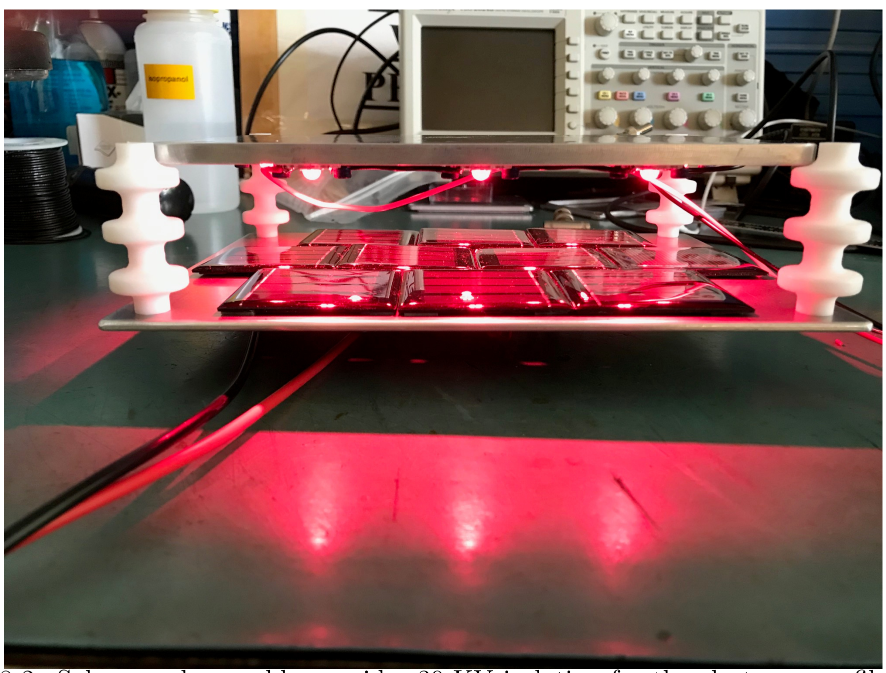

Figure 8.8-2. Solar panel assembly provides 30-KV isolation for the electron gun filament power.

3. A 7 channel RTD readout was constructed for Project 8.
4. Design of a trigger circuit for the SELENA readout ADC amplifier board.
5. Construction of DAMIC-M signal/power breakouts, cables and adapters.

CENPA compute cluster

8.9 Operation of the cenpa-rocks computer cluster

G. Holman and D. J. Prindle

We continue to operate the cenpa-rocks Linux cluster as a computing resource for CENPA. This is a heterogeneous cluster consisting of roughly 130 nodes. These compute nodes are DELL Power Edge R410 blades of three types: one with 12 cores and 48 GB of memory per node, one with eight cores and 24 GB of memory per node and one with eight cores and 16 GB of memory per node. The cluster is managed with rocks cluster software[1]. Users connect to a login node and interact with the compute nodes using Sun Grid Engine (SGE). In addition to the compute nodes we have significant data storage in three large raid systems offering a total of 175 TB of storage. The raid systems are connected to DELL Power Connect 6248 switches with paired 10 Gb/s fiber connections and the switches are connected to the compute nodes via 1 Gb/s ethernet. There are also hard drives distributed throughout the compute nodes managed as a single 40 TB filesystem using XRootD.

We have been able to operate the cluster inexpensively by relying on the infrastructure (and some of the compute nodes) left from the previous Athena cluster which was installed in 2009. This infrastructure includes the power and power distribution, the cooling and the racks and physical setup. Two years ago we reported on augmenting our compute nodes with nodes surplussed from NERSC[2]. These nodes and our original Athena nodes are all over ten years old and over the past year a number of them have gone offline. We acquired 150 Dell R620 servers from the generous donation by Bryce Livingston at The Institute for Health Metrics and Evaluation (IHME). These were acquired through an inventory transfer UW form 1024. Lastly Some of the Power Connect switches are showing signs of age. We plan to replace these with refurbished units at less than $200 each or upgrade the backplane to 10GBE.

At over 1000 cores and significant data storage cenpa-rocks offers a powerful computing platform at very low cost. As much of the infrastructure is quite old there are a number of possible failure points. Among these are the switches, power strips and cooling fans. These can be replaced at low cost. We expect to be able to maintain and, with new nodes obtained from surplus, enhance the cenpa-rocks cluster as a computing resource for CENPA over the next year and hopefully beyond.

8.10 Building maintenance, repairs, and upgrades

G. Holman

During the 2021 calendar year, 150 work orders (WOs) were placed for the North Physics Laboratory buildings which house the CENPA research facility. Of which there are 99 closed

[1]https://www.rocksclusters.org/

[2]CENPA Annual Report, University of Washington (2019) p. 161.

and 51 open. Of the total WOs, 78 are for yearly maintenance and 72 CENPA requests by CENPA staff.

1. Water hammer in the hydronic heating system.

There has been a water hammer in the hydronic heating system for the Van de Graaff Accelerator Building high bay setup area and adjacent offices. This problem still has not been solved.

2. Replacement of fluorescent lamps with LED lamps.

An effort is ongoing to replace any failed fluorescent lamp fixtures (i.e. failed lamp ballasts), both indoor and outdoor, with LED lamp fixtures and lamps. The outdoor lights under the eaves are being preemptively replaced with LED fixtures and lamps at UW Electricians availability.

3. Compressed-air leak in highbay.

There is an air leak in the compressed-air line in the highbay cement floor. This issue is currently being addressed by UW facilities. This issue impacts the environmental controls in some parts of the Van de Graaff building.

4. Multistack Maglev (TurboCor) Chiller.

The Multistack Maglev chiller with FlexSys control system in RM 154, which provides chilled water for CENPA, is again operational. The differential water pressure sensor of chilled water input and output experiencing 100+ psig pressures, that are above of the sensor's 100 psig limit, which caused the sensor to output a value below the acceptable operating limit of the control system. UW Refrigeration Group has installed sensor with a 250 psig limit. Once the chilled water and condenser lines were tuned and balanced, interestingly enough, the differential pressure is again below 100 psig and the system is performing optimally.

UW Refrigeration consultants visited CENPA, installed four Variable Frequency Drive (VFD) controlled chilled water pump motors, pressure sensors, and various automatic control valves.

9 CENPA Personnel

10 CENPA Personnel

10.1 Faculty

Alvaro Chavarria	Assistant Professor
Jason Detwiler	Associate Professor
Peter J. Doe	Research Professor
Sanshiro Enomoto	Research Associate Professor
Alejandro García	Professor
David W. Hertzog	Professor; Director
Peter Kammel	Research Professor
R. G. Hamish Robertson	Professor Emeritus
Gray Rybka	Associate Professor

CENPA Faculty not with DOE CENPA grant support

Eric G. Adelberger	Professor Emeritus
John G. Cramer	Professor Emeritus
Jens H. Gundlach	Professor
Blayne R. Heckel	Professor Emeritus
Leslie J Rosenberg	Professor Emeritus
Derek W. Storm	Research Professor Emeritus

10.2 Postdoctoral Research Associates

Chelsea Bartram[1]	ADMX
Christine Claessens	Project 8 / Muon $g-2$
Conner Gettings[1]	ADMX
Brent Graner	He-6 CRES
Zachary Hodge	Muon $g-2$
Alexander Marsteller	KATRIN / Project 8
Tatsumi Nitta[1]	ADMX
Elise Novitski	Project 8
Michael Ross[1]	Gravity
Patrick Schwendimann	Muon $g-2$ / PIONEER
David Sweigart	LEGEND
Clint Wiseman	MAJORANA / LEGEND

[1]Not supported by DOE CENPA grant.

10.3 Predoctoral Research Associates

Hannah Binney	Muon $g-2$
Sam Borden	LEGEND
Thomas Braine[1]	ADMX
William (Drew) Byron	He-6 CRES
Raphael Cervantes[1]	ADMX
Winston Degraw	He-6 CRES
Madison Durand	COHERENT
Nick Du[1]	ADMX
Michaela Guzzetti[1]	ADMX
Heather Harrington	He-6 CRES
Alexandru Hostiuc	MAJORANA
Joshua La Bounty	Muon $g-2$
Brynn MacCoy	Muon $g-2$
Kellie McGuire[1]	DAMIC
Ethan Muldoon	MuSun
Christian Nave	LEGEND
Xiaochen Ni[1]	Selena
Alexander Piers[1]	DAMIC
Nicholas Ruof	MAJORANA / LEGEND
Erik Shaw[1]	Gravity
James Sinnis[1]	ADMX
Grace Song[1]	LEGEND

10.4 Master's Student

Kelly Burroughs	He-6 CRES
Edward Hanes	He-6 CRES
Savannah Hightower	He-6 CRES
Melanie Kimsey Lin	He-6 CRES

[1]Not supported by DOE CENPA grant.

10.5 Professional staff

Tom H. Burritt	RS/Engr Sr	Precision design, machining
Brittney Dodson	RS/E1	Jr. Engineer, ADMX safety officer
Gary T. Holman[1]	Associate Director	Computer systems
Michael Huehn	RS/E1	Jr. Engineer, Project 8, DAMIC
Matthew Kallander	RS/E Assistant	Jr. Engineer, Project 8
Grant H. Leum	RS/E1	ADMX Liquifier
Duncan J Prindle	RS/E4	MuSun research, Cluster admin
Ryan Roehnelt	RS/E4	Sr. Mechanical Engineer
Eric B. Smith	RS/E3	Accelerator, ion sources
H. Erik Swanson	RS/Engr Sr	Precision experimental equipment
Timothy Van Wechel	RS/E4	Analog and digital electronics design

10.6 Technical staff

James H. Elms[1]	Instrument Maker
David A. Peterson	Electronics Technician

10.7 Administrative staff

Ida Boeckstiegel[2]	Office Administrator
TBD	Fiscal Specialist 2

10.8 Part-time staff and student helpers

Gwen Bayarbaatar	Kyle Fitzsimmons
Kiera Hansen	Dylan Soh

[1] Retired December 2021; replacement search in progress.
[2] Departed November 1st, 2021; replacement search in progress.

11 Publications

Published papers

1. Aker, M. *et al.* Bound on 3+1 Active-Sterile Neutrino Mixing from the First Four-Week Science Run of KATRIN. *Physical Review Letters* **126.** ISSN: 1079-7114. `http://dx.doi.org/10.1103/PhysRevLett.126.091803` (Mar. 2021).
2. Aker, M. *et al.* Analysis methods for the first KATRIN neutrino-mass measurement. *Physical Review D* **104.** ISSN: 2470-0029. `http://dx.doi.org/10.1103/PhysRevD.104.012005` (July 2021).
3. Formaggio, J. A., de Gouvêa, A. L. C. & Robertson, R. G. H. Direct measurements of neutrino mass. *Physics Reports* **914,** 1–54. ISSN: 0370-1573. `http://dx.doi.org/10.1016/j.physrep.2021.02.002` (June 2021).
4. Ashtari Esfahani, A. *et al.* Bayesian analysis of a future beta decay experiment's sensitivity to neutrino mass scale and ordering. *Physical Review C* **103.** ISSN: 2469-9993. `http://dx.doi.org/10.1103/PhysRevC.103.065501` (June 2021).
5. Aker, M. *et al.* Precision measurement of the electron energy-loss function in tritium and deuterium gas for the KATRIN experiment. *The European Physical Journal C* **81.** ISSN: 1434-6052. `http://dx.doi.org/10.1140/epjc/s10052-021-09325-z` (July 2021).
6. Aker, M. *et al.* The design, construction, and commissioning of the KATRIN experiment. *Journal of Instrumentation* **16,** T08015. ISSN: 1748-0221. `http://dx.doi.org/10.1088/1748-0221/16/08/T08015` (Aug. 2021).
7. Gando, Y. *et al.* The nylon balloon for xenon loaded liquid scintillator in KamLAND-Zen 800 neutrinoless double-beta decay search experiment. *JINST* **16,** P08023. arXiv: `2104.10452 [physics.ins-det]` (Apr. 2021).
8. Akimov, D. *et al.* A D2O detector for flux normalization of a pion decay-at-rest neutrino source. *JINST* **16,** P08048. arXiv: `2104.09605 [physics.ins-det]` (2021).
9. Abe, S. *et al.* Search for Low-energy Electron Antineutrinos in KamLAND Associated with Gravitational Wave Events. *Astrophys. J.* **909,** 116. arXiv: `2012.12053 [astro-ph.HE]` (2021).
10. Akimov, D. *et al.* Development of a ^{83m}Kr source for the calibration of the CENNS-10 liquid argon detector. *JINST* **16,** P04002. arXiv: `2010.11258 [physics.ins-det]` (2021).
11. Arnquist, I. J. *et al.* Search for double-β decay of ^{76}Ge to excited states of ^{76}Se with the MAJORANA DEMONSTRATOR. *Phys. Rev. C* **103,** 015501. arXiv: `2008.06014 [nucl-ex]` (2021).
12. Akimov, D. *et al.* First Measurement of Coherent Elastic Neutrino-Nucleus Scattering on Argon. *Phys. Rev. Lett.* **126,** 012002. arXiv: `2003.10630 [nucl-ex]` (2021).
13. Abgrall, N. *et al.* ADC Nonlinearity Correction for the Majorana Demonstrator. *IEEE Trans. Nucl. Sci.* **68,** 359–367. arXiv: `2003.04128 [physics.ins-det]` (2021).

14. Albahri, T. *et al.* Beam dynamics corrections to the Run-1 measurement of the muon anomalous magnetic moment at Fermilab. *Phys. Rev. Accel. Beams* **24,** 044002. arXiv: 2104.03240 [physics.acc-ph] (2021).

15. Abi, B. *et al.* Measurement of the Positive Muon Anomalous Magnetic Moment to 0.46 ppm. *Phys. Rev. Lett.* **126,** 141801. arXiv: 2104.03281 [hep-ex] (2021).

16. Albahri, T. *et al.* Magnetic-field measurement and analysis for the Muon $g-2$ Experiment at Fermilab. *Phys. Rev. A* **103,** 042208. arXiv: 2104.03201 [hep-ex] (2021).

17. Albahri, T. *et al.* Measurement of the anomalous precession frequency of the muon in the Fermilab Muon $g-2$ Experiment. *Phys. Rev. D* **103,** 072002. arXiv: 2104.03247 [hep-ex] (2021).

18. Hong, R. *et al.* Systematic and statistical uncertainties of the hilbert-transform based high-precision FID frequency extraction method. *Journal of Magnetic Resonance* **329,** 107020. ISSN: 1090-7807. https://www.sciencedirect.com/science/article/pii/S1090780721001099 (2021).

19. Schreckenberger, A. P. *et al.* The fast non-ferric kicker system for the Muon g−2 Experiment at Fermilab. *Nucl. Instrum. Meth. A* **1011,** 165597. arXiv: 2104.07805 [physics.ins-det] (2021).

20. Carey, R., Gorringe, T. & Hertzog, D. Mulan: a part-per-million measurement of the muon lifetime and determination of the Fermi constant. *SciPost Phys. Proc.* **5,** 016. arXiv: 2108.09182 [nucl-ex] (2021).

21. Kammel, P. MuSun - Muon Capture on the Deuteron. *SciPost Phys. Proc.* **5,** 018 (2021).

22. Li, X. *et al.* Measurement of the ionization response of amorphous selenium with 122 keV γ rays. *JINST* **16,** P06018. arXiv: 2012.04079 [physics.ins-det] (2021).

Papers submitted or to be published

23. Aker, M. *et al.* First direct neutrino-mass measurement with sub-eV sensitivity. arXiv: 2105.08533 [hep-ex] (2021).

24. Barinov, V. V. *et al.* Results from the Baksan Experiment on Sterile Transitions (BEST). arXiv: 2109.11482 [nucl-ex] (Sept. 2021).

25. Abe, S. *et al.* Limits on astrophysical antineutrinos with the KamLAND experiment. arXiv: 2108.08527 [astro-ph.HE] (Aug. 2021).

26. Abgrall, N. *et al.* The Large Enriched Germanium Experiment for Neutrinoless $\beta\beta$ Decay: LEGEND-1000 Preconceptual Design Report. arXiv: 2107.11462 [physics.ins-det] (July 2021).

27. Agostini, M. *et al.* Testing the Inverted Neutrino Mass Ordering with Neutrinoless Double-Beta Decay. arXiv: 2107.09104 [hep-ph] (July 2021).

28. Abe, S. *et al.* Search for Solar Flare Neutrinos with the KamLAND detector. arXiv: `2105.02458 [astro-ph.SR]` (May 2021).

29. Abe, S. *et al.* A Search for Charged Excitation of Dark Matter with the KamLAND-Zen Detector. arXiv: `2101.06049 [hep-ex]` (Jan. 2021).

30. Edmonds, A. *et al.* A Measurement of Proton, Deuteron, Triton and Alpha Particle Emission after Nuclear Muon Capture on Al, Si and Ti with the AlCap Experiment. arXiv: `2110.10228 [physics.ins-det]` (Oct. 2021).

Invited talks

31. Novitski, E. *Direct Neutrino Mass Measurements: Future Status and Interplay with CMB-S4* CMB-S4 Science Workshop, hosted by the University of Chicago.

32. Novitski, E. *Project 8: the path to improved neutrino mass* 17th International Conference on Topics in Astroparticle and Underground Physics, online, hosted by Instituto de Fisica Corpuscular.

33. Hertzog, D. *First Results from the Fermilab Muon g-2 Experiment* Colloquium, University of Washington.

34. Hertzog, D. *First Results from the Fermilab Muon g-2 Experiment* Colloquium, University of British Columbia.

35. Hertzog, D. *First Results from the Fermilab Muon g-2 Experiment* Special Invited Session, American Physical Society April Meeting.

36. Hertzog, D. *First Results from the Fermilab Muon g-2 Experiment* Colloquium, University of Bern, Switzerland.

37. Hertzog, D. *First Results from the Fermilab Muon g-2 Experiment* Colloquium, Dresden University, Germany.

38. Hertzog, D. *First Results – and afterthoughts – from the Fermilab Muon g-2 Experiment* Colloquium, Paul Scherrer Institute, Switzerland.

39. Hertzog, D. *A next-generation rare pion decay experiment to study LFUV and CKM unitarity* Tau Lepton Physics (TAU2021).

40. Hertzog, D. *First Results – and afterthoughts – from the Fermilab Muon g-2 Experiment* Colloquium, Stanford University.

41. Detwiler, J. *How Neutrinos Go Bump in the Night: The COHERENT Experiment's quest to map out the faintest interaction of nature's most elusive particle* Physics Department Colloquium, Mainz University, Germany.

42. Chavarria, A. *Neutrino Physics with Selena* Physics Seminar, online, Wichita State University.

43. Graner, B. *Precision Nuclear Physics with Microwaves* The Collaboration for Astronomy Signal Processing and Electronics Research (CASPER) conference.

44. Graner, B. *Cyclotron Radiation Emission Spectroscopy: Precision Nuclear Physics with Microwaves* Indiana University Physics departmental seminar.

Abstracts and contributed talks

45. Chavarria, A. *The Selena Neutrino Experiment* 17th International Conference on Topics in Astroparticle and Underground Physics, online, hosted by Instituto de Fisica Corpuscular.
46. Graner, B. M. *Recent improvements to the 6He-CRES apparatus, data acquisition system, and analysis methods* Contributed talk to 2021 Fall Meeting of the APS Division of Nuclear Physics. https://meetings.aps.org/Meeting/DNP21/Session/PL.
47. Harrington, H. S. *Report of First Data from the 6He-CRES Experiment and Future Outlook* Contributed talk to 2021 Fall Meeting of the APS Division of Nuclear Physics. https://meetings.aps.org/Meeting/DNP21/Session/PL.
48. Byron, W. *An Introduction to the 6He-CRES Experiment* Contributed talk to 2021 Fall Meeting of the APS Division of Nuclear Physics. https://meetings.aps.org/Meeting/DNP21/Session/PL.

Book publications

49. García, A. Section: Experimental Tools - Accelerators. *Encyclopedia of Nuclear Energy, edited by E. Greenspan* (2021).
50. García, A. Section: What is the Universe Made Of? *Encyclopedia of Nuclear Energy, edited by E. Greenspan* (2021).

Ph.D. degrees granted

51. Hempstead, J. *Measuring the anomalous precession frequency* ωa *for the Muon g-2 experiment* PhD thesis (University of Washington, Department of Physics, Apr. 2021).